



UNIL | Université de Lausanne

Unicentre

CH-1015 Lausanne

<http://serval.unil.ch>

Year : 2012

CONSEQUENCES OF MODIFIED LIPID AND GLUCOSE METABOLISM ON PERIPHERAL NERVOUS SYSTEM STRUCTURE AND FUNCTION

Zenker Jennifer

Zenker Jennifer, 2012, CONSEQUENCES OF MODIFIED LIPID AND GLUCOSE
METABOLISM ON PERIPHERAL NERVOUS SYSTEM STRUCTURE AND FUNCTION

Originally published at : Thesis, University of Lausanne

Posted at the University of Lausanne Open Archive.
<http://serval.unil.ch>

Droits d'auteur

L'Université de Lausanne attire expressément l'attention des utilisateurs sur le fait que tous les documents publiés dans l'Archive SERVAL sont protégés par le droit d'auteur, conformément à la loi fédérale sur le droit d'auteur et les droits voisins (LDA). A ce titre, il est indispensable d'obtenir le consentement préalable de l'auteur et/ou de l'éditeur avant toute utilisation d'une oeuvre ou d'une partie d'une oeuvre ne relevant pas d'une utilisation à des fins personnelles au sens de la LDA (art. 19, al. 1 lettre a). A défaut, tout contrevenant s'expose aux sanctions prévues par cette loi. Nous déclinons toute responsabilité en la matière.

Copyright

The University of Lausanne expressly draws the attention of users to the fact that all documents published in the SERVAL Archive are protected by copyright in accordance with federal law on copyright and similar rights (LDA). Accordingly it is indispensable to obtain prior consent from the author and/or publisher before any use of a work or part of a work for purposes other than personal use within the meaning of LDA (art. 19, para. 1 letter a). Failure to do so will expose offenders to the sanctions laid down by this law. We accept no liability in this respect.

Department of Medical Genetics

**CONSEQUENCES OF MODIFIED LIPID AND GLUCOSE
METABOLISM ON PERIPHERAL NERVOUS SYSTEM STRUCTURE
AND FUNCTION**

Doctoral thesis in Neurosciences

presented by the

Faculty of Biology and Medicine
of the University of Lausanne

by

Jennifer Zenker

Graduate student of the University of Stuttgart-Hohenheim, Germany

Jury

Prof. Jean-Pierre Hornung, President
Prof. Roman Chrast, Director
Prof. Jacques S. Beckmann, Co-Director
Prof. Ueli Suter, Expert
Dr. Gesine Saher, Expert

Lausanne, February 2012

***Interuniversity doctoral program in neuroscience
of the University of Lausanne and Geneva***

**Programme doctoral interuniversitaire en Neurosciences
des Universités de Lausanne et Genève**

Imprimatur

Vu le rapport présenté par le jury d'examen, composé de

Président	Monsieur Prof. Jean-Pierre Hornung
Directeur de thèse	Monsieur Prof. Roman Chrast
Co-directeur de thèse	Monsieur Prof. Jacques S. Beckmann
Experts	Monsieur Prof. Ueli Suter Madame Dr Gesine Saher

le Conseil de Faculté autorise l'impression de la thèse de


Madame Jennifer Zenker

Biologiste diplômée de l'Université de Hohenheim, Allemagne

intitulée

CONSEQUENCES OF MODIFIED LIPID AND GLUCOSE METABOLISM ON PERIPHERAL NERVOUS SYSTEM STRUCTURE AND FUNCTION

Lausanne, le 25 mai 2012



pour Le Doyen
de la Faculté de Biologie et de Médecine

Prof. Jean-Pierre Hornung

Acknowledgements

I would like to thank Prof. Jean-Pierre Hornung, Prof. Ueli Suter and Dr. Gesine Saher for their participation in the thesis committee.

This thesis would not have been possible unless the enthusiastic supervision of Prof. Roman Chrast who has supported me throughout my thesis with his help, knowledge and encouragement. Furthermore, I would like to express my sincere gratitude to my co-director Prof. Jacques Beckmann. I am indebted to all my colleagues at the Department of Medical Genetics (DGM). It was a great pleasure to work with them. Special thanks go to Estelle Arnaud and Anne-Sophie de Preux Charles for their teaching, guidance and stimulating discussions at any time. Olivier Poirot contributed to my thesis with a great work on the *ex vivo* electrophysiological measurements of db/db mice. I would like to acknowledge also Jean-Jacques Médard for his help with the mouse husbandry and his technical support and Valérie Verdier for the proofreading of my thesis.

I am grateful to all collaborators for their work. The ongoing work of the myelin lipid composition analysis and *in vitro* experiments for the P2 project have been performed by Dr. Jos Brouwers and by the group of Dr. Mark Stettner respectively. Thierry Kuntzer helped us with the set up and evaluation of nerve conduction recordings and in collaboration with Catherine Lacroix he provided us human biopsies of diabetic patients to assess the clinical relevance of our data.

Without the support of my family and friends this thesis would not have been possible. Mama, it is impossible to describe in words what you gave to me – thanks for your incomparable strength, love and support. Likewise, I would like to thank the two most important men in my life, my brother Jan and my boyfriend Holger.

Abstract

284 million people worldwide suffered from type 2 diabetes mellitus (T2DM) in 2010, which will, in approximately half of them, lead to the development of diabetic peripheral neuropathy (DPN). Although DPN is the most common complication of diabetes mellitus and the leading cause of non-traumatic amputations its pathophysiology is still poorly understood. To get more insight into the molecular mechanism underlying DPN in T2DM, I used a rodent model of T2DM, the db/db mice.

In vivo electrophysiological recordings of diabetic animals indicated that in addition to reduced nerve conduction velocity db/db mice also present increased nerve excitability. Further *ex vivo* evaluation of the electrophysiological properties of db/db nerves clearly established a presence of the peripheral nerve hyperexcitability (PNH) phenotype in diabetic animals. Using pharmacological inhibitors we demonstrated that PNH is mostly mediated by the decreased activity of K_v1 channels. In agreement with these data I observed that the diabetic condition led to a reduced presence of the K_v1.2 subunits in juxtaparanodal regions of db/db peripheral nerves whereas its mRNA and protein expression levels were not affected. Importantly, I confirmed a loss of juxtaparanodal K_v1.2 subunits in nerve biopsies from type 2 diabetic patients. Together these observations indicate that the type 2 diabetic condition leads to potassium-channel mediated changes of nerve excitability thus identifying them as potential drug targets to treat some of the DPN related symptoms.

Schwann cells ensheath and isolate peripheral axons by the production of myelin, which consists of lipids and proteins in a ratio of 2:1. Peripheral myelin protein 2 (= P2, Pmp2 or FABP8) was originally described as one of the most abundant myelin proteins in the peripheral nervous system. P2, which is a member of the fatty acid binding protein (FABP) family, is a 14.8 kDa cytosolic protein expressed on the cytoplasmic side of compact myelin membranes. As indicated by their name, the principal role of FABPs is thought to be the binding and transport of fatty acids.

To study its role in myelinating glial cells I have recently generated a complete P2 knockout mouse model ($P2^{-/-}$). I confirmed the loss of P2 in the sciatic nerve of $P2^{-/-}$ mice at the mRNA and protein level. Electrophysiological analysis of the adult (P56) mutant mice revealed a mild but significant reduction in the motor nerve conduction velocity. Interestingly, this functional change was not accompanied by any detectable alterations in general myelin structure. However, I have observed significant alterations in the mRNA expression level of other FABPs, predominantly FABP9, in the PNS of $P2^{-/-}$ mice as compared to age-matched $P2^{+/+}$ mice indicating a role of P2 in the glial myelin lipid metabolism.

Résumé

Le diabète de type 2 touche 284 million de personnes dans le monde en 2010 et son évolution conduit dans la moitié des cas à une neuropathie périphérique diabétique. Bien que la neuropathie périphérique soit la complication la plus courante du diabète pouvant conduire jusqu'à l'amputation, sa physiopathologie est aujourd'hui encore mal comprise. Dans le but d'améliorer les connaissances moléculaires expliquant les mécanismes de la neuropathie liée au diabète de type 2, j'ai utilisé un modèle murin du diabète de type 2, les souris db/db.

In vivo, les enregistrements électrophysiologiques des animaux diabétiques montrent qu'en plus d'une diminution de la vitesse de conduction nerveuse, les souris db/db présentent également une augmentation de l'excitabilité nerveuse. Des mesures menées *Ex vivo* ont montré l'existence d'un phénotype d'hyperexcitabilité sur les nerfs périphériques isolés d'animaux diabétiques. Grâce à l'utilisation d'inhibiteurs pharmacologiques, nous avons pu démontrer que l'hyperexcitabilité démontrée était due à une réduction d'activité des canaux K_v1 . En accord avec ces données, j'ai observé qu'une situation de diabète conduisait à une diminution des canaux $K_v1.2$ aux régions juxta-paranodales des nerfs périphériques db/db, alors que l'expression du transcrit et de la protéine restait stable. J'ai également confirmé l'absence de canaux $K_v1.2$ aux juxta-paranoeuds de biopsies de nerfs de patients diabétiques. L'ensemble de ces observations montrent que les nerfs périphériques chez les patients atteints de diabète de type 2 est due à une diminution des canaux potassiques rapides juxtaparanodaux les identifiant ainsi comme des cibles thérapeutiques potentielles.

Les cellules de Schwann enveloppent et isolent les axones périphériques d'une membrane spécialisée, la myéline, composée de deux fois plus de lipides que de protéines. La protéine P2 (Pmp2 « peripheral myelin protein 2 » ou FABP8 « fatty acid binding protein 8 ») est l'une des protéines les plus abondantes du système nerveux périphérique. P2 appartient à la famille de protéines FABP liant et transportant les acides gras et est une protéine cytosolique de 14,8 kDa exprimée du côté cytoplasmique de la myéline compacte.

Afin d'étudier le rôle de P2 dans les cellules de Schwann myélinisantes, j'ai généré une souris knockout ($P2^{-/-}$). Après avoir validé l'absence de transcrit et de protéine P2 dans les nerfs sciatiques $P2^{-/-}$, des mesures électrophysiologiques ont montré une réduction modérée mais significative de la vitesse de conduction du nerf moteur périphérique. Il est important de noter que ces changements fonctionnels n'ont pas pu être associés à quelconque changement dans la structure de la myéline. Cependant, j'ai observé dans les nerfs périphériques $P2^{-/-}$, une altération significative du niveau d'expression d'ARNm d'autres FABPs et en particulier FABP9. Ce dernier résultat démontre l'importance du rôle de la protéine P2 dans le métabolisme lipidique de la myéline.

List of abbreviations

4-AP	4-aminopyridine
ACSF	artificial cerebrospinal fluid
APO	action potential
CAP	compound action potential
Co-IP	co-immunoprecipitation
CMAP	compound muscle action potential
CMT	Charcot-Marie-Tooth disease
CNS	central nervous system
CRAC	cholesterol recognition amino acid consensus
DM	diabetes mellitus
DPN	diabetic peripheral neuropathy
DRG	dorsal root ganglia
DTX-1	dendrotoxin 1
EAN	experimental allergic neuritis
FA	fatty acid
FABP	fatty acid binding protein
FFA	free fatty acids
GBS	Guillain-Barré Syndrome
GDAP1	ganglioside-induced-differentiation-associated protein 1
IENF	intraepidermal nerve fibers
KO	knockout
K _v	voltage-gated potassium channels
LMND	lower motor neuron diseases
MAG	myelin associated glycoprotein
MBP	myelin basic protein
MNCV	motor nerve conduction velocity
MPZ	myelin protein zero
Na _v	voltage-gated sodium channels
NCV	nerve conduction velocity
NFκB	nuclear factor κB
P2, PMP2	peripheral myelin protein 2
PBS	phosphate buffered saline
PCR	polymerase chain reaction
PLEKHG5	pleckstrin homology domain-containing, family G member 5
PLP	proteolipid protein
PMP22	peripheral myelin protein 22
PNH	peripheral nerve hyperexcitability

PNS	peripheral nervous system
qPCR	quantitative polymerase chain reaction
RP	refractory period
RT	room temperature
Scap	SREBP cleavage-activating protein
Scip	suppressed cAMP-induced POU
SLI	Schmidt-Lanterman Incisures
SNCV	sensory nerve conduction velocity
STZ	Streptozotocin
T1DM	type 1 diabetes mellitus
T2DM	type 2 diabetes mellitus
TBS-T	tris-buffered saline containing 0,1% Tween
TEA	tetraethylammonium
TTX	tetrodotoxin
WT	wild-type

Table of contents

ACKNOWLEDGEMENTS	II
ABSTRACT	III
RESUME.....	IV
LIST OF ABBREVIATIONS	V
LIST OF FIGURES	X
LIST OF TABLES	XII
1. INTRODUCTION	1
1.1 The structure of the peripheral nervous system	1
1.1.1 The neuron	2
1.1.2 The Schwann cell and the process of myelination.....	3
1.1.3 Node of Ranvier.....	6
1.1.4 Myelin composition	7
1.2 Function of the peripheral nervous system	8
1.2.1 Action potential	9
1.2.2 Compound action potential	9
1.2.3 Peripheral nerve excitability	10
1.2.4 Peripheral neuropathies.....	11
1.3 Diabetes mellitus	12
1.3.1 Pathophysiology	12
1.3.2 Diabetic peripheral neuropathy	13
1.3.3 Animal models for diabetes mellitus.....	14
1.4 Fatty acid binding proteins	15
1.4.1 P2.....	16
2. MATERIAL AND METHODS.....	18
2.1 Animals and human biopsies.....	18
2.1.1 db/db mice	18
2.1.2 Human biopsies.....	18
2.1.3 P2 ^{-/-} mouse model.....	18
2.1.4 P2 ^{-/-} /Shi ^{-/-} mice	19
2.2 Physiological and electrophysiological methods.....	19
2.2.1 Measurement of glycemia and plasma insulin levels.....	19
2.2.2 Determination of free fatty acids from blood plasma	19
2.2.3 Motor and sensory nerve conduction velocity	19
2.2.4 Ex vivo compound action potential recording	20

2.3	Histological and molecular biological methods	20
2.3.1	Morphometric analysis	20
2.3.2	Tissue fixation and embedding	21
2.3.3	Immunohistochemistry	21
2.3.4	Intraepidermal nerve fiber density	21
2.3.5	X-Gal staining	22
2.3.6	PCR and quantitative PCR.....	22
2.3.7	Total protein extraction	23
2.3.8	Western blot analysis.....	23
2.3.9	Co-immunoprecipitation	23
2.3.10	Cellular fractionation	23
2.3.11	Microarray.....	24
2.4	Others	26
2.4.1	Microdissection of sciatic nerve	26
2.4.2	Tail or toe DNA isolation	26
2.4.3	Statistics	26
3.	RESULTS.....	27
3.1	Altered distribution of juxtaparanodal K_v1-channels mediates peripheral nerve hyperexcitability in type 2 diabetes mellitus.....	27
3.1.1	Characterization of type 2 diabetes mellitus and diabetic peripheral neuropathy in db/db mice	27
3.1.2	Peripheral nerve morphology in db/db mice at 23 weeks of age	28
3.1.3	Peripheral nerve hyperexcitability in db/db mice mediated by altered K _v 1-channel activity	30
3.1.4	Altered juxtaparanodal K _v 1.2 localization under type 2 diabetic conditions.....	33
3.1.5	Molecular mechanism underlying the altered K _v 1.2 distribution.....	37
3.2	Generation of a knockout mouse model to study the role of peripheral myelin protein P2	39
3.2.1	Selective P2 expression in a subset of Schwann cells in wild-type mice	39
3.2.2	P2 expression profile in mouse models of peripheral neuropathies.....	42
3.2.3	Characterization of P2 ^{-/-} mouse strain with preserved myelination	43
3.2.4	Gene expression profiling of P2 ^{-/-} mice identified differentially gene expression of other FABP family members	48
3.2.5	<i>In vivo</i> analysis of P2-MBP interaction	51
4.	DISCUSSION	54
4.1	Altered distribution of juxtaparanodal K_v1-channels mediates peripheral nerve hyperexcitability in type 2 diabetes mellitus.....	54
4.1.1	db/db mice as a model for type 2 diabetes mellitus and diabetic peripheral neuropathy.....	54
4.1.2	Physiological and mechanistic implication of K _v 1-channels in PNH.....	54
4.1.3	Therapeutical applications	57
4.2	Generation of a knockout mouse model to study the role of peripheral myelin protein P2	58
4.2.1	P2 expression.....	58
4.2.2	Peripheral nerve function in P2 ^{-/-} mice	59
4.2.3	Lipid homeostasis-related role of P2 in Schwann cells.....	59
4.2.4	P2 and MBP are two independent myelin genes.....	61

5.	COLLABORATIVE PROJECTS.....	63
5.1	Global transcriptional programs in peripheral nerve endoneurium and DRG are resistant to the onset of type 1 diabetic neuropathy in <i>Ins2^{Akita/+}</i> mice	63
5.2	Mouse model of Charcot-Marie-Tooth disease type 4C	74
5.2.1	SH3TC2/KIAA1985 protein is required for proper myelination and the integrity of the node of Ranvier in the peripheral nervous system.....	75
5.2.2	SH3TC2, a protein mutant in Charcot–Marie–Tooth neuropathy, links peripheral .81 nerve myelination to endosomal recycling.....	81
5.3	Characterization of a mouse model of Charcot-Marie-Tooth disease type 4A and 2K.....	95
5.4	Characterization of a knockout mouse model of PLEKHG5	99
6.	REFERENCES	101

List of figures

Figure 1 : Structure of peripheral nerves.....	1
Figure 2 : Schematic drawing of a myelinated peripheral neuron.....	3
Figure 3 : Molecular pathways regulated by Nrg1/ErbB signaling.	4
Figure 4 : Transversal view of peripheral nervous system myelin.	5
Figure 5 : Longitudinal view of peripheral nervous system myelin.....	6
Figure 6 : Exemplary graph of an action potential and compound action potential.....	10
Figure 7 : Obese db/db mice and wild-type mice at 23 weeks of age.....	15
Figure 8 : P2 gene structure.	17
Figure 9 : Physiological profile of db/db and control mice during postnatal development and in adult mice at 23 weeks of age.....	27
Figure 10 : Myelin morphology in db/db mice as compared to wild-type mice.....	29
Figure 11 : Hyperexcitability of db/db peripheral nerves due to decreased K _v 1-channel function.....	32
Figure 12 : Altered K _v 1.2 distribution in db/db sciatic nerves at 23 weeks of age.	34
Figure 13 : Expression levels of ion channel subunits in WT and db/db mice at 5 and 23 weeks of age.	35
Figure 14 : Ion channel distribution and myelination of human nerve biopsies.	36
Figure 15 : Altered K _v 1.2 protein interactions and subcellular localization in db/db mice at 23 weeks of age.	37
Figure 16 : Expression profiles of FABPs present in the peripheral nervous system.....	40
Figure 17 : P2 protein localization in wild-type sciatic nerve and roots.....	41
Figure 18 : P2 expression in mouse models of peripheral neuropathy.....	43
Figure 19 : Generation of P2 ^{-/-} mice.....	44
Figure 20 : Physiological characterization of P10- and P56-old P2 ^{-/-} mice as compared to P2 ^{+/+} mice.....	45
Figure 21 : Preserved myelination of P2 ^{-/-} sciatic nerves at P10 and P56.	47
Figure 22 : Transcriptional changes in P2 ^{-/-} sciatic nerve endoneurium at P10.	48
Figure 23 : Comparison of microarray results with qPCR measurements of selected genes.	49
Figure 24 : FABP9 protein expression in P2 ^{-/-} mice.....	50
Figure 25 : Characterization of P2 ^{+/+} /Shi ^{-/-} and P2 ^{-/-} /Shi ^{-/-} mice versus P2 ^{+/+} /Shi ^{+/+} mice at P56.	51
Figure 26 : Preserved sciatic nerve myelination of P2 ^{+/+} /Shi ^{-/-} and P2 ^{-/-} /Shi ^{-/-} mice at P10 and P56.....	53
Figure 27 : Putative molecular mechanism underlying altered juxtaparanodal K _v 1.2 expression in db/db mice.	57

Figure 28 : The epigenetic and transcriptional landscape of the P2 locus.....	60
Figure 29 : Physiological properties of 2 and 5 months old GDAP1 ^{-/-} mice as compared to GDAP1 ^{+/+} mice.	96
Figure 30 : Preserved sciatic nerve morphology of GDAP1 ^{-/-} mice at 2 and 5 months of age.	97
Figure 31 : Physiological characterization of PLEKHG5 ^{-/-} mice at 6 months of age.....	99

List of tables

Table 1 : Major cell types of the peripheral nervous system.	2
Table 2 : Major peripheral myelin proteins.	8
Table 3 : Mouse models of peripheral neuropathies used in our lab.....	11
Table 4 : Established mouse models of type 1 and type 2 diabetes mellitus.	14
Table 5 : Annotated FABP genes and phenotypes of the corresponding knockout mouse models.....	16
Table 6 : PCR reaction mix.	22
Table 7 : List of primers.	25
Table 8 : List of antibodies.	25
Table 9 : Properties of CMAP shape of db/db and control mice at 23 weeks of age.....	28
Table 10 : Clinical profile of T2DM and control subjects.....	36
Table 11 : Properties of the CMAP curve of P2 ^{-/-} and P2 ^{+/+} mice at P56.....	46
Table 12 : Properties of the CMAP curve of P2 ^{+/-} /Shi ^{-/-} and P2 ^{-/-} /Shi ^{-/-} mice as compared to P2 ^{+/-} /Shi ^{+/-} mice at P56.....	51
Table 13 : Shape of the CMAP curve of GDAP1 ^{-/-} and GDAP1 ^{+/-} mice at 2 and 5 months of age.	96
Table 14 : Properties of the CMAP curve of 6 months old PLEKHG5 ^{-/-} and PLEKHG5 ^{+/-} mice.	100

1. Introduction

1.1 The structure of the peripheral nervous system

The peripheral nervous system (PNS) is the bond between the central nervous system (CNS) (brain and spinal cord) and the body's periphery (skin, muscles and other organs). The peripheral nerves serve as a "network" for the CNS to receive signals from the internal or external environment and, after being processed in the CNS, to send the appropriate responses back to the effector cell or tissue in the periphery. Therefore, the CNS and PNS are highly interacting with and depending on each other. However, anatomically both systems can be clearly separated from each other as the PNS consists of all nerves and ganglia outside of the brain and spinal cord. In total, a human being has 43 pairs of peripheral nerves, 12 cranial and 31 spinal nerve pairs, branching from the brain or spinal cord, respectively.

A peripheral nerve can be divided into three compartments. The inner most part, consisting of several bundles of nerve fibers, is called endoneurium. Each bundle is delineated by a fibroblast sheath, the perineurium, and these structures are embedded again in a collagenous matrix called the epineurium. Especially the epineurium contains high amount of adipocytes (1) (**Fig. 1**).

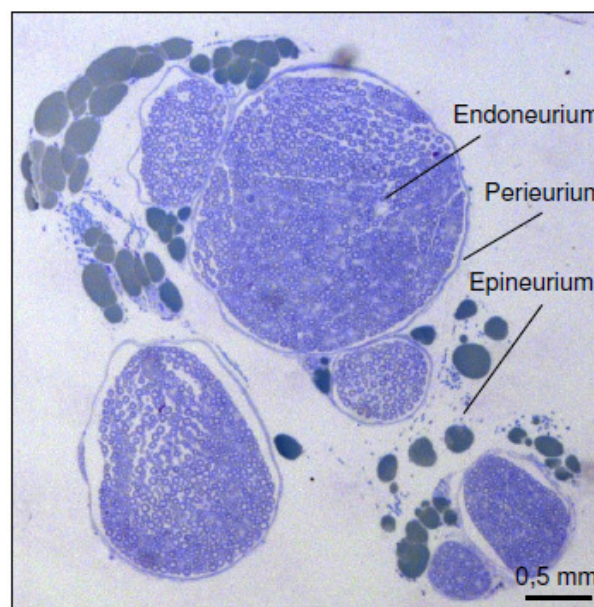


Figure 1 : Structure of peripheral nerves.

Cross semithin section of a murine sciatic nerve stained with Toluidine blue. Three layers of connective tissue can be identified: endoneurium, perineurium and epineurium.

Besides the neuron, a second cell type is crucial for the structural and functional composition of peripheral nerves, which are the glial cells. Glial cells of the PNS comprise the Schwann cells, Satellite cells and enteric glial cells (**Table 1**). Other cell types that are present in the endoneurium, albeit less frequently, are fibroblasts, endothelial cells, macrophages, mast cells and dendritic cells.

Cell type	Localization	Function
Neuron	cell bodies in the ventral horn (motor) or in DRGs (sensory) of the spinal cord; axons forming the peripheral nerve	electrical excitable cells, transmission of electrical signal;
Schwann cell		
- nonmyelinating	ensheathing small peripheral axons (< 1 μ m)	contribute to vitality und functionality of unmyelinated axons; one Schwann cell ensheaths multiple axons forming a Remak bundle;
- myelinating	ensheathing large peripheral axons (> 1 μ m)	to produce myelin and isolate the axons, one axon can be associated with several thousand Schwann cells; promote nerve regeneration; possess phagocytic properties;
- perisynaptic	at neuromuscular junctions	regulating the neuronal environment; involved in neurotransmission;
- terminal	at sensory axons	regulating the neuronal environment;
Satellite cell	surrounding cell bodies of DRGs and autonomic ganglia	controlling neuronal environment and the supply with nutrients and oxygen; function as diffusion barrier;
Enteric glia cell	enveloping autonomic ganglia of the gut	regulating neuronal environment and activity; involved in intestinal immune response;

Table 1 : Major cell types of the peripheral nervous system.

Both neurons and glial cells have the same developmental origin, deriving from the neural plate which is the most dorsal part of the ectoderm. During neurulation the neural plate becomes infolded and separated into the neural tube and the neural crest cells. Later in development, the neural tube differentiates into the brain and spinal cord of the CNS and into the motor neurons of the PNS. However, all sensory neurons and glial cells of the PNS are derived from the neural crest cells which are transient, multipotent cells that migrate away from the dorsal part of the neural tube to the periphery. Despite the same developmental origin neurons and glial cells have completely different roles in the PNS. (2)

1.1.1 The neuron

The neuron is the fundamental unit of the nervous system and is specialized in the transmission of electrical impulses. Functionally, neurons are commonly classified into two categories: sensory (= afferent) and motor (= efferent) neurons. Sensory neurons provide information about the external or internal environment to the CNS and their cell nuclei are accumulated close to the spinal cord within the dorsal root ganglia (DRGs). The CNS then sends the signal for the behavioural response via motor neurons to the target tissue (muscle or organs). The cell nuclei of motor neurons are located in the ventral horn of the spinal cord. Structurally (and functionally) the PNS can be divided into the somatic and autonomic PNS, which regulate the conscious and unconscious activities of the body respectively. Thus, peripheral neurons must be able to convey electrical signals along distances ranging from millimeters to meters. Consequently the structure of a neuron is characterized by its high

number of cell processes (**Fig. 2**). First, dendrites are fine and short branched extensions, receiving signals in case of a motor neuron from upstream neurons and they transmit the information towards the cell body. The cell body contains the cell nuclei, the majority of the cytoplasm and all important organelles. Second, the stimulated motor neuron carries the information away from the cell body to the target cell or tissue via a long, singular process – the axon. In sensory neurons the signal transmission is reversed. During development, the axon is growing out from the cell body to its target directed by interactions with the extracellular matrix via chemoattractant or repellent molecules and by neurotrophic factors of the target cell. The established communication site between the axon terminal and another neuron or peripheral tissue is called synapse. (3)

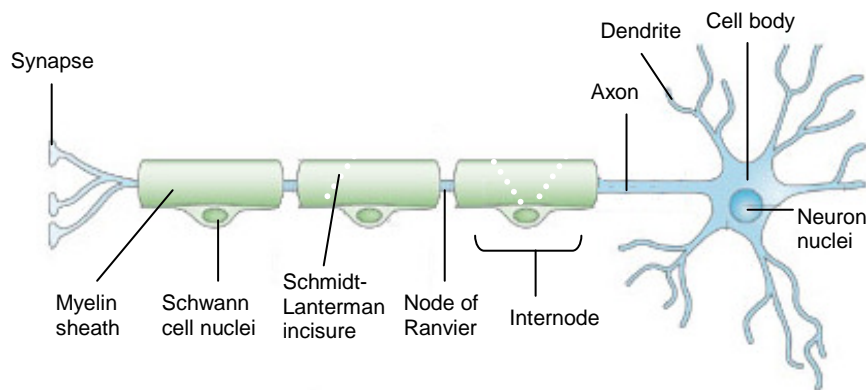


Figure 2 : Schematic drawing of a myelinated peripheral neuron.

The neuron is presented in blue with its major structures, including dendrites, cell body with cell nuclei, axon and synapse. Myelin sheaths produced by Schwann cells are labeled in green. The myelin sheaths of adjacent Schwann cells, referred to internodes, are separated by the node of Ranvier. Each myelin sheath is crossed by cytoplasmic channels called Schmidt-Lanterman incisures. (adapted from (4));

As majority of proteins of the neuron are synthesized in the cell body, they have to be carried out to the multiple processes of the cell. Thus, axonal transport is crucial for the functionality and survival of the neuron. In general, microtubuli and actin filaments serve as transport support. Specific adaptor proteins allow motor proteins of the kinesin family to recognize and bind their cargos and transport them anterogradely towards the axonal terminal. A retrograde transport is carried out by dynein motor proteins. Many different motor and adaptor proteins have already been identified for the selective transport of different neuronal molecules (5, 6).

1.1.2 The Schwann cell and the process of myelination

Glial cells are not electrically excitable but are crucial for the development of the PNS as well as for the isolation, survival and regeneration of neurons. By numbers, the PNS has many more glial cells than neurons.

The Schwann cell is the major type of peripheral glial cells and the counterpart of the oligodendrocyte in the CNS. The maturation of neural crest cells to mature Schwann cells, usually present around birth, goes through two intermediate stages (2). First, Schwann cell

precursors can be found at embryonic stages E12/E13 in mice, followed by immature Schwann cells at E15/E16 in mice. Except the transition from Schwann cell precursor to immature Schwann cells, all stages are reversible. Furthermore, the three cell types of Schwann cell maturation are characterized by their close association with axons and dependence on axonal survival and differentiation factors. Immature Schwann cells already extend processes in order to segregate axons into smaller bundles and produce the basal lamina. Once matured, Schwann cells exit the cell cycle and adopt either a myelinating or non-myelinating phenotype. Although all matured Schwann cells are theoretically able to synthesize myelin, Schwann cells associated with axons of a smaller size (diameter < 1 μm) do not produce myelin but enwrap a bundle of multiple axons only with a thin layer of Schwann cell membrane to separate and support them. Such bundles of unmyelinated axons are called Remak bundles. Schwann cells in contact with larger axons (diameter > 1 μm) establish a 1:1 contact with them and enwrap the underlying axon with myelin.

Initiation and regulation of the process of myelination is relatively well characterized in the PNS (**Fig. 3**) (7). Binding of axonal Nrg1 type III to ErbB2/ErbB3 receptors on the Schwann cell membrane plays a critical role in the determination of the amount of myelin produced by Schwann cells (as myelin thickness is proportional to the axonal diameter) (8). Following this initial signaling events, multiple transcription factors are known to promote the initiation and progression of myelination (e.g. Sox10, Scip and Krox20) (9).

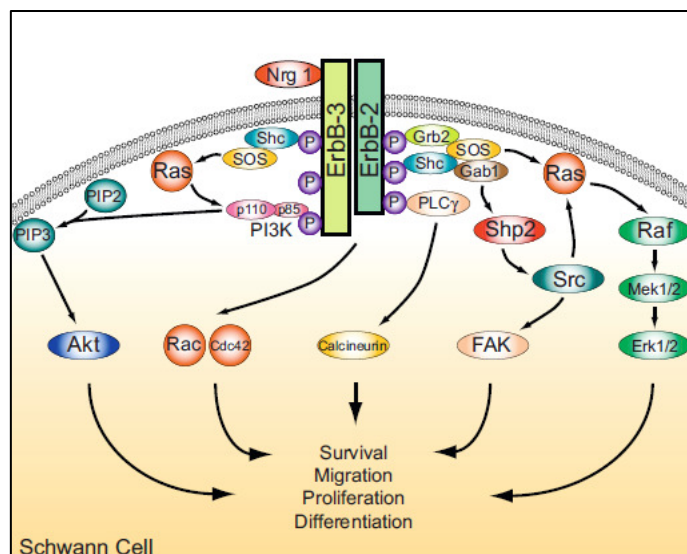


Figure 3 : Molecular pathways regulated by Nrg1/ErbB signaling.

Binding of neuronal Nrg1 type III to ErbB2/3 receptors on the Schwann cell membrane regulates various downstream pathways as depicted, which are involved in the control of Schwann cell survival, migration, proliferation, differentiation and thus myelination. (taken from (7));

Myelin is a tightly packed, multilayer membrane which isolates the axonal membrane in order to increase the nerve conduction velocity (NCV) (**Fig. 2 and 4**). In the PNS, every myelin sheath is covered by a basal lamina, which is secreted by the Schwann cell and most likely essential for myelination and neuronal regeneration (10). The mechanism how the myelin sheath is deposited around the axon was unclear until 1989. At this time it was shown

by Bunge et al. that the inner lip of the myelin sheath (inner mesaxon) is rotating around the axon and producing the new myelin layers and not the external lip (outer mesaxon) by rotations of the Schwann cell nuclei (11). While the medial myelin sheaths are free of cytoplasm, the outer and inner most layers (ab- and adaxonal membrane) still contain cytoplasm and the former one includes the Schwann cell nucleus.

As the very tight compaction of the myelin layers reduces the presence of conductive material (cytoplasm or extracellular medium), it enhances the isolating function of it. The cytoplasmic leaflets of a myelinating Schwann cell membrane are fused together forming the dark dense line while the exoplasmic leaflets form the intraperiod line of the myelin sheath (12). (**Fig. 4**). The intracellular transport of nutrients, ions and other small molecules has to be assured by restricted areas of non-compacted myelin. These regions of non-compact myelin are called the Schmidt-Lantermann incisures (SLI) which are narrowed cytoplasmic channels within the internode providing access from the cell body through the whole myelin sheath (**Fig. 2**), the mesaxons to the inner- and outermost limits (**Fig. 4A**) and the paranodes to the lateral edges (**Fig. 5**). These regions are characterized by the absence of dark dense and intraperiod lines as well as by a unique subset of myelin proteins (e.g. MAG and Cx32).

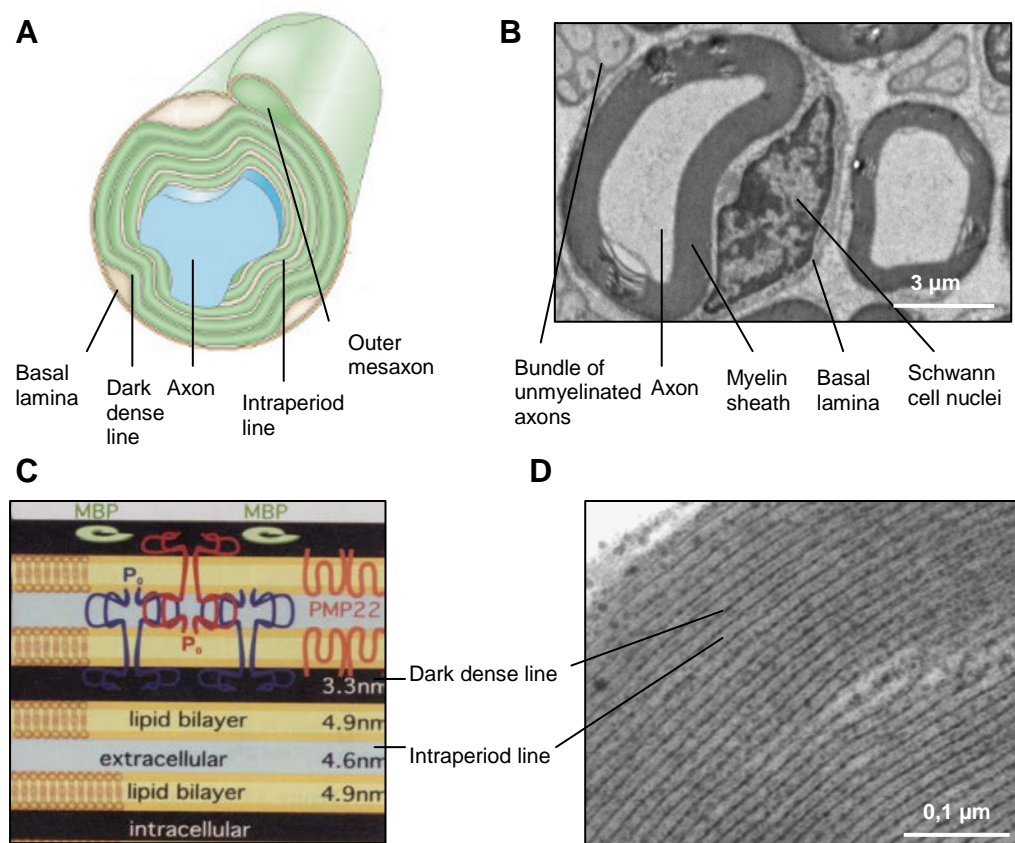


Figure 4 : Transversal view of peripheral nervous system myelin.

(A) Schematic graph of the multilayer myelin sheath. The close apposition of the inner plasma membranes form the dark dense lines while that of the outer plasma membrane layers form the intraperiod lines. The cytoplasmic ridge of the outer mesaxon is shown. All peripheral nerves are surrounded by a basal lamina. (B) Ultrathin cross section of a murine adult sciatic nerve. (C) Scheme of protein localization in compact myelin. (D) Myelin compaction as observed *in vivo* in ultrathin cross sections of adult murine sciatic nerve. (A) adapted from (4); (C) from (12);

1.1.3 Node of Ranvier

In unmyelinated fibers ion channels are diffusely distributed along the whole nerve fiber, hence the electrical signal transmission is continuous and slow. Myelinated fibers are divided into regions of molecular, structural and functional specification which enhance the speed of signal conduction (13). Internodes are the consecutive myelin segments produced by a Schwann cell and are separated by unmyelinated gaps called nodes of Ranvier (**Fig. 2 and 5**) which are flanked on each side by the paranodal and juxtaparanode regions (**Fig. 5**).

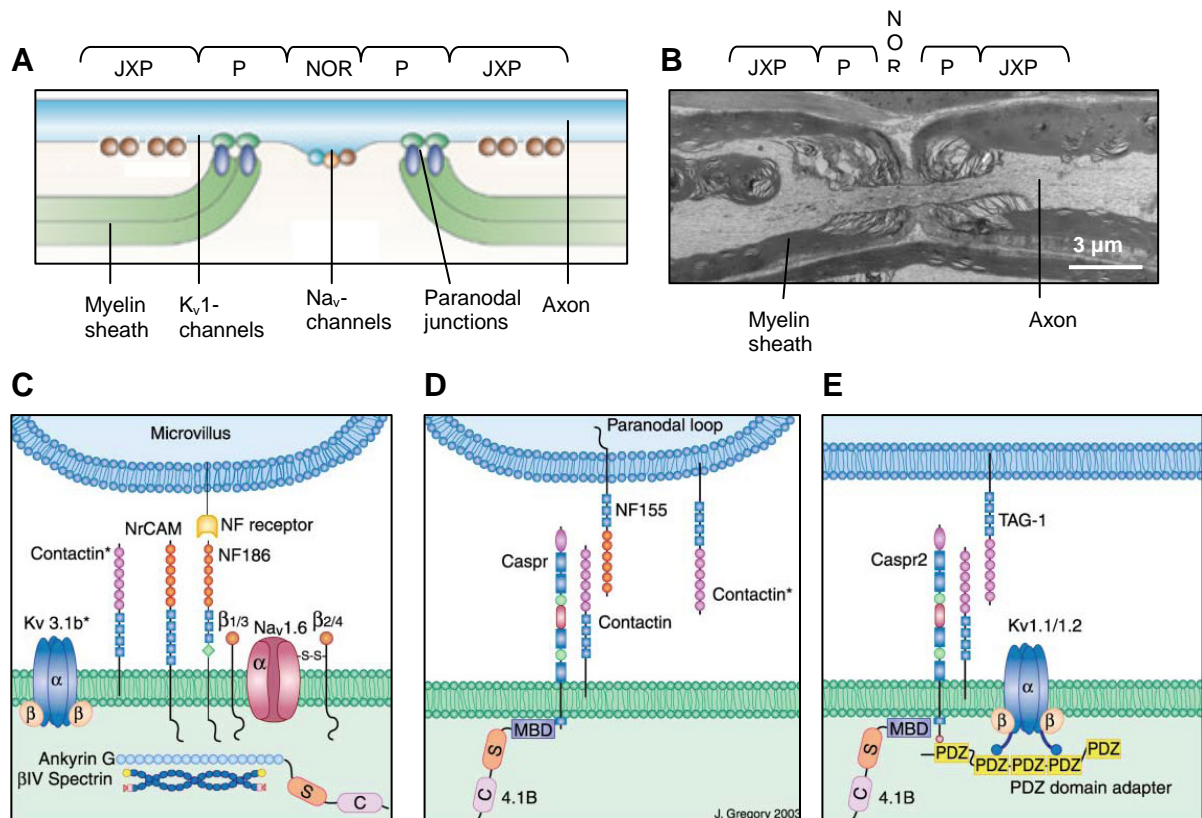


Figure 5 : Longitudinal view of peripheral nervous system myelin.

(**A and B**) Order of the nodal domains, node of Ranvier (NOR), paranode (P) and juxtaparanode (JXP), in a peripheral nerve presented schematically and *in vivo* respectively. The molecular components characteristic for each domain is further described for the node of Ranvier (**C**), the paranode (**D**) and the juxtaparanode (**E**). (Scheme (**A**) adapted from (4) and (**C-E**) from (13));

Voltage-gated Na^+ -channels (Na_v) are crucial for the propagation of the electrical signal along the axon and are highly concentrated at the node of Ranvier. Therefore, the electrical signal jumps from one node to the next one leading to a fast saltatory conduction velocity along myelinated fibers. Na_v -channels are composed of one large pore-forming α -subunit, predominantly $\text{Na}_v1.6$ in the PNS, and two transmembrane β -subunits. Ankyrin G anchors the Na_v -channels to the node of Ranvier by connecting it to the cytoskeleton protein βIV spectrin. Other neuronal adhesion molecules, NF186 and NrCAM, interact with ankyrin G and might be involved in the localization of Na_v -channels as well. Also present at the node, are voltage-gated K^+ -channels (K_v): $\text{K}_v3.1b$ the function of which is still unknown and $\text{K}_v7.2/\text{K}_v7.3$ controlling the slow potassium current and nerve excitability (14, 15). Unlike in

the CNS, the nodes in peripheral nerves are covered by microvilli of the Schwann cell. (**Fig. 5C**)

The paranodal region is characterized by the presence of paranodal junctions, which are complexes of two adhesion molecules, Caspr and Contactin. These junctions connect the lateral margins of the myelin sheath, the paranodal loops, with the axon reflecting the closest neuron-glia apposition in the PNS. On the axonal site the paranodal junctions are further connected to the cytoskeleton protein 4.1B and on the paranodal loops with NF155. The paranodal junctions represent a diffusion barrier between the node and juxtaparanode (**Fig. 5D**). Loss of Caspr or Contactin leads to a widening of the paranodal space and altered localization of juxtaparanodal ion channels (16, 17).

The juxtaparanodal region is enriched in voltage-gated Shaker-like potassium channels (K_v1) that are responsible for the fast potassium conductance in axons. K_v1 -channels are composed of four pore-forming α -subunits, either $K_v1.1$ or $K_v1.2$, and four cytoplasmic β -subunits. The adhesion molecules Caspr2 and TAG-1 are responsible for the targeting of the K_v1 -channels to the juxtaparanodal regions (18, 19), which are connected to 4.1B via an unknown PDZ domain protein (**Fig. 5E**).

1.1.4 Myelin composition

Majority of cell membranes are composed of lipids and proteins mixed with a 1:1 ratio. The lipid bilayer of the plasma membrane defines the cell and only small, uncharged molecules can pass this barrier. Proteins integrated into the lipid bilayer, allows the cell to exchange larger, charged molecules to receive and transmit signals from the outside or to make contact with other cells. Indeed, the set of membrane proteins and not the lipids defines the functional differences between membranes of the ER, Golgi, mitochondria or myelin. The role of the myelin membrane is to isolate the axon from its environment. This is achieved by an increased lipid-to-protein ratio to 2:1 and by the presence of myelin-specific proteins involved in the tight compaction of the multiple layers of myelin.

Lipids:

Phospholipids, glycolipids and cholesterol are the three major lipid classes present in myelin and other plasma membranes. However, the amount of cholesterol, galactolipids (= glycolipid), plasmalogens (= phospholipid) and saturated long-chain fatty acids (FA) are significantly increased in myelin membranes (20). Overall, CNS and PNS myelin have a similar lipid composition except that PNS myelin contains a much higher amount of sphingomyelin than CNS myelin (20, 21).

For the insulating role of myelin the optimization of the membrane fluidity, compaction and permeability of polar molecules, predominantly ions, is crucial. Lack of one lipid component can already disturb these biophysical properties of the myelin membrane as demonstrated by

knockout (KO) mouse models for cholesterol (22) or galactolipid synthesis (23). Thus, the lipid composition of myelin can be an indicator for defects in the myelin integration and/or nerve function.

Proteins:

Myelin contains a large set of relatively specific proteins with significant differences between PNS and CNS (24-26). The three major PNS myelin proteins are MPZ, Periaxin and MBP (**Table 2**), while in the CNS these are PLP and MBP which can be found in smaller amounts as well in the PNS. Animal models deficient for important PNS myelin genes provided insight about their function and thus the myelin structure (**Table 2**). Overall myelin proteins are involved in myelin compaction, stabilization, protein transport, cell adhesion and signaling as well as in lipid and glucose metabolism (24).

Protein name	Abundance	Function	KO mouse model
Cx32	< 0,5%	expressed in uncompact myelin; forming gap junctions crucial for ion homeostasis	axonal abnormalities with secondary demyelination
MAG	< 0,3%	expressed in uncompact myelin and periaxonal space; axo-glial interaction and myelin integrity	late-onset degeneration of myelinated axons; disruption of paranodal loops
MBP	5 - 15%	myelin compaction - to fuse the cytoplasmic sides of one myelin layer forming the dark dense line	"Shiverer-mice", severe tremors and demyelination in the CNS; increased number of SLI in PNS
MPZ	> 50%	myelin compaction - MPZ tetramers between two adjacent myelin layers forming the intraperiod line	severe hypomyelination with enlarged intraperiod lines; axonal degeneration
P2	1 - 10%	still unknown; suggested role in lipid transport	
Periaxin	5%	expressed early on in adaxonal membrane linked to the axon, later in abaxonal membrane bound to basal lamina; myelin stabilization	neuro-muscular defects in regions of demyelinated nerve fibers
Pmp22	2 - 5%	still unknown; most likely myelin stabilization	"Trembler-mice", hypermyelination followed by demyelination and axonal defects

Table 2 : Major peripheral myelin proteins.

References for the following KO mouse models: Cx32 (27), MAG (28), MBP (29, 30), MPZ (31), Periaxin (32) and Pmp22 (33).

1.2 Function of the peripheral nervous system

At rest, the neuronal membrane has a difference in the electrical potential between the outside and the inside of the cell, like every other cell. This voltage gradient is called membrane potential and is caused by an uneven distribution of ions along the membrane. The passive transport of ions is driven by the ion gradient and the selective permeability of the membrane with a predominance of potassium ion efflux. Consequently, the inside of the

cell has typically -70 mV with respect to the outside. However, neurons (and muscle cells) possess additional voltage-gated ion channels integrated in their membrane. These channels allow the cells to actively modify their membrane potential and to send electrical signals from one cell to another. (3)

1.2.1 Action potential

The electrical signal, triggered from the dendrites or cell body of a neuron to the tip of the axon, is called action potential (APO) and is produced by a consecutive exchange of ion currents through the plasma membrane.

Following the stimulation of a neuron, Na_v -channels at the node of Ranvier open. The influx of Na^+ -ions causes a depolarization of the membrane potential. In case the stimulus depolarizes the membrane to a threshold of -55 mV an APO will be induced. The APO leads to the maximal depolarization of the membrane as all remaining Na_v -channels open immediately and is thus an “all-or-none” response. Any stronger stimulation cannot further increase the response. Temporally delayed the juxtaparanodal K_v1 -channels open leading to a repolarization of the APO due to an enhanced efflux of K^+ -ions, at about the same time the Na_v -channels close. As the K_v -channels remain open longer than necessary to re-establish the initial membrane potential, it causes a transient hyperpolarization (**Fig. 6A**) During this time, called refractory period (RP), the neuronal membrane is unable to generate a new APO thus determining the frequency of the APO and inhibiting its reversion. Once the APO reached the synapse it induces neurotransmitter release to stimulate the postsynaptic neuron or muscle cell. However, such a stimulation can also be inhibitory causing a further hyperpolarization of the membrane potential and preventing the generation of an APO.(3)

1.2.2 Compound action potential

The APO described above is the response of one single nerve fiber. However, in a peripheral nerve many nerve fibers are activated synchronously by a stimulus. The resulting response of the nerve is the sum of all individual APOs and is called compound action potential (CAP). If the response is recorded in the corresponding muscle it is referred to compound muscle action potential (CMAP).

Compared to the single peaked “all-or-none” response of the APO, the CAP curve has multiple peaks and is graded (**Fig. 6B**). First, as the conduction velocity is directly linked to the axonal diameter, the curve of the CAP can be subdivided into three components. The first peak corresponds to the large, myelinated and thus the fastest $\text{A}\alpha/\beta$ -fibers, followed by the second peak of thinly myelinated $\text{A}\delta$ -fibers and later the slow unmyelinated C-fibers. Second, at a low stimulus strength only large fibers are activated. An increase in the stimulus strength leads to the activation of more and more small-size axons until every fiber is

stimulated at the maximal stimulus. Therefore, the CAP is graded because the excitability of a nerve fiber is inversely correlated to its axonal diameter.

Alterations in the CAP area and amplitude are used in diagnostics to give information about the number of stimulated nerve fibers and the onset and duration of the CAP about the NCV (3, 34).

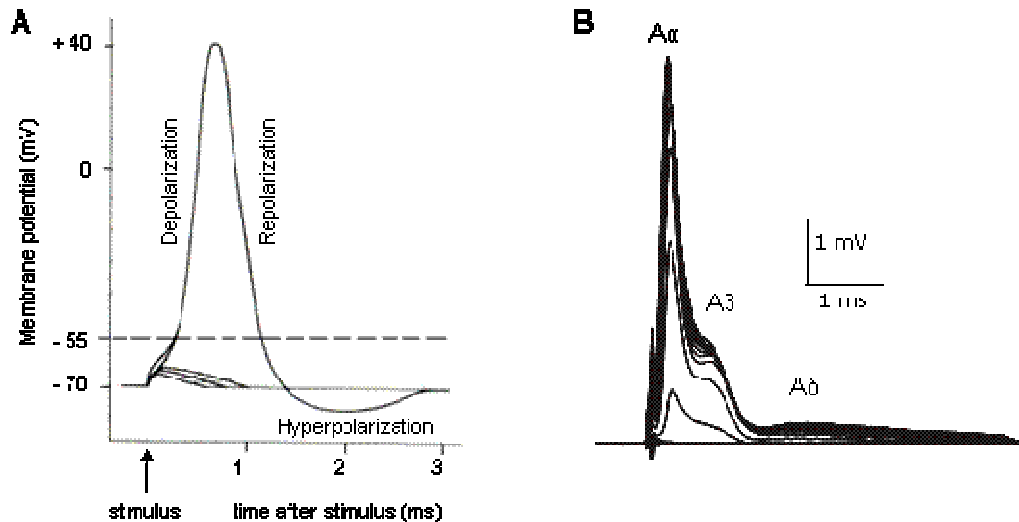


Figure 6 : Exemplary graph of an action potential and compound action potential.

(A) Graph showing exemplarily the different stages of an APO. After being stimulated to threshold the membrane potential becomes depolarized due to the opening of Na_v -channels. The repolarization is induced by a delayed opening of K_v -channels, followed by the closing of the Na_v -channels. A short overshoot of the repolarization leads to membrane hyperpolarization before reaching the membrane resting potential again. (B) shows a typical trace of a CAP, which is the sum of all APOs of a nerve. It is characterized by its graduated shape and multiple peaks corresponding to the speed of the different nerve fibers respectively.

1.2.3 Peripheral nerve excitability

The excitability of a peripheral nerve describes its ability to respond to a stimulus. As already described above the nerve excitability is inversely proportional to the fiber size (3). Alterations in the nerve excitability can lead to neurologocical disorders (35-37). Symptoms of peripheral nerve hyperexcitability (PNH) are muscular overaction, slow reaction, cramps and pain, and symptoms of peripheral nerve hypoexcitability are hypesthesia and anesthesia which are often characteristic for a wide range of peripheral neuropathies. However, alterations in nerve excitability are often associated with a normal NCV (38).

K^+ -currents are crucial for regulating the membrane potential. A reduction in the K^+ -current causes not only a less negative membrane potential but also an increase in peripheral nerve excitability as demonstrated in disease situation. Issac's syndrome (= neuromyotonia) is characterized by PNH due to an autoimmune reaction against K_v -channels. Episodic ataxia type 1, Diabetes mellitus (DM), Guillain-Barré-Syndrom (GBS) or amyotrophic lateral sclerosis are other diseases with PNH related to defects in K_v -channels (35, 36, 39, 40). This was further supported by KO mouse models of K_v1 -channels (41) and pharmacological block of the fast Shaker K_v1 -channels with 4-aminopyridine (4-AP) and dendrotoxin 1 (DTX-1), two

known blockers of these channels, which induced PNH (42). In addition to the K^+ -current, the Na^+ - and Ca^{2+} -currents can influence the nerve excitability as well (40).

1.2.4 Peripheral neuropathies

Peripheral neuropathies are disorders of the PNS caused by diseases or damage to the peripheral nerve. DM is the most common cause for peripheral neuropathy and will be discussed in-depth in chapter 1.3. Other prominent causes for peripheral neuropathy are inherited (e.g. Charcot-Marie-Tooth diseases (CMT)), autoimmune-induced (e.g. GBS) and toxin-induced disorders (e.g. by alcohol). Due to such a large diversity it is crucial to identify the cause for the peripheral neuropathy in order to treat the patient accordingly.

CMT diseases are caused by mutations in genes encoding proteins with specific roles in the Schwann cell or the neuron and thus can lead to either a demyelinating, axonal or intermediate phenotype. Nerve conduction studies are the most common tool to distinguish between the different phenotypes on electrophysiological level. Reduction in amplitude and/or area of the motor (or sensory) response is suggestive of axonal or neuronal loss and reduction in NCV suggestive of demyelination or defects in the integrity of the nodal region. Up to date, more than 50 genes are identified to be causative for the different forms of CMT (43). Animal models highly contributed to the understanding of the various CMT diseases. In our lab, we were involved in either the characterization (33, 44) or the generation and characterization (45) of several mouse models for different types of CMT as listed up in **Table 3**. In addition, we developed and/or characterized *Lpin1* and *Scap* knockout mice which develop peripheral neuropathy, thus demonstrating their role in the lipid metabolism of myelin (46, 47), however they are not (yet) linked to any human pathology (**Table 3**).

Gene mutation	Disease	Clinical feature
Mitofusin 2	CMT2A	axonal
Sh3tc2	CMT4C	demyelination
GDAP1	CMT4A	axonal, demyelinating or intermediate
PMP22	HNPP	dysmyelination/ax onal loss
PLEKHG5	?	demyelination or axonal
<i>Lpin</i>	-	demyelination
<i>Scap</i>	-	demyelination

Table 3 : Mouse models of peripheral neuropathies used in our lab.

GBS is triggered by an abnormal immunological response against the body's own myelin that ensheaths peripheral nerves (48). This might be the consequence of an infectious disease. Interestingly, GBS in animal models, referred to experimental allergic neuritis (EAN), can be induced by injections of peripheral myelin or specific protein domains of P0 (49), P2 (50) or Pmp22 (51).

1.3 Diabetes mellitus

DM is a group of metabolic diseases characterized by hyperglycemia resulting from defects in insulin secretion, insulin action or both. Its prevalence has reached epidemic rates with over 366 million people affected worldwide in 2011. In 2030, it is estimated that this number will reach ~552 million (<http://www.idf.org/diabetesatlas/5e/the-global-burden>).

A tight regulation of the glucose homeostasis is crucial for life. After a meal, the blood glucose level rises up immediately. In a healthy person, the glucose level is regulated by the secretion of the hormone insulin from the β -cells of the pancreas. Insulin induces the integration of the glucose transporter GLUT4 into the cell membrane of the target cells (muscle, adipocytes and liver) thus regulating glucose uptake (52). Glucose can be converted to ATP in a multiple-step reaction and thus serves as an energy source for the cell. In addition, liver and muscle cells are able to store glucose as glycogen via glycogenesis which is also triggered by insulin.(53)

1.3.1 Pathophysiology

In diabetic patients the mechanism of glucose uptake and storage cannot be induced by insulin which leads to hyperglycemia. Consequently, part of the excessive blood glucose is released by the kidneys. The term “diabetes mellitus” is derived from the Greek word “siphon” for passing through and the Latin word “mel” for honey (sweet). Instead of the unavailable glucose, the cells of diabetic patients use fat as an alternative energy source. However, this can lead to acidic metabolites in the blood.

There are two most prominent forms of DM: type 1 and type 2 DM (T1DM and T2DM respectively). Although the pathologies are different, both forms cause severe secondary complications as heart attacks, stroke, renal failure, adult blindness and amputation of lower limbs.

T1DM:

Even though T1DM is the best-known form of DM in the population, it affects only ~5-10 % of all diabetic patients. It is characterized by an autoimmune reaction against the insulin-producing β -cells of the pancreas and is triggered by genetic and/or environmental factors. T1DM patients, usually children and adolescents, are treated by insulin supply to control the blood glucose levels. (53)

T2DM:

~90% of all diabetic patients are suffering from T2DM which correlated to 284 million people worldwide in 2010 (54). These patients do produce insulin, however the target tissues (muscle, white adipose tissue or liver) cannot respond to it, leading to so called “insulin resistance”. The body can compensate the insulin resistance for a while by an

overproduction of insulin leading to hyperinsulinaemia. However, this overproduction is not sufficient and already at this stage the patients will start to show a slight hyperglycemia. As a consequence of the insulin overproduction, the β -cells are degenerating causing β -cell dysfunction. At this stage, T2DM patients demonstrate severe hyperglycemia and hypoinsulinaemia similar to T1DM patients. T2DM appears usually in older ages, but nowadays it is increasingly seen in childhood and adolescence (53). The danger of the disease is that it is often diagnosed only very late, at the time when secondary complications became already irreversible (55).

T2DM is strongly associated with obesity but there are also other genetic and environmental factors influencing the development of the disease (54). An efficient treatment is still missing in case of T2DM. Most likely, a change to a healthier lifestyle (healthy diet, exercise, no alcohol and cigarettes) is the best available treatment. Moreover, hypoglycemic drugs and sometimes insulin supply might help regulating the blood glucose level.

Independently of the cause of the disease, chronic hyperglycemia is leading to long-term defects in various organs causing retinopathy, nephropathy and neuropathy in all forms of DM. However, the effects in T2DM are slightly milder since insulin, which has multiple functions in the human metabolism, is produced at least during the initial phase of this type of DM (53).

1.3.2 Diabetic peripheral neuropathy

Diabetic neuropathy can impair different parts of the nervous system and is hence classified into four categories: peripheral, proximal, autonomic and focal.

Diabetic peripheral neuropathy (DPN), affecting symmetrically the distal parts of sensory and motor peripheral nerves in arms and legs, is the most common but also least understood complication of both T1DM and T2DM. The prevalence of DPN varies from 10 % in the first year of DM to ~50 % in patients which are diabetic for more than 25 years (56). It is characterized by either “positive” (paresthesia, dysesthesia, pain, cramps, fasciculations) and/or “negative” (hypesthesia, anesthesia, tiredness, muscle weakness) symptoms (40, 57). Nerve conduction studies are commonly used to diagnose DPN, showing a reduced motor nerve conduction velocity (MNCV) and sensory nerve conduction velocity (SNCV) in diabetic patients. Such functional defects in diabetic patients are often associated with loss of unmyelinated and/or myelinated nerve fibers, axonal swellings as well as de- and remyelination events leading to the formation of onion bulbs (57-60). Interestingly, while axo-glial dysjunctions are more prominent in T1DM patients, T2DM patients show more severe signs of Wallerian degeneration (58). However, such morphological alterations appear only late and might not explain the early reduced NCV in diabetic patients. It has been hypothesized that metabolic changes or reduction in the nerve blood flow might be

responsible for the earlier DPN symptoms (55, 60). Moreover, previous clinical electrophysiological studies suggested that altered neuronal ion channel expression and function may contribute to DPN symptoms (40, 61-64). As a consequence, peripheral nerve hyper- or hypoexcitability, which is part of the DPN phenotype, can contribute to the positive or negative symptoms, respectively.

Despite many years of research, the development of effective therapies for DPN still remains challenging. To study the pathophysiology of DM and DPN in more detail animal models might help and might improve the evaluation of new potential treatments.

1.3.3 Animal models for diabetes mellitus

In the field of DM research, particularly rodent models are highly contributing to the understanding of the genetic and environmental factors of the disease, its pathophysiology, the establishment of secondary complications and to the development of new therapies. Many different T1DM and T2DM models exist, including both spontaneous and chemically-induced (e.g. with streptozotocin (STZ)) models (**Table 4**).

Animal model	Type of DM	Mechanism
STZ rat	T1DM	chemically induced destroying of pancreatic β -cells by STZ
BB/W rat	T1DM	autoimmune reaction against pancreatic β -cells
STZ mouse	T1DM	chemically induced destroying of pancreatic β -cells by STZ
Akita mouse	T1DM	mutation of the insulin receptor
NOD mouse	T1DM	autoimmune reaction against pancreatic β -cells
BB/Z rat	T2DM	mutation in the leptin receptor
ZDF rat	T2DM	mutation in the leptin receptor
db/db mouse	T2DM	leptin receptor mutation; autosomal-recessive
ob/ob mouse	T2DM	leptin mutation; autosomal-recessive

Table 4 : Established mouse models of type 1 and type 2 diabetes mellitus.

Such a large variety makes it rather difficult to choose the correct model. Therefore, it is crucial to compare both the animal and human physiologies. In the last years, the db/db mouse strain became a well established animal model for T2DM and DPN (**Fig. 7**) (65, 66). The mutated gene in db/db mice codes for the leptin receptor in the hypothalamus of the brain, and binding of the receptor to the leptin hormone balances the energy intake. As a consequence homozygous db/db mice show typical symptoms of T2DM as polyuria (frequent urination), polydipsia (increased thirst) and polyphagia (increased hunger) aside from becoming obese within their first weeks of life. As for T2DM patients hyperinsulinaemia is followed by hyperglycemia. In addition, db/db mice are sterile. About DPN it is reported that db/db mice develop a decrease in MNCV shortly after the onset of hyperglycemia (55).

However, morphometric changes, including a loss of intraepidermal nerve fibers (IENF) as in T2DM patients (67, 68), occur only late after the onset of DM (69, 70).



Figure 7 : Obese db/db mice and wild-type mice at 23 weeks of age.

1.4 Fatty acid binding proteins

The family of fatty acid binding proteins (FABPs) comprises low molecular mass proteins of ~15 kDa which bind predominantly long-chain FA and other hydrophobic molecules. These ligands serve as energy source and metabolic regulators of multiple enzymatic and transcriptional processes in the cell. Consequently, FABPs are especially present in lipid-rich tissues, like white adipose tissue, liver, muscles and others. FA do not only bind to FABPs but they also regulate the gene expression level, for instance of some FABPs by binding to their promoter region, or potentially of general metabolic and inflammatory factors. However, the biological function of FABPs is still poorly understood. The ligand binding increases FABPs solubility in the cytoplasm to potentially facilitate the uptake, transport and/or storage of lipids. Interestingly, the expression level of FABPs is thought to be most likely proportional to the rate of lipid metabolism within the cell. (71)

Both the gene and protein structures of FABPs are highly conserved. Each FABP gene has 4 exons separated by 3 introns. The tertiary structure of the resulting protein includes a 10-stranded antiparallel β -barrel. The uncharged hydrophobic ligand-binding core lies inside the β -barrel and is surrounded by a hydrophilic surface. The N-terminal part is capped by a helix-loop-helix (71).

Up to date, 10 family members (FABP1 to 9, and 12) are described (71, 72) (**Table 5**), each characterized by its expression pattern, its ligand selectivity and affinity. Most tissues express several FABPs and consequently most FABPs are present in several tissues. FABPs expressed in the nervous system are FABP3, 5, 7 and 8. Interestingly, FABP8 is the only one to be expressed in the PNS and not in the CNS in most species (73). FABP4, 5, 8, 9 and 12 are known to be clustered in the same chromosomal region (72, 74). Together with

their similarity at the DNA and protein structural level, this suggests that FABPs are derived from one common ancestor gene.

The generation of KO mouse models for the majority of FABPs substantially improved our understanding of the role of FABPs (71). However, it also rose up new questions. **Table 5** summarizes the main outcomes of the analysis of FABP KO mice.

Gene	Name	Important facts	KO mouse model
FABP1	Liver FABP; L-FABP	FA regulates its mRNA expression; can bind two ligands simultaneously	healthy; variable results under high fat diet;
FABP2	Intestinal FABP; I-FABP	FABP2 polymorphism associated with insulin resistance in Pima Indians	elevated insulin plasma levels; males gained weight, females not; suggested compensation by other FABPs;
FABP3	Heart-FABP; H-FABP	FA uptake and transport to mitochondria in muscle cells; expression proportional to lipid/FA exposure	FA uptake strongly impaired, resulting in increased FFA concentrations in plasma; switch from FA oxidation to glucose oxidation -> less tolerance to exercises
FABP4	Adipocyte-FABP; A-FABP, aP2	named aP2 due to high sequence similarity to P2; highly regulated during adipocyte differentiation; FA and insulin regulate its expression; in macrophages inducing inflammatory response and cholesterol accumulation	in obese FABP4 ^{-/-} mice, reduced hyperinsulinaemia and insulin resistance; loss of FABP4 compensated by overexpression of FABP5 in adipocytes but not macrophages; minor increase in plasma FFA concentration
FABP5	Epidermal-FABP; E-FABP; mal1	similar selectivity and affinity as FABP4	healthy, slight compensation in liver by H-FABP; increased insulin sensitivity; minor increase in plasma FFA concentration
FABP6	Ileal-FABP; Il-FABP; gastrotropin		
FABP7	Brain-FABP; B-FABP	mainly expressed early on; strong affinity to n-3 polyunsaturated FA; increased in Down's syndrome and Schizophrenia	viable without macroscopic abnormalities; but altered emotional behaviour; attenuated neurogenesis
FABP8	Myelin-FABP; M-FABP; P2	see chapter 1.4.1	
FABP9	Testis-FABP; T-FABP	proposed binding of sperm membrane with cytoskeleton; upregulated in apoptotic testicular germ cells;	mice are viable and fertile, sperm head abnormalities but normal sperm function and sperm fatty acid composition
FABP12		expressed in retina and testis but with different pattern of expression as FABP9	

Table 5 : Annotated FABP genes and phenotypes in the corresponding knockout mouse models.

1.4.1 P2

P2 (= FABP8, Pmp2) is recognized both as a FABP and as one of the major peripheral myelin proteins besides MPZ and MBP (26). Its gene and protein structure is consistent with the other members of the FABP family as described above. In addition, previous reports (75, 76) demonstrated that the P2 gene contains several positive and negative regulatory sequences in its 5' region and that two P2 mRNAs might be produced due to different transcription start sites (75) (**Fig. 8**). On the protein level, multiple regulatory regions have been identified as well including phosphorylation sites, cholesterol recognition amino acid consensus (CRAC) - motifs and potentially a myristoylation domain (77). However, except for

the CRAC motif which plays a role in cholesterol recognition, their relevance remains still elusive.

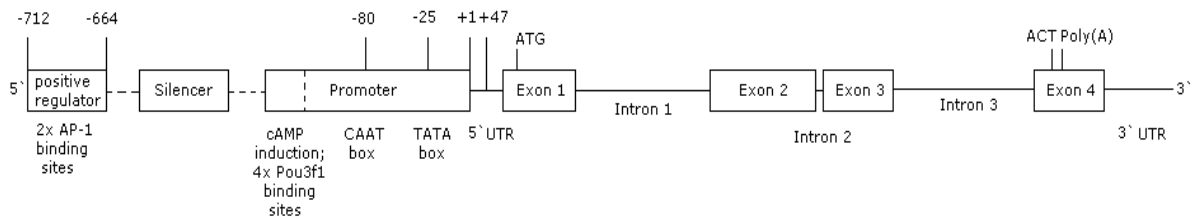


Figure 8 : P2 gene structure.

The P2 gene is composed of 4 exons and 3 introns which is typical for members of the FABP family. Furthermore multiple regulatory sequences in the 5' region of the P2 gene have been identified, including the TATA-box, CAAT-box, cAMP induction site and two AP-1 binding sites, as well as a potential second transcription start site.

As described above, P2 is mainly expressed in the PNS but can be found also in the CNS of some species (e.g. CNS of rabbit, bovine, human and guinea pig but not rat, mouse or dog) (21, 78). Overall P2 has a very unique expression pattern compared with other peripheral myelin proteins. First, it is present only in a proportion of Schwann cells and second it shows a strong expression in the Schwann cell cytoplasm (79, 80). Second, it is suggested to be produced on free ribosomes and to be associated with the cytoplasmic side of the myelin membrane and of other membranes of organelles apposed to the Schwann cell cytoplasm classifies P2 to a peripheral membrane protein (79). Moreover, the expression level of P2 varies highly between species, between different fiber tracts of the same organism and between separate nerve fibers within the same nerve (80).

KO mouse models for the different myelin genes helped us to understand the functionality of each of these genes and of the entire PNS (**Table 2**). However, such information is still missing for P2. As a member of the FABP family, it is suggested that P2 might be involved in the transport and/or storage of lipids in myelinating glial cells. High binding affinity to cholesterol, oleic acid, retionic acid and retinol of P2 has been observed previously (77, 81). Furthermore, P2 is considered to be a candidate inducing EAN, an animal model of GBS (50). Others have shown that P2 might rather interact with MBP or even replace it, highlighting its potential role in myelin compaction.

2. Material and Methods

2.1 Animals and human biopsies

2.1.1 db/db mice

A breeding colony to generate db/db animals was established starting with C57BL/KSJrj-db/db mice obtained from Janvier, France (Official Strain Name: B6.BKS(D)-Lepr^{db}/J; Stock Number: 000697). Generated animals were genotyped according to the previously established protocol by the Jackson Laboratory (<http://jaxmice.jax.org/strain/000642.html>). All animals were housed in a controlled environment with a 12 h light/12 h dark cycle with free access to water and standard laboratory diet. Only male animals were used for experiments. Only db/db mice with established hyperglycemia at the age of 6 weeks were considered as diabetic and used in this study. We used db/db animals exposed to diabetes for 16 weeks (23 weeks old). Experiments were performed in accordance with the legal requirements of the University of Lausanne and the Canton of Vaud.

2.1.2 Human biopsies

Biopsies have been obtained from the “Centre de Référence des Neuropathies Amyloïdes & autres Neuropathies Rares” of the Centre Hospitalier Universitaire de Bicetre in Paris (France). All donors gave a written consent for the biopsy. Biopsies of the peroneal nerve and adjacent muscle were performed under local anesthesia. The nerve specimens were fixed in 3,6% glutaraldehyde and embedded in paraffin for routine analysis, or were embedded in plastic for semithin and ultrathin sectioning analyzed by light and electron microscopy respectively. Paraffin sections were stained with hematoxylin-eosin and Masson's trichrome. Semithin sections were stained with thionine blue.

2.1.3 P2^{-/-} mouse model

The P2 targeted embryonic stem cells were developed by Regeneron (www.velocigene.com) and were used to generate the P2^{-/-} via the service of Knockout Mouse Project organization (www.komp.org). While the targeted embryonic stem cells are publically available, we have the proprietary rights over the generated P2^{-/-} animals. All 4 coding exons of P2 were replaced by lacZ (in frame after the original ATG of the P2 gene) and neomycin cassette. To genotype mice, the combination of F, R-WT and R-lacZ primers were used (**Fig. 19A and Table 7**). PCR conditions were as described in chapter 2.3.6. As the annealing temperature for the wild-type (WT) allele was 56°C and for the mutant allele 58°C two separate PCR reactions had to be prepared. WT and mutant allele amplicons were 1039 and 484 bp long, respectively.

Since the neomycin cassette is flanked by loxP sites, P2^{-/-} mice were crossed to the nestin-Cre deleter strain leading to the generation of P2^{-/-ΔNeo} mice.

2.1.4 P2^{-/-}/Shi^{-/-} mice

Shiverer mice Shi^{-/-} (lacking MBP) were obtained from Jackson Laboratory (C3Fe.SWV-*Mbp*^{shi}/J; stock number: 001428). Animals were genotyped according to the previously established protocol by the Jackson Laboratory (<http://jaxmice.jax.org/strain/000642.html>), primers are listed in **Table 7**. First male Shi^{-/-} mice were crossed to P2^{-/-} females and secondly, the obtained double heterozygous mice P2^{+/-}/Shi^{+/-} were mated together in order to achieve double KO mice of P2 and MBP (P2^{-/-}/Shi^{-/-}).

2.2 Physiological and electrophysiological methods

2.2.1 Measurement of glycemia and plasma insulin levels

Tail vein blood glucose was determined with a glucometer Ascencia Contour (Bayer). Plasma insulin levels were measured by using the Rat/Mouse Insulin Elisa Kit from Millipore (Cat. #EZRMI-13K) according to the manufacturer's protocol.

2.2.2 Determination of free fatty acids from blood plasma

Blood was collected from beheaded mice and let blood clot for 30 min at room temperature (RT). Afterwards, the clotted blood was centrifuged for 15 min at 4°C, supernatant contained the plasma and was transferred into a new tube.

To measure the concentration of free fatty acids (FFA) in the plasma the half-micro test from Roche (Cat. #11383175001) was used according to the manufacturer's protocol.

2.2.3 Motor and sensory nerve conduction velocity

Animals were anesthetized with a mixture of 10 mL/g Ketanarkon 100 (1 mg/mL; Streuli) with 0.1% Rompun (Bayer) in phosphate buffered saline (PBS) and fixed in the prone position. MNCV recordings were performed as previously described (45). Briefly, both left and right sciatic nerves were stimulated at the sciatic notch and distally at the ankle via bipolar electrodes with supramaximal square-wave pulses (5 V) of 0.05 ms. The latencies of the CMAP were recorded by a bipolar electrode inserted between digits two and three of the hindpaw and measured from the stimulus artifact to the onset of the negative M-wave deflection. MNCV was calculated by dividing the distance between the stimulating and recording electrodes by the result of subtracting the distal latency from the proximal latency. For SNCV, the caudal nerve of the tail was stimulated distally. The sensory response was recorded by bipolar electrode inserted proximally at the base of the tail. Latency of the compound sensory action potentials was determined by measuring the stimulus artifact to

the onset of the S-wave deflection. SNCV was calculated by dividing the distance between the stimulating and recording electrode by the latency.

2.2.4 *Ex vivo* compound action potential recording

Recordings have been performed as previously described (44). Briefly, mice were anesthetized with Isofluran (Baxter) and beheaded. Sciatic nerve were dissected and placed in artificial cerebrospinal fluid (ACSF) composed of (in mM) : NaCl, 126 ; KCl, 3 ; NaH₂PO₄, 1.25 ; CaCl₂, 2 ; MgCl₂, 2 ; NaHCO₃, 26 ; glucose, 10 ; pH7.4 (all salts from VWR), and continuously bubbled with carboxygen, (95% O₂/5% CO₂). Nerves were allowed to equilibrate for 60 min before electrophysiological measurement. For recordings, nerves were transferred to a home made chamber perfused with ACSF. Electrical stimuli (0 to 10V) were applied using a suction electrode filled with ACSF at the proximal end of the nerve with an Omnicol 2001 stimulator (World Precision Instruments). For the RP, nerves were stimulated with a supramaximal stimulus. CAPs were recorded in current-clamp mode at the distal end with a similar pipette using a Multiclamp 700B amplifier. Signals were filtered and digitized with a Digidata 1440A (Molecular devices). We used pClamp 10 for protocol generation, and data acquisition and analysis. Nerve isolation and recordings were done at room temperature (20-22°C). For pharmacological analysis, the isolated nerves were exposed to the drugs between 20 min and 1 h until the effects seem stable. TTX was purchased from Enzo Life Sciences, TEA and 4-AP from Sigma, DTX-1 from Alomone Labs and Flupirtine from Tocris.

2.3 Histological and molecular biological methods

2.3.1 Morphometric analysis

Mice were perfused with 2,5% glutaraldehyde in PBS for 5 min. Sciatic nerves were dissected and postfixed by immersion in the fixative solution for 2 h at 4 °C, washed in 0.1 M cacodylate buffer (pH 7.3), and osmicated for 4 h in 1% OsO₄ (Fluka). Nerves were rinsed in water, dehydrated, and embedded in Epon 812 resin (Fluka). Half-micrometer sections were stained with 1% toluidine blue and examined by light microscopy. Subsequent morphometric analyses were performed on micrographs using Image J (National Institutes of Health, Bethesda, MD) plug-in (g-ratio calculator) developed in collaboration with the cellular imaging facility of the University of Lausanne and available at <http://cifweb.unil.ch>. For electrone microscopy analysis, ultrathin sections were cut, collected on celloidin-coated single-slot grids, and stained with uranyl acetate and lead citrate. Preparations were observed on the electron microscope Philips CM 10.

2.3.2 Tissue fixation and embedding

For cryostat sections the appropriate tissues were dissected and fixed with 4% paraformaldehyde in PBS for 10 min at RT and subsequently overnight at 4°C. After cryoprotection in 20% sucrose in PBS overnight at 4°C, tissues were embedded in OCT medium (Sakura) and longitudinal or cross sections of 8 µm were prepared. Prior to specific staining the slides were post-fixed in 4% paraformaldehyde for 10 min.

Nerve biopsies were embedded directly in OCT compound (Tissue-Tek) after removal. 20 µm thick sections were cut, dried on glass slides and fixed with Zamboni's fixative for 15 min at RT.

For teased fiber analysis, sciatic nerves were dissected and incubated for 15 min at RT in Zamboni's fixative. Subsequently, nerves were washed in PBS, and individual fibers were separated in PBS on glass slides coated with Tespa (Sigma).

2.3.3 Immunohistochemistry

Samples were permeabilized with methanol at -20°C for 10 min. Next, specimen were blocked in 10% normal goat serum, 0.3% Triton X-100 in PBS for 1 h at RT and incubated overnight at 4°C with primary antibodies in blocking buffer (antibodies are listed in **Table 8**). The next day, the slides were washed in PBS and hybridized with the appropriate secondary fluorescent antibodies (Alexa Fluor 594 or 488, diluted 1:200; Invitrogen) in blocking buffer for 2 h at RT. Slides were washed and mounted with Vectashield mounting medium containing DAPI to counterstain cell nuclei (Vector Laboratories). Sections were visualized under a Leica SP5 AOBS confocal microscope.

For Nile red staining on teased fibers, stock solution (Sigma) was diluted 1:1000 in 75% glycerol. Fibers were first stained with DAPI, washed once in PBS and subsequently mounted with one drop of Nile red working solution.

2.3.4 Intraepidermal nerve fiber density

Skin of hindpaws, attached to a small piece of paper, were fixed for 2 h in Zamboni's fixative at RT. Followed by three washes with PBS, the hindpaws were incubated in 30% sucrose overnight at 4°C, embedded in OCT and stored at -80°C. Footpads were cut into 50 µm sections, using every fourth section. Free-floating sections were blocked in 0,3 % Triton-X 100 in PBS overnight at 4°C. Next, the sections were incubated with the primary antibody against Collagen-IV overnight at 4°C, washed in PBS and subsequently incubated with the secondary antibody Alexa 594 anti-goat for 2 h at RT. After washes with PBS, the same procedure was repeated with the primary antibody for PGP9.5 and its appropriate secondary antibody Alexa 488 anti-rabbit, finished by washes with PBS. To mount the sections with Vectashield mounting media containing DAPI, the sections were transferred onto a slide in a drop of PBS. Four different frames of three sections per animal were

analyzed using a Leica SP5 AOBS confocal microscope. Z-stacks of 2 μm intervals were obtained and the number of nerve fibers/mm crossing the dermal-epidermal junction in the superimposed image was counted.

2.3.5 X-Gal staining

Sciatic nerves were fixed in 0,5% Glutaraldehyde in PBS for 2 h at RT, cryoprotected in 30% sucrose and 2 mM MgCl_2 in PBS overnight at 4°C and embedded in OCT medium. Sections of 8 μm thickness transferred onto a glass slide were fixed in 4°C-cold X-Gal fixative (4% paraformaldehyde, 0,5% glutaraldehyde, 0,1 M PBS) for 4 min. After 2x washes in PBS, sections were stained with 50 mg/ml X-Gal diluted 1:50 in X-Gal staining solution (5 mM $\text{K}_3\text{Fe}(\text{CN})_6$, 5 mM $\text{K}_4\text{Fe}(\text{CN})_6 \cdot 3\text{H}_2\text{O}$, 2 mM MgCl_2 in PBS) at 37°C. Staining reaction was stopped by washes in PBS at several time points ranking from 30 min to overnight.

2.3.6 PCR and quantitative PCR

Total RNA from the various tissues used here was isolated using Qiagen RNeasy lipid tissue kit and reverse transcribed with SuperScript III First-Strand Synthesis System for RT-PCR (Invitrogen) following manufacturer's instructions.

Table 6 shows the composition of the PCR mixture and the PCR conditions were 95°C for 5 min, followed by 35 cycles (95°C for 30 s, primer-specific annealing temperature given in **table 7** for 30 - 45 s, and 72 °C for 2 min) and 2 min extension at 72°C. Next, loading dye (0,25% Orange G, 30% Glycerol, 70% H_2O) was added to each PCR reaction and separated on a 1% Agarose gel.

Component	Volume (μl)
H_2O	38,1
10x PCR buffer	5
50 mM MgCl_2	1,5
10 mM dNTPs	1
forward primer	1
reversed primer	1
Taq DNA polymerase (5 units/ μl)	0,4
DNA	2
Total volume	50

Table 6 : PCR reaction mix.

QPCR analysis was performed with the resulting cDNA, using ABI Prism 7500 Fast Real-Time PCR system and SYBR Green (Applied Biosystems). All primers were designed to prevent amplification of genomic DNA. Cycling conditions were 95°C for 10 min, followed by 40 cycles of 95°C for 15 s, and then 60°C for 1 min. Quantitation was performed using a standard curve established from a serial dilution of a mix of the samples. Results were normalized by using the reference genes Actin or Ubiquitin. All primers used are listed in **table 7**. QPCR for FABP9 was performed using Taqman probe (Applied Biosystem) and

normalized with Taqman probe against Ubiquitin. The same system and program as described above were used.

2.3.7 Total protein extraction

Sciatic nerve endoneurium and DRG isolated from at least three animals per genotype were pooled and lysed in ice-cold lysis buffer (20 mM $\text{Na}_2\text{H}_2\text{PO}_4$, 250mM NaCl, 1% Triton X-100, 0.1% SDS) supplemented with Complete protease inhibitors (Roche). After spin down for 15 min at 4°C, supernatant was used as protein extract.

2.3.8 Western blot analysis

Protein levels were quantified using the Bio-Rad protein assay with BSA as a standard. Equal amounts of protein extracts were boiled for 5 min at 95°C and were then resolved by 8-12% SDS-PAGE and electro-transferred onto a polyvinylidene difluoride membrane (Amersham Biosciences). Blots were blocked in tris-buffered saline containing 0,1% Tween (TBS-T) supplemented with 5% milk powder for 1 h at RT and subsequently incubated overnight at 4°C in the same buffer supplemented with the specific primary antibody (**Table 8**). After washing in TBS-T, blots were exposed to the appropriate horseradish peroxidase-conjugated secondary antibody (Dako) in the blocking buffer for 1 h at RT. Finally, blots were developed using the ECL reagents (Pierce) and Kodak Scientific Imaging Films (Kodak).

2.3.9 Co-immunoprecipitation

The lysis buffer used for co-immunoprecipitation (Co-IP) was composed as followed: 25 mM Hepes, 150 mM NaCl, 1% NP-40, 0,25% sodium deoxycholate, 10% Glycerol, 25mM NaF, 1mM EDTA and 1 mM Orthovanadate, supplemented with Complete protease inhibitors (Roche). Proteins of sciatic nerve endoneurium were extracted as explained in 2.3.7. The Co-IP was performed using Dynabeads coupled to protein G (Invitrogen) and the magnetic particle concentrator Dynal MPCTM-S from Invitrogen. Co-IP was done according to the manufacturer's instructions, except the incubation temperature was 4°C instead of RT. The protein input reflects 10% of the total protein amount used for the Co-IP and the negative control was performed without antibody.

2.3.10 Cellular fractionation

Similar to total protein extraction, tissues were collected and homogenized in a pre-cooled lysis buffer containing 10 mM Tris-HCl pH 7,5, 100 mM NaCl, 1 mM EDTA, 1 mM Na_3VO_3 , and 1% Triton supplemented with Complete protease inhibitors (Roche). For nuclear protein extraction, lysed tissues were spun down for 10 min at 3'000 g at 4°C and the pellet was resolved in lysis buffer. Supernatant was spun down again with 80'000 g for 30 min at 4°C. The resulting pellet contained all organelles and membrane proteins and was resolved in

lysis buffer supplemented with 1% CHAPS. The final supernatant presented the cytosolic fraction. Subsequent Western Blot analysis was performed as described in chapter 2.3.8.

2.3.11 Microarray

Total RNAs from the complete sciatic nerve of six P10-old P2^{+/+} and P2^{-/-} mice were isolated and purified with Qiagen RNeasy lipid tissue kit. All RNA quantities were assessed by NanoDrop®ND-1000 spectrophotometer and the RNA quality was assessed using RNA 6000 NanoChips with the Agilent 2100 Bioanalyzer (Agilent, Palo Alto, USA). Two RNA extracts per genotype were pooled together to obtain three biological replicates. For each pooled sample, 100 ng of total RNA were amplified using the WT sense strand Target Labelling kit (Affymetrix, Cat.no. 900223); 5.5 µg of the resulting sense cDNA was fragmented by UDG (uracil DNA glycosylase) and APE 1 (apurinic/apyrimidic endonuclease 1) and biotin-labelled with TdT (terminal deoxynucleotidyl transferase) using the GeneChip® WT Terminal labelling kit (Affymetrix Cat.no. 900671, Santa Clara, USA). Affymetrix Mouse Gene 1.0 ST arrays (Affymetrix, Santa Clara, CA, USA) were hybridized with 2.7 µg of biotinylated target, at 45°C for 17 h washed and stained according to the protocol described in Affymetrix GeneChip® Expression Analysis Manual (Fluidics protocol FS450_0007).

The arrays were scanned using the GeneChip® Scanner 3000 7G (Affymetrix) and raw data were extracted from the scanned images and analyzed with the Affymetrix Power Tools software package (Affymetrix).

All statistical analysis were performed using the free high-level interpreted statistical language R and various Bioconductor packages (<http://www.Bioconductor.org>). Hybridization quality was assessed using the Expression Console software (Affymetrix). Normalized expression signals were calculated from Affymetrix CEL files using RMA normalization method. Differential hybridized features were identified using Bioconductor package “limma” that implements linear models for microarray data (82). The *P* values were adjusted for multiple testing with Benjamini and Hochberg’s method to control the false discovery rate (FDR) (83). Probe sets showing at least twofold change and a false discovery rate < 0.05 were considered significant.

Gene	forward primer (5' - 3')	reversed primer (5' - 3')
Actin (58°C)	GCCCTGAGGCTCTTTCCAG	TGCCACAGGATTCCATACCC
Cystatin B (55°C)	TGAAGTCCCAGCTTGAATCG	TAGGAGAGCTCATCGTGCCT
db/db genotyping (52°C)	AGAACGGACACTCTTTGAAGTCTC	CATTCAAACCATAGTTTAGGTTTGTGT
Fasn	GCTGGCATTTCGTGATGGAGTCGT	AGGCCACCAAGTGATGATGTAACCTCT
FABP3	ATGGCGGACGCCTTTGTCGG	TGGCAAAGCCACACCGAGTG
FABP5	GCACCAGCAATGGGACGGGA	GCATTGTTTCATGACACACTCCACG
FABP7	TACGGTGGTGGGTAAGACCCGA	CCCACGCCCAGAGCTTTCATG
K _v 1.1	AAGGACGGGAAACGCGAGGG	ATCGATGGACGCTGGCGGG
K _v 1.2	CTGGTACCCATCTGCAAG	GTGTGCTCTAGGACTGGATG
K _v β2	AGACAGGCTCCCCGGGATG	CATGGCCCCGCACGGTCTCTTC
LacZ (66°C)	GGTAACTGGCTCGGATTAGGG	TTGACTGTAGCGGCTGATGTTG
MAG	CGGGTTGGATTTACCACAC	CTGCCTTCAACCTGTCTGTG
MBP ^{+/+} genotyping (58°C)	AGCTCTGGTCTTTCTTGACAG	CCCCGTGGTAGGAATATTACATAAC
MBP ^{-/-} genotyping (58°C)	ACCGTCCTGAGACCAATTGTC	GTGCTTATCTAGTGTATGCCTGTG
MBP	GCCTGTCCCTCAGCAGATT	GCCTCCGTAGCCAAATCC
MPZ	TTCACAAGTCTTCTAAGGACTCCTCG	GCACTGGCGTCTGCCG
Myogenin (56°C)	TTACGTCCATCGTGGACAGC	TGGGCTGGGTGTTAGTCTTA
Na _v 1.6	ACACTAGTGGAAGAGCTGGA	ACGATCAGGTTCAACAATCTC
Nestin-Cre genotyping (56°C)	CAGGGTGTATAAGCAATCCC	CCTGGAAAATGCTTCTGTCCG
P2 ^{+/+} F and R-WT (56°C)	TATAGAAGGGCTTAAGCATG	CAGAACAAAGTCTCCACCACAC
P2 ^{-/-} F and R-LacZ (58°C)	TATAGAAGGGCTTAAGCATG	GTCTGTCCTAGCTTCCTCACTG
P2 (58°C)	AGCTCTAGGTGTGGGGTTAGCC	CCATTCTCCCATCCAGCAGCGT
PMP22	TTGCTCTTCGTCTCCACCATC	TCGTGTGTCCATTGCCAC
Resistin	GCTGTAAGCTGCAGGTCGCT	GGAAACCACGCTCACTTCCC
Ubiquitin	CAGCCACCAAGACTGACCAA	CATTCAACCAAGTGCTATGAGGGA
Uncoupling protein 1	TCCATGTACACCAAGGAAGGACC	AAGCCACAAACCCTTTGAAAAAG

Table 7 : List of primers.

Antibody	Manufacturer	raised in	Dilution used
Actin	Sigma, A5316	mouse	1:2000
Actin	Sigma, A2066	rabbit	1:200
Caspr	NeuroMab, 75-001	mouse	1:100
Collagen-IV	Chemicon, AB769	goat	1:40
E-Cadherin	BD Transduction Labs, 610404	mouse	1:100
FABP9	R&D Systems, MAB2750	mouse	1:100 (IH), 1:500 (WB)
Histone H3	Abcam, ab 1791	rabbit	1:1000
K _v 1.1	Alomone Labs, APC-009	rabbit	1:100
K _v 1.2	NeuroMab, 75-008	mouse	1:200 (IH), 1:500 (WB)
K _v β2	Alomone Labs, APC-117	rabbit	1:100
MBP (IH)	Chemicon, MAB386	rat	1:100
MBP (WB)	Santa Cruz, sc-13912	goat	1:200
Ndufs-4	Mitoscience, MS 104	mouse	1:1000
pan-Na _v	Sigma, S6936	rabbit	1:100
P2 (IH)	Proteintech, 12717-AP	rabbit	1:100
P2 (WB)	Abcam, ab 36387	rabbit	1:200
PGP9.5	Ultraclone, RA95101	rabbit	1:400
α/β-Tubulin	Cell Signaling, #2148	rabbit	1:1000

Table 8 : List of antibodies.

2.4 Others

2.4.1 Microdissection of sciatic nerve

Sciatic nerves from adult mice were placed in ice-cold PBS (pH 7.4). The perineurium and epineurium were gently dissected away from the endoneurium along the whole length of the nerve as previously described (84).

2.4.2 Tail or toe DNA isolation

750 µl of DNA lysis buffer composed of 50 mM Tris-HCl pH 8,0, 100 mM EDTA, 100 mM NaCl, 1% SDS, 0,5 mg/ml Proteinase K (Merck 1,24568) were added to the piece of tail/toe and incubated overnight at 56°C. After mixing 5 min, 250 µl 6 M NaCl was added, again 5 min mixed and subsequently spin down for 5 min. Next, the liquid phase was transferred to a new tube, washed with 500 µl by mixing 2 min and spun down for 1 min. A second wash with 1,5 ml ethanol was spin down for 1 min. After drying, the DNA pellet was dissolved in 100 µl TE by incubating it shaking at 37°C for 2 h.

2.4.3 Statistics

All data are presented as mean \pm standard error of the mean. P-values have been calculated with the Student's t-test or one-way ANOVA followed by Bonferroni's Multiple Comparison Test.

3. Results

3.1 Altered distribution of juxtaparanodal K_v1-channels mediates peripheral nerve hyperexcitability in type 2 diabetes mellitus

3.1.1 Characterization of type 2 diabetes mellitus and diabetic peripheral neuropathy in db/db mice

Most people with T2DM will develop DPN leading to tingling, pain and loss of feeling. Even though the pathological changes are relatively well described, the molecular mechanisms causing DPN remain poorly understood. I used the db/db mice as a rodent model for T2DM to investigate the mechanism behind DPN. In order to compare the etiopathology of db/db mice with T2DM patients, I determined the onset of T2DM in db/db mice by measuring their body weight, blood glucose and plasma insulin levels in their first weeks of life compared to age-matched control mice (**Fig. 9A-C**).

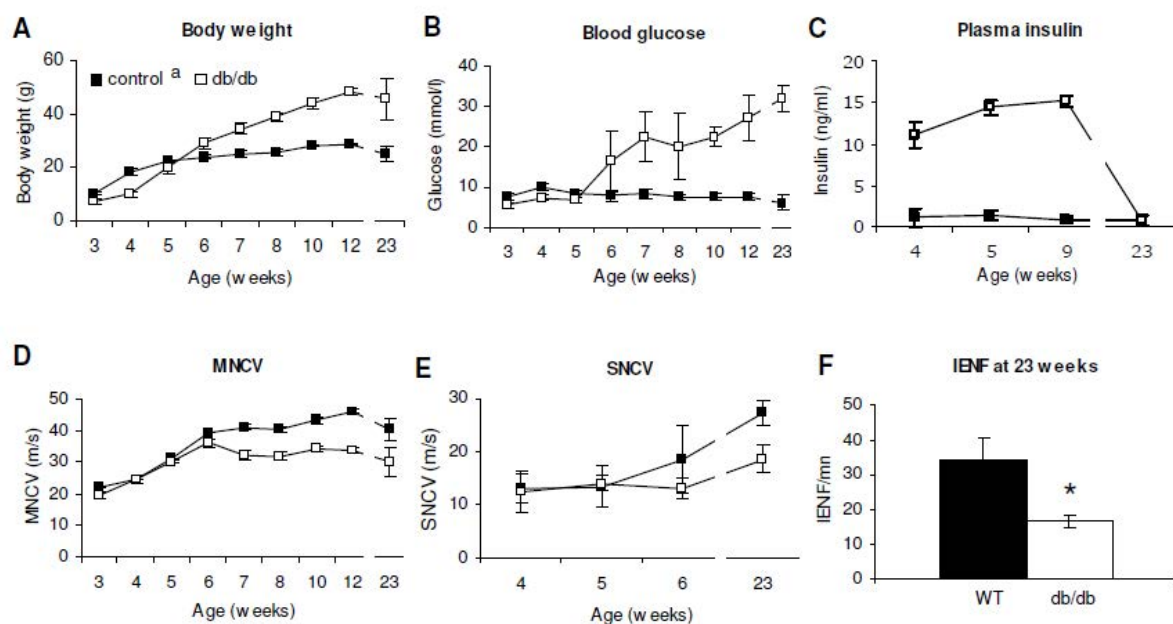


Figure 9 : Physiological profile of db/db and control mice during postnatal development and in adult mice at 23 weeks of age

Measurements of (A) body weight, (B) blood glucose levels, (C) plasma insulin levels, (D) MNCV, (E) SNCV and (F) IENF illustrated the course of T2DM and DPN in db/db mice. An increase in body weight and blood glucose levels set the onset of T2DM at 6 weeks of age in db/db mice. Prior to this, db/db mice were already hyperinsulinaemic indicating insulin resistance but in adult db/db mice the insulin secretion was declined. DPN, demonstrated by a reduced MNCV and SNCV, was present immediately after the onset of T2DM. At 23 weeks of age, after 16 weeks exposed to hyperglycemia, a significant reduction in the number of IENF was observed in db/db mice as compared to control mice displaying an additional small fiber neuropathy. n= 4 from 3 to 12 weeks; n=15 at 23 weeks; n=3 for IENF. ^a from 3 to 12 weeks of age db/+ mice and at 23 weeks of age WT mice have been used as control mice; * p-value < 0,05

Due to an initial insulin resistance, 5 weeks old db/db mice were already hyperinsulinaemic but did not present any additional diabetic phenotypes corroborating

previous studies (66, 85). I therefore considered the onset of T2DM in db/db mice at 6 weeks of age, when the affected animals started to gain weight and exhibited a marked hyperglycemia as compared to control mice. To diagnose an implication of nerve function, I measured MNCV on the sciatic nerve, which is a mixed nerve, and SNCV on the tail. Already at this stage of the disease I observed a slight reduction of the median MNCV (39,25 m/s for control mice; 35,96 m/s for db/db mice) and SNCV (18,4 m/s for control mice; 13,12 m/s for db/db mice), indicating the presence of DPN in db/db mice. One week later the reduction in MNCV became significant (41,04 m/s for control mice; 32,03 m/s for db/db mice) and I therefore considered the onset of DPN in db/db mice at 7 weeks of age (**Fig. 9D and E**).

To study the long-term consequences of T2DM on peripheral nerves, I exposed the db/db mice to hyperglycemia for 16 weeks (this, based on the estimated lifespan, represents ~10 years in humans). Consequently, I performed all physiological analysis using mice that were 23 weeks old. At this age, db/db mice were severely obese and hyperglycemic compared to control mice (**Fig. 9A and B**). The initial insulin resistance was followed by a β -cell dysfunction leading to a decline in the plasma insulin levels in db/db mice at 23 weeks of age as previously observed (66, 86) (**Fig. 9C**). NCV studies confirmed the significantly reduced MNCV and SNCV as already observed at 7 weeks of age (**Fig. 9D and E**). Further characterization of the shape of the CMAP curve from MNCV recordings showed a prolonged CMAP latency, duration and F-wave latency in db/db mice indicating myelin defects along the complete sciatic nerve. The CMAP amplitude and area did not change significantly between db/db and control mice excluding any axonal alterations (**Table 9**).

	MNCV (m/s)	Latency (ms)	Duration (ms)	Amplitude (mV)	Area (mV/ms)	F-wave latency (ms)
control	41,5 (+/- 0,82)	1,15 (+/- 0,08)	0,96 (+/- 0,13)	2,74 (+/- 0,59)	1,17 (+/- 0,28)	5,79 (+/- 0,28)
db/db	34,5 (+/- 1,8)	1,38 (+/- 0,14)	1,18 (+/- 0,19)	3,155 (+/- 1,32)	1,54 (+/- 0,44)	7,63 (+/- 0,28)
p-value	0,0035	0,0105	0,0482	0,5924	0,2765	5,1471 ⁻⁶

Table 9 : Properties of CMAP shape of db/db and control mice at 23 weeks of age.

In addition to the reduced MNCV, a reduction of CMAP latency and duration were observed in db/db mice as compared to control mice. The F-wave latency is also significantly downregulated in db/db mice. However, CMAP amplitude and area were normal. n=4.

However, NCV studies do not give any information about defects of small unmyelinated fibers, which are known to be affected in diabetic patients (67, 68). I therefore determined the IENF density in db/db and WT mice at 23 weeks of age. At this age, db/db mice have lost ~50 % of their IENF as compared to WT mice (**Fig. 9F**) demonstrating a strong small fiber neuropathy as previously reported (70).

3.1.2 Peripheral nerve morphology in db/db mice at 23 weeks of age

A reduction in the speed of the NCV is suggestive of demyelination or defects in the integrity of the peripheral nerve myelin. However, semithin cross sections of the sciatic nerve of 23 weeks old db/db mice illustrated normal myelin thickness as compared to age-matched

WT mice (**Fig. 10A**). Likewise, I could not observe any signs of segmental demyelination on db/db teased fibers stained with Nile red (**Fig. 10B**). Measurements of the mRNA level of two important peripheral myelin proteins, MPZ and PMP22, as well as g-ratio calculations (= ratio of axonal diameter/fiber diameter) for WT and db/db mice supported this observation (**Fig. 10C and D**).

A slight shift towards medium size axons (3,5 - 6,5 μm) was observed, leading to a slight decrease in the number of small axons (1 - 3,5 μm) in db/db mice at 23 weeks of age. Large fibers (> 6,5 μm) were not affected (**Fig. 9E**). In agreement with the CMAP shape analysis, the count of the total number of nerve fibers per sciatic nerve in WT and db/db mice revealed no axonal loss (**insert in Fig. 9E**).

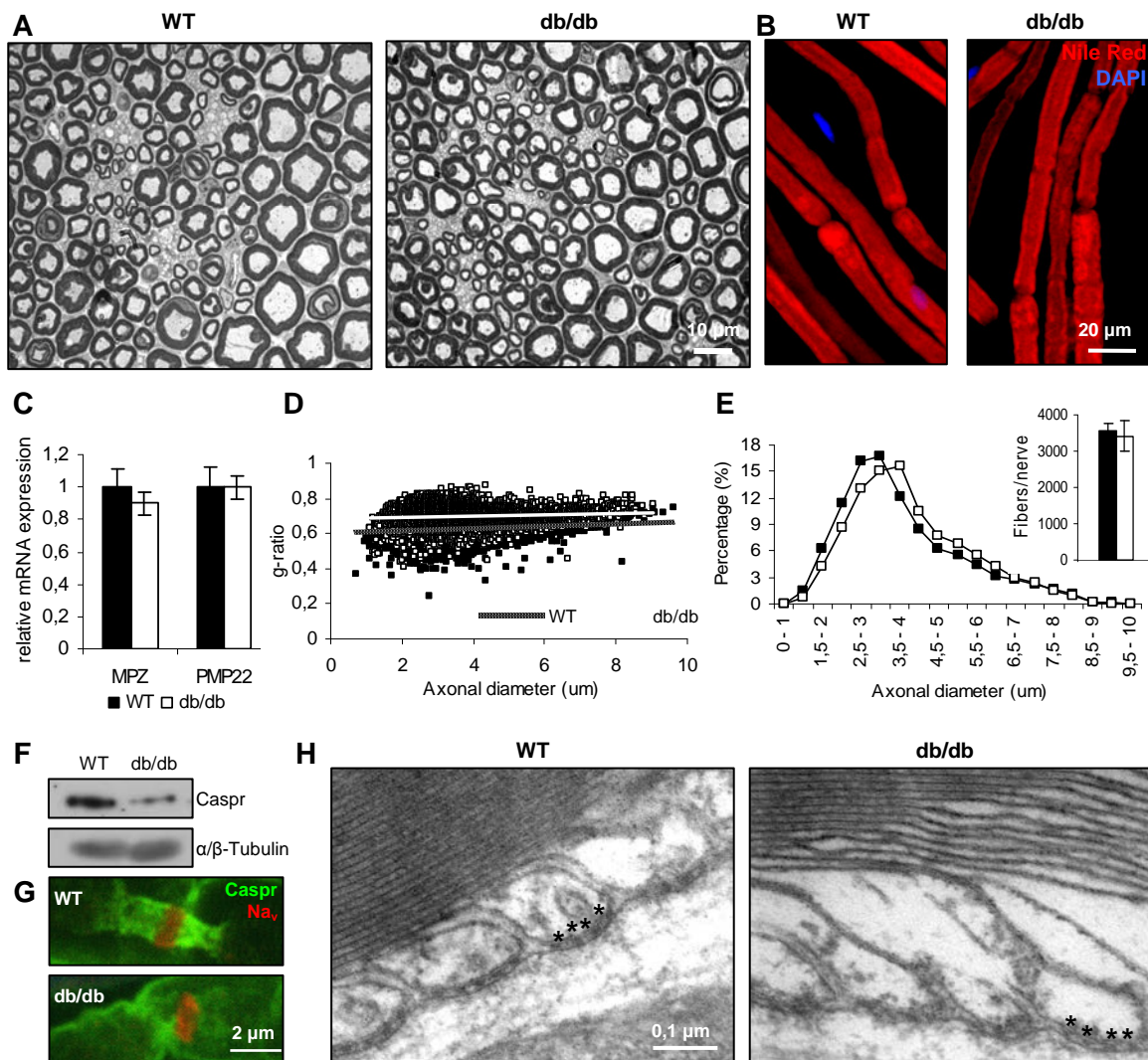


Figure 10 : Myelin morphology in db/db mice as compared to wild-type mice

(A) Toluidine blue stained semithin cross sections of WT and db/db sciatic nerves of 23 weeks old mice showed that 16 weeks of hyperglycemia had no detectable effects on both the axonal and myelin structures. (B) Nile-red stained sciatic nerve teased fibers demonstrated no segmental demyelination or widening of the node in db/db mice as compared to WT mice at 23 weeks. (C) qPCR analysis of two peripheral myelin genes (MPZ and PMP22), (D) g-ratio, (E) axonal distribution and (**insert in E**) axonal count corroborated the previous results. However, both (F) Western blot analysis on DRG extracts and (G) co-immunostainings on sciatic nerve teased fibers revealed a strong downregulation of the paranodal adhesion molecule Caspr in db/db mice as compared to WT mice. (H) Despite the reduction in Caspr expression, no defects on the formation of paranodal junctions (asterisks) were observed on longitudinal ultrathin sections. n=3 for each experiment, except semithin sections n=6;

As described in chapter 1.1.3, node formation and maintenance is crucial for the propagation of the APO. Interestingly, I observed a significant downregulation of the protein expression of the paranodal adhesion molecule Caspr on western blot analysis of DRG samples (**Fig. 10F**) and immunostainings on teased fibers (**Fig. 10G**) of db/db mice compared to WT mice at 23 weeks of age. As a complete loss of Caspr leads to the disruption of the paranodal junctions (87), I analyzed ultrathin longitudinal sections of WT and db/db mice for their nodal morphology. Despite the downregulation of Caspr expression, paranodal loops were present in db/db mice (**Fig. 10H**) and no defects in the nodal structure of db/db mice that could potentially explain a reduced NCV were observed.

3.1.3 Peripheral nerve hyperexcitability in db/db mice mediated by altered K_v1 -channel activity

While performing MNCV recordings in db/db mice at 23 weeks of age, I observed that the sciatic nerves of db/db mice were more sensitive to low electrical stimuli than the nerves of WT animals. The stimuli threshold to initiate a first response was significantly lower in db/db mice as compared to WT mice ($p < 0,0003$), indicating hyperexcitability of db/db nerves (**Fig. 11A**).

We extended our above mentioned *in vivo* electrophysiological characterization by *ex vivo* CAP recordings on db/db and WT sciatic nerves at 23 weeks of age. *Ex vivo* CAP recording on isolated nerves using suction electrodes has been shown to be a powerful tool to study nerve excitability and alterations in axonal ion channels or myelin structure (88). It allows recording of both $A\alpha\beta$ (faster and larger peak) and $A\delta$ CAPs. We tested WT and db/db sciatic nerve excitability by increasing progressively the strength of the stimulation by 10 or 100 mV steps. Typical traces of CAP of WT and db/db nerves at 300 mV or the one to get the maximal amplitude confirmed the presence of an increased excitability in db/db nerves (**Fig. 11B**). In the resulting normalized $A\alpha\beta$ CAP amplitude/stimulus strength curve we observed a leftward shift for db/db mice which corresponds to PNH. The threshold to generate an $A\alpha\beta$ CAP was also significantly reduced as well as the stimulus necessary to get 50% of the maximal CAP amplitude (**Fig. 11C and insert**). We observed similar results with thinly myelinated $A\delta$ fibers (**Fig. 11D**). Together these data suggest that db/db sciatic nerves are more excitable than WT nerves indicating the presence of PNH similar to the one observed in diabetic patients (89, 90).

Alterations in the potassium currents in either disease situation or in nerves treated with 4-AP and DTX-1, two known blockers of the fast Shaker K_v1 -channels, were previously observed to contribute to altered axonal properties including aberrant nerve excitability (42, 91-94). We therefore evaluated the contribution of changes in K_v1 -channel activity to PNH in T2DM by exposing isolated sciatic nerves to 500 μ M 4-AP or 100 nM DTX-1. In the nerves from WT mice, both treatments reproduced the increased excitability as observed in db/db

nerves *ex vivo* (**Fig. 11E and F**). Importantly, the 4-AP and DTX-1 treatment did not reproduce the same effect on db/db nerves whose excitability was only barely affected. These results indicate that major part of the observed PNH phenotype in db/db fibers is the consequence of decreased K_v1 -channel activity.

Blocking axonal K_v1 -channels was previously shown to lead to an increase in the RP (95, 96). The RP is the interval (Δt) following the generation of a first CAP where the initiation of a second one is inhibited. Unexpectedly, RP was not lengthened in db/db nerves (**Fig. 11G**). The time necessary to recover 50% of the maximal CAP amplitude during the second pulse ($\Delta t_{1/2}$) was 2,10 (\pm 0,01 ms) in WT and 2,06 (\pm 0,11 ms) in db/db nerves. However, 4-AP (**Fig. 11G**) and DTX-1 treatments (data not shown) induced a far more significant enhancement of the RP in WT nerves than in db/db nerves. $\Delta t_{1/2}$ after 4-AP treatment was increased only to 2,63 (\pm 0,14 ms) in db/db compared to 6,25 (\pm 0,82 ms) in WT animals. These results corroborate our observation that K_v1 -channel activity is decreased in myelinated db/db axons.

We also tested the possibility that other ion channels might be implicated in the PNH of db/db mice including Na_v -channels (62, 64) and slow KCNQ K_v7 -channels ($K_v7.2$ and $K_v7.3$) (14, 97). Increased nerve excitability in human diabetic neuropathy could also potentially be a consequence of increased persistent nodal Na_v -currents (62, 64). These currents are mediated by tetrodotoxin (TTX)-resistant Na_v -channels. If a higher expression of these channels was involved in hyperexcitability, CAP in db/db should be more resistant to block by TTX. We measured the residual CAP amplitude after exposure to 100 nM or 1 μ M TTX and did not observe any significant differences between WT and db/db mice (**Fig. 11H**) suggesting that TTX-resistant Na_v -channels have unlikely a critical role in the noticed difference in excitability. Next, nodal K_v7 -channels can be blocked by tetraethylammonium (TEA). We evaluated if TEA (10 mM), in presence of 4-AP, would induce a further increase in the excitability of WT nerves reaching similar values as observed in db/db nerves. However, the CAP amplitude/stimulus strength curve was not further shifted by co-exposure of 4-AP and TEA (**Fig. 11I**). Therefore, a potential decrease in slow K_v7 -channels is as well unlikely implicated in the observed PNH in db/db mice. We then tested if Flupirtine, an analgesic which activates K_v7 -channels and suppresses axonal hyperexcitability resulting from exposure of rat and human peripheral nerves to oxaliplatin (98), might have an improving effect on the db/db PNH. 10 μ M flupirtine reduced significantly db/db nerve excitability inducing a rightward shift of the CAP amplitude/stimulus strength and a decrease of the threshold ($p < 0,05$) (**Fig. 11J and insert**). These data confirm the functionality of K_v7 -channels in db/db mice and suggest that the K_v7 -channels represent an interesting target to treat some of the DPN-related symptoms.

Ultrastructural changes of the axon or the myelin sheath of single nerve fibers could also induce alterations in nerve excitability (99). However as shown in **Fig. 10A**, I excluded any

major morphological alterations in db/db mice at the time of PNH. These data therefore further support our conclusion that PNH in db/db mice is mediated predominantly by a decreased K_v1 -channel activity and not by significant structural changes in the myelin sheath.

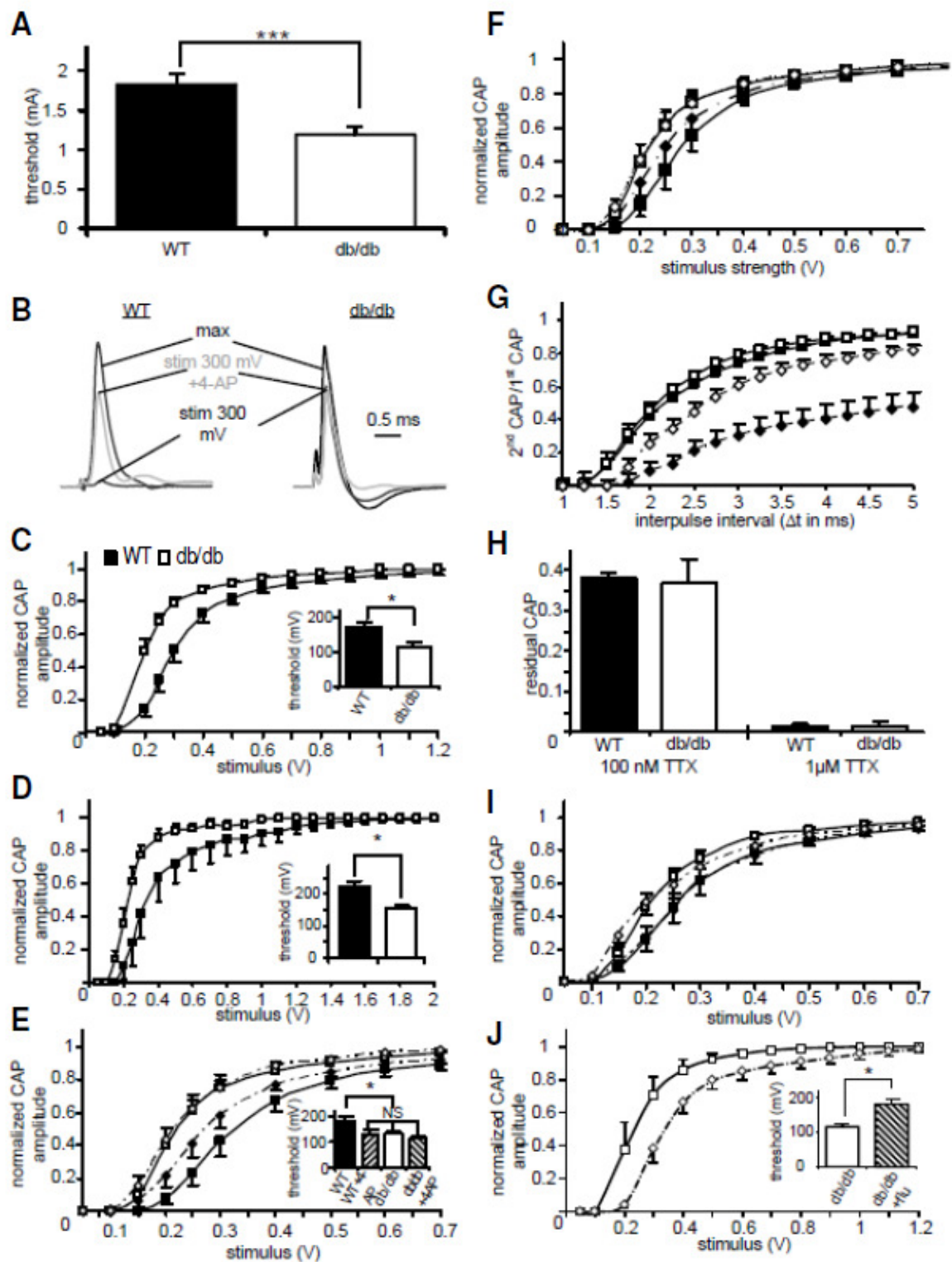


Figure 11 : Hyperexcitability of db/db peripheral nerves due to decreased K_v1 -channel function.
(legend on next page)

(A) *In vivo* measure of the threshold stimulus to induce a first CMAP on sciatic nerves. Threshold was significantly decreased in db/db (n=20) as compared to WT (n=20) mice. (B-J) Data obtained performing *ex vivo* recordings of CAPs on isolated mouse sciatic nerves. (B) Typical traces of CAP of WT and db/db nerves at different stimulus strengths (300 mV or the one to get the maximal amplitude) in presence or absence of 4-AP. The amplitudes of the traces were normalized to get the same maximal amplitude in WT and db/db nerves. (C) A α β CAP amplitude of WT (n=11) and db/db (n=12) nerves normalized by the maximal amplitude as function of the stimulus strength. We observed a leftward shift of the db/db curve corresponding to PNH. **Insert:** a significantly reduced threshold in db/db nerves confirmed PNH. (D) A δ CAP amplitude/stimulus strength curves. As for larger A α β fibers, thinly myelinated A δ sensory fibres were more excitable in db/db (n=5) as compared to WT (n=7) nerves. **Insert:** the threshold to generate an A δ CAP was also significantly decreased in db/db nerves. (E) 4-AP (500 μ M), a blocker of K $_v$ 1-channels, induced hyperexcitability in WT (n=6) but not in db/db (n=6) nerves. Labeling of WT and db/db was the same as in (C), diamonds correspond to the 4-AP condition. (F) DTX-1, a toxin blocking specifically K $_v$ 1-channels, had a similar effect than 4-AP on db/db and WT nerve excitability (n=6). (G) Effect of 4-AP on A α β CAP RP. The RP is represented as the ratio of the second CAP on the first CAP amplitude in function of the interpulse interval. 4-AP increased RP significantly more in WT (n=6) than in db/db (n=6) nerves. Labeling is as in (E). (H) Bar graph represents the residual CAP after application of 100 nM or 1 μ M TTX on WT and db/db nerves. The effect was similar for the two genotypes for both concentrations. (I) Effect of co-exposure of TEA (10 mM) with 4-AP (500 μ M) on nerve excitability. TEA, which blocks nodal K $_v$ 7-channels, did not induce any further increase in excitability in WT (n=5) or in db/db (n=4) nerves. Squares correspond to 4-AP and diamonds to 4-AP+TEA. (J) Flupirtine (10 μ M), an activator of K $_v$ 7-channels, significantly decreased db/db nerve excitability (n=5) thus reversing PNH. Diamonds correspond to the flupirtine condition. Error bars indicate SEM. * p < 0,05; *** p < 0,001; n= number of measurements.

3.1.4 Altered juxtaparanodal K $_v$ 1.2 localization under type 2 diabetic conditions

As previously observed, altered channel localization may explain the decreased function of K $_v$ 1-channels and the consequent PNH phenotype (37, 100). Therefore, I characterized the K $_v$ 1-channel distribution along peripheral axons. Teased fibers of sciatic nerves from 5 and 23 weeks old WT mice co-immunostained for K $_v$ 1.2 and pan-Na $_v$ showed typical accumulation of nodal Na $_v$ -subunits and specific localization of juxtaparanodal K $_v$ 1.2-subunits (**Fig. 12A and B left panels**). The same expression pattern was detected in db/db teased fibers at 5 weeks of age before the onset of T2DM and DPN (**Fig. 12A middle panel**). Interestingly, I observed a strong reduction of juxtaparanodal K $_v$ 1.2-subunits in db/db teased fibers at 23 weeks of age, whereas Na $_v$ -clusters were well preserved (**Fig. 12B middle panel**). For quantifications I evaluated the K $_v$ 1.2 signal intensity of 100 nodes, labeled with Na $_v$, per genotype and per age. At 5 weeks of age only very few nodes had a reduced staining signal of K $_v$ 1.2 for both WT and db/db mice. This number was significantly increased at 23 weeks of age for db/db mice. Moreover, about one third of db/db nodes had no K $_v$ 1.2 signal at all (**Fig. 12A and B right panels**). Interestingly, the other K $_v$ 1-channel subunits, K $_v$ 1.1 and K $_v$ β 2, were not affected in their distribution in db/db mice compared to WT mice and were normally distributed even at juxtaparanodes with reduced or absent K $_v$ 1.2 (**Fig. 12C and D**).

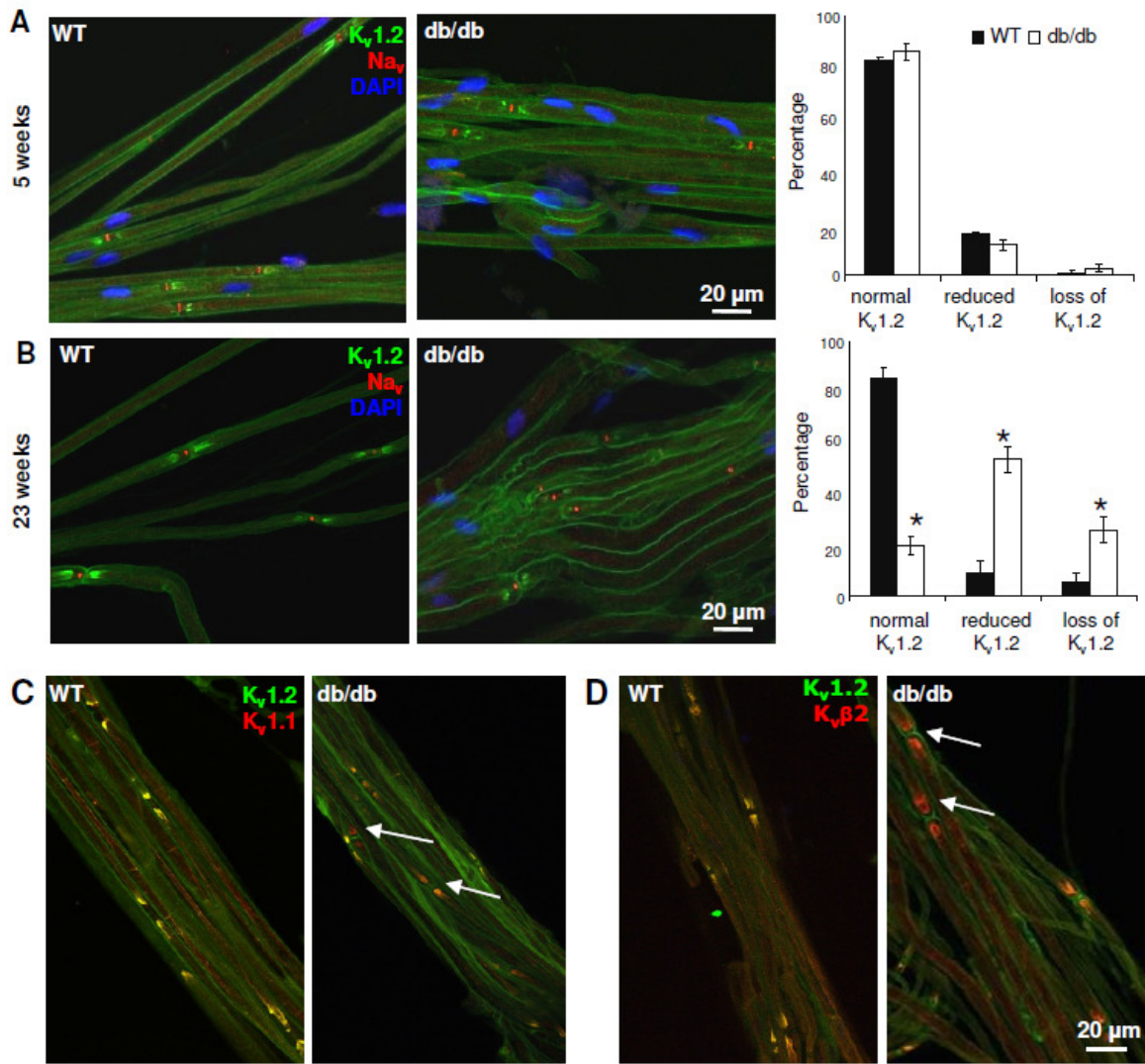


Figure 12 : Altered K_v1.2 distribution in db/db sciatic nerves at 23 weeks of age.

(A) At 5 weeks of age, before the onset of T2DM and DPN in db/db mice, Na_v-channels are accumulated at the node of Ranvier and K_v1.2-subunits at the juxtaparanodal regions in teased fibers from both WT and db/db mice. On the right, bar graphs illustrate the percentage of juxtaparanodes with reduced or absent K_v1.2 signal of 100 counted nodes, co-stained for Na_v. At 5 weeks of age, a low but equal number of juxtaparanodes demonstrated an abnormal K_v1.2 clustering in WT (15 %) and db/db mice (13%). (B) At 23 weeks of age, WT mice showed typical expression pattern of K_v1.2 and Na_v but in db/db teased fibers the K_v1.2 expression was strongly reduced. However, the nodal Na_v-clusters remained unaffected. As shown in the bar graph at 23 weeks of age, 80 % of juxtaparanodes in db/db mice had a reduced or absent K_v1.2 distribution as compared to 14 % in WT mice. (C) On the left, in WT mice all juxtaparanodal regions were co-localized for K_v1.1 and K_v1.2 (yellowish staining). On the right, while K_v1.1 was expressed in all juxtaparanodal regions in db/db teased fibers, K_v1.2 was lost in some of them (red colour; arrows). (D) Co-immunostainings for K_vβ2 and K_v1.2 revealed the same results as for K_v1.1. n=3 for all experiments, except WT at 5 weeks of age n=2; * p < 0,05.

Defects in multiple molecular mechanisms can lead to the observed altered distribution of K_v1.2 channels and I evaluated some of them (37, 100, 101). I tested for potential changes in the expression of ion channel subunits in both soma-rich dorsal DRG and axon-rich sciatic nerve endoneurial extracts of 5 and 23 weeks old mice. In DRG, I observed no differences in the mRNA expression levels of K_v1.2, K_vβ2 and Na_v1.6 (the major subunit of nodal Na_v-channels) at 5 and 23 weeks of age. While K_v1.1 showed a slight downregulation at 5 weeks of age, it is later slightly upregulated in db/db mice as compared to WT mice (Fig. 13A and

B). Moreover, the protein expression of the mature (glycosylated) and immature isoforms of $K_v1.2$ in DRG and in sciatic nerve endoneurium was similar between db/db and WT mice (**Fig. 13C**) indicating that $K_v1.2$ was normally expressed, translated and transported to the axon. In addition, demyelination is also known to affect juxtaparanodal K_v1 -channel distribution (101) but db/db mice did not possess any demyelination at this age as shown in **Fig. 10**. Together, these observations indicate that most likely the juxtaparanodal $K_v1.2$ channel clustering was affected under diabetic conditions.

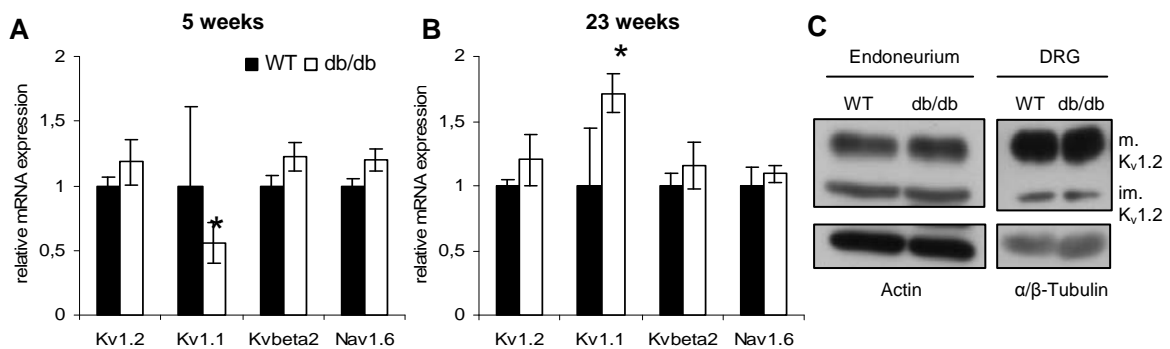
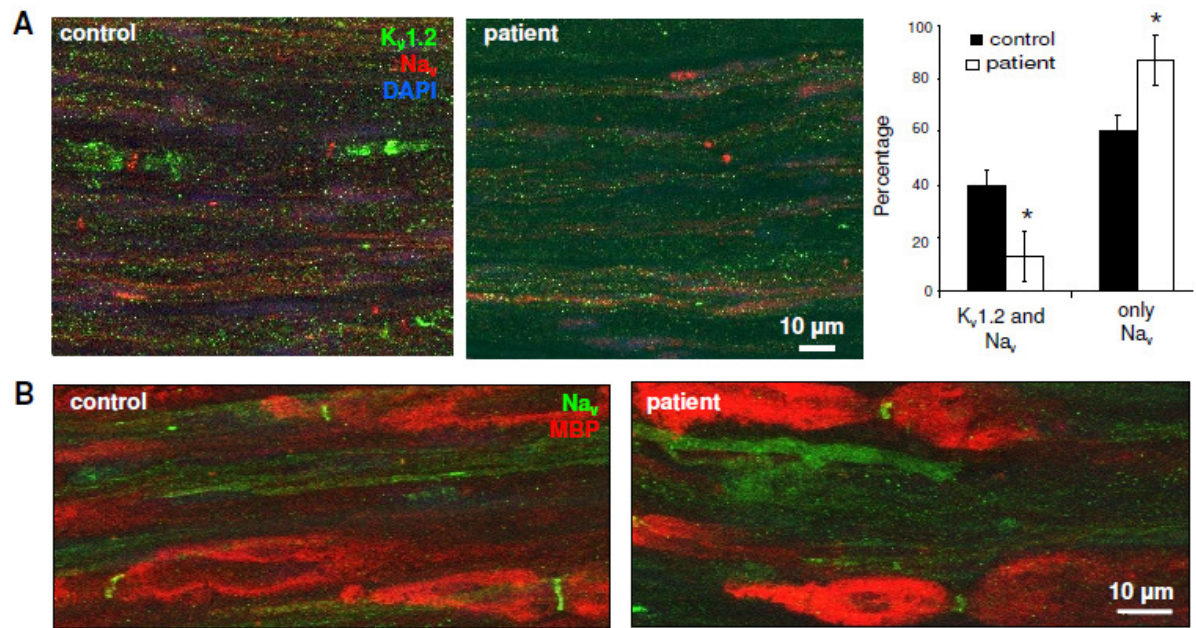


Figure 13 : Expression levels of ion channel subunits in WT and db/db mice at 5 and 23 weeks of age.

(A) At 5 weeks of age, before the onset of T2DM and DPN, mRNA expression of $K_v1.2$, $K_v\beta2$ and $Na_v1.6$ subunits were not different in db/db versus WT DRGs whereas $K_v1.1$ was significantly but slightly lower in db/db DRGs. **(B)** At 23 weeks of age, after 16 weeks of hyperglycemia, $K_v1.2$, $K_v\beta2$ and $Na_v1.6$ mRNA expression was still preserved. Interestingly, $K_v1.1$ expression switched being significantly upregulated in db/db DRGs as compared to WT DRGs. **(C)** Western blot analysis revealed an equal protein expression of immature (im.) and mature (m.) $K_v1.2$ isoforms in both sciatic nerve endoneurium and DRGs of db/db and WT mice. * $p < 0,05$; $n=3$.

To assess the clinical relevance of our data, I evaluated the channel distribution in nerve biopsies from T2DM patients with an axonal form of DPN (**Table 10**). Co-immunostainings of $K_v1.2$ and pan- Na_v on longitudinal sections of the peroneal nerve, a major branch of the mixed sciatic nerve, of control subjects revealed the typical accumulation of nodal Na_v -channels and juxtaparanodal K_v1 -channels. Similar to the phenotype of db/db mice, I observed a significant reduction of juxtaparanodal $K_v1.2$ subunits in all analyzed T2DM patients (**Fig. 14A**) while nodal Na_v -clusters were well preserved. 87% of the counted nodes had an impaired or absent $K_v1.2$ signal in T2DM patients as visualized in **Fig. 14A**. Although all T2DM patients presented a loss of myelinated fibers (**Table 10**), none of them showed obvious signs of segmental demyelination (**Fig. 14B**).



Patient	Sex	Age (y)	Time of T2DM (y)	Neuropathy	Symptoms	Nerve morphology
08N01013	M	52	-	-	neurogenic muscular atrophy; sensory defects until knee; squeezed lateral cutaneous nerve from thigh to spinal cord;	normal
09N01460	F	63	-	-	chronic neurogenic muscular atrophy; walking/balance problems since 2 years, progressive, sensory defects;	normal
10N00090	M	51	-	impairment of L5-S1 bilateral	muscular atrophy; disease of vertebral discs, pain, motor and sensory defects	normal, rare regeneration
08N00894	M	57	3	axonal, motor-sensory	motor defects fast progressive, lower limbs as well sensory defects; amyotrophie	loss of small and medium size myelinated fibers as well as unmyelinated fibers; WD; infiltration of immune cells
09N01529	F	72	14	axonal, sensory and severe motor defects	since 4 years progressive motor-sensory defects, hypoesthesia, reduced balance/vibration sense;	loss of medium and small size myelinated fibers as well as unmyelinated fibers; signs of WD and microangiopathy.
10N00300	M	41	n.d.	axonal and demyelination	Paresthesia since 6 months of lower limbs, sensory defects at all 4 limbs	moderate loss of large myelinated fibers; WD and oedema, inflammatory processes; diabetic microangiopathy

Table 10 : Clinical profile of T2DM and control subjects.

WD = Wallerian degeneration;

3.1.5 Molecular mechanism underlying the altered K_v1.2 distribution (preliminary data)

As demonstrated in **Fig. 13**, the mRNA and protein expression level of K_v1.2 is normal and cannot be causative for the altered juxtaparanodal distribution of K_v1.2. Thus, I started to further explore the molecular mechanism behind the altered K_v1.2 distribution in T2DM.

There is a multiple-step process from K_v1.2 protein expression until its juxtaparanodal membrane integration consisting of K_v1.2 maturation (glycosylation), subunit assembly, vesicle inclusion, axonal transport and juxtaparanodal clustering. I used endoneurial protein extracts of WT and db/db mice to perform Co-IP experiments against K_vβ2 (**Fig. 15A**). Preliminary data showed an increased concentration of K_vβ2 protein in the co-immunoprecipitated samples of both WT and db/db mice compared to their corresponding input samples. Furthermore, I could not observe any expression of K_vβ2 in both genotypes co-immunoprecipitated without primary antibody (negative control) validating the set up of the experiment. Interestingly, it demonstrated a reduced attachment of mature K_v1.2 to K_vβ2 in parallel with an increased amount of immature K_v1.2 in db/db mice as compared to WT mice. Likewise, I observed a reduced attachment of K_vβ2 to microtubules in db/db mice. Equal amounts of K_v1.2 and α/β-tubulin were obtained for the input samples of both genotypes and normalized to actin which could not be detected in the immunoprecipitated samples.

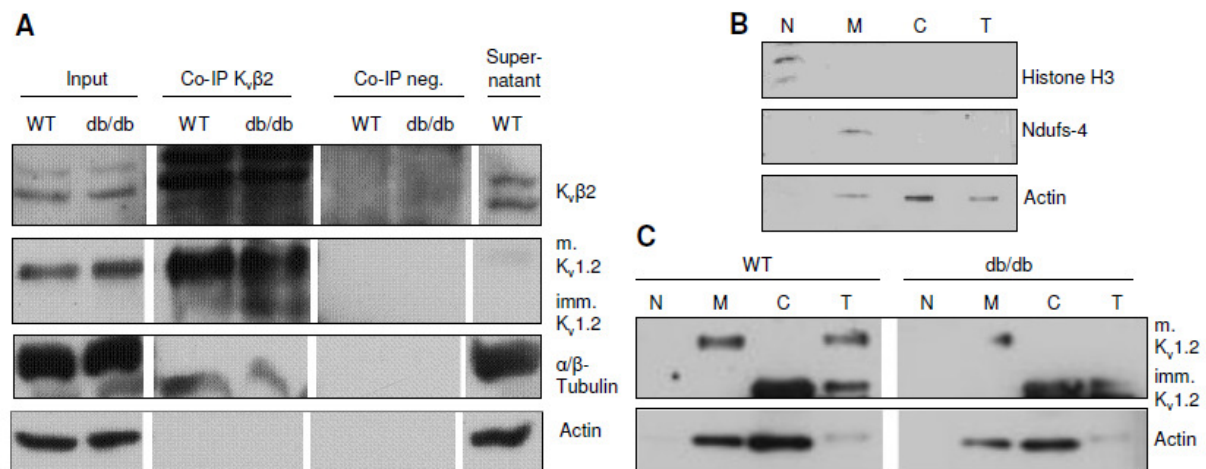


Figure 15 : Altered K_v1.2 protein interactions and subcellular localization in db/db mice at 23 weeks of age.

(A) Co-IP experiments of WT and db/db sciatic nerve extracts against K_vβ2 subunits showed a reduced binding of matured K_v1.2 but more of immature K_v1.2 to K_vβ2 in db/db mice as in WT mice. Moreover, K_vβ2 showed a worse binding to tubulin in db/db mice. In both WT and db/db mice no binding to Actin filaments was observed. (B, C) Cellular fractionation was performed to identify differences in subcellular K_v1.2 localization. (B) Separation of membrane (M), nuclei (N) and cytoplasmic fractions (C) was verified by fraction specific markers including Histone H3, mitochondrial Ndufs-4 and Actin respectively and was compared to the total lysate (T). (C) In sciatic nerve endoneurium of WT mice mature K_v1.2-subunits were specifically integrated into the axonal membranes whereas immature K_v1.2 was only found in the cytoplasm. The amount of integrated mature K_v1.2-subunits was substantially lower in db/db endoneurium but immature K_v1.2 was only observed in the cytoplasm too. However, with this technique I observed even in the total lysate a lower expression of K_v1.2 in db/db mice than in WT mice. n=3 for Western blot; n=2 for Co-IP and cellular fractionation. m. = mature; imm. = immature;

Next, the inability of K_v1.2 to reach its final target at the juxtaparanodal membrane of the axon may lead to an altered subcellular localization within the sciatic nerve. Therefore, I performed cellular fractionation to characterize K_v1.2 subcellular distribution. Efficient separation of proteins found in nuclei, membrane or cytosol was confirmed with specific markers for each fraction by immunoblot analyses on test samples (**Fig. 15B**). While in the total protein extract of WT mice both the immature and mature forms of K_v1.2 were present, the two isoforms were separated into two distinguished subcellular fractions (**Fig. 15C**). In the WT situation all matured K_v1.2 were integrated into the axonal membrane in the lysate of sciatic nerve endoneurium whereas immatured K_v1.2 was exclusively found in the cytosol fraction. I observed the same subcellular separation in db/db animals, however the amount of integrated mature K_v1.2 was much lower in db/db mice as in WT mice. Unexpectedly, I even could not detect any mature K_v1.2 in the total extract of the cellular fractionation experiment of db/db animals.

3.2 Generation of a knockout mouse model to study the role of peripheral myelin protein P2

3.2.1 Selective P2 expression in a subset of Schwann cells in wild-type mice

Previous publications indicated that P2 may play a role in PNS myelination (79, 80). However, the functional role of P2 remains still unknown.

To date, P2 (= FABP8) is the only family member of FABPs known to be expressed in the PNS. I made use of the microarray data generated in our laboratory (102) to evaluate the expression levels of all FABP family members (**see table 5**) in the PNS, either in DRGs (= neuronal expression) or in sciatic nerve endoneurium (= glial expression). Interestingly, I observed an expression for three FABPs: FABP3, FABP5 and P2 (**Fig. 16A to C**). While both FABP3 and FABP5 were predominantly expressed by DRG neurons, P2 was the only FABP specifically expressed by Schwann cell in sciatic nerve endoneurium. Furthermore, the neuronal FABPs showed a more constant expression from birth until 28 months of age whereas P2 demonstrated a very dynamic expression profile. At birth it starts to be expressed, reaching its maximal expression after 2 weeks of age before being decreased again. Genes involved in the process of PNS maturation and which are as well expressed specifically by Schwann cells, e.g. MPZ and MBP, revealed a similar mRNA expression pattern as P2 during PNS myelination (**Fig. 16D**) thus highlighting its role as a PNS myelin gene. But unlike the other myelin genes whose expression were absent in older ages, P2 remained expressed albeit at a lower expression level in mature myelinated Schwann cells. In addition, Scip, a transcription factor involved in the Schwann cell differentiation (103), is expressed prior to all myelin genes and downregulated with the beginning of myelination. Furthermore, I have also observed a similar profile of P2 expression at the protein level, where I detected its maximal amount in sciatic nerve samples of P10 old mice (**Fig. 16E**). qPCR analysis of various neuronal and non-neuronal tissues from adult WT mice confirmed the Schwann cell-specific expression of P2 (**Fig. 16F**).

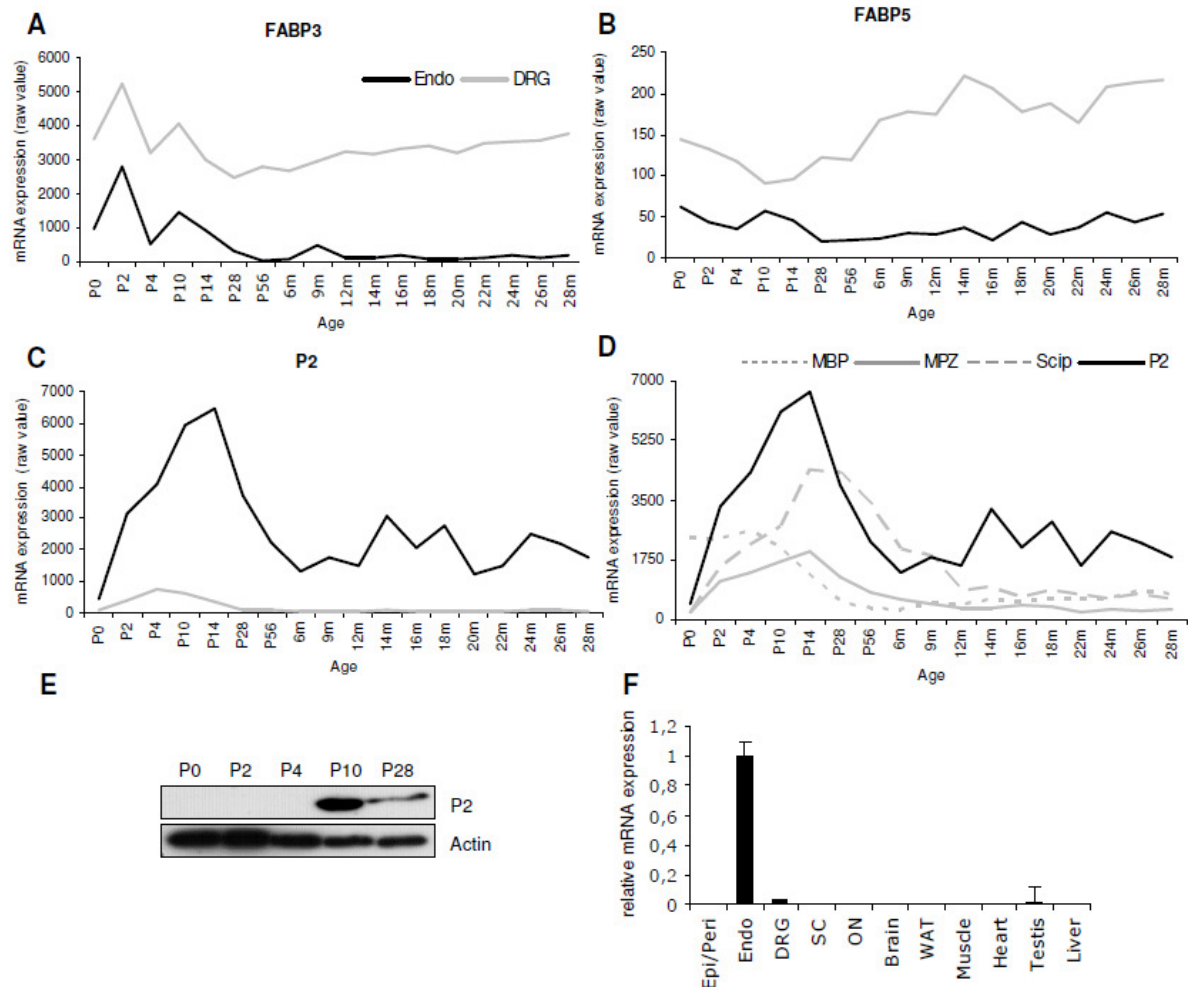


Figure 16 : Expression profiles of FABPs present in the peripheral nervous system.

(A) FABP3 and (B) FABP5 revealed a strong neuronal mRNA expression profile in mouse DRGs from birth until 28 months of age with only a minor expression in sciatic nerve endoneurium. (C) P2 (= FABP8) showed a highly specific and dynamic mRNA expression in Schwann cells enriched in sciatic nerve endoneurium. (D) Similar to MBP and MPZ, P2 is predominantly expressed during the first two weeks after birth. However, P2 is still expressed during aging (P56 until 28 of months). In contrast, Scip is expressed prior to all myelin genes. (E) Western Blot analysis confirmed the dynamic expression profile of P2 during postnatal development. (F) qPCR analysis demonstrated tissue-specific P2 mRNA expression only in sciatic nerve endoneurium as compared to other neuronal and non-neuronal tissues of adult mice (P56) as indicated.

In order to localize P2 expression in the sciatic nerve, I performed co-immunostainings of P2 and MBP on cross sections of P10- old mice (**Fig. 17A and B**). Both MBP and P2 were detected in the myelin sheaths of Schwann cells. Interestingly, while MBP labeled all myelin sheaths, only some of them were P2-positive which confirmed previous observations (80). Furthermore, unlike MBP, P2 was also detected in the Schwann cell cytoplasm (**Fig. 17B**). The observation that P2 is expressed in only some of the myelin sheaths rises up the question of what distinguishes P2-positive and P2-negative Schwann cells. As suggested earlier (80), it could be the function or the size of the nerve fiber. First, co-immunostainings on dorsal and ventral roots containing only sensory or motor nerve fibers respectively, revealed P2 expression in myelin sheaths of both roots (**Fig. 17C and D**).

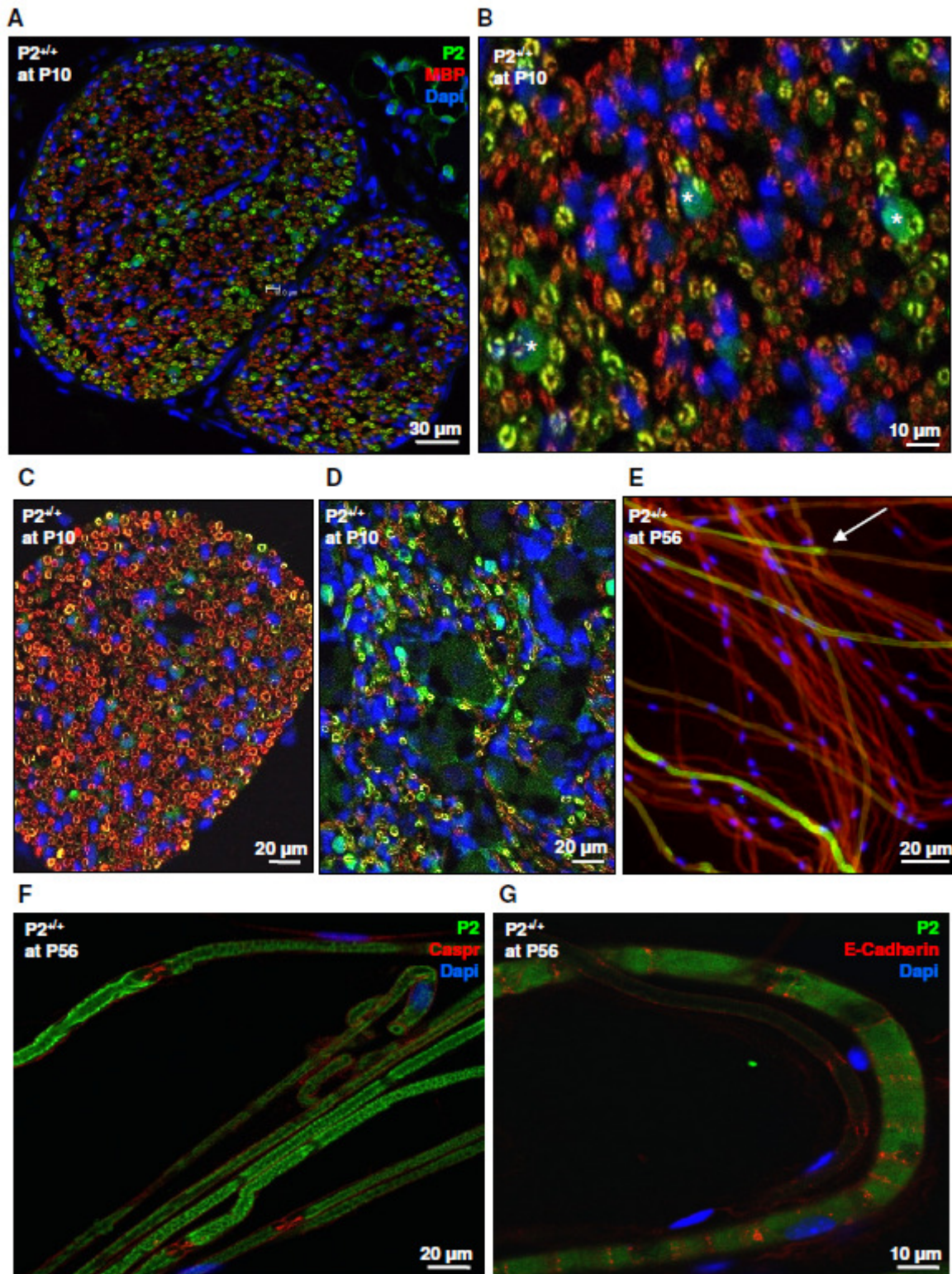


Figure 17 : P2 protein localization in wild-type sciatic nerve and roots.

(A) In cross sections of WT sciatic nerves at P10 all myelin sheaths were immunolabeled with MBP, however only a subset of them expressed P2. (B) Higher magnification confirmed a strong cytoplasmic expression of P2 in Schwann cells (asterisks). Co-immunostainings of MBP and P2 on (C) ventral and (D) dorsal roots showed P2 expression of both Schwann cells associated with motor or sensory fibers respectively. (E) Adult sciatic nerve teased fibers confirmed the partial expression of P2 by Schwann cells and moreover revealed changes in P2 expression of adjacent Schwann cells along the same nerve fiber (arrow). Teased fibers stained for P2 and (F) Caspr or (G) E-Cadherin, which are markers of non-compact myelin at paranodes and SLI respectively, showed a specific localization of P2 in compact myelin. n=3 for sciatic nerves; n=2 for roots.

This observation excludes the functionality of the fiber as determinant and is in agreement with an earlier study (80). Second, on immunostainings of sciatic nerve cross sections, P2 seemed to be expressed preferentially by large fibers (**Fig. 17B**). Co-immunostainings of teased fibers of adult sciatic nerves for MBP and P2 confirmed the selective Schwann cells expression of P2 (**Fig. 17E**). However, it also demonstrated that neuronal size cannot be the only factor determining P2 expression as adjacent myelin segments along the same nerve fiber could switch from being P2-positive to P2-negative.

Next, I asked if P2 is specific for compact or non-compact myelin. To answer this question, I performed co-immunostainings on adult teased sciatic nerve fibers with P2 and Caspr or P2 and E-Cadherin. Both are markers for regions of non-compact myelin, the paranodes and SLI respectively. As shown in **Fig. 17F and G**, P2 did not co-localize with these markers of non-compact myelin. Therefore, P2 is specifically expressed in compact myelin.

3.2.2 P2 expression profile in mouse models of peripheral neuropathies

P2 expression profile alone makes it difficult to understand its role in PNS myelination. As analysis under disease-like situations helps figuring out the role(s) of a gene. Therefore, I compared the P2 mRNA expression in various mouse models of peripheral neuropathy, namely Lpin1 (Lpin1^{-/-}), Pmp22 (Pmp22^{-/-}) and Scap (Scap^{-/-}) KO mouse models at P56 (102) (**Fig. 18A**). In all three situations a reduction in myelin has been observed, correlated with a significant downregulation of the major PNS myelin genes MPZ, MBP and Pmp22. In contrast, P2 was only downregulated to a minor extent in Lpin1^{-/-} and Pmp22^{-/-} mice, whereas in Scap^{-/-} mice P2 was even slightly upregulated at P56. Uncompacted genes, like MAG, are however upregulated in both Scap^{-/-} and Pmp22^{-/-} mice and did not correlate with the expression pattern of P2. Again, this observation reflects a unique situation for P2.

Performing immunostainings on sciatic nerve cross sections of adult Lpin1^{+/+} and Lpin1^{-/-} mice at P56 (**Fig. 18B**) clearly demonstrated the severe demyelination effect in Lpin1^{-/-} mice. However, P2 was still well expressed in many myelin sheaths of mutant mice. The reduced P2 mRNA expression in Lpin1^{-/-} mice as shown in **Fig. 18A** might be caused by the overall reduction of the number of myelinated SCs (47). While in Lpin1^{+/+} mice predominantly myelin sheaths of large fibers were P2-positive, in Lpin1^{-/-} mice there were apparently myelin sheaths of both P2-positive large and small fibers. Moreover, the cytoplasmic expression in Lpin1^{-/-} mice was more prominent as in Lpin1^{+/+} mice, potentially correlating with the higher amount of immature Schwann cells in the Lpin1^{-/-} mice. Interestingly, few myelin sheaths in the Lpin1^{-/-} mice expressed only P2 but not MBP which was never observed in WT mice (at P10 and P56).

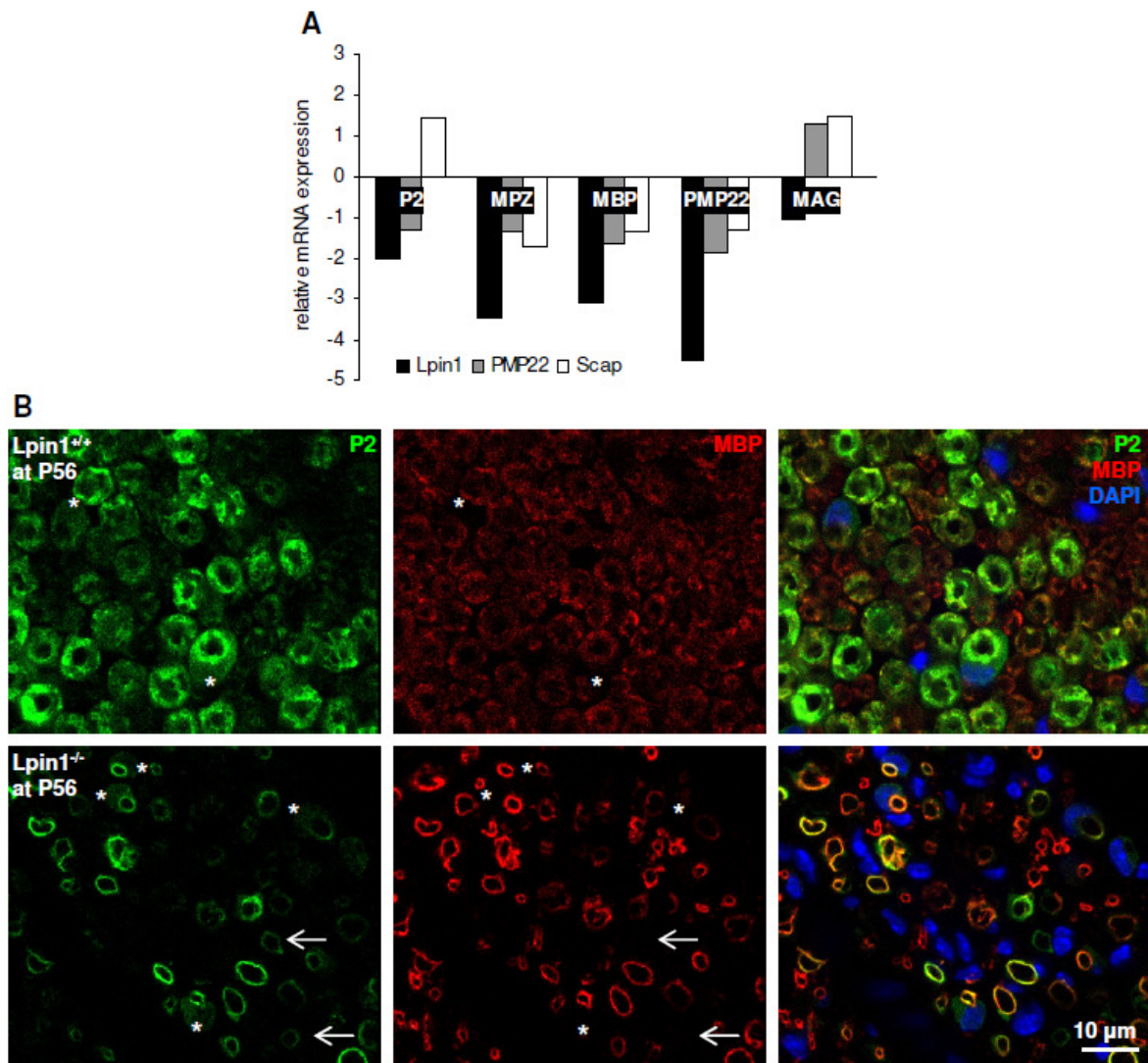


Figure 18 : P2 expression in mouse models of peripheral neuropathy.

(A) Comparison of changes of P2 mRNA expression in mouse models of demyelination (*Lpin1*^{-/-}), dysmyelination (*Pmp22*^{-/-}) and hypomyelination (*Scap*^{-/-}) revealed no congruence with any other myelin gene. P2 being the only marker downregulated in *Lpin1*^{-/-} and *Pmp22*^{-/-} mouse models and slightly upregulated in *Scap*^{-/-} mice. (B) Co-immunostainings of P2, MBP and the merge of both on sciatic nerve cross sections of P56-old *Lpin1*^{+/+} and *Lpin1*^{-/-} mice. It clearly showed the demyelinating phenotype in *Lpin1*^{-/-} mice but a similar P2 expression pattern for both genotypes. However, few myelin sheaths in *Lpin1*^{-/-} mice expressed only P2 and not MBP which was never seen in *Lpin1*^{+/+} mice (arrows). The cytoplasmic expression of P2 in *Lpin1*^{-/-} was more obvious than in *Lpin1*^{+/+} mice (asterisks). n=3.

3.2.3 Characterization of *P2*^{-/-} mouse strain with preserved myelination

In order to study the role of P2 *in vivo*, I have generated a P2 KO mouse model (*P2*^{-/-}) with a complete loss of P2. The P2 targeted embryonic stem cells were developed by Regeneron (www.velocigen.com) and were used to generate the *P2*^{+/-} mice via the service of Knockout Mouse Project organization (www.komp.org). In a mutated allele all 4 coding exons of P2 were replaced by a LacZ-neomycin cassette in frame after the original ATG start codon of the P2 gene (Fig. 19A). Since the inserted neomycin gene was flanked by loxP sites, homozygous *P2*^{-/-} mice were crossed with the deleter strain nestin-Cre. Elimination of the

neomycin-gene lead to the generation of $P2^{+/-\Delta neo}$ mice. However, all experiments described here were performed with $P2^{-/-}$ mice.

The successful disruption of the P2 gene was confirmed on both mRNA and protein levels. As shown in **Fig. 19B** for PCR and in **Fig. 19C** for Western blot analysis, the level of P2 expression in sciatic nerve endoneurium was substantially decreased in $P2^{+/-}$ mice and absent in $P2^{-/-}$ mice at P56. Co-immunostainings of P2 and MBP on sciatic nerve cross sections of P10-old $P2^{-/-}$ and $P2^{+/+}$ mice confirmed the loss of P2 expression in all Schwann cells (**Fig. 19D**). Furthermore, I verified by PCR the LacZ expression in $P2^{+/-}$ and $P2^{-/-}$ but not in $P2^{+/+}$ mice (**Fig. 19B**). The functionality of the LacZ gene was assayed by the enzymatic reaction of X-Gal. Interestingly, in samples of $P2^{+/-}$ mice the majority of myelin sheaths was stained in blue (**Fig. 19E**), more than P2-positive immunostained myelin sheaths in $P2^{+/+}$ mice (**Fig. 19D**).

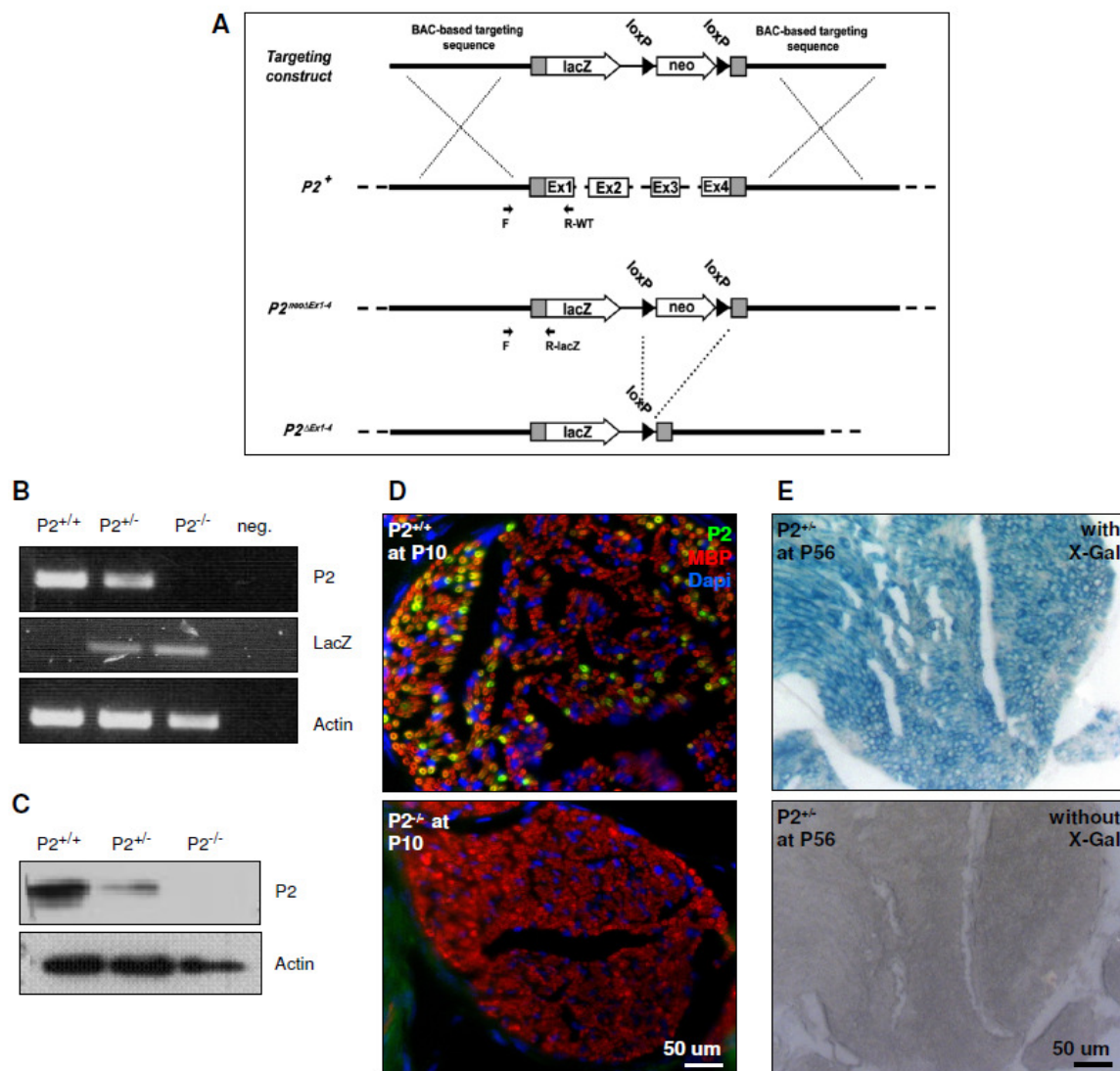


Figure 19 : Generation of $P2^{-/-}$ mice.

(A) Strategy for the generation of $P2^{-/-}$ mice. The complete P2 gene was replaced by the LacZ-neomycin cassette. As the neomycin-gene was flanked by FloxP-sites it was removed by crossing $P2^{+/-}$ mice to the deleter strain nestin-Cre. (B) QPCR analysis for P2 and LacZ, (C) Western Blots against P2, (D) co-immunostaining against P2 and MBP and (E) enzymatic reactions for β -Gal confirmed a reduced P2 expression in $P2^{+/-}$ mice and a complete loss of P2 in $P2^{-/-}$ mice together with the successful integration of the LacZ gene.

$P2^{-/-}$ mice developed normally, were fertile and produced offspring in the normal Mendelian ratio (**Fig. 20A**). They had normal body weight and blood glucose levels compared to age-matched control mice at P10 and P56 (**Fig. 20B and C**). Interestingly, the plasma insulin level tended to be lower in young (P10-old) $P2^{-/-}$ mice (not significant) whereas the older mice (P56) had significantly increased plasma insulin levels as compared to age-matched $P2^{+/+}$ mice indicative of insulin resistance (**Fig. 20D**). The plasma levels of FFA were not altered in both P10- and P56-old $P2^{-/-}$ mice as compared to $P2^{+/+}$ mice (**Fig. 20E**). To check for presence of any defects in the PNS, I performed MNCV measurements on the sciatic nerves of $P2^{+/+}$ and $P2^{-/-}$ mice at P28 (P10 too young to be measured) and P56 (**Fig. 20F**). At both ages, I observed a slight reduction in the MNCV which became significant at P56 suggestive for a demyelinating phenotype of peripheral nerves. To further characterize this electrophysiological differences between $P2^{-/-}$ and $P2^{+/+}$ mice at P56 I compared the properties of the shape of the CMAP (**Table 11**). While CMAP latency and duration were normal in $P2^{-/-}$ mice, CMAP amplitude and area were significantly increased as compared to $P2^{+/+}$ mice at P56.

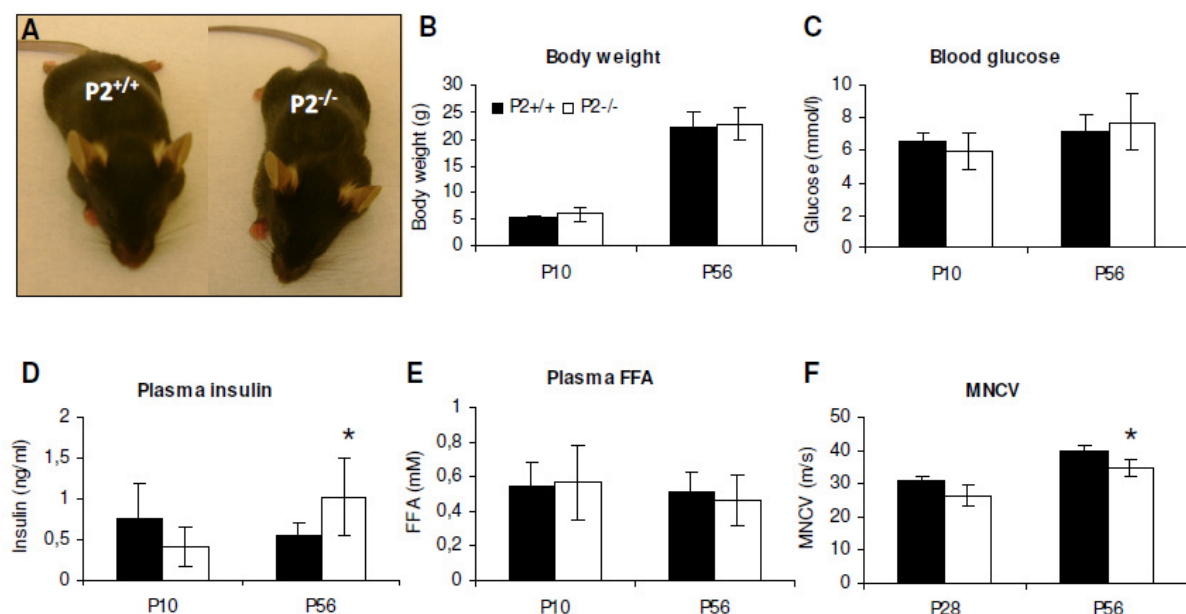


Figure 20 : Physiological characterization of P10- and P56-old $P2^{-/-}$ mice as compared to $P2^{+/+}$ mice.

(A) Phenotypically adult $P2^{-/-}$ mice were healthy with no alterations in (B) body weight and (C) blood glucose levels as compared to age-matched $P2^{+/+}$ mice. (D) Interestingly, the plasma insulin level was significantly increased in P56-old $P2^{-/-}$ mice versus $P2^{+/+}$ mice while (E) the level of plasma FFA showed no alterations. (F) MNCV was significantly lower in $P2^{-/-}$ mice as compared to $P2^{+/+}$ mice at P56. n=5 at P10; n=3 at P28; n=10 at P56.

	MNCV (m/s)	Latency (ms)	Duration (ms)	Amplitude (mV)	Area (mV/ms)
P2^{+/+}	39 (+/- 1,0)	1,13 (+/- 0,09)	0,8 (+/- 0,17)	3,59 (+/- 0,62)	1,34 (+/- 0,14)
P2^{-/-}	33,78 (+/- 3,29)	1,04 (+/- 0,07)	0,83 (+/- 0,1)	7,04 (+/- 1,09)	2,78 (+/- 0,26)
p-value	0,0055	0,2367	0,7866	0,0065	0,0044

Table 11 : Properties of the CMAP curve of P2^{-/-} and P2^{+/+} mice at P56.

In addition to a significant reduction of the MNCV, the CMAP amplitude as well as the CMAP area was significantly increased in P2^{-/-} mice as compared to P2^{+/+} mice at P56. CMAP latency and duration was not different. n=3.

To evaluate potential morphological abnormalities in the sciatic nerve of P2^{-/-} versus P2^{+/+} mice semithin cross sections of the sciatic nerve at P10 and P56 were performed (**Fig. 21A and C**). Surprisingly, no gross alterations during the development (P10) and in the maintenance (P56) of the PNS could be observed. Additional quantitative measurements on the semithin cross sections including g-ratio calculations (**Fig. 21B and D**), axonal distribution (**Fig. 21E**) and axonal counting (**Fig. 21F**) excluded any major demyelinating or neuronal phenotypes in P2^{-/-} mice as compared to age-matched P2^{+/+} mice.

Crucial for the generation and transmission of an APO along myelinated nerve fibers is the exchange of Na⁺- and K⁺-ions at the nodal region. Therefore, I analysed the presence and localization of the corresponding voltage-gated Na_v- and K_v1-channels of adult sciatic nerve fibers of P2^{+/+} and P2^{-/-} mice at P56. Immunostainings on teased fibers revealed the typical accumulation of Na_v-channels at the node of Ranvier and K_v1-channels at the juxtaparanode in both P2^{+/+} and P2^{-/-} mice (**Fig. 21G**).

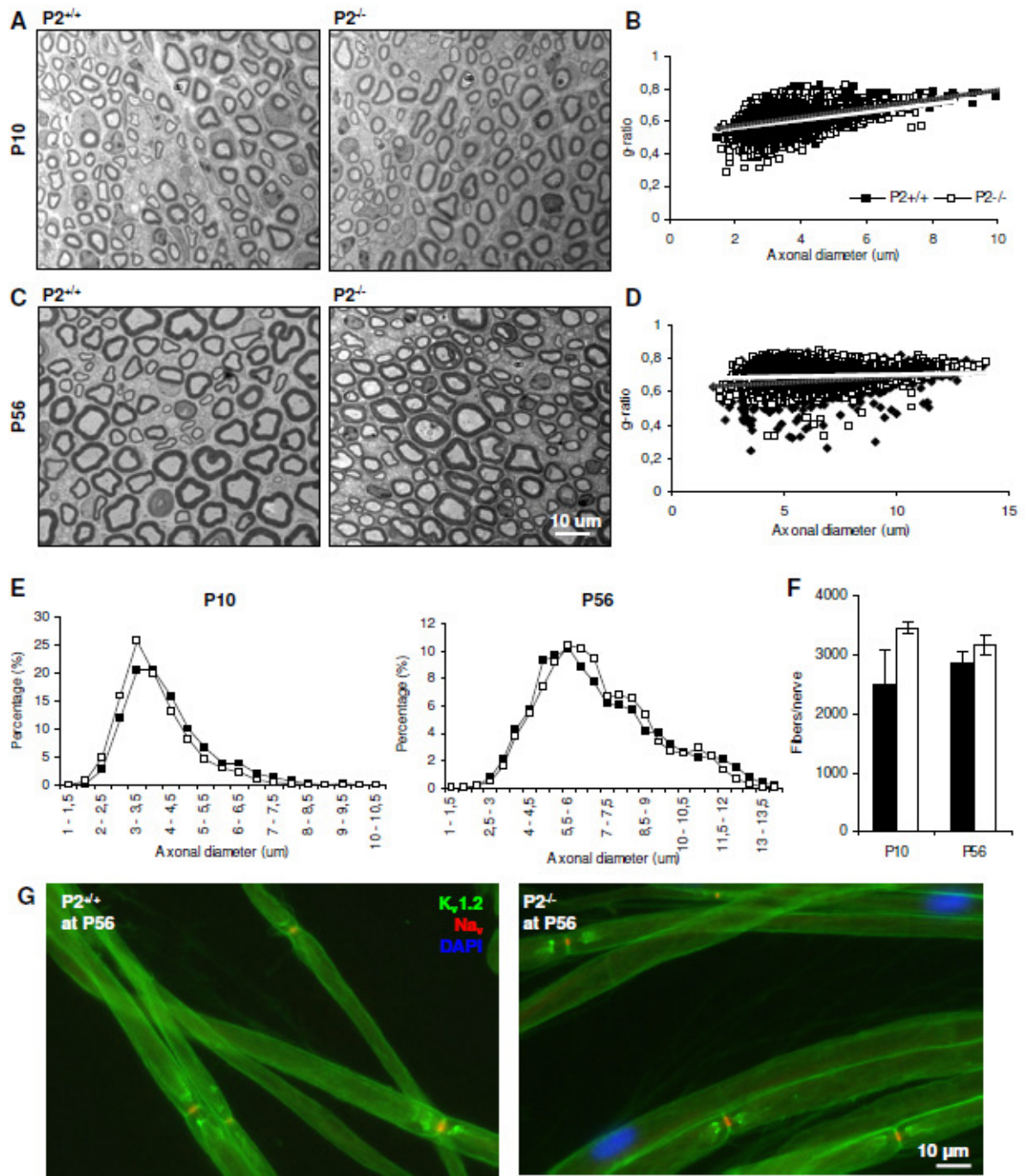


Figure 21 : Preserved myelination of P2^{-/-} sciatic nerves at P10 and P56.

Any early (P10) or late (P56) defects in PNS myelination has been observed in P2^{-/-} mice as compared to age-matched P2^{+/+} mice. (**A** and **C**) Semithin cross sections stained with Toluidin Blue, (**B** and **D**) g-ratio calculations, (**E**) measurements of the axonal distribution and (**F**) total nerve fiber counts of sciatic nerves revealed no changes in peripheral nerves caused by the loss of P2 expression. (**G**) In sciatic nerve teased fibers of P56-old P2^{+/+} mice Na_v-channels are accumulated at the node of Ranvier while K_v1-channels, labeled against K_v1.2, are clustered at the juxtaparanodes. The same distribution of both ion channels was observed in P56-old P2^{-/-} mice. n=3;

3.2.4 Gene expression profiling of P2^{-/-} mice identified differentially gene expression of other FABP family members

To comprehensively check for any alterations in gene expression in P2^{-/-} mice, I performed microarray analysis of the sciatic nerve of P10-old P2^{+/+} versus P2^{-/-} mice. I chose P10-old mice as this time-point reflects the main peak of the P2 expression and in order to identify early, and therefore predominantly primary, effects in the process of myelination.

A strong downregulation of P2 gene expression in P2^{-/-} mice confirmed the loss of P2 in our mouse model (**Fig. 22**). Interestingly, the P2 deficiency had no influence on the gene expression of any other myelin or lipid gene crucial for the process of myelination. However, I observed alterations in the gene expression of other FABP family members. In particular, FABP9 was significantly upregulated and FABP5 significantly downregulated. Contrary to FABP9, FABP5 was already strongly expressed in P2^{+/+} mice. In addition, a minor (not significant) downregulation of multiple adipocyte-related genes (Resistin, Adiponectin, Ucp1 and Car3) was revealed.

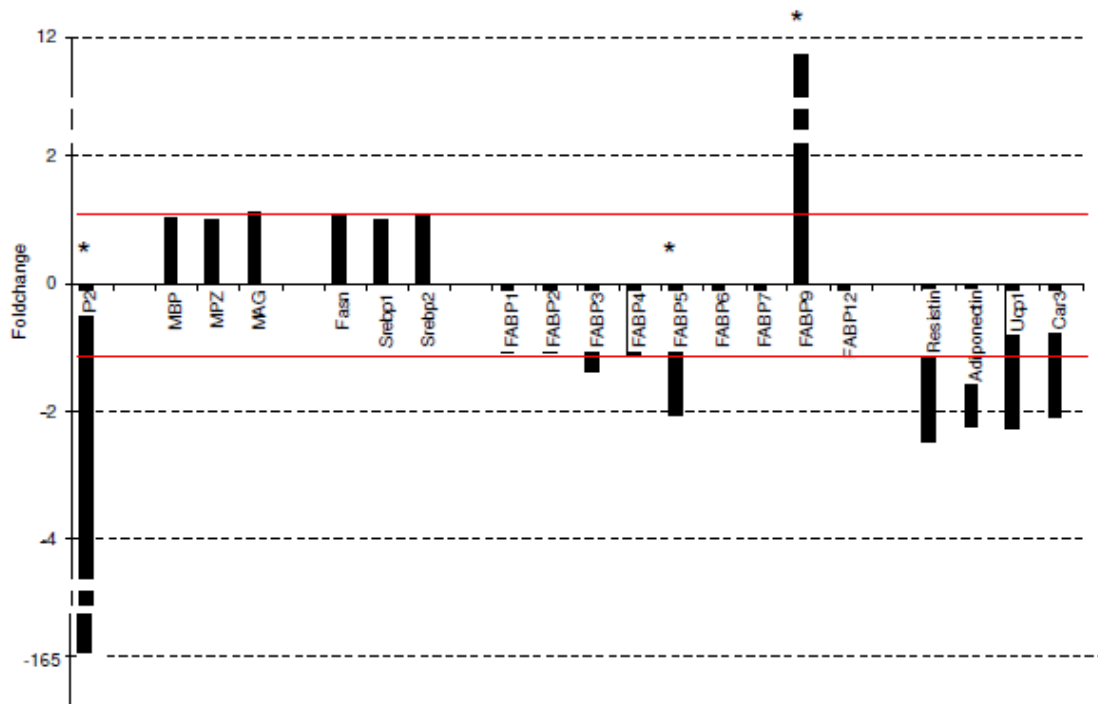


Figure 22 : Transcriptional changes in P2^{-/-} sciatic nerve endoneurium at P10.

Microarray data of P2^{-/-} versus P2^{+/+} sciatic nerve endoneurium at P10, confirmed a strong downregulation of P2 in P2^{-/-} mice by which no other major myelin (MBP, MPZ, MAG) or lipid genes (Fasn, Srebp1, Srebp2) was influenced. The only genes being significantly differentially expressed are FABP5 and FABP9. Adipocyte-related genes (Resistin, Adiponectin, Ucp1, Car3) showed a (not significant) downregulation of more than twofold. * adjusted p-value < 0,05. Red lines indicate foldchange of 1 (= no change in expression in P2^{-/-} mice versus P2^{+/+} mice).

Next, I performed qPCR analysis of P56-old P2^{+/+} and P2^{-/-} mice to corroborate the microarray results (**Fig. 23**). First, at this age it was possible to separate the endoneurium from the epi- and perineurium, which contain a high amount of adipocytes. Second, FABP5 and FABP9 were highly expressed in white adipocyte tissue and testis/ovaries respectively (**see table 5**). Therefore these tissues were used as control tissues. As expected, P2 was

specifically expressed in sciatic nerve endoneurium of $P2^{+/+}$ mice but in none of the tissues in $P2^{-/-}$ mice (**Fig. 23A**). I confirmed the strong upregulation of FABP9 and mild downregulation of FABP5 in $P2^{-/-}$ sciatic nerve endoneurium. However, both changes in gene expression were also present in the other tissues tested and thus were not sciatic nerve endoneurium specific (Fig. 23B, C). Resistin was highly expressed in lipid-rich tissues as white adipocyte tissue and epi- and perineurium but not in sciatic nerve endoneurium in both $P2^{+/+}$ and $P2^{-/-}$ mice. While I observed no differential expression of Resistin in white adipocyte tissue, it was downregulated in epi- and perineurium of $P2^{-/-}$ mice as compared to $P2^{+/+}$ mice at P56 (**Fig. 23D**). Thus, the differential gene expression of adipocyte-related genes is most likely derived from the adipocytes of the epi- and perineurium and not from Schwann cells in the endoneurium. Normal expression of the major myelin and lipid genes was confirmed by using an independent sample of sciatic nerve endoneurium of P10-old $P2^{-/-}$ and $P2^{+/+}$ mice (**Fig. 23E**). Moreover, I observed no alterations even later at P56 using $P2^{-/-}$ and $P2^{+/+}$ sciatic nerve endoneurium.

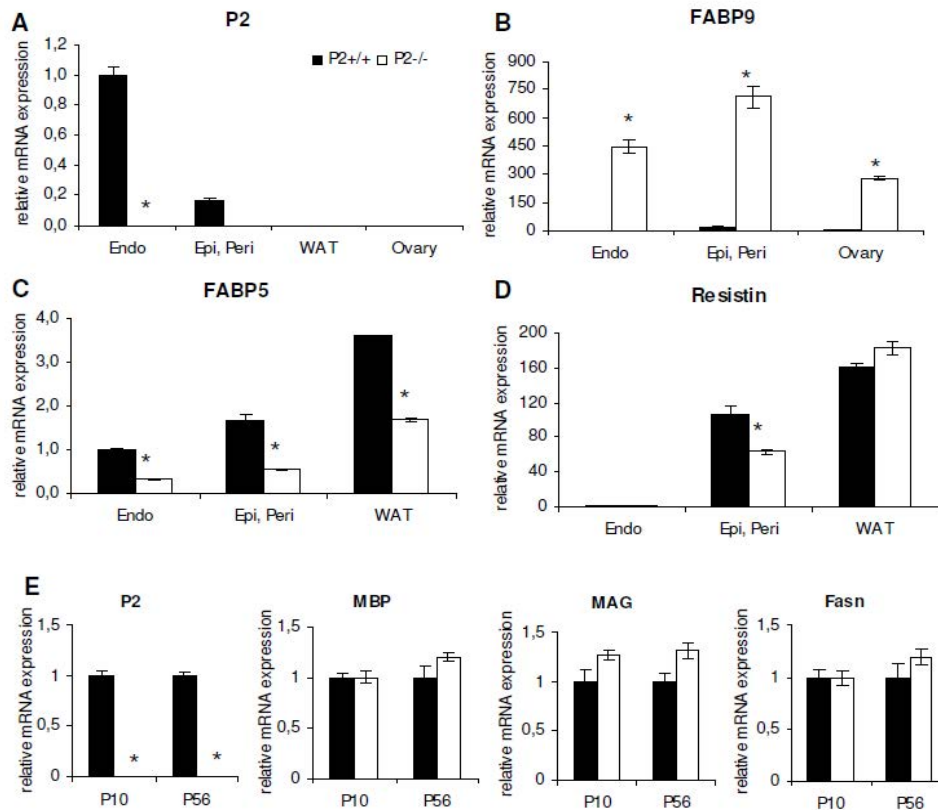


Figure 23 : Comparison of microarray results with qPCR measurements of selected genes.

(A) P2 was specifically expressed in $P2^{+/+}$ sciatic nerve endoneurium and in none of the tissues in $P2^{-/-}$ mice at P56. Slight expression in epi-/perineurium might be due to some residual Schwann cells after dissection. (B) FABP9 was also significantly higher expressed in P56-old $P2^{-/-}$ as compared to $P2^{+/+}$ sciatic nerve endoneurium. FABP9 was upregulated in epi-/perineurium and ovaries of $P2^{-/-}$ mice too. (C) Likewise, FABP5 was downregulated in sciatic nerve endoneurium as well as for other tissues tested in P56-old $P2^{-/-}$ mice as compared to age-matched $P2^{+/+}$ mice. (D) While Resistin was not expressed in sciatic nerve endoneurium of both genotypes, it showed a specific downregulation only in $P2^{-/-}$ epi-/perineurium. (E) No alterations in mRNA expression for any myelin or lipid gene was observed in P10-old and P56-old $P2^{-/-}$ mice as compared to age-matched $P2^{+/+}$ mice. $n=2$ with pooled RNA of 3 mice per genotype each time. Epi, Peri = epineurium, perineurium; WAT = white adipocyte tissue. All data normalized to $P2^{+/+}$ endoneurium = 1; * p -value < 0,05.

To evaluate the FABP9 protein expression in $P2^{-/-}$ mice, I performed western blot analysis on $P2^{-/-}$ and $P2^{+/+}$ sciatic nerves and testis, used as control tissue (**Fig. 24A**). First, I obtained a strong FABP9 expression in both $P2^{-/-}$ and $P2^{+/+}$ testis at P56. Taking in consideration the normalized protein amounts of Actin, FABP9 might be slightly increased in $P2^{-/-}$ testis as compared to $P2^{+/+}$ testis. However, I was unable to detect any FABP9 expression in the sciatic nerve of P10-old $P2^{-/-}$ as well as in $P2^{+/+}$ mice. Furthermore, I obtained similar results by performing immunostainings on testis at P56 and on sciatic nerves at P10. Cross sections of the seminiferous tubules of $P2^{-/-}$ and $P2^{+/+}$ testis showed a specific localization of FABP9 in late elongating spermatids in both genotypes. Interestingly, the intensity of staining was much more intense for $P2^{-/-}$ testis than for $P2^{+/+}$ testis (**Fig. 24B**). As FABP9 is not expressed in $P2^{+/+}$ sciatic nerves I could not observe any specific staining there. However, despite a potentially increased background staining, I detected also no specific expression pattern of FABP9 in $P2^{-/-}$ sciatic nerves (**Fig. 24C**). Therefore, it is most likely that the increased amount of FABP9 mRNA in $P2^{-/-}$ mice might not be translated into FABP9 protein.

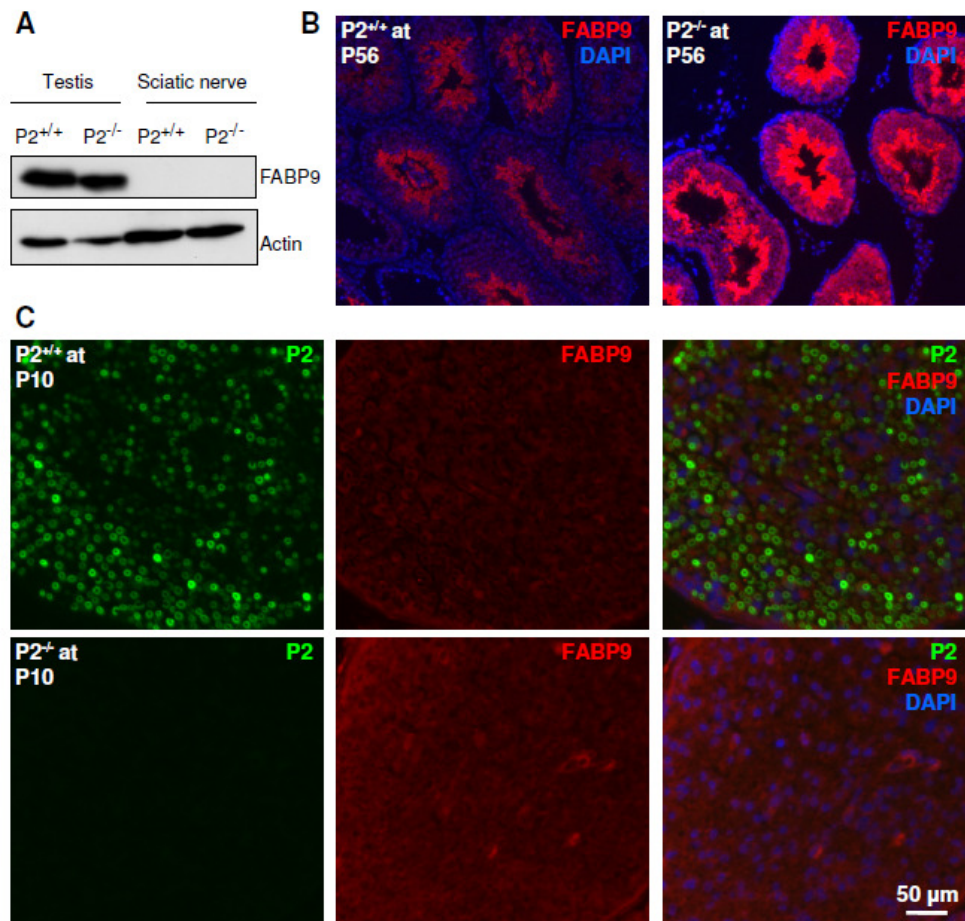


Figure 24 : FABP9 protein expression in $P2^{-/-}$ mice.

(A) Western Blot analysis showed a strong expression of FABP9 in both $P2^{-/-}$ and $P2^{+/+}$ testis at P56. However, no FABP9 expression was obtained neither in $P2^{-/-}$ sciatic nerves nor in $P2^{+/+}$ sciatic nerves at P10. (B) FABP9 immunostainings revealed the expected expression in cross sections of adult $P2^{+/+}$ and $P2^{-/-}$ testis. Interestingly, the staining intensity in $P2^{-/-}$ testis was much higher. (C) Sciatic nerve cross sections of P10-old mice demonstrated a strong P2 expression in $P2^{+/+}$ mice but not in $P2^{-/-}$ mice. However, no specific stainings were obtained for FABP9 on $P2^{-/-}$ sections similar to $P2^{+/+}$ sections. n=2

3.2.5 *In vivo* analysis of P2-MBP interaction

MBP is a small, basic, cytoplasmic myelin protein like P2. It colocalizes with P2 in the myelin sheath of peripheral nerves and recent biochemical data suggest that P2 and MBP may work together in the formation and maintenance of compact myelin (104). Mice with an autosomal recessive mutation for MBP, the Shiverer mice (here: $P2^{+/+}/Shi^{-/-}$), possess strong myelin defects in the CNS but not in the PNS (105, 106). Due to their similarity it is suggested that P2 might overtake the function of MBP in the PNS but not in the CNS (107, 108). To evaluate a possible interaction between P2 and MBP *in vivo*, I generated double KO mice for P2 and MBP ($P2^{-/-}/Shi^{-/-}$).

Similar to $P2^{+/+}/Shi^{-/-}$ mice, the $P2^{-/-}/Shi^{-/-}$ mice developed a severe tremor phenotype by 2 weeks of age demonstrating the persistent presence of CNS defects. Furthermore, both genotypes showed a very severe hindlimb clasping phenotype in adult mice (P56) indicating defects in the PNS as well. The body weight and blood glucose levels were equal in mice of all genotypes at P56 (**Fig. 25A and B**) and mice were fertile, producing pups according to expected Mendelian frequency. On the electrophysiological level, both $P2^{+/+}/Shi^{-/-}$ and $P2^{-/-}/Shi^{-/-}$ mutant mice had a significant lower MNCV at P56 suggesting myelin defects (**Fig. 25C**). In addition, $P2^{+/+}/Shi^{-/-}$ had a significant increase in the CMAP amplitude and area while this increase was not significant anymore for $P2^{-/-}/Shi^{-/-}$ mice (**Table 12**).

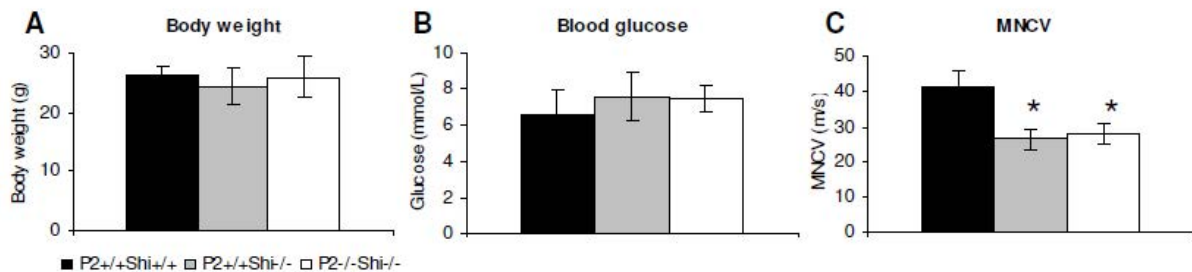


Figure 25 : Characterization of $P2^{+/+}/Shi^{-/-}$ and $P2^{-/-}/Shi^{-/-}$ mice versus $P2^{+/+}/Shi^{+/+}$ mice at P56. While (A) the body weight and (B) the blood glucose level were identical for all three genotypes, (C) the MNCV was significantly lower in $P2^{+/+}/Shi^{-/-}$ and $P2^{-/-}/Shi^{-/-}$ mice as compared to $P2^{+/+}/Shi^{+/+}$ mice. n=5. * p-value < 0,05.

	MNCV (m/s)	Latency (ms)	Duration (ms)	Amplitude (mV)	Area (mV/ms)
$P2^{+/+}/Shi^{+/+}$	39,75 (+/- 5,24)	1,26 (+/- 0,23)	0,96 (+/- 0,09)	1,56 (+/- 1,36)	0,78 (+/- 0,43)
$P2^{+/+}/Shi^{-/-}$	25,5 (+/- 2,8)	1,15 (+/- 0,11)	0,93 (+/- 0,06)	3,63 (+/- 0,91)	1,55 (+/- 0,38)
p-value	0,0002	0,4209	0,5401	0,0164	0,0178
$P2^{-/-}/Shi^{-/-}$	28,79 (+/- 3,12)	1,35 (+/- 0,18)	0,97 (+/- 0,22)	3,00 (+/- 1,43)	1,22 (+/- 0,53)
p-value	0,0162	0,5494	0,974	0,1754	0,2612

Table 12 : Properties of the CMAP curve of $P2^{+/+}/Shi^{-/-}$ and $P2^{-/-}/Shi^{-/-}$ mice as compared to $P2^{+/+}/Shi^{+/+}$ mice at P56.

Besides a significant reduction in MNCV, the CMAP amplitude as well as the CMAP area was increased in $P2^{+/+}/Shi^{-/-}$ mice (significantly) and in $P2^{-/-}/Shi^{-/-}$ mice (not significantly) as compared to $P2^{+/+}/Shi^{+/+}$ mice at P56. However, the CMAP latency and duration was not different. n=5. p-values are for both mutants as compared to $P2^{+/+}/Shi^{+/+}$ mice.

Semithin cross sections at P10 and P56 should give information about early and/or late alterations of the sciatic nerve morphology (**Fig. 26A and B**). As previously described (106) no major structural defects in PNS myelination could be observed in $P2^{+/+}/Shi^{-/-}$ mice as compared to $P2^{+/+}/Shi^{+/+}$ mice at P10 and P56. Interestingly, deletion of both P2 and MBP in $P2^{-/-}/Shi^{-/-}$ mice had as well no significant effects on PNS myelin structure. To evaluate the nodal structure I stained teased fibers generated from sciatic nerves of $P2^{+/+}/Shi^{-/-}$, $P2^{-/-}/Shi^{-/-}$ and $P2^{+/+}/Shi^{+/+}$ mice with Nile Red, a fluorescent stain labeling the lipid-rich myelin (**Fig. 26C**). This technique showed a normal formation of the node of Ranvier for both $P2^{+/+}/Shi^{-/-}$ and $P2^{-/-}/Shi^{-/-}$ mice as compared to $P2^{+/+}/Shi^{+/+}$ mice at P56. However, as reported previously (30), $P2^{+/+}/Shi^{-/-}$ mice had a strong increase in the number of SLI, a phenotype which was less pronounced in $P2^{-/-}/Shi^{-/-}$ mice.

A possible cause for the reduced MNCV and increased CMAP amplitude and area in $P2^{+/+}/Shi^{-/-}$ and $P2^{-/-}/Shi^{-/-}$ mice may be alterations in ion conductance. Therefore, I compared the distribution of Na_v - and K_v1 -channels in teased fibers of $P2^{+/+}/Shi^{-/-}$ and $P2^{-/-}/Shi^{-/-}$ mice with $P2^{+/+}/Shi^{+/+}$ mice at P56. In all three genotypes Na_v -channels were correctly accumulated at the node of Ranvier and K_v1 -channels at the juxtaparanodes excluding a mislocalization of these ion channels along myelinated fibers (**Fig. 26D**).

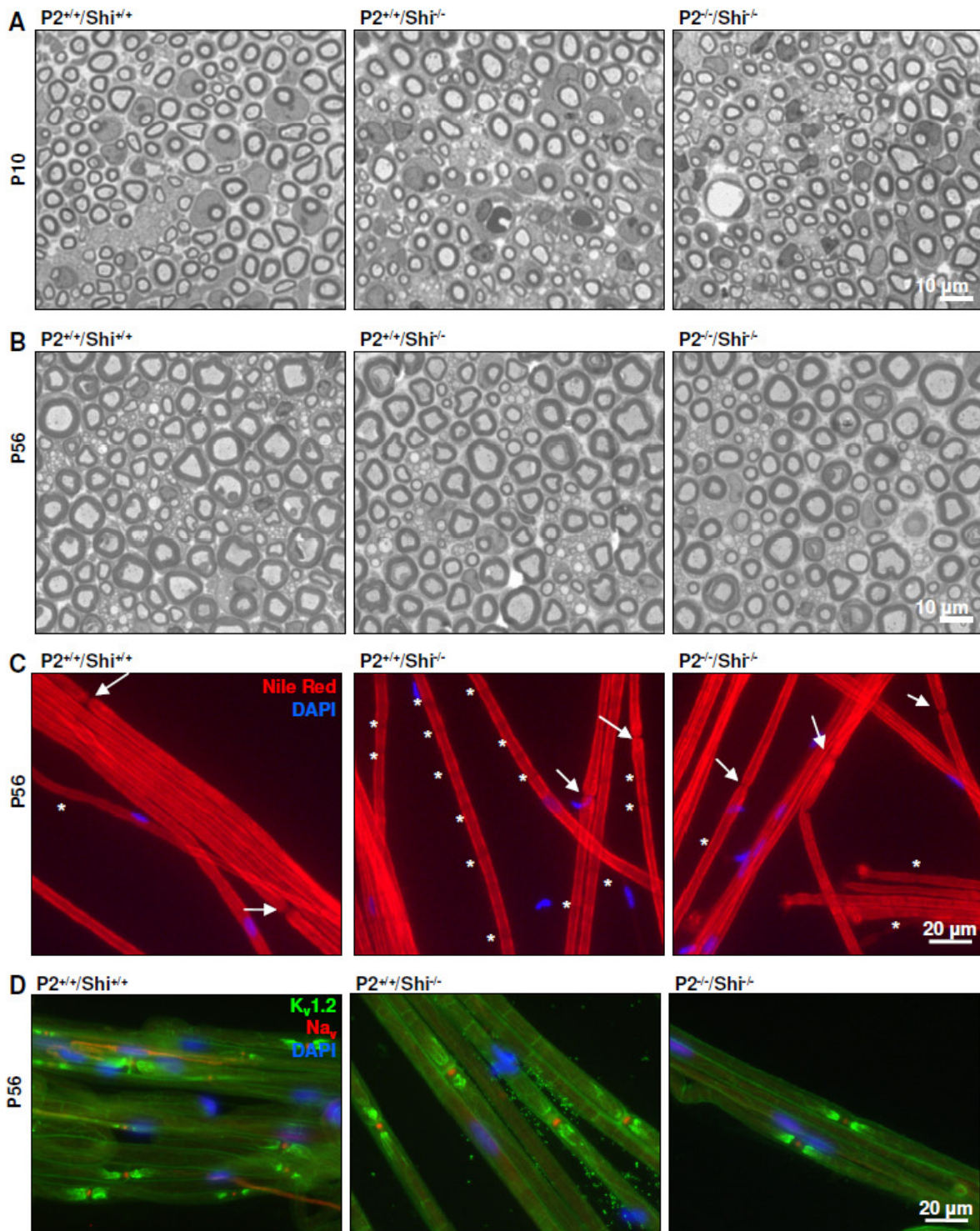


Figure 26 : Preserved sciatic nerve myelination of $P2^{+/+}/Shi^{-/-}$ and $P2^{-/-}/Shi^{-/-}$ mice at P10 and P56. Semithin cross sections of the sciatic nerve (**A**) at P10 and (**B**) at P56 of all three genotypes showed no differences in the myelination of nerve fibers. (**C**) Segmental demyelination was excluded by Nile Red staining of adult sciatic nerve teased fibers. However, a higher number of SLI in $P2^{+/+}/Shi^{-/-}$ was observed which was less severe in $P2^{-/-}/Shi^{-/-}$ mice as compared with $P2^{+/+}/Shi^{+/+}$ mice. (**D**) Co-immunostainings of Na_v and $K_v1.2$ on teased fibers of P56-old mice showed for both $P2^{+/+}/Shi^{-/-}$ and $P2^{-/-}/Shi^{-/-}$ mice no defects in the accumulation of ion channels as compared to $P2^{+/+}/Shi^{+/+}$ mice. Again, an increased presence of SLI was observed in $P2^{+/+}/Shi^{-/-}$. n=3, except ion channel stainings n=2.

4. Discussion

4.1 Altered distribution of juxtaparanodal K_v1-channels mediates peripheral nerve hyperexcitability in type 2 diabetes mellitus

In this work, I showed that db/db mice, a mouse model for T2DM, developed a PNH phenotype in addition to reduced NCV similar to the one observed in diabetic patients (40, 61, 62, 89, 90, 109). This phenotype was caused by an altered distribution of juxtaparanodal K_v1.2 channels and can be attenuated by flupirtine, suggesting it as a potential drug for PNH in T2DM.

4.1.1 db/db mice as a model for type 2 diabetes mellitus and diabetic peripheral neuropathy

In the last years, the db/db mouse strain became a well established animal model of T2DM (69, 70, 110-114). We confirmed previous studies showing altered physiology and development of peripheral neuropathy in db/db mice (55, 70, 112) and determined the onset of T2DM in db/db mice at 6 weeks of age, immediately followed by DPN at 7 weeks of age. At 23 weeks of age, when I analyzed them, the mice were severely diabetic. Moreover, at this age β -cell degeneration started in db/db mice, which results in insulin deficiency. Therefore, db/db mice switch to a more T1DM-like phenotype around the age of 23 weeks (115). Similar to previous observations (55), there were no structural changes affecting sciatic nerve myelination even after 16 weeks of hyperglycemia that could explain its pronounced reduction in MNCV and SNCV. The slight shift in the axonal distribution from small to medium size fibers correlated with the loss of IENF and might explain the small fiber neuropathy. The reduction of the paranodal adhesion molecule Caspr is not leading to a loss of paranodal junctions and might have therefore only minor structural consequences confirming a previous freeze-fracture study which found little evidence for axo-glial dysjunctions in the paranodal regions of some fibers in 24 weeks old db/db animals (116).

4.1.2 Physiological and mechanistic implication of K_v1-channels in PNH

Importantly, we observed for the first time that db/db nerves were more excitable than control nerves thus validating it as a model to characterize this part of the DPN phenotype. Similar to the situation in diabetic patients where PNH is thought to be responsible for the positive symptoms of DPN (40, 61, 62), it could explain allodynia in db/db mice (117). We asked if the PNH phenotype in db/db animals led to a prolonged RP and might be causative for the reduced NCV. However, we could not observe any alterations in db/db RP as

compared to WT mice and therefore conclude that PNH and reduced NCV are two independent phenotypes.

Clinical studies of immune (Isaac's syndrome) or genetic (episodic ataxia type 1) diseases, caused by alterations in K_v1 -channel functions, have demonstrated that the pathophysiological consequences on the nerve functions include PNH or myokymia (35, 36, 38). By pharmacological blocking of the relevant K_v -channels present in the PNS, we clearly demonstrated that a reduced activity of K_v1 -channels was involved in the PNH phenotype of db/db mice. However, inhibition of K_v1 -channels of isolated WT nerves did not reproduce the hyperexcitability to the same degree as observed in db/db nerves, suggesting the existence of other mechanisms involved in db/db nerve hyperexcitability. We excluded slow KCNQ K_v7 -channels ($K_v7.2$ and $K_v7.3$) (14, 97) and Na_v -channels (54, 56) as candidates indicating that this difference may rather reflect variation in accessibility and/or kinetics of action of drugs used to block K_v1 -channels in either control or db/db animals. The preserved function of Na_v -channels was corroborated by immunostainings on teased fibers of db/db and WT mice at 5 and 23 weeks of age. However, a pan- Na_v antibody was used and thus the immunostaining gives no information about the identity of the α -subunit isoform of the nodal Na_v -channels in db/db versus WT mice.

The functional loss of K_v1 -channels was in line with an altered distribution of juxtaparanodal $K_v1.2$ -channels, in both db/db mice and T2DM patients. These data are in line with and extend a previous observation that paranodal/juxtaparanodal potassium binding sites (which may represent K_v -subunits) are reduced in nerves from diabetic patients (118) and are to our knowledge the first direct demonstration of such an alteration in axonal ion channels in diabetic patients. qPCR and western blot analysis excluded a reduced expression level of $K_v1.2$ in db/db mice as being responsible for the lower expression of $K_v1.2$ at the juxtaparanodal regions. Furthermore, myelin defects which could impair ion channel localization (99, 101) were also excluded in db/db animals and T2DM patients.

Matured and assembled K_v1 -channels are transported to their target site at the axolemma (119). My preliminary results of Co-IP experiments against $K_v\beta2$ showed a reduced attachment of mature $K_v1.2$ and an increased amount of immature $K_v1.2$ in db/db mice as compared to WT mice. In WT mice the expression of the immature isoform of $K_v1.2$ is enriched in soma-rich DRGs and specifically mature $K_v1.2$ is transported to the axon (119). However, I detected in both western blot and Co-IP analysis an expression of immature $K_v1.2$ even in WT endoneurial extracts. Therefore, I cannot exclude that some of the Schwann cell $K_v1.2$ expression (120) is reflected in my protein analysis of sciatic nerve endoneurium and might influence the interpretation of these results, especially concerning immature $K_v1.2$. Furthermore, in the co-immunoprecipitated samples there was no actin (or other proteins) present in order to normalize the immunoblots. K_v1 -channels are transported along axonal microtubuli within post-Golgi carrier vesicles associated with KIF3 and its

adaptor protein EB1 (121). Therefore, α/β -tubulin cannot be used as normalizer and thus the reduced amount of α/β -tubulin to $K_v\beta 2$ demonstrates rather a reduced attachment in db/db mice as compared to WT mice than a lower amount of loaded protein. Unpublished data of Jeffrey D. Milbrandt communicated at the PNS meeting in 2009 showed a similar failure in the localization of $K_v1.2$ in conditional KO mice of the deacetylase Sirt2. As previously reported, the recruitment of the molecular motor proteins and its adaptor proteins is regulated by microtubule acetylation (122). I compared the acetylation status of Sirt2 in db/db and WT sciatic nerve endoneurium at 23 weeks of age. Interestingly, my preliminary data showed a reduced activity of Sirt2 in db/db mice suggesting potential defects in microtubule dynamics. However, further experiments are necessary to prove an involvement of Sirt2 in the pathophysiology of T2DM.

The reduced amount of integrated $K_v1.2$ into the membrane in db/db mice as observed in my cellular fractionation experiments correlated with the altered $K_v1.2$ distribution at juxtaparanodal regions on teased fibers. However, it was not accompanied by an increased expression of $K_v1.2$ in the cytoplasm of db/db mice maybe because the $K_v1.2$ -subunits are still included within transport vesicles. Moreover, it is possible that the different buffer composition of western blot, Co-IP and cellular fractionation experiments might have influenced these results as even $K_v1.2$ expression in the total lysate of db/db mice in the cellular fractionation experiments was reduced.

I conclude, that $K_v1.2$ is normally expressed in db/db mice but it is clustering to the juxtaparanodal regions, which is mediated by the adhesion molecules TAG-1 and Caspr2 (19), is impaired. As opposed to most ion channel subunits which possess intrinsic targeting motifs, both transport and TAG1-mediated clustering of $K_v1.2$ is mainly dependent on its phosphorylation status (123) which may be affected under diabetic condition. Moreover, $K_v1.2$ subunits are not retained in the cell bodies of (at least) sensory neurons and they reach the axoplasm. However, I suggest that most $K_v1.2$ subunits do not reach their final juxtaparanodal regions due to a lower transportation rate or a random release of the transport vesicles from the microtubules and/or from the attached KIF3/EB1/ $K_v\beta 2$ -complex away from any juxtaparanodal regions being clustered there (**Fig. 27**). This assumption is based on preliminary data and must be further explored.

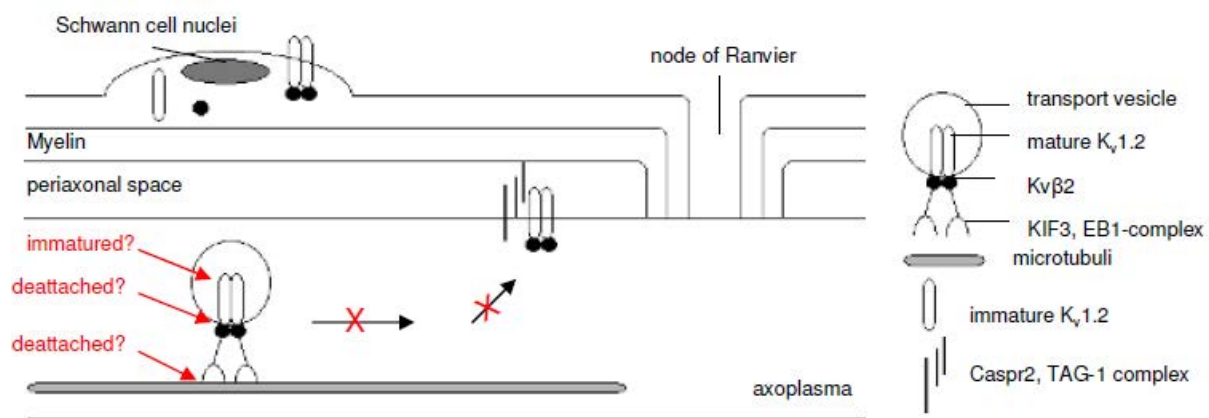


Figure 27 : Putative molecular mechanism underlying altered juxtaparanodal $K_v1.2$ expression in db/db mice.

In WT mice K_v1 -channels, consisting of 4 α - and 4 β -subunits are integrated into transport vesicles. Within these vesicles they are transported to their juxtaparanodal targets along microtubuli which is triggered by the motor protein complex of KIF3/EB1. My preliminary results revealed a potential reduced interaction of $K_v\beta2$ with $K_v1.2$ and Tubulin and/or impaired maturation (indicated in red) of $K_v1.2$ in db/db mice at 23 weeks of age. Consequently, less $K_v1.2$ might reach the juxtaparanodal regions of the axolemma.

4.1.3 Therapeutical applications

How does hyperglycemia damage peripheral nerves? This is still an unanswered question which makes it difficult to develop efficient therapies for DPN. Therefore, the best therapy is still to achieve normal blood glucose levels in diabetic patients e.g. by insulin therapies. Our data indicate at least two different approaches how to improve DPN condition (particularly PNH) for which there are no effective therapies. First, one may try to enhance the targeting of $K_v1.2$ to its juxtaparanodal location thus improving the hypersensitivity phenotype. Alternatively, our expression and pharmacology data generated in db/db mice showed that there are multiple ion channel-types (including $Na_v1.6$, $K_v1.1$, $K_v7.2$ and $K_v7.3$) that are well preserved in the diabetic peripheral nerve. Both the inhibition of Na_v -channels and the activation of preserved K_v -channels might alleviate the PNH phenotype. We validated the clinical potential of the second approach by suppressing PNH in db/db nerves with the K_v7 -activator flupirtine. Interestingly, flupirtine, which is an analgesic, has already been shown to suppress PNH resulting from exposure of rat and human peripheral nerves to oxaliplatin (98).

Overall, my study focused on T2DM, the major form of DM. However, it would be of interest if these results and the therapeutical suggestions might be adapted to other diseases. This might compass diseases with described K_v1 -mediated PNH as shown for amyotrophic lateral sclerosis (37) or other forms of DM, e.g. T1DM. While some groups claim more severe nodal and paranodal defects in T1DM patients and rats than in T2DM (58, 124, 125), others described no alterations in the expression of any nodal, paranodal or juxtaparanodal marker (126). Therefore, further studies are required to clarify the pathological differences (or similarities) between T1DM and T2DM.

4.2 Generation of a knockout mouse model to study the role of peripheral myelin protein P2

P2 is a small lipid-binding protein, localized at the cytoplasmic side of some myelin sheaths in the PNS (79, 80). I confirmed and extended the unique expression profile of P2. The most striking feature of P2 expression was its presence in only some myelin sheaths which raises up challenging questions concerning P2: what is the difference between P2-positive and P2-negative Schwann cells? What is the functional role of P2? To get some insight into the function of P2 I generated a P2^{-/-} mouse model. Surprisingly, the P2^{-/-} mice showed no major defects in myelination of the PNS as compared with P2^{+/+} mice. However, the results of gene profiling indicated a potential role of P2, which is a member of the FABP family, in the glial lipid metabolism.

4.2.1 P2 expression

The developmental expression profile of P2 correlated very well with that of other major peripheral myelin proteins like MBP and MPZ. However, the P2 expression is most likely differentially regulated as MBP or MPZ leading to a partial and more longstanding expression in peripheral myelin. By immunostainings of P2 on dorsal and ventral roots I excluded the nerve fiber function as possible regulator, as suggested earlier (80). While in sciatic nerve cross sections predominantly large nerve fibers were P2-positive, immunostainings on teased fibers further excluded the fiber size as the only factor regulating P2 expression. Interestingly, FABP expression is known to be proportional to the rate of lipid metabolism within the cell (71). As Schwann cells associated with large fibers start first to myelinate and show as well a higher lipid (and protein) demand this might explain the fact that predominantly large fibers were labeled by P2 but not the differences along the same fiber. The expression rate in Schwann cells associated with small fibers might be too small to be detected by immunostaining approaches. Possibly, P2 is also involved in myelin maintenance and/or myelin repair explaining its expression in only some myelin sheaths. Interestingly, in P2^{+/-} mice the majority of Schwann cells reacted to X-Gal although the LacZ gene was under the control of the P2 promoter. Thus, this supports my hypothesis that all Schwann cells are theoretically able to produce P2.

While MPZ and MBP, involved in myelin compaction, are specifically located in the myelin sheaths, P2 showed a strong expression in the Schwann cell cytoplasm as well (79). As FABPs are known to be cytoplasmic, it might correlate with its potential role in FA binding and transport from the cell cytoplasm into the myelin sheath. Previously described as a peripheral membrane protein (79), P2 might maintain or store the lipids afterwards within the lipid sheath. This can be achieved either indirectly by interactions to another peripheral myelin protein or directly by interactions to lipid components via its potential myristoylation

domain (77) or by unspecific electrostatic interactions of the positively charged P2 protein with the negatively charged myelin membrane.

In situations of demyelination P2 is present in some of the thin myelin sheaths which are labeled by MBP as in healthy nerves. The more pronounced cytoplasmic expression of P2 in *Lpin1*^{-/-} mice might be correlated to the dedifferentiation of Schwann cells to more immature Schwann cells. However, in demyelinating nerves of *Lpin1*^{-/-} mice I noticed myelin sheaths that were only positive for P2 but not for MBP. I never observed such myelin sheaths in *P2*^{+/+} mice neither at P56 nor at P10 highlighting a potential role of P2 in myelin maintenance and/or repair.

4.2.2 Peripheral nerve function in *P2*^{-/-} mice

Unexpectedly, the *P2*^{-/-} mice did not show any gross morphological alterations in PNS myelination. However, this stays in correlation with other KO mouse models of the FABP family. In none of them gross alterations have been observed possibly due to compensatory mechanisms by other FABPs expressed in the same tissue (71). Despite normal myelinated peripheral nerves in *P2*^{-/-} mice as compared to *P2*^{+/+} mice, I observed a mild but significant downregulation of the MNCV in P56-old *P2*^{-/-} mice. While the reduced MNCV did not lead to a prolonged CMAP latency or duration it was accompanied by a significant increase in CMAP area and amplitude. The combination of reduced MNCV and increased CMAP amplitude and area is described for reinnervation of a muscle after nerve injury accompanied by de- and remyelination (127). However, this was not the case in the *P2*^{-/-} mice. Moreover, nodal Na_v- and juxtaparanodal K_v1-channels were normally expressed and could not contribute to the observed phenotype. Therefore, it has to be analyzed if more subtle alterations in myelin structure and/or myelin composition might impair the isolating property of the myelin sheath.

4.2.3 Lipid homeostasis-related role of P2 in Schwann cells

Through my transcriptomic analysis of sciatic nerves of P10-old *P2*^{-/-} versus *P2*^{+/+} mice, I observed significant alterations in the mRNA expression level of two other FABP family members. FABP5 was significantly downregulated while FABP9 was significantly and highly upregulated, indicating that the loss of P2 might have major effects on the glial lipid metabolism. Such an upregulation of FABP9 is suggestive for a compensatory effect as observed in adipocytes from *FABP4*^{-/-} mice by FABP5. But in this situation FABP5 is already present in small amounts in normal adipocytes whereas FABP9 is not expressed in *P2*^{+/+} sciatic nerves.

Interestingly, qPCR analysis of P56-old *P2*^{-/-} versus *P2*^{+/+} mice revealed a differential expression of FABP5 and FABP9 not only in sciatic nerve endoneurium but also in other tissues tested. This is unexpected as P2 is specifically expressed in sciatic nerve endoneurium in *P2*^{+/+} mice and in no other tissues. Furthermore, I could not detect any

FABP9 protein expression in P2^{-/-} sciatic nerves at P10 by both western blot analysis and immunostainings suggesting that FABP9 mRNA is not translated into protein.

P2 is located on mouse chromosome 3 in a gene cluster together with FABP4/5/9 and 12 which is conserved in other mammalian species, e.g. human and rat. Such conserved chromosomal regions are often maintained together as they are regulated by common non-coding cis- or trans-acting elements (128, 129). Indeed, in humans there is an annotated anti-sense non-coding RNA (ncRNA) that maps to the 3' end of P2 and overlaps FABP9 (and FABP4) (**Fig. 28A, B**). It is most likely that the same ncRNA is also present in mice and that the loss of antisense mediated repression induced the observed upregulation of FABP9 in P2^{-/-} mice. Analysis of the P2 expression in FABP9^{-/-} mice might demonstrate if P2 is also regulated by this ncRNA. In addition, on the mouse track of embryonic stem cells appears an epigenetic mark (methylation) associated with the cis regulatory sequences in the last exon of P2 (**Fig. 28C**). This might play a role as an active regulatory enhancer. The loss of it may be responsible for the downregulation of FABP5 and/or of the anti-sense ncRNA. Therefore, the functional relevance of the altered mRNA expression of FABP5 and FABP9 is still elusive.

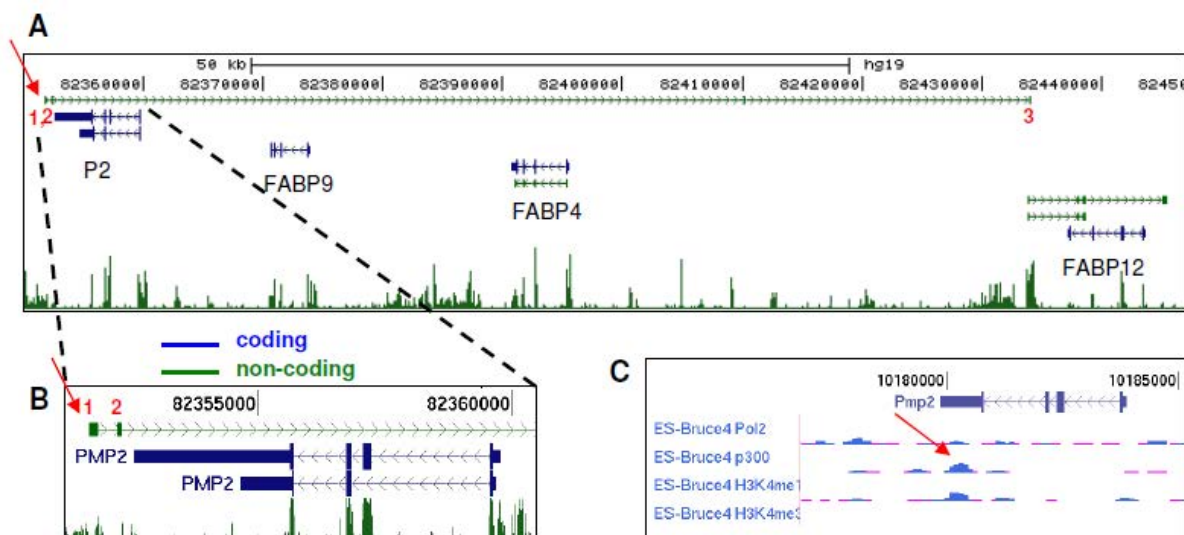


Figure 28 : The epigenetic and transcriptional landscape of the P2 locus.
(UCSC Gene annotations)

(A) Human genomic region containing the coding transcripts (blue) of P2 (= Pmp2, FABP8), FABP9, FABP4 and FABP12. Non-coding transcripts are represented in green. Importantly, a long non-coding RNA was annotated to the 3' end of P2 which overlaps FABP9 and FABP4 (red arrow). It consists of three exons (small red numbers) which are spliced as for coding transcripts. At the bottom the green bar graphs show highly conserved regions in mammals. (B) Enlarged view of human P2 locus. The first two exons of the long non-coding RNA are just after the coding P2 transcript and correlates with a highly conserved regions in mammals. The second annotated P2 transcript (lower one) encodes most likely a intragenic enhancer and has no protein-coding potential. (C) In mouse embryonic stem cells (ES) the last exon of the P2 gene is epigenetically marked by methylation (p300 and H3K4me1 marks) (red arrow) which might act as a putative enhancer.

The physiological characterization of P2^{-/-} mice revealed a significant increase of the plasma insulin levels at P56 suggestive for insulin resistance. Alterations in the insulin metabolism, induced by increased levels of FFA, is commonly described for other FABP KO

mouse models (71). FFA-induced insulin resistance is often associated with an altered production of adipocyte-related genes, like Resistin and Adiponectin, prior to alterations in the immune response (130). While I could not observe any alterations in FFA levels in plasma samples of P2^{-/-} mice as compared to P2^{+/+} mice at P10 and P56, my microarray data revealed differential expression of relevant adipocyte-related genes in P2^{-/-} mice already at P10 which might contribute to the development of insulin resistance at P56.

To clarify the potential role of P2 in the lipid homeostasis of the neuronal system I am currently characterizing the FA and lipid composition of sciatic nerve myelin in P2^{-/-} mice as compared to P2^{+/+} mice at P10. Moreover, I will make use of already established DRG explants of P2^{-/-} and P2^{+/+} mice to evaluate the ability of FA uptake *in vitro*.

Apart from that, P2 is known to be a target of autoimmune reactions in patients with GBS (48). In collaboration with Dr. Mark Stettner at the Department of Neurology at the Heinrich-Heine-University in Düsseldorf (Germany) we might have access to plasma samples of GBS patients. To validate the relevance of the P2 protein in GBS we plan to inject P2^{-/-} and P2^{+/+} mice with the human plasma samples.

4.2.4 P2 and MBP are two independent myelin genes

To evaluate the suggested interplay between P2 and MBP *in vivo* I generated P2^{-/-}/Shi^{-/-} mice (104). While P2^{+/+}/Shi^{-/-} mice possess major myelin defects in the CNS, resulting in a severe tremor phenotype, the PNS remains mainly unaffected (105, 106, 131). However, a dramatic increase in the number of SLI in the PNS of P2^{+/+}/Shi^{-/-} mice has been reported previously (30). After my knowledge, I have for the first time measured the MNCV of the sciatic nerve in P2^{+/+}/Shi^{-/-} mice and observed a significant downregulation of the speed as compared to P2^{+/+}/Shi^{+/+} mice at P56. This might correlate at least to some extent to the increased number of SLI. Such an increase in the number of SLI was also described for cerebroside sulfotransferase-deficient mice but these mice had a normal MBP expression. The effects on nerve function was not described (132). Despite the loss of P2, P2^{-/-}/Shi^{-/-} mice showed no further impairment of the MNCV compared to P2^{+/+}/Shi^{-/-} mice. I rather observed a slight tendency to a faster MNCV in P2^{-/-}/Shi^{-/-} mice (**Table 12**). Interestingly, the increase of SLI in teased sciatic nerves was much less pronounced in P2^{-/-}/Shi^{-/-} as compared to P2^{+/+}/Shi^{-/-} mice. In addition to the reduced MNCV I observed a significant increase in CMAP amplitude and area in P2^{+/+}/Shi^{-/-} mice at P56. As for the number of SLI, this phenotype was improved in P2^{-/-}/Shi^{-/-} mice as compared to P2^{+/+}/Shi^{-/-} mice even though I measured as well an increase in CMAP area and amplitude for P2^{-/-} mice as compared to P2^{+/+} mice at P56. The reason for the increased CMAP area and amplitude remains elusive. In chapter 4.2.2 I suggested that more subtle alterations of the myelin sheath or the myelin composition might provoke such alterations in the electrophysiology of the nerve. Interestingly, major alterations

in the lipid composition of sciatic nerve myelin of $P2^{+/+}/Shi^{-/-}$ as compared to $P2^{+/+}/Shi^{+/+}$ mice have been reported accompanied by enhanced hypotonic swellings in the extracellular space (133). Consequently, the higher amount of negatively charged lipids changed the electrostatic properties of the myelin sheath and might impair its isolating function and/or the ion current. Thus, the results of the lipid profiling of $P2^{-/-}$ sciatic nerve myelin will help to understand the consequences of the additional loss of P2 in $P2^{-/-}/Shi^{-/-}$ mice.

A potential improvement of the phenotypes in $P2^{+/+}/Shi^{-/-}$ mice by the loss of P2 was unexpected. Interestingly, a similar situation was described for double KO mice for MBP and proteolipid protein (PLP) in the CNS (134). These double KO mice for MBP and PLP had not only a longer lifespan and less pronounced tremors, they showed also an improvement in myelination of the optic nerve as compared to $P2^{+/+}/Shi^{-/-}$ mice.

5. Collaborative projects

5.1 Global transcriptional programs in peripheral nerve endoneurium and DRG are resistant to the onset of type 1 diabetic neuropathy in *Ins2^{Akita/+}* mice

In the research field of DM a lot of effort is put into the understanding of the morphological and electrophysiological alterations in diabetic patients or appropriate animal models. However, the potential molecular changes in DPN still remain elusive. We decided to use a genetic mouse model of T1DM, the Akita mice (*Ins2^{Akita/+}*) (**Table 4**), to compare the transcriptional profiles of presymptomatic and symptomatic animals. To do so, we characterized the onset and progression of T1DM and DPN in these mice. I had the opportunity to contribute to this publication by performing the morphometric analysis of *Ins2^{Akita/+}* mice as compared to *Ins2^{+/+}* mice including g-ratio and axonal distribution analysis on toluidin-blue stained semithin cross sections. Moreover, I determined the IENF density by PGP9.5 immunostainings on hindpaw cryostat sections of *Ins2^{Akita/+}* and *Ins2^{+/+}* mice.

Global Transcriptional Programs in Peripheral Nerve Endoneurium and DRG Are Resistant to the Onset of Type 1 Diabetic Neuropathy in *Ins2^{Akita/+}* Mice

Anne-Sophie de Preux Charles^{1,2}, Valérie Verdier¹, Jennifer Zenker^{1,2}, Bastian Peter^{1,3}, Jean-Jacques Médard¹, Thierry Kuntzer⁴, Jacques S. Beckmann^{1,5}, Sven Bergmann^{1,3}, Roman Chrast^{1*}

1 Department of Medical Genetics, University of Lausanne, Lausanne, Switzerland, **2** Graduate Program in Neurosciences, University of Lausanne, Lausanne, Switzerland, **3** Swiss Institute of Bioinformatics, University of Lausanne, Lausanne, Switzerland, **4** Service of Neurology, Centre Hospitalier Universitaire Vaudois, Lausanne, Switzerland, **5** Service of Medical Genetics, Centre Hospitalier Universitaire Vaudois, Lausanne, Switzerland

Abstract

While the morphological and electrophysiological changes underlying diabetic peripheral neuropathy (DPN) are relatively well described, the involved molecular mechanisms remain poorly understood. In this study, we investigated whether phenotypic changes associated with early DPN are correlated with transcriptional alterations in the neuronal (dorsal root ganglia [DRG]) or the glial (endoneurium) compartments of the peripheral nerve. We used *Ins2^{Akita/+}* mice to study transcriptional changes underlying the onset of DPN in type 1 diabetes mellitus (DM). Weight, blood glucose and motor nerve conduction velocity (MNCV) were measured in *Ins2^{Akita/+}* and control mice during the first three months of life in order to determine the onset of DPN. Based on this phenotypic characterization, we performed gene expression profiling using sciatic nerve endoneurium and DRG isolated from pre-symptomatic and early symptomatic *Ins2^{Akita/+}* mice and sex-matched littermate controls. Our phenotypic analysis of *Ins2^{Akita/+}* mice revealed that DPN, as measured by reduced MNCV, is detectable in affected animals already one week after the onset of hyperglycemia. Surprisingly, the onset of DPN was not associated with any major persistent changes in gene expression profiles in either sciatic nerve endoneurium or DRG. Our data thus demonstrated that the transcriptional programs in both endoneurial and neuronal compartments of the peripheral nerve are relatively resistant to the onset of hyperglycemia and hypoinsulinemia suggesting that either minor transcriptional alterations or changes on the proteomic level are responsible for the functional deficits associated with the onset of DPN in type 1 DM.

Citation: de Preux Charles A-S, Verdier V, Zenker J, Peter B, Médard J-J, et al. (2010) Global Transcriptional Programs in Peripheral Nerve Endoneurium and DRG Are Resistant to the Onset of Type 1 Diabetic Neuropathy in *Ins2^{Akita/+}* Mice. PLoS ONE 5(5): e10832. doi:10.1371/journal.pone.0010832

Editor: Rafael Linden, Universidade Federal do Rio de Janeiro (UFRJ), Brazil

Received: December 14, 2009; **Accepted:** April 20, 2010; **Published:** May 26, 2010

Copyright: © 2010 de Preux Charles et al. This is an open-access article distributed under the terms of the Creative Commons Attribution License, which permits unrestricted use, distribution, and reproduction in any medium, provided the original author and source are credited.

Funding: This work was supported by grants from the Swiss National Science Foundation to R.C. (grant PP00P3_124833/1), J.S.B. (grant 310000-112552) and S.B. (3100AO-116323/1), as well as from the Giorgi-Cavaglieri (S.B.) and the European Framework Project 6 (EuroDia and the AnEuploidy projects, S.B.). The funders had no role in study design, data collection and analysis, decision to publish, or preparation of the manuscript.

Competing Interests: The authors have declared that no competing interests exist.

* E-mail: roman.chrast@unil.ch

Introduction

Diabetic peripheral neuropathy (DPN) is the most common complication of diabetes mellitus (DM) [1]. Up to half of all individuals with DM develop DPN with a lifetime risk of lower extremity amputations estimated at 15% [2]. Typically, symptoms begin in the feet and progress to proximal regions, finally affecting the upper limbs, the abdomen and the thorax [3]. Diabetic patients may experience impaired tactile, thermal and pain sensations with dysautonomic manifestations such as sexual dysfunction, gastrointestinal abnormalities and cardiac arrhythmias. On the other hand, some patients also experience neural hyperexcitability inducing tingling, itching, burning, cramps and neuropathic pain [4,5,6]. A decrease in nerve conduction velocity (NCV) is the most consistent electrophysiological marker of DPN [4,6]. Progression of DPN can be divided into 2 main phases [7]. The early stage of DPN is characterized by reversible deficits such as decreased NCV, decreased endoneurial blood flow, impairment of Na⁺/K⁺-ATPase and nitric oxide activities. Using animal models of type 1 DM (streptozotocin (STZ)-injected rats), it has

been shown that these early defects cannot be attributed to nerve structural abnormalities [8]. At the later stage, other pathogenic components are progressively added, inducing structural changes such as segmental demyelination, axo-glial dysjunction and axonal atrophy. These structural modifications are irreversible [7].

Even though the above-mentioned pathological alterations affecting neuronal structures are relatively well described, molecular mechanisms underlying DPN remain poorly understood. Several interrelated metabolic abnormalities resulting from hyperglycemia, insulin and C-peptide deficiencies may be involved. So far, proposed mechanisms include altered metabolism of glucose via the polyol pathway, advanced glycation end products, increased protein kinase C (PKC) activity, altered neurotrophism, perturbation of lipid metabolism, ischemia and reactive oxygen species [4,6,9,10]. Currently, also the identity of the cell type first to be affected in DPN is unclear, as defects are observed in basically all cell types composing the nerve. Some authors claimed that DPN is primarily an axonal pathology [11,12], whereas others support the hypothesis that DPN is a Schwann cell-related disorder [7,13].

The search for changes in expression levels of candidate genes underlying DPN pathological hallmarks has been attempted previously, in either sciatic nerve or DRG compartments of the PNS [14–22]. These studies were complemented by more global transcriptomic approaches in either sympathetic ganglia [23], DRG [24] or in immortalized adult mouse Schwann cells [25]. However, the comparison of the effects of hyperglycemia on the stability of transcriptional programs *in vivo*, between the neuronal (DRG) and glial compartments of the peripheral nerve, was never attempted.

To address this question, we used *Ins2^{Akita/+}* mice as a model of type 1 DM related DPN, and we concentrated on the early stages of DPN development when the pathological changes affecting neuronal function are still reversible. To define the progression of DPN in this model, we performed a detailed phenotypic characterization of *Ins2^{Akita/+}* mice. NCV changes could be detected quite rapidly in this type 1 DM model, only one week after the onset of hyperglycemia. Based on these phenotypic data, we performed a gene expression profile of the sciatic nerve endoneurium (mostly containing Schwann cells) and DRG (mostly containing somas of sensory neurons) isolated from pre-symptomatic and early symptomatic *Ins2^{Akita/+}* mice. We observed that both neuronal and glial transcriptomes are stable during early stages of diabetes. These data therefore suggest that the functional deficits associated with the onset of DPN are rather a consequence of a combination of minor transcriptional alterations and/or changes on the proteomic level.

Results

Phenotypic characterization of the development of DPN in *Ins2^{Akita/+}* mice

We have selected *Ins2^{Akita/+}* mice as a model of type 1 DPN. In this mouse model, diabetes is a consequence of an autosomal dominant mutation in the *Ins2* gene resulting in the improper folding of the Proinsulin 2 protein leading to hypoinsulinemia and hyperglycemia [26]. *Ins2^{Akita/+}* mice develop multiple secondary complications associated with diabetes including neuropathy [27] and retinopathy [28].

In order to select time-points for transcriptional analysis that are matching the onset of neuropathy in *Ins2^{Akita/+}* mice, we first characterized the development of DPN in this model. Weight, tail vein blood glucose and motor nerve conduction velocity (MNCV) were followed in four male *Ins2^{Akita/+}* and four control littermates between three and ten weeks of age. No significant variation of

weight was observed between *Ins2^{Akita/+}* mice and their control littermates (Fig. 1A). Blood glucose level started to increase in *Ins2^{Akita/+}* between three to four weeks of age (Fig. 1B) and reached a plateau approximately five weeks after the onset of hyperglycemia. In order to match the onset of hyperglycemia with the onset of DPN, we measured MNCV in *Ins2^{Akita/+}* mice and control littermates. Reduced NCV is an established early marker of DPN in patients [6]. At three and four weeks of age, no difference in MNCV was detected between *Ins2^{Akita/+}* mice and control littermates. At five weeks of age, about one week after the onset of hyperglycemia, a decrease in MNCV was clearly present in *Ins2^{Akita/+}* mice and this condition was maintained (but it did not worsen) as mice aged (Fig. 1C). In order to determine if the observed decrease in MNCV was also reproduced in sensory fibers, tail sensory NCV (SNCV) and MNCV were measured in two and five month old animals. SNCV could not be determined in younger mice, the tail being too small to allow reproducible results. In control animals, measured SNCV were lower than that of motor fibers, however the obtained values were in the range of the previously published results [27]. Similar to MNCV, the tail SNCV was decreased in *Ins2^{Akita/+}* mice as compared to control littermates at two and five months of age, suggesting that both sensory and motor NCV are affected in this model of DPN (Fig. 2A and B). We have also observed a similar tendency for a decrease in SNCV at the level of the sciatic nerve (Fig. S1).

Sensory symptoms observed in DPN patients often include both loss of sensations and neuropathic pain [4,29]. To evaluate *Ins2^{Akita/+}* mice sensory behavior, the development of a thermal hypo- or hyper-sensitivity was assessed in two month old animals using a hotplate. In this test, *Ins2^{Akita/+}* mice showed a significantly slower reaction time to heat at 49°C ($p = 0.002$) and 52°C ($p = 0.005$) (Fig. 2C). In contrast, no difference was observed at 55°C. These sensory symptoms were not associated with changes in intraepidermal nerve fiber density which is a marker of small fiber damage in more advanced human DPN (Fig. S2, [30]).

The *Ins2^{Akita/+}* animals presented a reduction of MNCV at five weeks of age. At this time-point, the peripheral nerves are still maturing as demonstrated by an increase in MNCV in wild-type animals between the ages of 5 and 10 weeks (Fig. 1C). In order to eliminate the possibility that the decreased MNCV present in *Ins2^{Akita/+}* animals is a consequence of slowed PNS maturation leading to either hypomyelination and/or change in radial axonal growth (insulin signaling is known to affect Schwann cell and neuronal development [4,5,6]), we evaluated the level of myelination and axonal size distribution in three month old

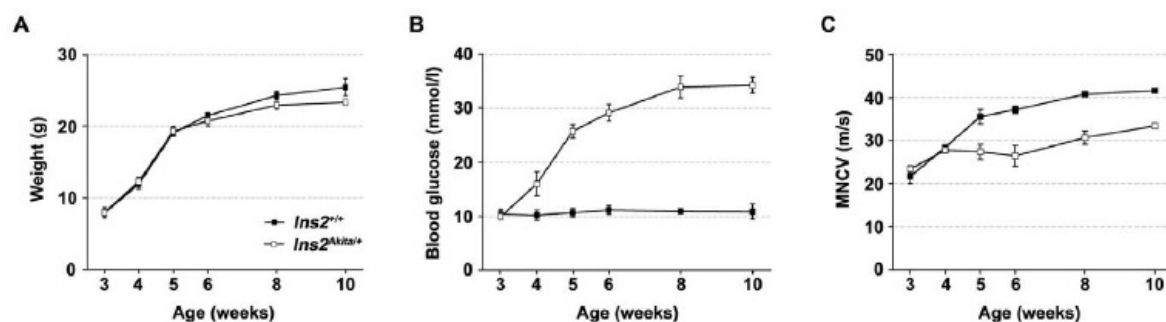


Figure 1. Phenotypic characterization of *Ins2^{Akita/+}* mice. Body weight (A), tail vein blood glucose (B) and motor nerve conduction velocity (MNCV, C) were measured at depicted time-points in *Ins2^{Akita/+}* and *Ins2^{+/+}* mice. All results are expressed as the mean \pm standard error of the mean (S.E.M.). (*Ins2^{+/+}*; n = 4; *Ins2^{Akita/+}*; n = 4). doi:10.1371/journal.pone.0010832.g001

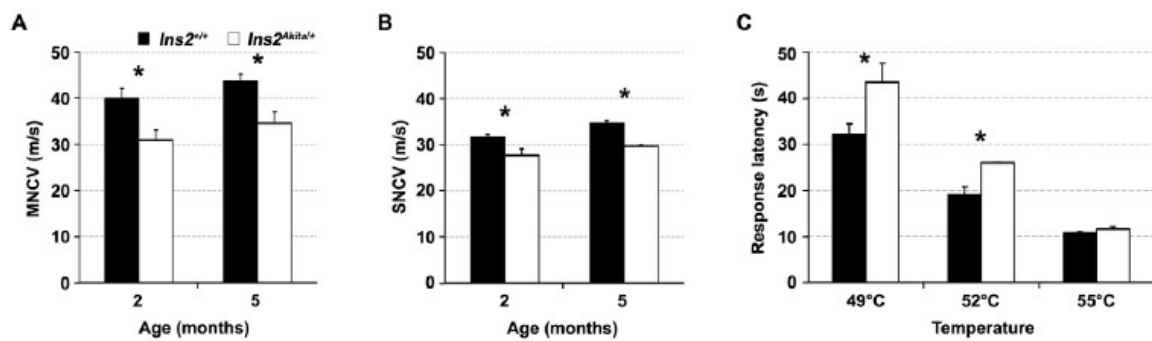


Figure 2. Characterization of motor and sensory behavior in *Ins2^{Akita/+}* mice. Sciatic nerve motor (MNCV, A) and tail sensory (SNCV, B) nerve conduction velocities were compared in diabetic (*Ins2^{Akita/+}*) and control (*Ins2^{+/+}*) mice at two and five months of age. Results are expressed as the mean \pm standard error of the mean (S.E.M). (*Ins2^{+/+}*: n=4; *Ins2^{Akita/+}*: n=4). C) Sensory performances were evaluated in two month old *Ins2^{Akita/+}* and control littermates using the hot plate test at 49, 52 and 55°C. Results are expressed as the mean \pm standard error of the mean (S.E.M) and analyzed by Student's t test (*Ins2^{+/+}*: n=8; *Ins2^{Akita/+}*: n=7). (*) p<0.05. doi:10.1371/journal.pone.0010832.g002

control and *Ins2^{Akita/+}* animals. While at this developmental stage *Ins2^{Akita/+}* animals presented decreased MNCV, SNCV and slower reaction time to heat (Fig. 2), we could not detect any structural changes in their PNS (Fig. 3A–C). Together our data therefore suggest that the DPN phenotypes observed in *Ins2^{Akita/+}* animals during the early phase of the disease (the first two months after the onset) are a consequence of the effect of the diabetic condition on their PNS function and not on the structure.

Analysis of the effect of the onset of diabetes on endoneurial and neuronal transcriptomes

To detect the primary transcriptional changes associated with the development of DPN in *Ins2^{Akita/+}* mice, gene expression profiling of the DRG and of the sciatic nerve endoneurium were carried out. Based on phenotypical characterization described above, eight time-points (postnatal days P20, P24, P28, P32, P36, P40, P48 and P56) covering the early stages of the neuropathy were selected (Fig. 4A). Until P24 (P20 and P24), *Ins2^{Akita/+}* mice did not show any pathological phenotype (hyperglycemia or neuropathy). Starting from P28, glycemia was increased in affected

mice and DPN was clearly detectable at P36, approximately one week after the onset of hyperglycemia. While hyperglycemia increased in *Ins2^{Akita/+}* mice between P36 and P56, symptoms of DPN did not progressively worsen over time.

“Present”, “marginal” and “absent” calls were used for the first step of microarray data filtering (Fig. 4B). Since very closely spaced time-points were used, we considered all genes called “present” only at one developmental stage as artifacts and eliminated them from further analysis. Thus only probes called “present” in at least 2 consecutive time-points were selected leading to the elimination of approximately two thirds of the probes present on the chip (32'561 out of 48'318 total probes were eliminated in DRG arrays; 33'121 out of 48'318 total probes were eliminated in endoneurium arrays). As no chip replicate was included in our experiment we decided to filter the probes according to the coherence of their expression profiles. For this, we selected probes up- or down- regulated more than 3 or 1.5-fold in two or more consecutive time-points, with the additional constraint that the expression level of the selected probes should not vary over 1.5-fold outside these consecutive time-points

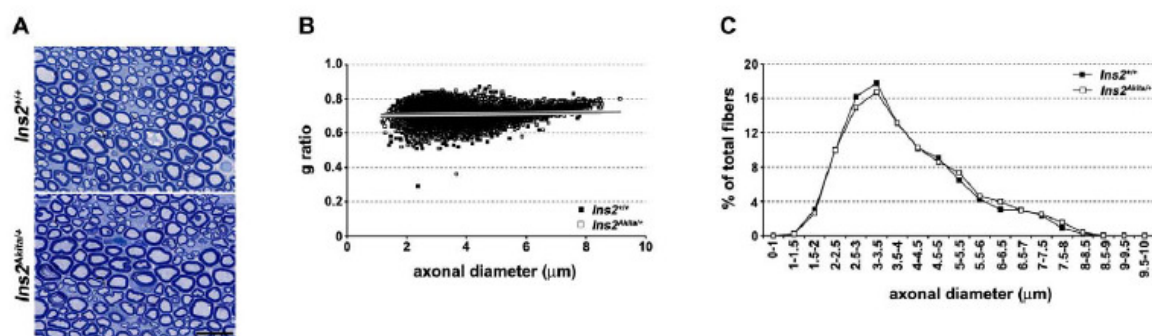


Figure 3. Morphometric evaluation of peripheral nervous system of *Ins2^{Akita/+}* mice. A) Semi-thin toluidin blue stained cross sections of sciatic nerves from three month old *Ins2^{Akita/+}* and control mice show well preserved nerve structures in both genotypes (scale bar: 15 μ m). B) The scatter plot displays g ratios (g ratio = axon area/axon+myelin area) of individual axons as a function of the respective axonal diameters determined using sciatic nerves of three month old wild-type and *Ins2^{Akita/+}* mice. Each point corresponds to one fiber. Thin dark-grey and thick light-grey lines represent the trend-lines for *Ins2^{Akita/+}* and wild-type mice respectively. The two lines are superimposed reflecting close similarity of the two data sets. C) Axonal distribution represented as the percentage of axons for each class of sizes does not reveal any differences between wild-type and *Ins2^{Akita/+}* mice. doi:10.1371/journal.pone.0010832.g003

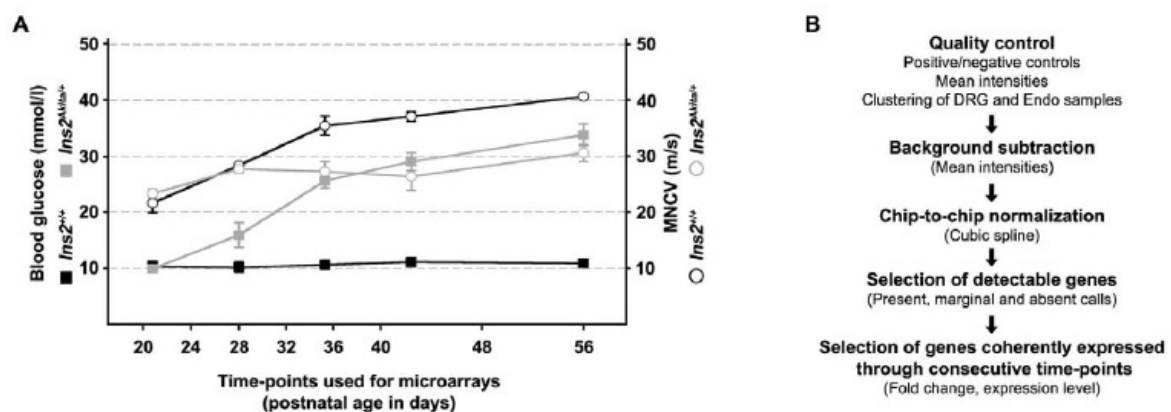


Figure 4. Design of the microarray experiment. A) Eight time-points were selected between 20 and 56 days of age. This time window covers the pre-symptomatic situation (P20, 20 days old), the onset of hyperglycemia (P24–P28), the onset of DPN (P32–P36) and later time-points with a clear symptomatic situation (P36–P56) in *Ins2*^{Akita/+} mice. Squares: blood glucose; circles: MNCV. B) Schematic view of the microarray data analysis. doi:10.1371/journal.pone.0010832.g004

(Fig. S3). This strategy aimed at selecting the most robust gene expression changes present through multiple time-points and helped us to efficiently eliminate the “zigzagging” expression profiles especially observed with genes expressed at low level (raw expression <100, see methods).

Using these filtering criteria, no probe showed a fold change greater than 3 in at least two consecutive time-points in either DRG or sciatic nerve endoneurium samples. Based on previously published studies (Price et al., 2006), we decided to also use a less stringent criterion of 1.5-fold change. In DRGs, 220 probes were selected using this threshold as being differentially regulated in at least 2 consecutive time-points (Table 1). However, the majority of these probes (146 out of 220) had a low expression level. Out of the 220 probes only 31 were up- or down-regulated in more than two consecutive time-points. In sciatic nerve endoneurium, 331 probes met our filtering criteria as being differentially regulated in at least two consecutive time-points (Table 1). As in DRG samples, most of these probes (267 out of 331) had a low expression level. Out of the 331 probes, 71 displayed a fold change above 1.5 in more than two consecutive time-points.

The lowering of the fold change threshold to 1.5-fold had as a consequence the decrease in the filtering stringency. In order to assess the confidence of the filtering procedure, we have examined some of the selected transcripts by quantitative PCR (qPCR, the list of tested transcripts is provided in Table S1). For both tissues, sets of probes differentially expressed in either 2, 3, 4, 5 or 6 consecutive time-points were selected. None of the 20 transcripts selected based on the 1.5-fold change criteria and evaluated by qPCR reproduced the expression pattern obtained with microarrays. All qPCR reactions designed for these confirmations resulted in PCR fragments of the expected size with good PCR efficiency. In addition, the specificity of all primers was confirmed by BLAST searching of the mouse genome database. Several housekeeping genes were used as normalizers, however using distinct normalizer genes did not affect the qPCR results. These different controls exclude PCR reaction problems as an explanation for the lack of reproducibility of our microarray results by qPCR.

Our analysis therefore showed that some expression profiles (mostly derived from genes with very low expression levels) pass our filtering criterion of at least 1.5 fold change in two or more consecutive time-points. However, the subsequent evaluation by

qPCR revealed that the majority if not all of these candidates are false positives. Using more conservative filtering criteria (3 fold change in two or more consecutive time-points) we were unable to detect any transcriptional alterations in either endoneurial or neuronal compartments of diabetic mice.

Effect of the onset of diabetes on the expression of genes playing a role in DRG neuron development and function

Since our expression profiling analysis did not reveal any global transcriptional changes in either the endoneurium or the DRG of diabetic mice, we decided to evaluate the expression of selected genes previously shown to play an important role in development or maintenance of these compartments.

In DRG, the expression of sodium channels (crucial for normal propagation of action potentials) and of neurotrophic factors

Table 1. Number of probes differentially expressed between *Ins2*^{Akita/+} and *Ins2*^{+/+} mice.

Tissue	# of consecutive time-points	# of probes observed
DRG	2	220 (12)
	3	31 (11)
	4	6 (5)
	5	3 (2)
	6	2 (1)
Sciatic nerve endoneurium	2	331 (8)
	3	71 (8)
	4	12 (5)
	5	2 (2)
	6	0

Only probes up- or down-regulated with a fold change of 1.5 in at least 2, 3, 4, 5 or 6 consecutive time-points and without any additional up- or down-regulation exceeding the 1.5-fold threshold were selected by our filtering criteria (see also Fig. S3). The number of genes tested by qPCR in each category is presented in brackets.

doi:10.1371/journal.pone.0010832.t001

(involved in neuronal survival) was already studied [31,32]. Recently, the developmental expression profiles of 17 sodium channels and neurotrophin associated genes had been reviewed [33]. These 17 genes were represented by 28 probes on the arrays that we used. Eight genes were previously shown to be expressed during early DRG development, but were absent in young adults (*Bdnf*, *Gdnf*, *Ngfa*, *Ngfb*, *Ngfg*, *Ntf3*, *Ntrn* and *Scn3a* [33]). The expression of these genes was concordantly undetectable in our DRG samples. Nine genes were described to be expressed at adult stages with no major dynamic changes. Out of these 9 genes, six (*Ntrk1*, *Ret*, *Scn7a*, *Scn8a*, *Scn10a* and *Scn11a* [33]) were detected in our DRG samples (Fig. 5). None of these six genes met our less stringent filtering criterion of 1.5-fold change in two or more consecutive time-points, indicating that neither expression of sodium channels nor that of neurotrophin associated genes were affected by the onset of type 1 diabetes.

Effect of the onset of diabetes on the expression of genes playing a role in Schwann cell myelination and myelin maintenance

Even though we could not detect any major modifications in myelin structure in *Ins2^{Akita/+}* PNS (Fig. 3A–C), subtle molecular alteration in myelin gene expression could provide an early marker of later stage irreversible pathological changes. We have therefore analyzed the expression of genes encoding proteins involved in myelin synthesis and/or maintenance in the sciatic nerve endoneurium samples. Two transcription factors (*Scip* and *Krox20*) regulating progression of myelination and myelin protein expression respectively, together with the expression of four myelin proteins (*Pmp22*, *Mbp*, *Mag* and *P0*) were evaluated. No difference in expression was observed between *Ins2^{Akita/+}* and *Ins2^{+/+}* mice (Fig. 6). *Scip* expression is known to peak during the onset of myelination (P2–P4) and then to decrease with time [34]. In our profiling, the decrease in the expression of this gene was accurately reproduced (Fig. 6). In addition, *Krox20*, *Pmp22*, *Mbp*, *Mag* and *P0* showed no dynamic changes in adult stages, similar to previous studies [34]. The

expression of cholesterol metabolism related genes was previously shown to closely match the expression of myelin genes [34]. None of the cholesterol metabolism related genes tested in our experiment met our filtering criterion of 1.5-fold change in two consecutive conditions (for example see *Cyp51*, *Dhcr7*, *Lss*, *Nsdhl*, *Sc4mol*, *Sqle*; Fig. S4). Together these data indicate that the decreased NCV observed in DPN is not the consequence of significant changes in myelin gene expression that could potentially underlie structural defects of myelin observed in more chronic stages of DPN.

Discussion

Phenotypic characterization of the development of DPN in *Ins2^{Akita/+}* mice

In the present study, we performed a detailed characterization of the onset of DPN in *Ins2^{Akita/+}* mice. The *Ins2^{Akita/+}* model provides the advantage of studying hyperglycemia without the confounding effect of toxic chemicals, such as streptozotocin, since *Ins2^{Akita/+}* animals spontaneously develop hyperglycemia at approximately four weeks of age. Type 1 diabetes in the *Ins2^{Akita/+}* mice is a consequence of an autosomal dominant mutation in the *Ins2* gene resulting in the improper folding of the Proinsulin 2 protein [26]. Transcription of the *Ins2* gene is normally responsible for the majority of the circulating insulin in the C57BL/6 wild-type mice. A recent report suggested that the intracellular accumulation of the misfolded Proinsulin 2 leads to progressive disruption of the insulin secretory pathway organelle architecture and thereby resulting in pancreatic β cell apoptosis [35].

Similarly to the previously described characterization of *Ins2^{Akita/+}* mice [36] we found a progressive increase in blood glucose level starting between three and four weeks of age. Interestingly, our experimental design allowed us to detect the presence of a DPN much earlier than previously reported [27]. We observed a decrease in MNCV already one week after the onset of hyperglycemia and a decrease in SNCV at P56, one month after the onset of hyperglycemia, indicating that DPN affects both

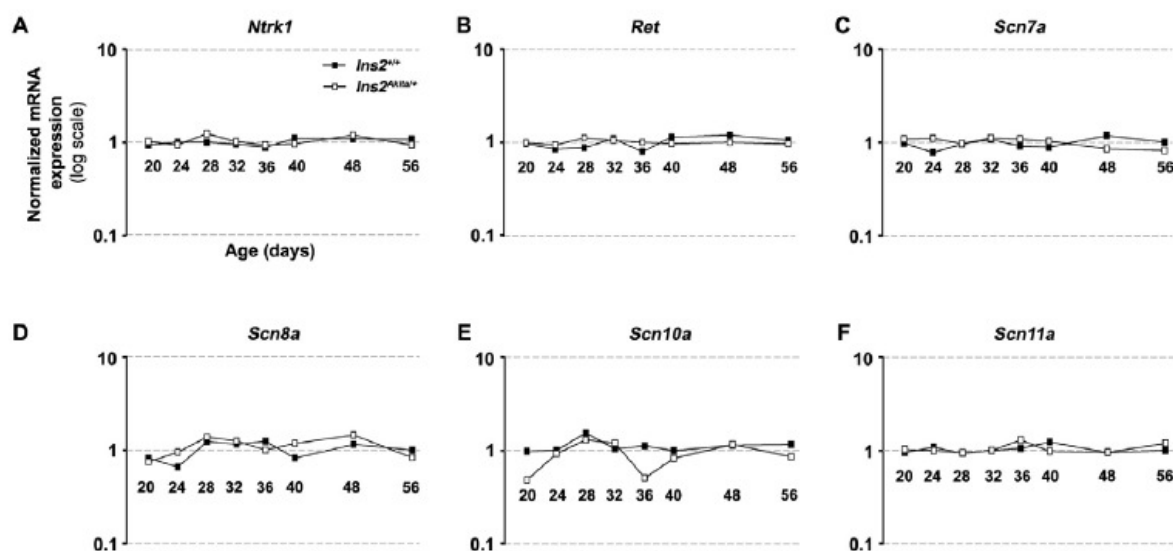


Figure 5. Expression profiles of selected genes involved in sensory neuron development and function. Normalized levels of expression at eight analyzed time-points (P20–P56) in both diabetic (*Ins2^{Akita/+}*) and control (*Ins2^{+/+}*) mice are shown. A) *Ntrk1*, B) *Ret*, C) *Scn7a*, D) *Scn8a*, E) *Scn10a*, F) *Scn11a*. All values were normalized by the median of the intensity obtained for a probe throughout the chips.
doi:10.1371/journal.pone.0010832.g005

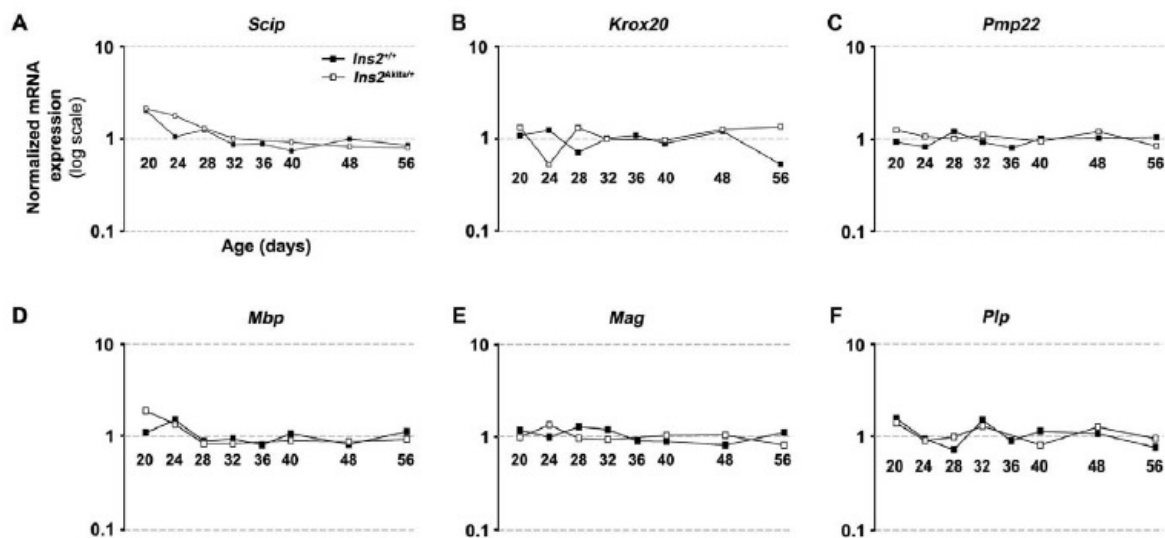


Figure 6. Expression profiles of selected genes involved in Schwann cell myelination. Normalized levels of expression at eight analyzed time-points (P20–P56) are shown for control (*Ins2*^{+/+}) mice. In diabetic (*Ins2*^{Akita/+}) mice, the expression was analyzed only at 7 time-points (data point P36 was excluded, see methods for more explanations). **A)** *Scip*, **B)** *Krox20*, **C)** *Pmp22*, **D)** *Mbp*, **E)** *Mag*, **F)** *Plp*. All values are normalized by the median of the intensity obtained for a probe throughout the chips.
doi:10.1371/journal.pone.0010832.g006

motor and sensory nerve fibers. In contrast, Choeiri and colleagues detected a decrease in SNCV in *Ins2*^{Akita/+} mice only at four months of age. As the decrease in NCV of sensory fibers is smaller than in motor fibers, the sensitivity of measurement could be responsible for this discrepancy. A modest reduction in sensory and motor function was also observed in six month-old diabetic *Ins2*^{Akita/+} mice [37].

The observed deficit in MNCV and SNCV in *Ins2*^{Akita/+} mice does not seem to reflect a delay of PNS maturation since we could not detect any differences in either myelin thickness or axonal size in three month old affected animals and our microarray data does not reveal any changes in the expression of genes involved in either Schwann cell or neuronal maturation or function (see discussion below). This is in line with results obtained from analysis of the onset of DPN in STZ-induced type 1 diabetes at different developmental stages. If diabetes is induced in older animals, deficits in MNCV and SNCV appear and progress with a similar speed as compared to the induction of the disease in younger animals ([38] and discussion within).

In the hot plate test, *Ins2*^{Akita/+} mice respond with increased latency to heat compared to the control littermates. These results are in line with the previously published evaluation of hind paw analgesia in older *Ins2*^{Akita/+} mice, six months after the onset of diabetes [37].

Overall, our phenotypic characterization of *Ins2*^{Akita/+} mice suggests that these mice develop DPN rapidly after the onset of diabetes and thus represent an interesting model of some of the DPN symptoms observed in patients which often present simultaneously positive (burning, neuropathic pain, abnormal sensation to temperature) and negative (numbness, injury insensitivity) sensory findings [4,29].

Transcriptional characterization of the development of DPN in *Ins2*^{Akita/+} mice

We generated a time course of whole-genome expression data covering the pre-symptomatic situation, the onset of hyperglyce-

mia, the onset of the DPN and finally the symptomatic period in *Ins2*^{Akita/+} mice.

In sciatic nerve endoneurium samples, our gene expression analysis of myelin and cholesterol genes showed a good reproducibility with respect to previously published gene expression in wild-type mice [34]. Also, both myelin and cholesterol metabolism gene expression was not affected in *Ins2*^{Akita/+} mice, thereby confirming previously observed stability of myelin structure even at a later developmental stage (48 weeks) in this model [36]. In DRG samples, we reproduced the previously described pattern of expression of sodium channels and neurotrophin associated genes [33]. The expression of these genes was not affected by the onset of diabetes in *Ins2*^{Akita/+} mice. These results are concordant with previous observations in STZ-injected rats. Alterations of the expression of sodium channels Na_v1.3, Na_v1.6, Na_v1.8 and Na_v1.9 [19] or modifications of DRG structure [39] have been reported only in later stages of DPN.

The effect of diabetes on sympathetic neurons was previously comprehensively analyzed in STZ-injected rats after two and six weeks of diabetes [23]. Each of the two diabetes durations (2 and 6 weeks) was considered as a unique time-point. None of the 110 genes described as differentially expressed in para-vertebral or pre-vertebral ganglia in STZ-injected rats was up- or down-regulated with a fold change greater than 1.5 in two or more consecutive time-points in our experiment. Global expression changes have also been previously analyzed in STZ-injected rat DRG after one, four and eight weeks of diabetes [24]. In this study the authors chose a low threshold of 1.2 to maximize the number of differentially expressed genes (from 800 to 1200 per time-point). Similarly to our results, very small changes in gene expression were observed in diabetic DRG compared to control littermates. Out of the 113 published genes, none met our filtering criteria of 1.5-fold change in two or more consecutive time-points. These discrepancies are likely due to the fact that the onset of STZ-induced diabetes is more rapid than the progressive destruction of β -cells observed in *Ins2*^{Akita/+} mice. STZ-injected rodents reach a very

high level of glycemia within two days, whereas glycemia increases progressively in *Ins2^{Akita}/+* mice.

DPN being a progressive disorder, we expected to find groups of transcripts progressively up- or down-regulated as hyperglycemia or DPN develops, with maximal changes in the later time-points. However, there was no correlation between phenotypic changes (onset of hyperglycemia and decreased MNCV) and transcriptional modifications in *Ins2^{Akita}/+* mice. Using conservative filtering criteria of 3-fold change in two or more consecutive time-points, we were unable to detect any transcriptional alterations in either endoneurial or neuronal compartments of diabetic mice. By lowering the stringency criteria to 1.5-fold change in two or more consecutive time-points, we detected some potentially differentially expressed genes in either endoneurium or DRG of diabetic mice. However, none of the 20 expression profiles selected based on 1.5-fold change criteria could be confirmed by qPCR. These results indicate that based on our experimental design, the 1.5-fold threshold criterion is too low to reliably detect genes that are differentially expressed over the time-course.

The observed gene expression stability in both the sciatic nerve endoneurium and the DRG early after the onset of diabetes suggest that the early (reversible) phase of DPN is not a consequence of substantial transcriptional changes. We cannot however exclude the existence of transcriptional changes present only in a small fraction of cells in either the endoneurium or the DRG. The sciatic nerve endoneurium is mainly composed of Schwann cells, but also contains other cell types such as fibroblasts, macrophages and blood vessels. It is considered that approximately 10% of the nuclei in the sciatic nerve endoneurium belong to fibroblasts and another 2–9% to macrophages, while the remainder are Schwann cell nuclei [40]. Similarly to the endoneurium, DRG is composed of several populations of sensory neurons and other cell types such as satellite and Schwann cells [41,42]. Thus, if transcriptional changes induced by diabetic conditions appear only in a specific cell population, these changes may be obscured by the messenger RNAs of the other cell types composing the tissues, which may prevent their detection by our current approach. We are working on new strategies that will allow us to efficiently purify mRNAs from selected endoneurial or DRG cell populations to test this hypothesis.

Together our data suggest that global transcriptional programs in both endoneurial and neuronal compartments of peripheral nerves are relatively resistant to the onset of type 1 DPN. The phenotypic changes observed during the onset of DPN, when the disease phenotypes are still reversible, are most probably a consequence of changes occurring at the post transcriptional level [9] or due to small changes in gene expression level or changes in restricted cell populations that are both below the level of sensitivity of the screen presented in this study. Major transcriptional changes may occur in the peripheral nervous system affected by DPN, but in more chronic stages when irreversible structural alterations appear.

Materials and Methods

Animals

All animals were housed in a controlled environment with a 12 h light/12 h dark cycle and free access to water and standard laboratory diet (except for fasting animals which had access only to water). Experiments were performed in accordance with the legal requirements of the University of Lausanne and the Canton of Vaud. C57BL/6J-*Ins2^{Akita}* (*Ins2^{Akita}/+*) mice were obtained from The Jackson Laboratory (Bar Harbor, Maine, USA) and genotyped according to a previously described protocol [26].

Measurement of blood glucose level

Tail vein blood glucose was determined with a glucometer Ascencia Contour (Bayer).

Motor and sensory nerve conduction velocity (MNCV and SNCV)

All animals were anesthetized with a mixture of 10 μ l/g of Ketanarcon 100 (1 mg/ml, Streuli) with 0.1% Rompun (Bayer) in PBS. For MNCV, the left and right sciatic nerves were stimulated at the sciatic notch and distally at the ankle via bipolar electrodes with supramaximal square-wave pulses (5 V) of 0.05 milliseconds. The latencies of the compound muscle action potentials were recorded by a bipolar electrode inserted between digits 2 and 3 of the hind paw and measured from the stimulus artifact to the onset of the negative M-wave deflection. MNCV was calculated by dividing the distance between the stimulating and recording electrode by the subtraction of the distal latency from the proximal latency. The sensory nerve action potential (SNAP) was recorded at the tail and sciatic nerve. For the tail recordings, the caudal nerve of the tail was stimulated distally and the bipolar electrode was inserted proximally at the base of the tail. Latency of the SNAPS was determined by measuring the stimulus artifact to the onset of the S-wave deflection. The SNCV of the sciatic nerve was recorded at the sciatic notch by stimulating the nerve with the bipolar electrodes placed in the dorsal part of the hindpaw. SNCV was calculated by dividing the distance between the stimulating and recording electrode by the latency. Results were expressed as the mean standard error of the mean (S.E.M.) and pair-wise comparisons performed using the Student's t-test.

Morphometric analysis

Mice were perfused with 1% PFA and 2% glutaraldehyde in 0.1 M cacodylate buffer (pH 7.3) for 5 min. Sciatic nerves were dissected and post fixed by immersion in the fixative solution for 2 h at 4°C, washed in 0.1 M cacodylate buffer, and osmicated for 4 h in 1% OsO₄ (Fluka). Nerves were rinsed in water, dehydrated, and embedded in epon 812 resin (Fluka). One-micrometer sections were stained with 1% toluidine blue and examined by light microscopy. Subsequent morphometric analyses were performed on micrographs using Image J plug-in (G ratio calculator) developed in collaboration with the cellular imaging facility of the University of Lausanne and available at <http://cifweb.unil.ch>.

Intraepidermal nerve fiber (IENF) density quantification

Footpads from 10 week old male *Ins2^{Akita}/+* and *Ins2^{+/+}* mice were removed from the plantar area of the hind feet and fixed in Zamboni's fixative for 2 hours at room temperature. Tissues were washed three times in PBS, kept in 30% sucrose/PBS overnight at 4°C and subsequently embedded in OCT medium (Sakura). Frozen sections (50 μ m) were prepared and six different sections (using every fourth section) from each animal were immunostained by a free-floating protocol. Sections were blocked in 0.3% Triton X-100 followed by an incubation with the goat anti-Collagen IV antibody (at a 1:40 dilution; Millipore) for 24 h at 4°C diluted in blocking reagent. After three washes in PBS, samples were stained with the secondary antibody anti-goat Alexa 594 (at a 1:200 dilution, Invitrogen) for 2 hours at room temperature. The sections were then stained with the rabbit anti-PGP 9.5 (at a 1:400 dilution; Ultracolor) and anti-rabbit Alexa 488 antibody (at a 1:200 dilution, Invitrogen). Finally, sections were transferred onto a slide in a drop of PBS and, after drying, mounted with Vectashield mounting medium containing DAPI to counterstain cell nuclei (Vector Laboratories). Four fields per section and three

sections per animal were quantified for IENF density. Images based on the stack of consecutive 2 μ m sections (usually 15 sections) were generated by using confocal microscopy (Leica SP5 AOBs Confocal Microscope). Single IENF crossing the basement membrane between dermis and epidermis were counted, whereas secondary branching and epidermal nerve fragments that do not cross the basement membrane were excluded from the quantification. The length of epidermis was measured using ImageJ and the linear density of IENF (IENF/mm) was obtained. Counting was carried out with the observer blinded to the origin (*Ins2^{Akita/+}* and *Ins2^{+/+}*) of the image.

Sensory behavior assessment

All experiments were carried out by the same person, in the same laboratory and in the same environment. Testing started after habituation of the mice to the experimenter and to the environment. The development of thermal hypersensitivity was measured using a hot plate (Columbus Instruments). Mice were placed on a hot plate set at 49°, 52° or 55°C. The nociceptive behavior (paw licking or jumping from the hot plate) response latency was recorded and animals were removed immediately from the hotplate. Without response, animals were removed after 1 min, 45 or 20 seconds for the three temperatures respectively, to diminish the potential of thermal injury. Three trials separated by over ten minutes were averaged for each data point.

Total RNA preparation

Sciatic nerve endoneuriums and L5 DRGs were dissected from P20, P24, P28, P32, P36, P40, P48 and P56 days old male *Ins2^{Akita/+}* and *Ins2^{+/+}* mice. Since we have previously shown that Schwann cells are sensitive to dietary changes [17], all animals were subjected to 14 h fasting and to a subsequent 6 h refeeding before sacrifice in order to limit the metabolic variation between individuals. For each group, tissues from five mice were pooled before RNA extraction. For each mouse, weight and blood glucose were measured (Table S2) to build groups that contained minimal phenotypic variation. In the set of animals used for microarray experiments, increased glycemia was initially observed at P24 and hyperglycemia became clear at P28, followed by a small decrease in weight at P48 and P56. Total RNA from sciatic nerve endoneuriums and DRGs was isolated using the Qiagen RNeasy lipid tissue kit (Qiagen) following the manufacturer's instructions. RNA quality was verified by agarose gel and/or by 2100 Bioanalyzer (Agilent) and the concentration was determined by the ND-1000 Spectrophotometer (NanoDrop).

cRNA synthesis

For each condition (pool of five mice), 300 ng of total RNA was used to synthesize cRNA using the Illumina TotalPrep RNA amplification kit (Ambion) following the manufacturer's instructions. cRNA concentration was determined using a spectrophotometer, whereas cRNA quality was determined by 2100 Bioanalyzer (Agilent).

Illumina arrays

The MouseWG-6 v1 expression Beadchips (Illumina) were used to determine differences in gene expression. Hybridizations were carried out using the Illumina gene expression system according to the manufacturer's instructions. Briefly, biotin-labelled cRNA (1.5 μ g) was added to the array and incubated for 16–20 hours at 55°C. The bound biotin-labelled cRNA was then stained with streptavidin-Cy3. After hybridization, the microarray chip was washed, dried, and scanned by the Illumina BeadArray Reader.

The absolute intensity of each probe on the image was generated with the BeadStudio software Version 1.5.1.3 (Illumina). Different controls were performed to assess the quality of the hybridization. The mean intensities of each chip, the mean intensities for negative or positive controls and the mean intensities obtained for random sequences (background level) were determined. All these mean intensities were within normal ranges and were also comparable among chips. Chips were also clustered based on their similarities. All chips hybridized with DRG samples were grouped within the same cluster. One of the chips hybridized with a sciatic nerve endoneurium sample (P36 *Ins2^{Akita/+}*) was clustered within the group of DRG samples. This chip was therefore eliminated from the analysis. BeadStation 5003 data were extracted using the cubic spline normalization option of BeadStudio Version 1.5.1.3 (Illumina). Each tissue was normalized independently. Absent, marginal and present calls were defined according to the mean intensity level of the probes (BeadStudio). Data were then imported into GeneSpring V7.2 (Agilent Technologies) for data visualization and filtering. Raw intensities of present genes were ranging from 10 to 40'000. Genes represented by probes with a raw intensity under 100 (44% of probes scored as present in DRG samples; 47% of probes scored as present in sciatic nerve endoneurium samples) were therefore considered as low expressors. The difference in expression level between the 2 genotypes was calculated by dividing raw data obtained for *Ins2^{Akita/+}* mice by raw data obtained for *Ins2^{+/+}* mice. In this case, raw expression values less than 10 were converted to 10 (expression values <10 = "absent" calls). The array data is accessible through the ArrayExpress database (accession number: E-TABM-987; <http://www.ebi.ac.uk/microarray-as/ae/>).

Quantitative RT-PCR

250–500 ng of total RNA was subjected to reverse transcription using the SuperScriptTM III First-Strand Synthesis System for RT-PCR (Invitrogen) following the manufacturer's instructions. Resulting cDNA was used as a template for quantitative PCR (qPCR). The cycling conditions were 95°C for 10 min, followed by 40 cycles of 95°C for 15 s, and 60°C for 1 min. To detect and eliminate possible primer-dimer artifacts, a dissociation curve was generated by adding a cycle of 95°C for 15 s, 60°C for 1 min and 95°C for 15 s. All primer sets produced amplicons of the expected size and their specificity was also verified by BLAST[®] searching of the mouse genome database. Sample quantitation was performed using a standard curve established from a serial dilution of a mix of the samples. Results were normalized using the reference genes cyclophilin or ubiquitin, which showed minimal changes in their level of expression in the array data. See Table S1 for a complete list of primers used for qPCR.

Supporting Information

Figure S1 Sciatic nerve SNCV measurements in three month old control and *Ins2^{Akita/+}* mice. A tendency for reduced SNCV was observed in diabetic (*Ins2^{Akita/+}*) mice ($p=0.12$). Results are expressed as the mean \pm standard error of the mean (S.E.M). (*Ins2^{+/+}*: $n=4$; *Ins2^{Akita/+}*: $n=4$).
Found at: doi:10.1371/journal.pone.0010832.s001 (0.15 MB TIF)

Figure S2 Intraepidermal nerve fiber density assessment in 10 week old control and *Ins2^{Akita/+}* mice. No difference was observed between control and diabetic (*Ins2^{Akita/+}*) mice. Results are expressed as the mean \pm standard error of the mean (S.E.M). (*Ins2^{+/+}*: $n=3$; *Ins2^{Akita/+}*: $n=3$).
Found at: doi:10.1371/journal.pone.0010832.s002 (0.15 MB TIF)

Figure S3 Schematic description of the microarray filtering criteria. Data are represented as a fold change between diabetic ($Ins2^{Akita/+}$) and control ($Ins2^{+/+}$) mice. A fold change of one represents an equal level of expression between $Ins2^{Akita/+}$ and $Ins2^{+/+}$ mice. Values above or below one represent, respectively, an increased or decreased level of expression in $Ins2^{Akita/+}$ mice. A cut-off of 1.5-fold change was used. In order for a probe to be selected by our filtering, fold change should therefore be >1.5 or <0.66 in 2, 3, 4, 5 or 6 consecutive time-points. In addition, we do not allow the probe to vary in the level of expression for more than 1.5-fold outside these consecutive time-points. Two examples of probes that would be selected using our criteria are shown: A) expression profile with an up-regulation in 2 consecutive time-points (black circles); B) expression profile with a down-regulation in 3 consecutive time-points. Two examples of probes that would be eliminated using our selection criteria are shown: C) expression profile with an up-regulation in two consecutive time-points (P28–P32), unchanged level of expression at P36–P40 and an up-regulation at P48 would be eliminated by our filtering; D) Expression profile with a down-regulation in 3 consecutive time-points (P28–P36) followed by an up-regulation in an additional time-point (P56) would also be eliminated by our filtering. Found at: doi:10.1371/journal.pone.0010832.s003 (0.59 MB TIF)

Figure S4 Expression of selected cholesterol metabolism related genes in sciatic nerve endoneurium samples. Normalized levels of expression at eight analyzed time-points (P20–P56) are shown for control ($Ins2^{+/+}$) mice. In diabetic ($Ins2^{Akita/+}$) mice the expression

was analyzed only at 7 time-points (data point P36 was excluded, see methods for more explanations). A) Cyp51, B) Dhcr7, C) Lss, D) Nsdhl, E) Sc4 mol, F) Sqle. All values are normalized by the median of the intensity obtained for a probe throughout the chips. Found at: doi:10.1371/journal.pone.0010832.s004 (0.72 MB TIF)

Table S1 List of primers used for qPCR confirmations.

Found at: doi:10.1371/journal.pone.0010832.s005 (2.73 MB TIF)

Table S2 Body weight and tail vein blood glucose measurements in $Ins2^{Akita/+}$ and control $Ins2^{+/+}$ mice used for the microarray experiment. Results represent the mean \pm standard error of the mean (S.E.M.; $Ins2^{+/+}$: $n = 5$; $Ins2^{Akita/+}$: $n = 5$).

Found at: doi:10.1371/journal.pone.0010832.s006 (1.24 MB TIF)

Acknowledgments

We wish to thank Dr. Patrick Descombes and Dr. Olivier Schaad from the genomic platform Frontiers in Genetics in Geneva for their help with the Illumina Beadchip experiment and the Cellular Imaging Facility (Faculty of Biology and Medicine and the University Hospitals, Lausanne) for help with intraepidermal nerve fiber density quantification.

Author Contributions

Conceived and designed the experiments: ASdPC RC. Performed the experiments: ASdPC VV JZ JJM. Analyzed the data: ASdPC VV JZ BP JJM TK JSB SB RC. Contributed reagents/materials/analysis tools: BP TK. Wrote the paper: ASdPC TK JSB SB RC.

References

- Greene DA, Sima AA, Feldman EL, Stevens MJ (1997) Ellenberg and Rifkin diabetic neuropathy. In: Rifkin H, Porte D, Sherwin R, eds. Diabetes Mellitus. Appleton and Lange ed. Stanford: Appleton and Lange. pp 1009–1076.
- Feldman EL, Stevens MJ, Russell JW, Greene DA (2001) Diabetic neuropathy. In: Becker KL, ed. Principles and Practice of Endocrinology and Metabolism. Philadelphia: Lippincott Williams & Wilkins.
- Thomas PK, Tomlinson DR (1993) Diabetic and hypoglycemic neuropathy. In: Dyck PJ, Thomas PK, Griffin JW, eds. Peripheral Neuropathy. 3 ed. Philadelphia: Saunders. pp 1219–1250.
- Zochodne DW (2007) Diabetes mellitus and the peripheral nervous system: manifestations and mechanisms. Muscle Nerve 36: 144–166.
- Apfel SC (1999) Neurotrophic factors and diabetic peripheral neuropathy. Eur Neurol 41 Suppl 1: 27–34.
- Sugimoto K, Murakawa Y, Sima AA (2000) Diabetic neuropathy—a continuing enigma. Diabetes Metab Res Rev 16: 408–433.
- Sima AA (2003) New insights into the metabolic and molecular basis for diabetic neuropathy. Cell Mol Life Sci 60: 2445–2464.
- Walker D, Carrington A, Cannon SA, Sawicki D, Sredy J, et al. (1999) Structural abnormalities do not explain the early functional abnormalities in the peripheral nerves of the streptozotocin diabetic rat. J Anat 195 (Pt3): 419–427.
- Tomlinson DR, Gardiner NJ (2008) Glucose neurotoxicity. Nat Rev Neurosci 9: 36–45.
- Pop-Busui R, Sima A, Stevens M (2006) Diabetic neuropathy and oxidative stress. Diabetes Metab Res Rev 22: 257–273.
- Yaghashi S, Matsunaga M (1979) Ultrastructural pathology of peripheral nerves in patients with diabetic neuropathy. Tohoku J Exp Med 129: 357–366.
- Leininger GM, Edwards JL, Lipshaw MJ, Feldman EL (2006) Mechanisms of disease: mitochondria as new therapeutic targets in diabetic neuropathy. Nat Clin Pract Neurol 2: 620–628.
- Thomas PK, Lascelles RG (1965) Schwann-Cell Abnormalities in Diabetic Neuropathy. Lancet 1: 1355–1357.
- Burnand RC, Price SA, McElhaney M, Barker D, Tomlinson DR (2004) Expression of axotomy-inducible and apoptosis-related genes in sensory nerves of rats with experimental diabetes. Brain Res Mol Brain Res 132: 235–240.
- Roberts RE, McLean WG (1997) Protein kinase C isozyme expression in sciatic nerves and spinal cords of experimentally diabetic rats. Brain Res 754: 147–156.
- Chavez JC, Ahnha K, Berti-Mattera LN (2005) Transient expression of hypoxia-inducible factor-1 alpha and target genes in peripheral nerves from diabetic rats. Neurosci Lett 374: 179–182.
- de Preux AS, Goosen K, Zhang W, Sima AA, Shimano H, et al. (2007) SREBP-1c expression in Schwann cells is affected by diabetes and nutritional status. Mol Cell Neurosci 35: 525–534.
- Calcutt NA, Allendoerfer KL, Mizisin AP, Middlemas A, Freshwater JD, et al. (2003) Therapeutic efficacy of sonic hedgehog protein in experimental diabetic neuropathy. J Clin Invest 111: 507–514.
- Craner MJ, Klein JP, Renganathan M, Black JA, Waxman SG (2002) Changes of sodium channel expression in experimental painful diabetic neuropathy. Ann Neurol 52: 786–792.
- Price SA, Gardiner NJ, Duran-Jimenez B, Zeef LA, Obrosova IG, et al. (2006) Thioredoxin interacting protein is increased in sensory neurons in experimental diabetes. Brain Res 1116: 206–214.
- Hong S, Wiley JW (2006) Altered expression and function of sodium channels in large DRG neurons and myelinated A-fibers in early diabetic neuropathy in the rat. Biochem Biophys Res Commun 339: 652–660.
- Pabbidi RM, Cao DS, Parihar A, Pauza ME, Premkumar LS (2008) Direct role of streptozotocin in inducing thermal hyperalgesia by enhanced expression of transient receptor potential vanilloid 1 in sensory neurons. Mol Pharmacol 73: 995–1004.
- Carroll SL, Cagen LM, Dorsey DA, Watson MA, Schmidt RE (2004) Ganglion-specific patterns of diabetes-modulated gene expression are established in prevertebral and paravertebral sympathetic ganglia prior to the development of neuroaxonal dystrophy. J Neuropathol Exp Neurol 63: 1144–1154.
- Price SA, Zeef LA, Wardleworth L, Hayes A, Tomlinson DR (2006) Identification of changes in gene expression in dorsal root ganglia in diabetic neuropathy: correlation with functional deficits. J Neuropathol Exp Neurol 65: 722–732.
- Sango K, Suzuki T, Yanagisawa H, Takaku S, Hirooka H, et al. (2006) High glucose-induced activation of the polyol pathway and changes of gene expression profiles in immortalized adult mouse Schwann cells IMS32. J Neurochem 98: 446–458.
- Wang J, Takeuchi T, Tanaka S, Kubo SK, Kayo T, et al. (1999) A mutation in the insulin 2 gene induces diabetes with severe pancreatic beta-cell dysfunction in the Mody mouse. J Clin Invest 103: 27–37.
- Choeiri C, Hewitt K, Durlin J, Simard CJ, Renaud JM, et al. (2005) Longitudinal evaluation of memory performance and peripheral neuropathy in the Ins2C96Y Akita mice. Behav Brain Res 157: 31–38.
- Barber AJ, Antonetti DA, Kern TS, Reiter CE, Soans RS, et al. (2005) The Ins2Akita mouse as a model of early retinal complications in diabetes. Invest Ophthalmol Vis Sci 46: 2210–2218.
- Said G (2007) Diabetic neuropathy—a review. Nat Clin Pract Neurol 3: 331–340.
- Quattrini C, Tavakoli M, Jeziorska M, Kallinikos P, Tesfaye S, et al. (2007) Surrogate markers of small fiber damage in human diabetic neuropathy. Diabetes 56: 2148–2154.
- Dib-Hajj SD, Black JA, Cummins TR, Kenney AM, Kocsis JD, et al. (1998) Rescue of alpha-SNS sodium channel expression in small dorsal root ganglion neurons after axotomy by nerve growth factor in vivo. J Neurophysiol 79: 2668–2676.
- Wright DE, Snider WD (1996) Focal expression of glial cell line-derived neurotrophic factor in developing mouse limb bud. Cell Tissue Res 286: 209–217.

33. Benn SC, Costigan M, Tate S, Fitzgerald M, Woolf CJ (2001) Developmental expression of the TTX-resistant voltage-gated sodium channels Nav1.8 (SNS) and Nav1.9 (SNS2) in primary sensory neurons. *J Neurosci* 21: 6077–6085.
34. Verheijen MH, Chrast R, Burrola P, Lenke G (2003) Local regulation of fat metabolism in peripheral nerves. *Genes Dev* 17: 2450–2464.
35. Izumi T, Yokota-Hashimoto H, Zhao S, Wang J, Halban PA, et al. (2003) Dominant negative pathogenesis by mutant proinsulin in the Akita diabetic mouse. *Diabetes* 52: 409–416.
36. Yaguchi M, Nagashima K, Izumi T, Okamoto K (2003) Neuropathological study of C57BL/6Akita mouse, type 2 diabetic model: enhanced expression of alphaB-crystallin in oligodendrocytes. *Neuropathology* 23: 44–50.
37. Sullivan KA, Hayes JM, Wiggin TD, Backus C, Su Oh S, et al. (2007) Mouse models of diabetic neuropathy. *Neurobiol Dis* 28: 276–285.
38. Biesels GJ, Cristino NA, Rutten GJ, Hamers FP, Erkelens DW, et al. (1999) Neurophysiological changes in the central and peripheral nervous system of streptozotocin-diabetic rats. Course of development and effects of insulin treatment. *Brain* 122 (Pt4): 757–768.
39. Kishi M, Tanabe J, Schmelzer JD, Low PA (2002) Morphometry of dorsal root ganglion in chronic experimental diabetic neuropathy. *Diabetes* 51: 819–824.
40. King RHM (2005) Nerve trunks and spinal roots. In: Dyck PJ, Thomas PK, eds. *Peripheral Neuropathy*. Fourth edition ed. Philadelphia: Elsevier Saunders, pp 35–42.
41. Marmigere F, Ernfor P (2007) Specification and connectivity of neuronal subtypes in the sensory lineage. *Nat Rev Neurosci* 8: 114–127.
42. Hanani M (2005) Satellite glial cells in sensory ganglia: from form to function. *Brain Res Brain Res Rev* 48: 457–476.

5.2 Mouse model of Charcot-Marie-Tooth disease type 4C

In 2003, Sh3tc2 (= KIAA1985) was identified as the causative gene for CMT4C, a recessive demyelinating form of CMT diseases (135). However, the role of Sh3tc2 protein was completely unknown. Sh3tc2 possess two SH3-domains, multiple TRP domains and a myristilation domain which might connect it to the plasma membrane. Mutations appearing in human patients are randomly distributed within the protein, including both missense and nonsense mutations. The disease is characterized by an early onset, progressive muscle weakness, reduced MNCV and is often associated with scoliosis. In order to understand the pathophysiological mechanism of CMT4C we analyzed the function of Sh3tc2 *in vitro* and *in vivo* in Sh3tc2^{ΔEx1/ΔEx1} mice that we generated.

I contributed to the publication below with the following experiments:

- participation in mouse dissections and tissue collections
- accomplishment of the microarray analysis comparing the gene expression of Sh3tc2^{ΔEx1/ΔEx1} and Sh3tc2^{+/+} sciatic nerve endoneurium at P28
- characterization of the nodal phenotype in Sh3tc2^{ΔEx1/ΔEx1} mice by co-immunostainings on teased fibers
- contribution to qPCR and Western blot analysis of various myelin markers in Sh3tc2^{ΔEx1/ΔEx1} sciatic nerves as compared to Sh3tc2^{+/+} mice
- Sh3tc2 antibody testing to detect its endogenous expression

5.2.1 SH3TC2/KIAA1985 protein is required for proper myelination and the integrity of the node of Ranvier in the peripheral nervous system

SH3TC2/KIAA1985 protein is required for proper myelination and the integrity of the node of Ranvier in the peripheral nervous system

Estelle Arnaud^a, Jennifer Zenker^{a,b}, Anne-Sophie de Preux Charles^a, Claudia Stendel^c, Andreas Roos^d, Jean-Jacques Médard^a, Nicolas Tricaud^c, Joachim Weis^a, Ueli Suter^c, Jan Senderek^{c,d,e}, and Roman Chrast^{a,1}

^aDepartment of Medical Genetics and ^bGraduate Program in Neurosciences, University of Lausanne, CH-1005 Lausanne, Switzerland; ^cInstitute of Cell Biology, Eidgenössische Technische Hochschule (ETH) Zurich, CH-8093 Zurich, Switzerland; and Institutes of ^dHuman Genetics and ^eNeuropathology, Rheinisch-Westfälische Technische Hochschule (RWTH), Aachen University of Technology, 52074 Aachen, Germany

Edited by Eric M. Shooter, Stanford University School of Medicine, Stanford, CA, and approved July 29, 2009 (received for review May 26, 2009)

Charcot-Marie-Tooth disease type 4C (CMT4C) is an early-onset, autosomal recessive form of demyelinating neuropathy. The clinical manifestations include progressive scoliosis, delayed age of walking, muscular atrophy, distal weakness, and reduced nerve conduction velocity. The gene mutated in CMT4C disease, *SH3TC2/KIAA1985*, was recently identified; however, the function of the protein it encodes remains unknown. We have generated knockout mice where the first exon of the *Sh3tc2* gene is replaced with an enhanced GFP cassette. The *Sh3tc2*^{ΔEx1/ΔEx1} knockout animals develop progressive peripheral neuropathy manifested by decreased motor and sensory nerve conduction velocity and hypomyelination. We show that *Sh3tc2* is specifically expressed in Schwann cells and localizes to the plasma membrane and to the perinuclear endocytic recycling compartment, concordant with its possible function in myelination and/or in regions of axoglial interactions. Concomitantly, transcriptional profiling performed on the endoneurial compartment of peripheral nerves isolated from control and *Sh3tc2*^{ΔEx1/ΔEx1} animals uncovered changes in transcripts encoding genes involved in myelination and cell adhesion. Finally, detailed analyses of the structures composed of compact and noncompact myelin in the peripheral nerve of *Sh3tc2*^{ΔEx1/ΔEx1} animals revealed abnormal organization of the node of Ranvier, a phenotype that we confirmed in CMT4C patient nerve biopsies. The generated *Sh3tc2* knockout mice thus present a reliable model of CMT4C neuropathy that was instrumental in establishing a role for *Sh3tc2* in myelination and in the integrity of the node of Ranvier, a morphological phenotype that can be used as an additional CMT4C diagnostic marker.

Charcot-Marie-Tooth disease | peripheral neuropathy | Schwann cell

With an estimated prevalence of 1 in 2,500 persons, Charcot-Marie-Tooth (CMT) neuropathies [also called hereditary motor and sensory neuropathies (HMSNs)] are among the most common inherited neurological disorders (1). Over the last 25 years, progress in genetics has led to the identification of more than 30 genes responsible for different CMT forms (www.molgen.ua.ac.be/CMTMutations). Identification of these genes, which encode proteins involved in various glial and axonal functions, contributed tremendously both to basic understanding of peripheral nerve function and to genetic counseling in affected families.

CMT4C is a demyelinating, autosomal recessive CMT neuropathy. The clinical manifestations observed in CMT4C patients include delayed age of walking, muscular atrophy, areflexia, sensory impairment, foot deformities (pes cavus), and reduced motor and sensory nerve conduction velocities. The histopathological examination of patient sural nerve biopsies revealed a demyelinating type of neuropathy. Electron microscopic analysis also demonstrated the presence of nonmyelinating Schwann cell complexes with abnormal cell processes and demyelinated and remyelinated axons surrounded by onion bulbs consisting of empty basal lamina sheaths (2–5). Disease

severity and the age of onset vary in and between families, but usually the sensorimotor neuropathy can be detected in the first decade of life (4–6). In addition to the peripheral neuropathy, almost all patients affected by CMT4C develop early-onset severe scoliosis.

CMT4C has originally been mapped in two large Algerian families to a 13-cM linkage interval on chromosome 5q23–q33 (7). By homozygosity mapping and allele-sharing analysis, this interval was narrowed down to a 1.7-megabase region, leading to the identification of mutations in a thus far uncharacterized transcript called *KIAA1985*, or *SH3TC2* (4). *SH3TC2* encodes a protein of 1,288 aa containing two Src homology 3 (SH3) and 10 tetratricopeptide repeat (TPR) domains sharing no overall significant similarity to any other human protein with known function. The presence of SH3 and TPR domains suggests that SH3TC2 could act as a scaffold protein. *SH3TC2* is well conserved among vertebrate species, whereas no nonvertebrate orthologs were identified (4).

The role of SH3TC2 in the peripheral nervous system remains largely unknown. Thus, we decided to analyze its function in vivo by creating a *Sh3tc2*^{ΔEx1/ΔEx1} mouse, a model of CMT4C disease. By detailed characterization of *Sh3tc2*^{ΔEx1/ΔEx1} peripheral nerve development and function, we found that these mice mimic neuropathy phenotypes present in CMT4C patients. Moreover, the characterization of the *Sh3tc2*^{ΔEx1/ΔEx1} mice led to the finding of lengthened nodes of Ranvier in these mice. This nodal phenotype was confirmed in biopsies from CMT4C patients, providing an additional clinical marker that may improve the diagnostic approach to this disease.

Results

Mice with a Disrupted *Sh3tc2* Gene Develop a Peripheral Neuropathy. Based on described mutations in exon 1 of *SH3TC2* in neuropathic patients affected by CMT4C leading to a premature stop codon (4), we decided to develop a mouse knockout model of CMT4C by replacing exon 1 of the *Sh3tc2* gene with an enhanced GFP (eGFP)-Neo cassette (Fig. 1A). Mice homozygous for the targeted allele (*Sh3tc2*^{neoΔEx1/neoΔEx1}) were crossed with the deleter strain nestin-Cre to eliminate the *neo* gene, leading to the generation of a *Sh3tc2*^{ΔEx1} allele. The mating of *Sh3tc2*^{ΔEx1/ΔEx1} mice led to a normal Mendelian ratio of the offspring genotypes. The generated *Sh3tc2* mutant mice (*Sh3tc2*^{ΔEx1/ΔEx1}) lacked exon 1 and expressed eGFP instead of *Sh3tc2* mRNA (Fig. S1A–C). We took advantage of the

Author contributions: E.A., J.S., and R.C. designed research; E.A., J.Z., A.-S.d.P.C., C.S., A.R., J.-J.M., N.T., and R.C. performed research; E.A., J.Z., A.-S.d.P.C., C.S., A.R., J.W., U.S., J.S., and R.C. analyzed data; and E.A., N.T., J.W., U.S., J.S., and R.C. wrote the paper.

The authors declare no conflict of interest.

This article is a PNAS Direct Submission.

¹To whom correspondence should be addressed. E-mail: roman.chrast@unil.ch.

This article contains supporting information online at www.pnas.org/cgi/content/full/0905523106 and www.pnas.org/supplemental.

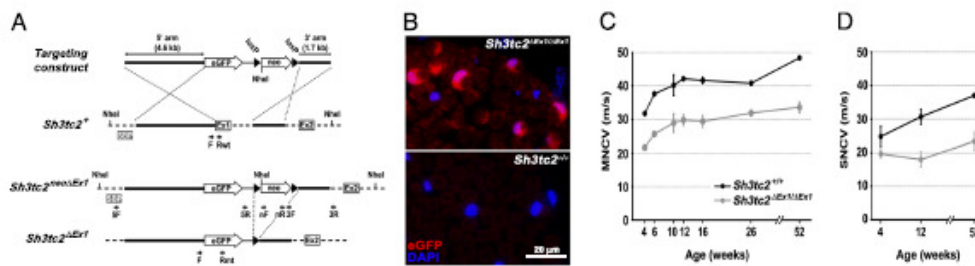


Fig. 1. *Sh3tc2*^{ΔEx1/ΔEx1} mice develop a peripheral neuropathy. (A) Schematic diagram showing the targeting vector containing a 5' homology arm up to the ATG start site, the eGFP and *LoxP-neo-LoxP* cassettes necessary for monitoring of the eGFP expression in vivo and Geneticin (G418) selection in ES cells, respectively, and a shorter 3' homology arm. After homologous recombination in embryonic stem cells, exon 1 (Ex1) of *Sh3tc2* gene was eliminated. The neo cassette was removed by crossing the resulting mice with a *nestin-Cre* deleter strain. Primers used for the ES cell screening (5F and 5R, and 3F and 3R), the mouse genotyping (F, Rwt, and Rmt), and the validation of the neo gene deletion (nF and nR) are indicated by arrows. (B) Amplification of GFP signal using anti-GFP antibody on sciatic nerve cross-sections. Typical cross-staining of the Schwann cell specificity of the *Sh3tc2* promoter in the homozygous knockout nerve (Upper). No signal was detected in the *Sh3tc2*^{+/+} nerves (Lower). (C and D) Nerve conduction velocity of *Sh3tc2*^{ΔEx1/ΔEx1} and control mice (n = 4) during their first year of life. At 4 weeks, motor [MNCV, (C)] and sensory [SNCV, (D)] nerve conduction velocities were already significantly slowed down in *Sh3tc2*^{ΔEx1/ΔEx1} mice.

eGFP cassette replacing *Sh3tc2* expression in heterozygote and homozygote animals (*Sh3tc2*^{ΔEx1/+} and *Sh3tc2*^{ΔEx1/ΔEx1}) to determine which cell types express *Sh3tc2*. In sciatic nerve cross-sections of *Sh3tc2*^{ΔEx1/+} or *Sh3tc2*^{ΔEx1/ΔEx1} mice, we found a typical cross-staining of the Schwann cell cytoplasm (Fig. 1B). In all other tested tissues (liver, brain, optic nerve, spinal cord, and dorsal root ganglia), eGFP was undetectable which, together with the endoneurium-restricted expression of endogenous *Sh3tc2* as detected by qPCR (Fig. S1D), revealed the specificity of the *Sh3tc2* promoter.

Mutant mice developed normally, were fertile, and lived as long as their wild-type or heterozygous littermates. In contrast to CMT4C-affected patients, who often develop a scoliosis, no skeletal abnormalities were detected by X-ray analysis of mutant mice (Fig. S2). Although appearing normal overall, *Sh3tc2*^{ΔEx1/ΔEx1} mice could be distinguished from control mice by an abnormal clenching of toes and clamping of hind limbs upon tail suspension (Fig. S3), suggesting peripheral nervous system (PNS) abnormalities. To address this issue further, we measured both motor nerve conduction velocity (MNCV) and sensory nerve conduction velocity (SNCV) in these animals. At 4 weeks after birth, *Sh3tc2* mutant mice already displayed electrophysiological characteristics of neuropathy, as indicated by a significantly lower nerve conduction velocity compared with control littermates (10-m/s decrease in mutant MNCV and 4-m/s decrease in SNCV). The neuropathy slowly progressed, reaching a reduction of 15 m/s for MNCV and 13 m/s for SNCV at 1 year of age in *Sh3tc2* mutant compared with control animals (Fig. 1C and D).

Peripheral Nerves of *Sh3tc2*^{ΔEx1/ΔEx1} Mice Are Hypomyelinated. The reduction of nerve conduction velocity suggested abnormalities in peripheral nerve fiber myelination in *Sh3tc2*^{ΔEx1/ΔEx1} mice. Light-microscopic examination of semithin sections of sciatic nerves isolated from animals 10 (P10), 23 (P23), 56 (P56), and 365 (P365) days old revealed obvious hypomyelination at P56 and at P365 (Fig. S4A). Ultrastructural analysis of sciatic nerve by electron microscopy at P56 demonstrated that in particular, bigger axons were substantially hypomyelinated, and this phenotype was even more visible at P365. However, even after 1 year of duration of the disease, the axons themselves appeared to be healthy (Fig. 2A). Rare onion bulbs and elongated, abnormally branched processes of nonmyelinating Schwann cells as described in CMT4C patients could be found in some sections of *Sh3tc2*^{ΔEx1/ΔEx1} sciatic nerve at P365. To evaluate the onset of the hypomyelination phenotype more quantitatively, we performed a morphometric analysis at all four developmental stages (P10–P365). This analysis revealed a

slightly higher g ratio in *Sh3tc2*^{ΔEx1/ΔEx1} sciatic nerves already at P10 and P23 that became more obvious at P56 and P365 (Fig. S4B). Moreover, representation of myelin thickness as a function of axonal diameter during development (P10–P365) showed that the *Sh3tc2*^{ΔEx1/ΔEx1} axons were rarely covered by a myelin sheath thicker than 1 μm, whereas we found that the sheath reached almost 2 μm in the largest control nerve fibers at P56 and P365 (Fig. 2B). The observed hypomyelination did not lead to significant axonal loss in mutant animals, as determined by counting the total number of axons per nerve at P56 (*Sh3tc2*^{ΔEx1/ΔEx1}, 3,772 ± 209, n = 3; controls, 4,089 ± 160, n = 3). However, a slight shift of the axonal size distribution was observed toward the population of small axons (<3 μm) in *Sh3tc2*^{ΔEx1/ΔEx1} nerve starting from P23 (Fig. S4B).

Optic nerve axons of *Sh3tc2*^{ΔEx1/ΔEx1} mice were myelinated normally, suggesting that the observed myelination defects are PNS-specific (Fig. S4C).

Sh3tc2 Localizes to the Plasma Membrane and the Endocytic Recycling Compartment. To identify its potential function, we have determined the subcellular localization of Sh3tc2 in cultured Schwann cells (MSC80 cell line). After transfection, a C-terminal FLAG-tagged form of Sh3tc2 (Sh3tc2-FLAG) was localized at the plasma membrane in a dotted pattern and in the pericentrosomal region, as assessed by γ-tubulin costaining (Fig. 3A Left). To further characterize the pericentriolar localization of Sh3tc2, we used Rab11 as a marker of the endocytic recycling compartment (8). We found that Rab11-eGFP partially colocalized in the endocytic recycling compartment with the FLAG-tagged Sh3tc2 (Fig. 3A Right). The identity of this cellular compartment was further confirmed by a transferrin uptake assay (Fig. 3B). Furthermore, analysis of the SH3TC2 amino acid sequence revealed a putative myristoylation site at the N terminus (4). We hypothesized that myristoylation could be responsible for the observed plasma membrane localization of Sh3tc2. An in vitro myristoylation assay revealed that SH3TC2 could indeed be myristoylated, whereas replacing the putative myristoylation site (glycine at position 2) with the nonmyristoylatable amino acid alanine (G2A) led to a loss of myristoylation capacity (Fig. 3C). In addition, transient transfection of COS-7 cells with the mutant or wild-type SH3TC2 protein showed that the localization at the plasma membrane was lost when SH3TC2 could not be myristoylated, whereas the localization in the endocytic recycling compartment was partially retained (Fig. 3D).

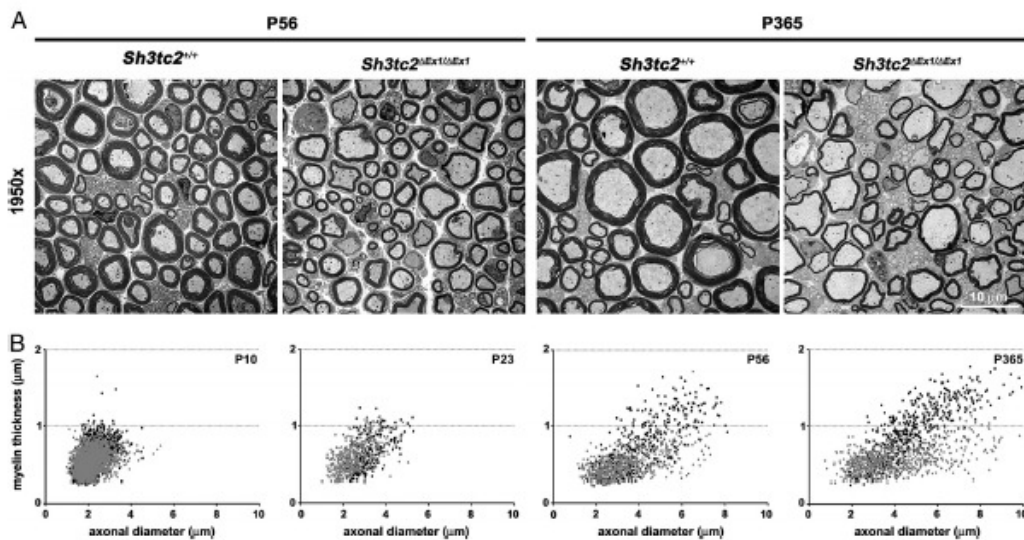


Fig. 2. Hypomyelination of sciatic nerve of *Sh3tc2*^{ΔEx1/ΔEx1} mice. (A) Electron micrographs of sciatic nerves isolated from wild-type and *Sh3tc2*^{ΔEx1/ΔEx1} mice at P56 and at 1 year of age (P365). Although reduced myelin sheath thickness is clearly visible at both stages, the axons themselves remain preserved, even in 1-year-old *Sh3tc2*^{ΔEx1/ΔEx1} animals. (B) The scatter plots display myelin thicknesses of individual axons as a function of their respective diameters determined at P10 ($n = 4$), P23 ($n = 4$), P56 ($n = 2$), and P365 ($n = 3$). Each point corresponds to one fiber (gray points, *Sh3tc2*^{ΔEx1/ΔEx1}; black points, *Sh3tc2*^{+/+}). Even at 1 year of age, the myelin in *Sh3tc2*^{ΔEx1/ΔEx1} animals did not reach the mature thickness.

Sh3tc2 Deletion Affects the Myelination-Related Gene Expression Program. To identify genes and pathways involved in the pathological mechanisms leading to CMT4C disease, we performed a microarray analysis of mRNA populations isolated from P28 sciatic nerve endoneuria of three *Sh3tc2*^{ΔEx1/ΔEx1} and three control mice. Analysis of signals obtained from *Sh3tc2* and *eGFP* probes confirmed the inactivation of the *Sh3tc2* gene in *Sh3tc2*^{ΔEx1/ΔEx1} mice (Fig. S5A). Focused analysis of the expression of myelination-related genes revealed slight down-regulation of some of the genes encoding the main structural myelin proteins, including myelin basic protein (Mbp) and myelin protein zero (Mpz), whereas the increased expression of transcription factors Scip/Oct-6 and Krox24 suggested the presence of incompletely differentiated Schwann cells in P28 *Sh3tc2*^{ΔEx1/ΔEx1} sciatic nerve (Fig. 4A). These data were confirmed by qPCR (Fig. S5B). Moreover, genes involved in cholesterol biosynthesis, which plays a crucial role in normal myelin membrane synthesis (9), were all down-regulated in absence of *Sh3tc2* (Fig. 4B). We also analyzed the global transcriptomic changes in *Sh3tc2* mutants. Despite the observed hypomyelination phenotype in *Sh3tc2*^{ΔEx1/ΔEx1} mice at P23, as indicated by altered g ratio (Fig. S4B), the transcriptome was not substantially affected by *Sh3tc2* depletion at P28, which is a relatively early stage of the disease. The expression of 179 probes differed significantly between *Sh3tc2*^{ΔEx1/ΔEx1} and controls (fold change >2 ; $P < 0.05$). Interestingly, annotation and classification of the corresponding genes based on biological functions revealed enrichment in genes involved in cell signaling and adhesion processes (Fig. 4C and Table S1).

Sh3tc2 Is Required for the Integrity of Nodes of Ranvier. Because adhesion plays a crucial role in myelin organization and in regions of close interactions between the Schwann cell and the underlying axon, we examined these structures more closely. By electron microscopy analysis, we could not detect alterations in either compact myelin or Schmidt–Lanterman incisures (which

connect Schwann cells' perinuclear cytoplasm to the adaxonal cytoplasm) in *Sh3tc2*^{ΔEx1/ΔEx1} compared with wild-type sciatic nerve (Fig. S6). However, we observed structural and molecular changes at the nodes of Ranvier. Sciatic nerve teased fibers were labeled with Nile red, a fluorescent lipophilic stain that intensively labels lipid-rich structures, such as myelin. Whereas internodal length was not significantly affected (*Sh3tc2*^{ΔEx1/ΔEx1}, $605 \pm 141 \mu\text{m}$; controls, $676 \pm 160 \mu\text{m}$; fiber diameter, $3\text{--}6 \mu\text{m}$), this analysis revealed substantially wider nodal spaces between two consecutive Schwann cells in mutant fibers (Fig. 5A and Table S2). We therefore extended our investigation by using markers specific for nodal (pan-Nav, phospho-ERM), paranodal (Caspr), and juxtaparanodal (Kv1.2) regions. The Caspr staining of teased fibers confirmed the presence of enlarged nodes (Fig. 5B and Table S2), whereas the Na⁺ channels remained tightly clustered at the nodes (Na, staining). The staining of Schwann cell microvilli with phospho-ERM showed reduced intensity in mutant nerves. In addition, potassium channel distribution was perturbed at the juxtaparanodes of *Sh3tc2*^{ΔEx1/ΔEx1} fibers (Kv1.2 staining). Previous data demonstrated that potassium channels are more concentrated near the paranodes and diffuse slightly away toward the internodes (10). We confirmed this staining in the wild-type situation, but in mutants, the staining appeared less intense and more diffuse than in controls. To determine whether the abnormalities observed by immunofluorescence correspond to alterations in the ultrastructure of the axoglial contact at the nodes of Ranvier, we performed electron microscopy of sciatic nerve longitudinal sections (1-year-old *Sh3tc2*^{ΔEx1/ΔEx1} mice, $n = 5$, and control mice, $n = 3$). All nodes of Ranvier ($n = 50$) analyzed in *Sh3tc2*^{ΔEx1/ΔEx1} sciatic nerve presented the enlarged phenotype. Both classes I and II of nodes (as previously defined in Phillips et al., ref. 11) were affected in *Sh3tc2*^{ΔEx1/ΔEx1} sciatic nerve, leading to a substantially larger nodal gap in mutant animals ($2.69 \pm 1.70 \mu\text{m}$) compared with controls ($0.77 \pm 0.27 \mu\text{m}$; Fig. 5C). Such a nodal

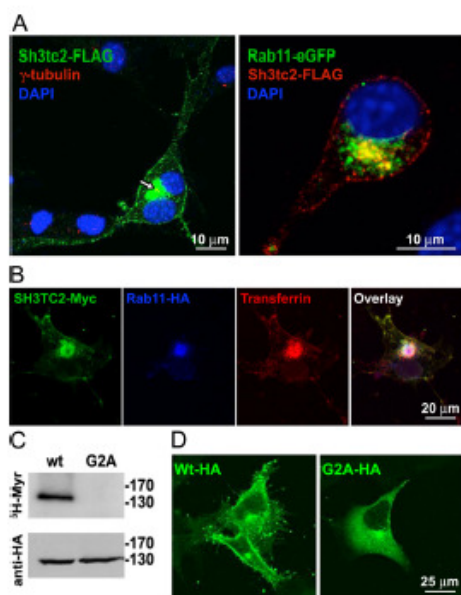


Fig. 3. Subcellular localization of Sh3tc2 at the plasma membrane and endocytic recycling compartment. (A) The mouse Schwann cell line (MSC80) cells were transfected with Sh3tc2-FLAG (Left) and with Sh3tc2-FLAG in combination with Rab11-eGFP (Right). Transfected cells were immunostained with anti-FLAG antibody and γ -tubulin and costained with DAPI to visualize the nuclei. Sh3tc2 localized at the membrane surface and in a cytoplasmic compartment near the centrosome (Left, arrow). This compartment is the endocytic recycling compartment, as shown by the colocalization of Sh3tc2-FLAG with Rab11-eGFP (Right). (B) Transferrin (red) was internalized by COS-7 cells that were transfected with Rab11-HA (blue) and SH3TC2-Myc (green). The overlay shows colocalization of the three molecules in the endocytic recycling compartment. (C) Autoradiography after *in vitro* myristoylation assay in COS-7 cells using [3 H]myristic acid (3 H-Myr) showed that wild-type SH3TC2 (wt) can be myristoylated at the N terminus, whereas myristoylation is lost if the N-terminal motif is mutated (G2A). (Lower) A Western blot documenting equal expression of mutant and wild-type SH3TC2-HA. (D) When transfected into COS-7 cells, mutation of the SH3TC2 myristoylation site (G2A-HA) led to diffuse cytoplasmic staining and loss of the plasma membrane localization, whereas the localization at the recycling endosome was partially preserved.

phenotype has not been described in CMT4C patients. Thus, we evaluated the structure of the nodes of Ranvier by using longitudinal sections of nerve biopsies from five CMT4C patients with SH3TC2 mutations (Table S3). Electron microscopy revealed changes at the nodes of Ranvier in three of the five CMT4C patients that are remarkably similar to those observed in *Sh3tc2* ^{Δ Ex1/ Δ Ex1} mice (Fig. 5D).

Discussion

During the last two decades, genetic studies have continuously documented new CMT4C cases (4, 5, 7, 12–15). Although the recent identification of SH3TC2 as the gene mutated in CMT4C (4) immediately led to substantially improved clinical diagnostic and genetic counseling in the affected families, the functional role of the SH3TC2 protein in peripheral nerves remained unknown. Here, we describe the generation and analysis of a mouse model of CMT4C disease that led to the discovery of a role for Sh3tc2 in myelination and in the structure of the node of Ranvier.

Our mutant mice show that Sh3tc2 is required for normal myelination in mouse peripheral nerve. In the absence of this gene, mice develop a peripheral neuropathy. Nerve conduction velocity measurements, morphometric analyses, and transcriptional analysis indicated the presence of the neuropathy already at 4 weeks of age, suggesting an early onset of the disease in *Sh3tc2* ^{Δ Ex1/ Δ Ex1} mice. The neuropathy was then slowly progressive; adult mutant mice presented MNCV and SNCV values \sim 15 m/s below controls, which is a decrease comparable to the values recorded in CMT4C patients (4). Whereas CMT4C disease is commonly classified as “demyelinating” disease, we did not observe any signs of demyelination (e.g., myelin debris, Schwann cell onion bulbs, or macrophage infiltration) in the early stages of the disease in *Sh3tc2* ^{Δ Ex1/ Δ Ex1} mice. Also, the DAPI staining of longitudinal sections or cross-sections of the *Sh3tc2* ^{Δ Ex1/ Δ Ex1} nerve did not show increased numbers of nuclei, and no cell cycle activators (e.g., cyclin-D1) were overexpressed in our microarray data. Moreover, internodal length was not reduced. Our data therefore suggest that conduction defects in *Sh3tc2* ^{Δ Ex1/ Δ Ex1} mice are primarily a consequence of hypomyelination and/or of disrupted structure of nodes of Ranvier (see discussion below). The demyelinating features, such as onion bulbs present in the patient biopsies (4, 5), which were absent in younger animals, were infrequently observed in *Sh3tc2* ^{Δ Ex1/ Δ Ex1} mice at 1 year of age. An explanation for this difference might be the progressive aspect of the disease; the demyelination phenotype present in symptomatic patient biopsies could be the consequence of an early hypomyelination. In addition, a substantial heterogeneity in the age of onset and severity of the disease was observed among patients with CMT4C (4, 5, 12–15).

Sh3tc2 is specifically expressed in Schwann cells in the mouse. Our *in vitro* experiments demonstrated its punctate localization at the plasma membrane and in the endocytic recycling compartment. Myelin biogenesis and maintenance is a complex process involving coordinated exocytosis, endocytosis, and cytoskeletal dynamics. Perturbations in the myelin protein trafficking and/or turnover are associated with major myelinopathies (16, 17). Current hypotheses suggest that recycling endosomes play a central role in protein sorting and trafficking, both during plasma membrane recycling and as an intermediate step during cargo transport from the trans-Golgi network to the plasma membrane (18). Sh3tc2 could be transported from endosomal storage sites to the plasma membrane when needed for myelin formation, as described recently for proteolipid protein (PLP) in oligodendrocytes (19). Alternatively, Sh3tc2 could be involved in the regulation of cargo transport through the recycling endosome. Such a transport route has been described recently for the myelin protein Mog in oligodendrocytes (20). Interestingly, transcripts encoding Gcc2 and Vps39, proteins that are involved in Rab GTPase-dependent vesicle trafficking (21, 22), were significantly down-regulated in *Sh3tc2* ^{Δ Ex1/ Δ Ex1} nerve (Table S1).

Analysis of the *Sh3tc2* ^{Δ Ex1/ Δ Ex1} nerve fibers led to the discovery of an interesting phenotype at the nodes of Ranvier. Using EM and immunohistological localization of markers of different parts of the nodal region, we observed that the nodes were substantially wider, whereas the clustering of sodium channels and the paranodal structures as stained by Caspr and analyzed by EM at the level of transverse bands were preserved in *Sh3tc2*-deficient mice. In addition, we detected less phospho-ERM in the microvilli and substantially more diffuse K_v1.2 staining at the juxtaparanodes in *Sh3tc2* ^{Δ Ex1/ Δ Ex1} mice. Such widening of the nodes associated with decreased phospho-ERM has been described in *Laminin* 2-deficient mice, where it is associated with impaired clustering of the sodium channels (23). Our data do not allow us to distinguish whether Sh3tc2 is directly involved in the formation and/or maintenance of the node of Ranvier or whether the observed nodal widening is a secondary effect of hypomyelination. However, previous data show that disruption of the nodal gene *Nfasc* in the CNS results in a reduction of myelination, suggesting that the nodal phenotype

disease in these patients compared with analyzed *Sh3tc2^{ΔEx1/ΔEx1}* animals. To our knowledge, such alteration of the structure of the node of Ranvier in CMT disease patients has so far been documented only in dominant X-linked CMT disease caused by mutations in the gap junction protein-β1, 32 kDa (GJB1), also called connexin 32 (Cx32) (27). Data from different CMT animal models (*CMT1A*, refs. 28 and 29; *CMT4B1*, ref. 30; and, recently, *CMT4E*, ref. 31) show that the eventual defects observed at the nodes vary between different mutants. Systematic analysis of the nodes of Ranvier would therefore be of great value to improve the characterization of different CMT forms that often remain difficult to discriminate.

In summary, our characterization of the *Sh3tc2^{ΔEx1/ΔEx1}* mice demonstrated that these animals represent a valid model of CMT4C neuropathy and allowed us to unveil the *Sh3tc2* function in the myelination process and in the node of Ranvier integrity. The *Sh3tc2^{ΔEx1/ΔEx1}* mice thus represent an *in vivo* model for further examination of CMT4C disease mechanisms and for evaluation of any potential therapeutic approach to treat this disease. Moreover, this study led to the discovery of a previously undescribed pathological feature of CMT4C disease that may lead to improvement of its diagnosis.

Experimental Procedures

Generation of *Sh3tc2*-Null Mice. We screened the 129SvEvTac mouse genomic BAC library (RPCI-22; BACPAC Resources Center, Children's Hospital Oakland Research Institute, Oakland, CA) and isolated clones containing the genomic region around exon 1 of the mouse *Sh3tc2* gene. We then used a recombineering-based approach (32) to obtain the targeting vector (Fig. 1) containing a 5' homology arm up to the ATG start site (4,655 bp) and the eGFP and Neo-LoxP cassettes, allowing us to monitor *Sh3tc2* expression and Genetec (G418) selection in ES cells, respectively, as well as a shorter 3' homology arm (1,714 bp). The linearized targeting construct was electroporated into 129Sv-derived ES cells by using standard procedures. A total of 384 G418-resistant ES clones were screened by PCR using primers 5F and 3R, located outside the 5' and 3' homology arms, respectively, and 5R and 3F, located in the eGFP-Neo cassette (Fig. 1A). Positive clones were confirmed by Southern blotting using ES cell genomic DNA digested with NheI and hybridized with 5' external probe SBP (Fig. 1A and Fig. S1A). Two correctly targeted clones were used for the injection into C57BL/6J

blastocysts that led to the subsequent development of mice with the targeted allele (*Sh3tc2^{ΔEx1/ΔEx1}*). To eliminate influence of the neo cassette on the expression of nearby genes, we crossed the generated mice with the Nes-Cre deleter (33). This led to the generation of *Sh3tc2^{ΔEx1/ΔEx1}* mice, which are also referred to as "*Sh3tc2* mutants." Genotyping PCR conditions are described in *SI Materials and Methods*.

Morphological, Electrophysiological, and Biochemical Analyses. Morphometric analysis, Nile red staining, electron microscopy, X-ray analysis, nerve conduction velocity measurements, immunohistochemistry, RT-PCR, qPCR, *Sh3tc2* subcellular localization, myristoylation assay, and transferrin uptake assay were performed according to standard methods, details of which and of the ensuing quantifications are described in *SI Materials and Methods*.

Microarray Analysis. Sciatic nerve endoneurium of three wild-type and three knockout males were dissected at P28 after 24 h of fasting. A total of 300 ng of total endoneurium RNA was used to synthesize cRNA by using the Illumina TotalPre RNA amplification kit (Ambion). The Mouse WG-v1.1 Expression Beadchips (Illumina) were hybridized with biotin-streptavidin Cy3-labeled cRNA and scanned by the Illumina BeadArray Reader. Microarray data analysis is described in detail in *SI Materials and Methods*.

ACKNOWLEDGMENTS. We thank the transgenic animal facility (Faculty of Biology and Medicine and the University Hospitals, Lausanne, Switzerland) for help in generating the *Sh3tc2^{ΔEx1/ΔEx1}* mice; Drs. P. Descombes and C. Delucinge Vivier (Genomics Platform, NCCR Frontiers in Genetics, Geneva, Switzerland) for their help with the microarray experiment; Y. Krempf for his help with the development of the g-ratio calculator software; Dr. S. Anrejevic for help with X-ray analysis; Dr. H. Kleins for help with the myristoylation assay; Dr. M. T. Damiani (Universidad Nacional de Cuyo, Mendoza, Argentina) for the Rab11-eGFP construct; Dr. A. Trumpf (Ecole Polytechnique Fédérale de Lausanne, Lausanne, Switzerland) for providing us with Nes-Cre deleter strain; F. Schupfer, D. Marek, and I. Labgaa for technical assistance; Dr. G. Lemke for support in the initial phase of the project; and Dr. J. Beckmann for his advice. This work was supported by Swiss National Science Foundation (SNSF) Grant PP00A-106714 (to R.C.), by grants from the SNSF, the Deutsche Forschungsgemeinschaft (DFG), and the National Center for Excellence in Research—Neural Plasticity and Repair (to U.S.), the DFG (to J.W.) the START program of Aachen University of Technology (to J.S.), and the interdisciplinary Centre for Clinical Research BIOMAT within the Faculty of Medicine, Aachen University of Technology (to J.W. and J.S.). J.S. is a Heisenberg fellow and C.S. a postdoctoral fellow of the DFG. A.R. received a Ph.D. scholarship from Aachen University of Technology.

1. Skre H (1974) Genetic and clinical aspects of Charcot-Marie-Tooth's disease. *Clin Genet* 6:98–118.
2. Gabreels-Festen AA, Gabreels FJ, Jennekens FG, Joosten EM, Janssen-van Kempen TW (1992) Autosomal recessive form of hereditary motor and sensory neuropathy type I. *Neurology* 42:1755–1761.
3. Kessali M, et al. (1997) A clinical, electrophysiologic, neuropathologic, and genetic study of two large Algerian families with an autosomal recessive demyelinating form of Charcot-Marie-Tooth disease. *Neurology* 48:867–873.
4. Senderek J, et al. (2003) Mutations in a gene encoding a novel SH3/TPR domain protein cause autosomal recessive Charcot-Marie-Tooth type 4C neuropathy. *Am J Hum Genet* 73:1106–1119.
5. Houlden H, et al. (2009) The phenotype of Charcot-Marie-Tooth disease type 4C due to *SH3TC2* mutations and possible predisposition to an inflammatory neuropathy. *Neuromuscul Disord* 19:264–269.
6. Guillbot A, et al. (1999) The autosomal recessive form of CMT disease linked to *Sq31-q33*. *Ann N Y Acad Sci* 883:453–456.
7. LeGuern E, et al. (1996) Homozygosity mapping of an autosomal recessive form of demyelinating Charcot-Marie-Tooth disease to chromosome 5q23–q33. *Hum Mol Genet* 5:1685–1688.
8. Ullrich O, Reinsch S, Urbe S, Zerial M, Parton RG (1996) Rab11 regulates recycling through the pericentriolar recycling endosome. *J Cell Biol* 135:913–924.
9. Verheijen MH, Christ R, Burrola P, Lemke G (2003) Local regulation of fat metabolism in peripheral nerves. *Genes Dev* 17:2450–2464.
10. Pollak S, Pelos E (2003) The local differentiation of myelinated axons at nodes of Ranvier. *Nat Rev Neurosci* 4:968–980.
11. Phillips DD, Hibbs RG, Ellison JP, Shapiro H (1972) An electron microscopic study of central and peripheral nodes of Ranvier. *J Anat* 111:229–238.
12. Gabreels-Festen A, et al. (1999) Study on the gene and phenotypic characterisation of autosomal recessive demyelinating motor and sensory neuropathy (Charcot-Marie-Tooth disease) with a gene locus on chromosome 5q23–q33. *J Neurol Neurosurg Psychiatry* 66:569–574.
13. Azzedine H, et al. (2006) Spine deformities in Charcot-Marie-Tooth 4C caused by *SH3TC2* gene mutations. *Neurology* 67:602–606.
14. Colomer J, et al. (2006) Clinical spectrum of CMT4C disease in patients homozygous for the p.Arg1109X mutation in *SH3TC2*. *Neuromuscul Disord* 16:449–453.
15. Gosselin I, et al. (2008) Founder *SH3TC2* mutations are responsible for a CMT4C French-Canadian cluster. *Neuromuscul Disord* 18:483–492.
16. Berger P, Niemann A, Suter U (2006) Schwann cells and the pathogenesis of inherited motor and sensory neuropathies (Charcot-Marie-Tooth disease). *Glia* 54:243–257.
17. Scherer SS, Wrabetz L (2008) Molecular mechanisms of inherited demyelinating neuropathies. *Glia* 56:1578–1589.
18. Ang AL, et al. (2004) Recycling endosomes can serve as intermediates during transport from the Golgi to the plasma membrane of MDCK cells. *J Cell Biol* 167:531–543.
19. Trajkovic K, et al. (2006) Neuron to glia signaling triggers myelin membrane exocytosis from endosomal storage sites. *J Cell Biol* 172:937–948.
20. Winterstein C, Trotter J, Kramer-Albers EM (2008) Distinct endocytic recycling of myelin proteins promotes oligodendroglial membrane remodeling. *J Cell Sci* 121:834–842.
21. Burguete AS, Fenn TD, Brunker AT, Pfeiffer SR (2008) Rab and Arf GTPase family members cooperate in the localization of the golgin GCC185. *Cell* 132:286–298.
22. Brett CL, et al. (2008) Efficient termination of vacuolar Rab GTPase signaling requires coordinated action by a GAP and a protein kinase. *J Cell Biol* 182:1141–1151.
23. Occhi S, et al. (2005) Both laminin and Schwann cell dystroglycan are necessary for proper clustering of sodium channels at nodes of Ranvier. *J Neurosci* 25:9418–9427.
24. Zonta B, et al. (2008) Glial and neuronal isoforms of neurofascin have distinct roles in the assembly of nodes of Ranvier in the central nervous system. *J Cell Biol* 181:1169–1177.
25. Ohashi T, et al. (2002) Bral1, a brain-specific link protein, colocalizing with the vesicular V2 isoform at the nodes of Ranvier in developing and adult mouse central nervous systems. *Mol Cell Neurosci* 19:43–57.
26. Altt G (1976) In *The Peripheral Nerve*, ed Landon DN (Chapman and Hall, London), pp 683–695.
27. Hahn AF, Ahnsworth PJ, Bolton CF, Bilbao JM, Vallat JM (2001) Pathological findings in the x-linked form of Charcot-Marie-Tooth disease: A morphometric and ultrastructural analysis. *Acta Neuropathol* 101:129–139.
28. Neuberg DH, Sancho S, Suter U (1999) Altered molecular architecture of peripheral nerves in mice lacking the peripheral myelin protein 22 or connexin32. *J Neurosci Res* 58:612–623.
29. Davaux JJ, Scherer SS (2005) Altered ion channels in an animal model of Charcot-Marie-Tooth disease type 1A. *J Neurosci* 25:1470–1480.
30. Bollino A, et al. (2004) Disruption of *Mtm2* produces CMT4B-like neuropathy with myelin outflow and impaired spermatogenesis. *J Cell Biol* 167:711–721.
31. Baloh RH, et al. (2009) Congenital hypomyelinating neuropathy with lethal conduction failure in mice carrying the *Egr2* I268N mutation. *J Neurosci* 29:2312–2321.
32. Liu P, Jenkins NA, Copeland NG (2003) A highly efficient recombineering-based method for generating conditional knockout mutations. *Genome Res* 13:476–484.
33. Dubois NC, Hofmann D, Kaloulis K, Bishop JM, Trumpf A (2006) Nestin-Cre transgenic mouse line Nes-Cre1 mediates highly efficient Cre/loxP mediated recombination in the nervous system, kidney, and somite-derived tissues. *Genesis* 44:355–360.

5.2.2 SH3TC2, a protein mutant in Charcot–Marie–Tooth neuropathy, links peripheral nerve myelination to endosomal recycling

In our recent paper (45) (chapter 5.2.1.), we have shown that $Sh3tc2^{\Delta Ex1/\Delta Ex1}$ mice developed a peripheral neuropathy similar to the one observed in CMT4C patients. However, it is still an open question how the loss of Sh3tc2 can affect PNS myelination. Interestingly, Sh3tc2 protein contains multiple protein-protein interaction domains but no binding partner has been identified so far. Here, we show a clear interaction between Sh3tc2 with Rab11 which is disrupted by mutations in the Sh3tc2 gene. This finding links peripheral neuropathy to the mechanism of endocytic recycling.

I performed the microarray analysis and contributed to the Western Blot analysis of Rab11 on sciatic nerves of P5-old $Sh3tc2^{\Delta Ex1/\Delta Ex1}$ versus $Sh3tc2^{+/+}$ mice.

SH3TC2, a protein mutant in Charcot–Marie–Tooth neuropathy, links peripheral nerve myelination to endosomal recycling

Claudia Stendel,^{1,*} Andreas Roos,^{2,*} Henning Kleine,^{3,#} Estelle Arnaud,^{4,#} Murat Özçelik,^{1,#} Páris N. M. Sidiropoulos,^{1,#} Jennifer Zenker,⁴ Fanny Schüpfer,⁴ Ute Lehmann,³ Radosław M. Sobota,⁵ David W. Litchfield,⁶ Bernhard Lüscher,³ Roman Chrast,⁴ Ueli Suter¹ and Jan Senderek¹

1 Institute of Cell Biology, Department of Biology, ETH Zürich, Zürich, Switzerland

2 Institute of Human Genetics, RWTH Aachen University, Aachen, Germany

3 Institute of Biochemistry and Molecular Biology, RWTH Aachen University, Aachen, Germany

4 Department of Medical Genetics and Service of Medical Genetics, University of Lausanne and Centre Hospitalier Universitaire Vaudois, Lausanne, Switzerland

5 Centre for Experimental Bioinformatics, Department of Biochemistry and Molecular Biology, University of Southern Denmark, Odense, Denmark

6 Department of Biochemistry, University of Western Ontario, London, Canada

*These authors contributed equally to this work.

#These authors contributed equally to this work.

Correspondence to: Dr Jan Senderek,
Institute of Cell Biology,
ETH Zürich,
Schafmattstr 18,
8093 Zürich, Switzerland
E-mail: jan.senderek@cell.biol.ethz.ch

Patients with Charcot–Marie–Tooth neuropathy and gene targeting in mice revealed an essential role for the SH3TC2 gene in peripheral nerve myelination. SH3TC2 expression is restricted to Schwann cells in the peripheral nervous system, and the gene product, SH3TC2, localizes to the perinuclear recycling compartment. Here, we show that SH3TC2 interacts with the small guanosine triphosphatase Rab11, which is known to regulate the recycling of internalized membranes and receptors back to the cell surface. Results of protein binding studies and transferrin receptor trafficking are in line with a role of SH3TC2 as a Rab11 effector molecule. Consistent with a function of Rab11 in Schwann cell myelination, SH3TC2 mutations that cause neuropathy disrupt the SH3TC2/Rab11 interaction, and forced expression of dominant negative Rab11 strongly impairs myelin formation *in vitro*. Our data indicate that the SH3TC2/Rab11 interaction is relevant for peripheral nerve pathophysiology and place endosomal recycling on the list of cellular mechanisms involved in Schwann cell myelination.

Keywords: SH3TC2 / KIAA1985; Rab11; recycling endosome; Schwann cell myelination; Charcot–Marie–Tooth neuropathy

Abbreviations: CMT4C = Charcot–Marie–Tooth neuropathy type 4C; DAPI = diamidino-2-phenylindole dihydrochloride; DMEM = Dulbecco's modified Eagle's medium; GFP = green fluorescent protein; GST = glutathione S-transferase; PBS = phosphate buffered saline; PNS = peripheral nervous system; SDS–PAGE = sodium dodecyl sulphate–polyacrylamide gel electrophoresis; SH3TC2 = Src homology 3 domain and tetratricopeptide repeats 2

Received January 25, 2010. Revised May 8, 2010. Accepted May 14, 2010

© The Author (2010). Published by Oxford University Press on behalf of the Guarantors of Brain. All rights reserved.

For Permissions, please email: journals.permissions@oxfordjournals.org

Introduction

Myelin is a specialized membranous sheath, made up of ~70% lipids and 30% proteins. It is produced by two types of glia cells, oligodendrocytes in the central nervous system (CNS) and Schwann cells in the peripheral nervous system (PNS). Myelin surrounds nerve axons, allowing saltatory nerve conduction and ensuring maintenance of the axon at a long distance from the cell body (Griffiths *et al.*, 1998; Lappe-Siefke *et al.*, 2003; Nave and Trapp, 2008). The importance of myelin formation is illustrated by the severe neurological deficits seen in inherited and non-genetic demyelinating diseases of the CNS (e.g. multiple sclerosis and leukoencephalopathies) and the PNS (e.g. autoimmune neuritis and hereditary neuropathies).

One condition associated with impaired myelination of the PNS is Charcot–Marie–Tooth disease type 4C (CMT4C) (LeGuem *et al.*, 1996). CMT4C is an autosomal recessive form of hereditary motor and sensory neuropathies (Dyck *et al.*, 1993) clinically presenting as distal muscle weakness and wasting, distal sensory deficits and prominent scoliosis (Kessali *et al.*, 1997; Azzedine *et al.*, 2006). Pathologically, CMT4C is characterized by layers of empty basal lamina encircling demyelinated and remyelinated axons, abnormal Schwann cell protrusions (Gabreels-Festen *et al.*, 1999) and disorganization of the node of Ranvier (Arnaud *et al.*, 2009).

We have previously shown that CMT4C is caused by mutations in the *SH3TC2* (*Src* homology 3 domain and tetratricopeptide repeats 2)/*KIAA1985* gene on chromosome 5q32 (Senderek *et al.*, 2003). CMT4C is associated with both nonsense and missense mutations throughout the gene, and a strict genotype–phenotype correlation has not been established because of interfamilial and intrafamilial variability of clinical expression as well as marked allelic heterogeneity (Senderek *et al.*, 2003; Azzedine *et al.*, 2006; Colomer *et al.*, 2006; Gosselin *et al.*, 2008). *SH3TC2* encodes SH3TC2/KIAA1985, a novel protein of unknown function containing several motifs potentially involved in protein–protein interactions. However, no protein binding to SH3TC2 has been identified so far. Very recently, we found that a mouse model without a functional copy of the *Sh3tc2* gene developed a peripheral neuropathy that largely reproduced the human phenotype (Arnaud *et al.*, 2009). Consistent with the tissue and the cell population involved in a demyelinating peripheral neuropathy, *Sh3tc2* is exclusively expressed in Schwann cells in peripheral nerves. SH3TC2 is tethered to cellular membranes through an N-terminal myristic acid anchor and localizes to the plasma membrane and a perinuclear membranous structure (Arnaud *et al.*, 2009; Lupo *et al.*, 2009) that corresponds to the endocytic recycling compartment (Arnaud *et al.*, 2009). However, as the physiological function of the gene product, SH3TC2, has not yet been identified, the pathomechanism causing impaired PNS myelination in CMT4C patients and *Sh3tc2* knockout mice has so far remained unclear.

Here, we show that SH3TC2 is a novel effector of the small GTPase Rab11, a key regulator of recycling endosome functions. Neuropathy-causing missense mutations in *SH3TC2* disrupt this interaction. These data, together with the demonstration of the role of Rab11 in myelination, support the importance of the SH3TC2/Rab11 interaction for normal myelination.

Materials and methods

Animals

All experiments with animals followed protocols approved by the veterinary office of the Canton of Zurich, Switzerland. The generation of *Sh3tc2* knockout mice has been described previously (Arnaud *et al.*, 2009). Genotypes were determined by polymerase chain reaction on genomic DNA derived from tail biopsies as reported earlier (Arnaud *et al.*, 2009).

Plasmids

The generation of plasmids is outlined in the Supplementary material.

Cell culture and transfections

COS7, HEK293, HEK293T and RT4-D6P2T cells were cultured in Dulbecco's modified Eagle's medium (DMEM; Invitrogen) supplemented with 10% foetal calf serum (Invitrogen) and 2 mM glutamine (Invitrogen). Culture medium for Flp-In T-Rex 293 cells (Invitrogen) additionally contained 100 µg/ml Zeocin™ (Invitrogen) and 15 µg/ml blasticidine (Invitrogen). All transfections in this study were performed using Lipofectamine 2000 (Invitrogen) according to the manufacturer's instructions.

Flp-In T-Rex 293 cells that stably express inducible SH3TC2 fused to a C-terminal tandem affinity purification (TAP) tag (SH3TC2-C-TAP) or the TAP tag alone (C-TAP) were generated according to the manufacturer's instructions (Invitrogen). Hygromycin B (Invitrogen) at a concentration of 10 µg/ml was used for selection of stable cell clones. Cells were cultured with 15 µg/ml blasticidine and 10 µg/ml hygromycin B. In order to induce expression of SH3TC2-C-TAP or C-TAP, doxycycline (Sigma) was administered to the cells at a final concentration of 1 µg/ml for 20–24 h.

Generation of lentiviral stocks

For production of high-titre lentiviruses, HEK293T cells were transiently cotransfected with the pSicoR vector harbouring the complementary DNA of choice and the packaging constructs pMD2.G and psPAX2 (Addgene). Cell culture supernatant was collected after 48 and 72 h. The filtered supernatant was first centrifuged in an SW28 rotor (Beckmann Coulter) for 2 h at 21 000 r.p.m. at 11°C. Afterwards, the pellet was resuspended in DMEM/10% foetal calf serum and centrifuged again for 1 h at 16 000 r.p.m. at 4°C in a T60i rotor (Beckmann Coulter). The pellet was resuspended in 40 µl phosphate buffered saline (PBS), aliquoted and stored at –80°C.

Antibodies

Antibodies used in this study are described in the Supplementary material.

Tandem affinity purification

Flp-In T-Rex 293 cells stably expressing SH3TC2-C-TAP in a doxycycline-inducible fashion and a control cell line expressing the C-TAP tag alone (C-TAP) were used for purification of an SH3TC2 protein complex. The detailed protocol for tandem affinity purification has been described previously (Kleine *et al.*, 2008).

Western blotting

Cultured cells were harvested, washed twice with PBS and lysed in lysis buffer (10 mM Tris-HCl, 5 mM EDTA, 150 mM NaCl, 1% Triton X-100) containing protease and phosphatase inhibitors (Sigma). Mouse and rat sciatic nerves were homogenized with a mortar and pestle in lysis buffer. Post-nuclear supernatants were boiled in sodium dodecyl sulphate (SDS) sample buffer (80 mM Tris pH 6.8, 10% glycerol, 2% sodium dodecyl sulphate, 0.002% bromophenol blue), resolved by sodium dodecyl sulphate polyacrylamide gel electrophoresis (SDS-PAGE) and electroblotted onto polyvinylidene fluoride membranes (Hybond-C; Amersham). Immunoblots were developed by incubation with appropriate antibodies followed by horse radish peroxidase- or alkaline phosphatase-chemiluminescence detection. Densitometry and quantification of protein levels were performed with Quantity One software (BioRad).

Coimmunoprecipitation

Transiently transfected HEK293 cells were harvested 24 h after transfection and the post-nuclear supernatant was pre-cleared with 30 μ l of Protein G-Sepharose (GE Healthcare) at 4°C for 2 h. The supernatant was incubated with 30 μ l of Protein G-Sepharose including 8 μ g/ml of mouse anti-Myc, mouse anti-green fluorescent protein (GFP) or mouse anti-FLAG antibodies or mouse IgG. Immunoprecipitation was carried out at 4°C on a rotating wheel for 16 h. The precipitates were washed six times with cold lysis buffer and boiled in SDS sample buffer to elute protein complexes. The supernatants were processed using standard SDS-PAGE and western blotting procedures.

Glutathione S-transferase pulldown assays

In vitro translation of SH3TC2/Sh3tc2 and the generation of glutathione S-transferase (GST) or GST-Rab11 fusion proteins is described in the Supplementary material. *In vitro* translated SH3TC2/Sh3tc2 proteins (10 μ l of standard reactions) were incubated for 1 h at 4°C with 50 μ l glutathione-Sepharose beads coupled with GST or GST-Rab11 fusion proteins. The beads were washed four times with TNN (50 mM Tris pH 7.5, 250 mM NaCl, 5 mM EDTA, 0.5% Nonidet-P40, 1 mM DTT) buffer before eluting proteins by boiling the beads in SDS sample buffer. Samples were resolved by SDS-PAGE followed by Coomassie Brilliant Blue staining and autoradiography.

Yeast two-hybrid assay

Protein interactions were assayed in yeast using a two-hybrid approach according to the manufacturer's protocol (Dualsystems Biotech). pLexA-SH3TC2 or pLexA-Lamin C were transformed into the NMY32 reporter strain together with pACT2-Rab11a using the lithium acetate method. Cells were plated on plates lacking tryptophane and leucine (TRP⁻, LEU⁻) to select for transformants. After 3 days of growth, five medium-size colonies for each condition were replated on selection plates lacking tryptophane, leucine and histidine (TRP⁻, LEU⁻, HIS⁻). After 3 days protein interactions were determined by growth of colonies. The results given are representative of at least three trials.

Immunofluorescence microscopy

Cells were fixed with 4% paraformaldehyde in PBS for 10 min at room temperature, washed in PBS and permeabilized with 0.1% Triton X-100 (Sigma). Fixed cells were blocked for 30 min with 10% goat serum in PBS containing 0.1% Triton X-100 before incubation in primary antibodies in blocking medium overnight at 4°C. Cells were washed in PBS and incubated with fluorescent secondary antibodies in blocking solution for 1 h at room temperature. After washing, cells were incubated with 4',6'-diamidino-2-phenylindole dihydrochloride (DAPI) (Sigma) to visualize nuclei, washed again and mounted in Immu-Mount (Thermo Scientific). For Rab11, p230 and GM130 stainings, 0.05% saponin (Sigma) was used as detergent instead of Triton X-100. Images were acquired using either an AxioVert Observer D1 fluorescence microscope (Carl Zeiss) or a TCS SP1 laser scanning confocal microscope (Leica). Images were further processed using Photoshop software (Adobe).

Subcellular fractionation

Cells were harvested, washed twice in PBS and lysed in homogenization medium (0.25 M sucrose, 1 mM EDTA, 10 mM Hepes-NaOH, pH 7.4) including protease and phosphatase inhibitors. Iodixanol gradient solutions of 5, 10, 15, 20 and 25% were prepared from a 50% Optiprep (Gibco) solution. Solutions were layered in 950 μ l fractions with 250 μ l post-nuclear supernatant on the top in Ultra-Clear centrifuge tubes (Beckmann Coulter) and centrifuged in an SW55 rotor (Beckmann Coulter) at 35 000 rpm for 20 h at 4°C. After centrifugation, fractions were collected from the bottom by tube puncture and proteins were precipitated with trichloroacetic acid. Equal volumes of each fraction were analysed by SDS-PAGE and immunoblotting.

Rab11a transcript quantification

Analysis of *Rab11a* mRNA expression is described in the Supplementary material.

Transferrin receptor recycling assay

HEK293 cells were transfected with SH3TC2-GFP wild-type or SH3TC2-GFP harbouring CMT4C missense mutations. Cells transfected with GFP alone or GFP transfected cells additionally treated with 10 μ M monensin [an inhibitor of transferrin receptor recycling (Stein *et al.*, 1984)] were used as controls. Twenty-four hours after transfection, cells were starved for 4 h at 37°C in serum-free DMEM with 0.1% bovine serum albumin and subsequently incubated for 30 min in serum-free DMEM/0.1% bovine serum albumin containing 8.4 mg/ml transferrin-Alexa Fluor 647 (Invitrogen). Cells were washed with ice-cold PBS and chased in serum-free DMEM/0.1% bovine serum albumin containing 1 mg/ml unlabelled holo-transferrin (Sigma) at 37°C for different lengths of time. Cells were washed, acid-stripped (0.2 M Na₂HPO₄, 0.1 M citric acid) and trypsinized. Cells were fixed in paraformaldehyde for 20 min, pelleted and resuspended in PBS containing 2% foetal calf serum, 20 mM EDTA and 0.02% NaN₃. The fluorescence intensity of cell bound transferrin was measured for 2000 GFP positive cells and the average intensities of the cell populations were calculated. Data acquisition was done on a FACSCalibur flow cytometer using CellQuest software (BD Biosciences). The experiment was repeated three times.

Surface reconstruction of recycling endosomes

COS7 cells were transfected with wild-type SH3TC2-FLAG, SH3TC2_N881S-FLAG or GFP. Cells were fixed with paraformaldehyde 24 h after transfection and stained with rabbit polyclonal anti-Rab11a and mouse monoclonal anti-FLAG antibodies, followed by fluorescently labelled secondary antibodies. Z-stacks in 0.122 μm intervals were taken for 100 transfected cells per condition (identified by FLAG staining or GFP fluorescence) with equal settings for zoom factor, laser intensity and pinhole. To estimate the surface of recycling endosomes, Rab11a positive surface areas were quantified with Imaris software (Bitplane) and corrected for cell size. The surface module of Imaris software was used for 3D reconstructions of recycling endosomes.

In vitro myelination

Preparation of dorsal root ganglia for dorsal root ganglion explant cultures, culture conditions and assessment of myelination are described in the Supplementary material.

Preparation and culture conditions of rat Schwann cells and dorsal root ganglion neurons for Schwann cell-dorsal root ganglion neuron co-cultures are described in the Supplementary material. Four days prior to adding Schwann cells to dorsal root ganglion neurons, Schwann cells were transduced by overnight incubation with the lentivirus of interest. Infected Schwann cells (200 000 per coverslip) were added and co-cultures were kept in C-medium (MEM; Invitrogen), supplemented with 10% foetal calf serum, 4 g/l D-glucose, 2 mM L-glutamine (Invitrogen), 50 ng/ml neural growth factor (Harlan) and 1% penicillin/streptomycin for 3 days. Myelination was induced over 10 consecutive days with C-medium supplemented with 50 $\mu\text{g}/\text{ml}$ ascorbic acid (Sigma). Subsequently cultures were fixed for 20 min in 4% paraformaldehyde and for additional 15 min in ice-cold methanol at -20°C and blocked for 20 min with PBS containing 5% bovine serum albumin, 0.1% goat serum and 0.2% Triton X-100. Coverslips were incubated overnight at 4°C with primary antibodies in blocking solution. After additional washing steps in PBS, cultures were incubated with fluorescent secondary antibodies for 1 h at room temperature. Coverslips were washed again, incubated with DAPI and mounted with Immu-Mount. Myelinated segments were stained with a rat monoclonal anti-myelin basic protein antibody, followed by a Cy3-conjugated goat anti-rat IgG antibody. Neurons were detected with a mouse monoclonal anti-neurofilament antibody and a goat anti-mouse IgG antibody conjugated to Cy5. Transduction efficiency was monitored by GFP fluorescence. Myelination was evaluated as follows: ten fields per coverslip were randomly acquired (magnification 10 \times) and mean Cy3 fluorescence as an estimate of the number of myelin basic protein positive segments was calculated using ImageJ software (National Institutes of Health). Experiments were done in triplicate, at least three coverslips per condition were analysed for each experiment.

Statistical analysis

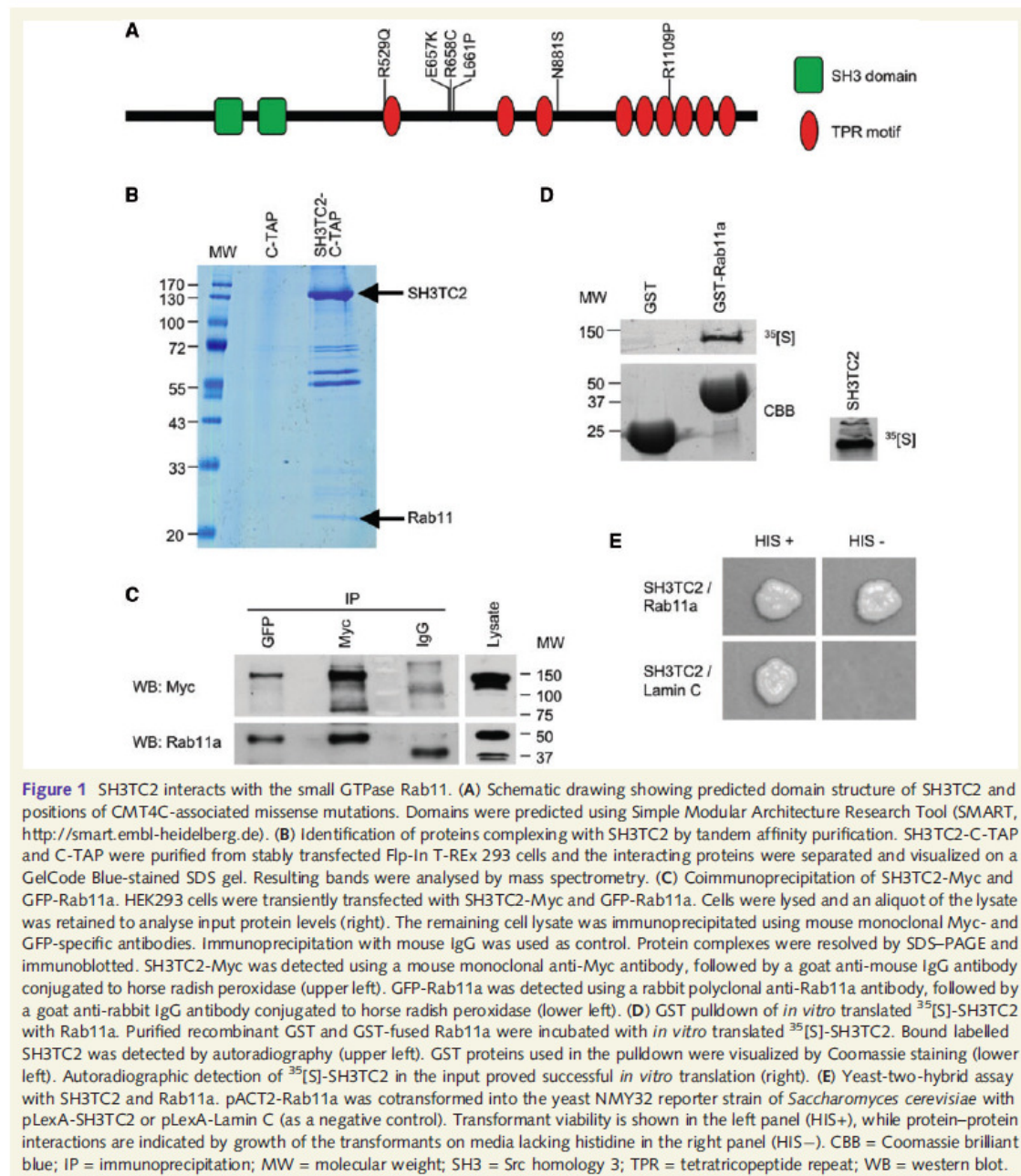
The data show the mean \pm SEM. Statistical significance was determined using a two-tailed Student's *t*-test. Significance was set at **P* < 0.05, ***P* < 0.01 or ****P* < 0.001.

Results

Based on the observation that SH3TC2 contains several protein motifs (Src homology 3 domain domains and tetratricopeptide repeat repeats, Fig. 1A) known to mediate the formation of protein complexes (Senderek *et al.*, 2003), we hypothesized that we might be able to deduce the function of SH3TC2 from already known functions of interacting proteins. As no proteins interacting with SH3TC2 were known and as the putative protein binding motifs in SH3TC2 did not allow prediction of a *bona fide* interaction partner, we decided to perform an unbiased screen for interacting proteins. We purified an SH3TC2 protein complex by means of tandem affinity purification from HEK293 cells, analysed the complex on an SDS gel and subjected the resulting protein bands to mass spectrometry. Among other proteins, we identified the small GTPase Rab11 as a protein potentially interacting with SH3TC2 (Fig. 1B and Supplementary Fig. 1A). Rab11 is a key regulator of recycling pathways from endosomes to the plasma membrane (Ullrich *et al.*, 1996) and consists of two isoforms, Rab11a and Rab11b, which are encoded by different genes and mainly differ in their C-termini. Rab11a and Rab11b are differentially expressed (Sakurada *et al.*, 1991; Lai *et al.*, 1994) and may also be functionally different to some extent (Lapierre *et al.*, 2003).

In order to confirm the results of the interaction screen, we expressed SH3TC2-Myc and GFP-Rab11a fusion proteins in HEK293 cells and performed coimmunoprecipitation in both directions. In addition to the co-precipitation of Rab11a along with SH3TC2, immunoprecipitation in the other direction showed that SH3TC2 could be coprecipitated with GFP-Rab11a as well (Fig. 1C). Results from GST pulldown and yeast two-hybrid experiments provided further evidence for the interaction between SH3TC2 and both Rab11 isoforms and showed that SH3TC2 binds directly to Rab11 (Fig. 1D and E; Supplementary Fig. 1B). However, we were not able to identify the particular protein region of SH3TC2 that mediates the interaction with Rab11 (Supplementary Fig. 2).

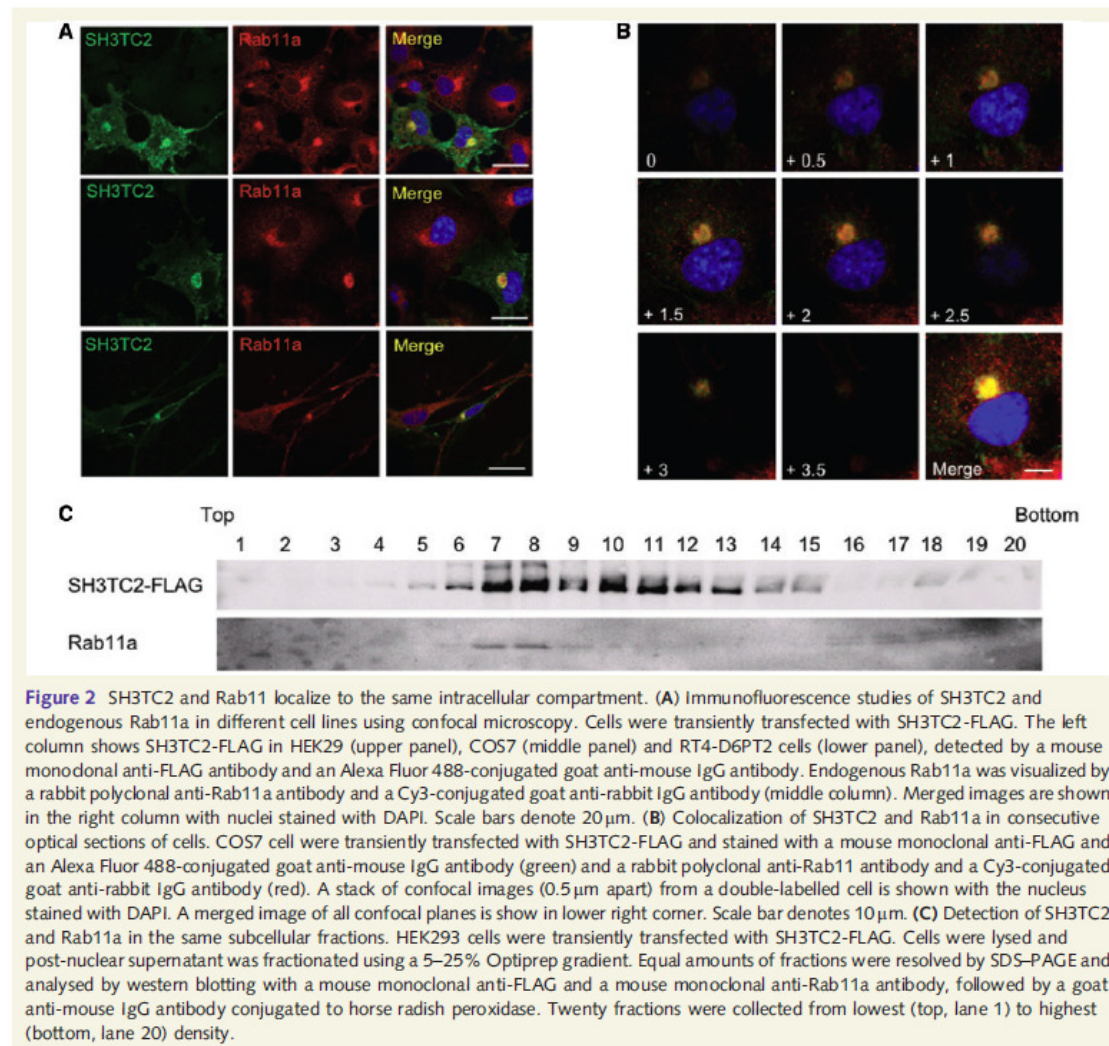
We have recently shown that both overexpressed proteins, SH3TC2 and Rab11a, colocalize with γ -tubulin and internalized transferrin in the perinuclear recycling endosome (Amaud *et al.*, 2009). We now expand our earlier findings by studying the distribution of SH3TC2-FLAG and endogenous Rab11a in epithelial cell lines (HEK293 and COS7) and a Schwann cell line (RT4-D6P2T). Since there was no antibody available against endogenous Sh3tc2, RT4-D6P2T cells that express Sh3tc2 on the transcript level (data not shown) had to be transfected with the FLAG-construct as well. The localization of both proteins overlapped in the perinuclear region in all three cell lines (Fig. 2A). Moreover, strong colocalization was confirmed in consecutive optical sections along the microscope z-axis (Fig. 2B). Conversely, we observed no colocalization of SH3TC2 with marker proteins for other perinuclear organelles (Supplementary Fig. 3). In order to provide independent biochemical support for fluorescent microscopic findings, we subjected cultured cells overexpressing SH3TC2 to subcellular fractionation using Optiprep gradient centrifugation. Fractions were analysed for the presence of SH3TC2



by immunoblotting and the profile was compared with the distribution of Rab11a. The bands for Rab11a were shown to overlap with the signal for SH3TC2 (Fig. 2C).

As there is increasing evidence that the development and maintenance of Schwann cells and the myelin sheath require endosomal sorting (Trapp et al., 2004; Simons and Trotter, 2007),

we decided to follow the SH3TC2/Rab11 interaction further. As there were no published data on Rab11 expression in the PNS, we studied Rab11a protein levels in Schwann cell lines, primary rat Schwann cell cultures and sciatic nerves of rat and mouse by western blotting (Fig. 3A). We found that Rab11a was prominently expressed in cultured Schwann cells and in the PNS of

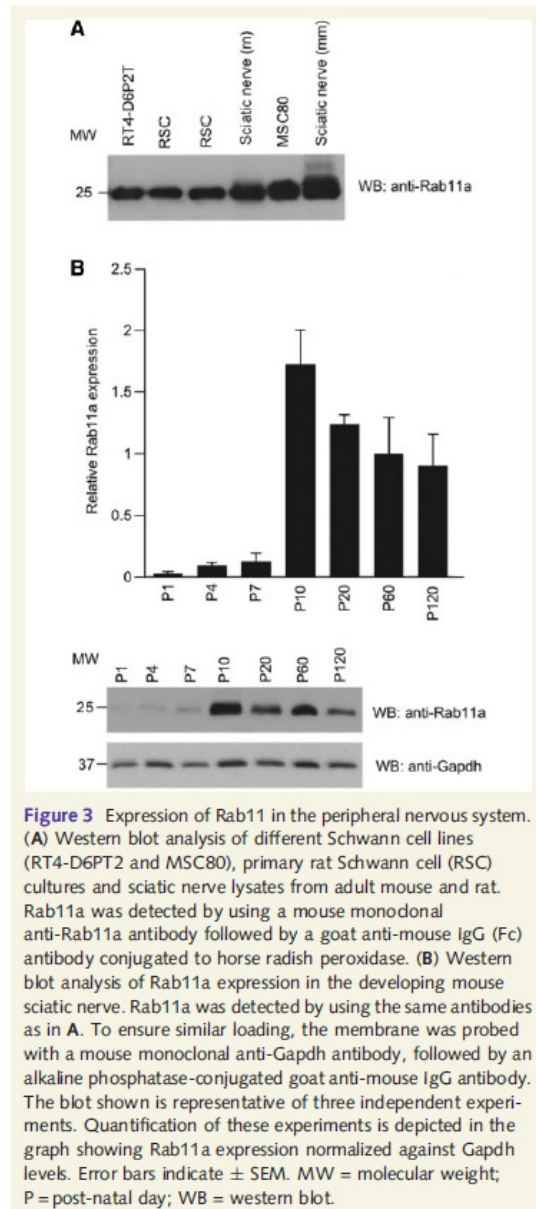


adult animals. Moreover, during the early stages of post-natal PNS development, Rab11a expression was strongly upregulated around post-natal day 10 (Fig. 3B), similar to the developmental expression profile of other proteins involved in myelination (Verheijen *et al.*, 2003).

In order to explore whether binding of SH3TC2 to Rab11 is specific or whether SH3TC2 might promiscuously associate with different Rab GTPases, we performed GST pull-down assays with several proteins of the Rab family. No association was observed with Rab4a and Rab5a (associated with early endosomes) and Rab7a (associated with late endosomes) (Supplementary Fig. 4A). Having shown that wild-type SH3TC2 associates with Rab11 specifically we attempted to clarify whether the SH3TC2/Rab11 interaction is relevant for the pathogenesis of CMT4C. One obvious strategy to approach this intriguing question was to test

CMT4C-causing SH3TC2 mutants (Fig. 1A) for their ability to associate with Rab11. We found that all tested amino acid substitutions related to missense mutations observed in patients with CMT4C disrupted the SH3TC2/Rab11a interaction (Fig. 4A). On the other hand, rat and mouse Sh3tc2 proteins bind to human Rab11a (Fig. 4B), although ~20% of amino acid residues are not conserved between the human and the rodent proteins (Fig. 4C, a multiple sequence alignment of human, mouse and rat SH3TC3/Sh3tc2 is shown in the Supplementary material). These findings establish that the disruption of the SH3TC2/Rab11 complex is a specific effect of CMT4C-causing missense mutations.

Next, we asked whether the SH3TC2/Rab11 interaction is dependent on the activation state of Rab11. Like all GTPases, Rab proteins cycle between an inactive (guanosine diphosphate-bound) and an active (GTP-bound) conformation. Interconversion



and accessibility of these two forms are temporally and spatially controlled by specific regulators (Stenmark, 2009). The GTP-bound, activated form of the GTPase associates with effector molecules through which it carries out its functions. We found that SH3TC2 interacts with the constitutive active GTP-bound Rab11_Q70L mutants, while there is no binding to the dominant negative guanosine diphosphate-bound Rab11_S25N mutants or to Rab11a_Q70L_I44E, a constitutively active mutant which has a second mutation in its effector domain abrogating effector binding

(Wallace et al., 2002) (Fig. 5A and Supplementary Fig. 4B). Thus, the SH3TC2/Rab11 interaction is consistent with SH3TC2 functioning as a Rab11 effector.

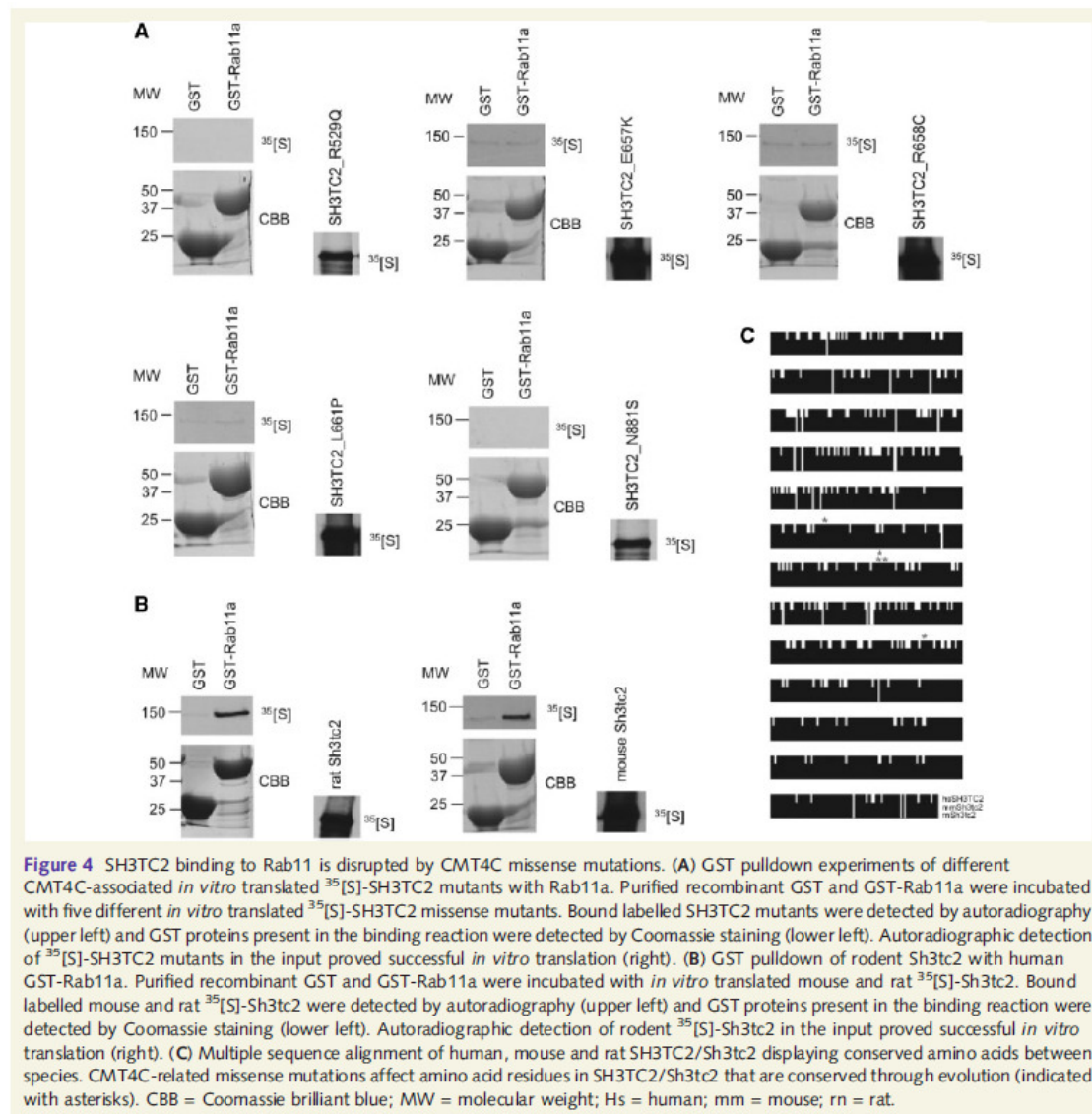
Rab11 effectors have been shown to influence various functions of the recycling endosome, e.g. recycling of the transferrin receptor from endosomes back to the cell surface (Maxfield and McGraw, 2004). Assays for transferrin receptor recycling are commonly used as a paradigm to test recycling endosome functions (Sager et al., 1984). Such assays allow a quantitative assessment of the recycling rate of transferring receptor by measuring the amount of intact ligand that is retained in the cell (or has returned to the plasma membrane) upon time. Overexpression of wild-type SH3TC2 resulted in moderate slowing of transferrin recycling as compared with transferrin retention in cells transfected with CMT4C mutants or a GFP control vector (Fig. 5B and Supplementary Table 1). This suggests that wild-type SH3TC2 affects the rate of recycling along the receptor-mediated endocytosis pathway and this activity is largely absent in cells expressing SH3TC2 mutant proteins.

There is at least one known Rab11 effector, Rab11-FIP4, which causes a dramatic condensation of the recycling endosome (Wallace et al., 2002). Similarly, when SH3TC2 is expressed in transfected cells, not only does the endogenous Rab11a signal appear stronger, but the Rab11a-positive compartment appears to be more condensed in a perinuclear location (Fig. 2A and B). We quantified this effect by calculating the surface of Rab11a-positive endosomes in cells expressing wild-type SH3TC2 and the CMT4C-associated N881S mutant. The data we obtained confirmed that wild-type SH3TC2 condenses the perinuclear recycling compartment in a considerable proportion of transfected cells, while the N881S mutant had only a slight effect on recycling endosome morphology (Fig. 5C). This is in line with findings in teased fibres prepared from sciatic nerves of adult mice. The perinuclear Rab11 positive compartments are moderately less compact in Schwann cells lacking *Sh3tc2* than in the wild-type situation (Fig. 5D).

Since a number of Rab11 effectors, including Rab11-FIP2 and Rab11-FIP4, have been shown to be capable of homodimerization (Lindsay and McCaffrey, 2002; Wallace et al., 2002), we were interested to determine if SH3TC2 displays similar properties. Using coimmunoprecipitation of full-length SH3TC2, we were able to demonstrate that SH3TC2 can self-interact (Supplementary Fig. 4C).

We finally compared the Rab11 expression levels in sciatic nerves of *Sh3tc2* knockout mice and wild-type littermates, as it has been shown that Rab effectors can stabilize Rab-GTPases (Ganley et al., 2004). Indeed, we found that Rab11a protein levels were reduced in sciatic nerves of *Sh3tc2* knockout mice (Fig. 5E). Conversely, levels of *Rab11a* mRNA were unchanged in *Sh3tc2*-deficient mice, suggesting that Rab11a expression is differently regulated at the protein level in knockout and wild-type animals.

Our results presented so far open the intriguing possibility that a new Rab11 effector, SH3TC2, regulates Schwann cell myelination. In order to explore a potential effect of Rab11 and endosomal recycling on the formation of myelin sheaths in the PNS directly,



we made use of two different established *in vitro* myelination systems.

Dorsal root ganglia were isolated from embryonic day 13.5 mice and infected with a lentivirus encoding dominant negative (S25N) or constitutively active (Q70L) forms of a Rab11a-GFP fusion protein or GFP alone. After 8 days in culture, myelination was induced by adding ascorbic acid to the medium. After 12 subsequent days of culturing, myelinated segments were visualized by myelin basic protein staining. Infection of dorsal root ganglia explants with a lentivirus encoding the dominant negative mutant of Rab11a impaired myelination compared with the control infected with a virus for GFP alone. On the other hand,

infection with a lentivirus containing constitutively active Rab11a resulted in an increased number of myelinated segments (Supplementary Fig. 5A and B).

However, as lentiviral infection of dorsal root ganglia explants targets both Schwann cells and neurons, our data left open the question whether overexpression of Rab11 mutants in Schwann cells or neurons, or in both populations, was responsible for altered myelination. In order to dissect Rab11 effects in Schwann cells and neurons, we used primary rat Schwann cell-dorsal root ganglion neuron co-cultures. Primary rat Schwann cells were infected with Rab11a variants or GFP control lentivirus and were added to cultured mouse dorsal root ganglia. Following

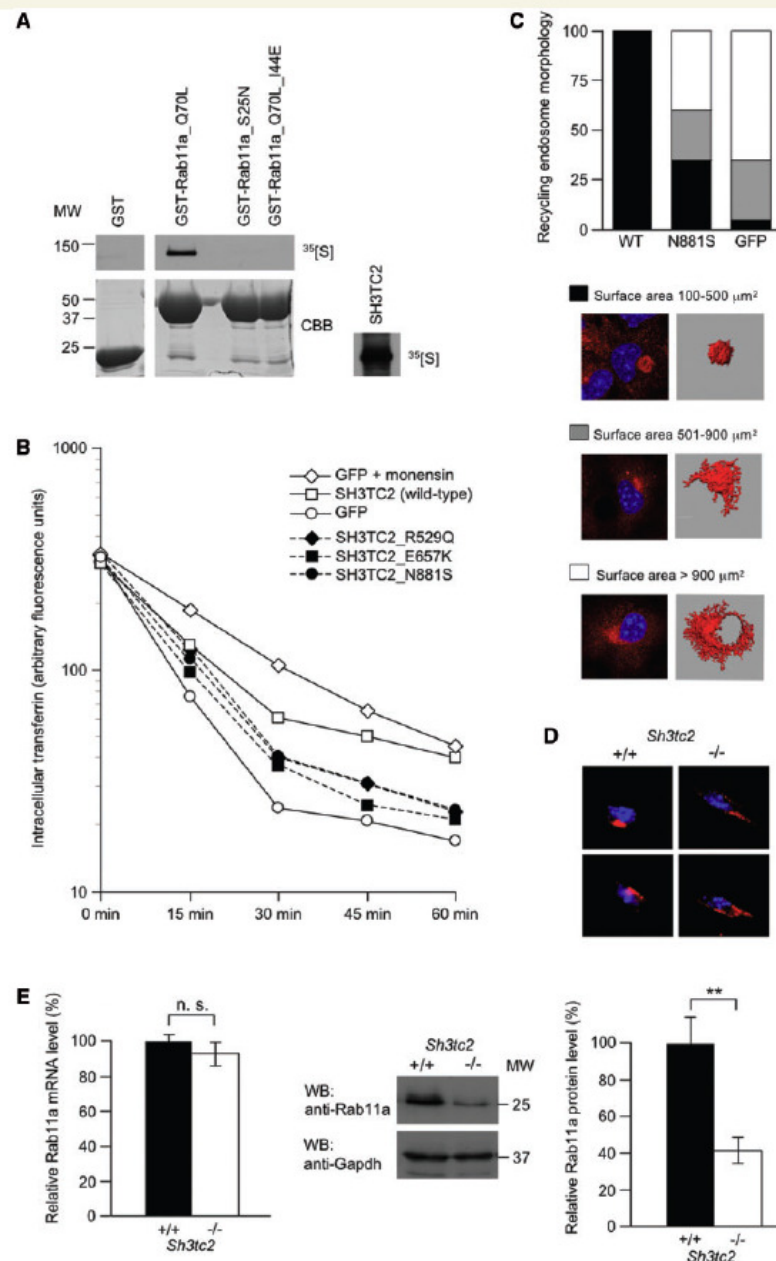


Figure 5 SH3TC2 is a potential new Rab11 effector. (A) GST pull-down of *in vitro* translated ³⁵[S]-SH3TC2 using Rab11a mutants interfering with nucleotide loading of the GTPase. GST and GST-Rab11a mutants [constitutively active, GTP bound (Q70L) and dominant negative, guanosine diphosphate bound (S25N)] were expressed as recombinant proteins and incubated with full length *in vitro* translated ³⁵[S]-SH3TC2. Binding of labelled SH3TC2 was detected by autoradiography (upper left). GST proteins present in the binding reaction were detected by Coomassie staining (lower left). Autoradiographic detection of labelled SH3TC2 in the input proved successful *in vitro* translation (right). (B) Kinetic analysis of transferrin recycling measured by fluorescent activated cell sorting. HEK293 cells were transfected with SH3TC2-GFP wild-type or SH3TC2-GFP harbouring CMT4C missense mutations. Cells transfected with GFP alone or GFP transfected cells additionally treated with 10 μM monensin [a potent inhibitor of transferrin receptor recycling (Stein *et al.*, 1984)] were used as

Continued

induction of myelination by adding ascorbic acid, the amount of myelin production was assessed by myelin basic protein staining. Similar to dorsal root ganglion explant cultures, expression of the dominant negative mutant of Rab11a strongly impaired myelination, while expression of the constitutively active Rab11a resulted in moderately increased myelination (Fig. 6A and B). Altogether our data suggest that Rab11 controls Schwann cell myelination, most likely through regulation of SH3TC2 activity.

Discussion

We have previously shown that mutations in the *SH3TC2/Sh3tc2* gene cause demyelinating hereditary neuropathy in humans and mice (Senderek *et al.*, 2003; Arnaud *et al.*, 2009). The work presented here takes our understanding of the role of SH3TC2 in peripheral nerve demyelination to a new level: SH3TC2 acts as an effector of Rab11, a master regulator of recycling endosome functions (Maxfield and McGraw, 2004). In addition, we have shown that Rab11 itself is involved in the regulation of Schwann cell myelination *in vitro*, supporting the pathophysiological relevance of the observed SH3TC2/Rab11 interaction for peripheral nerves. Obviously, there is still the possibility that SH3TC2 can also influence myelination in a Rab11 independent manner. Potential candidates could be other proteins found in the SH3TC2 complex (Fig. 1A), whose role in the PNS and in Schwann cells has not yet been investigated.

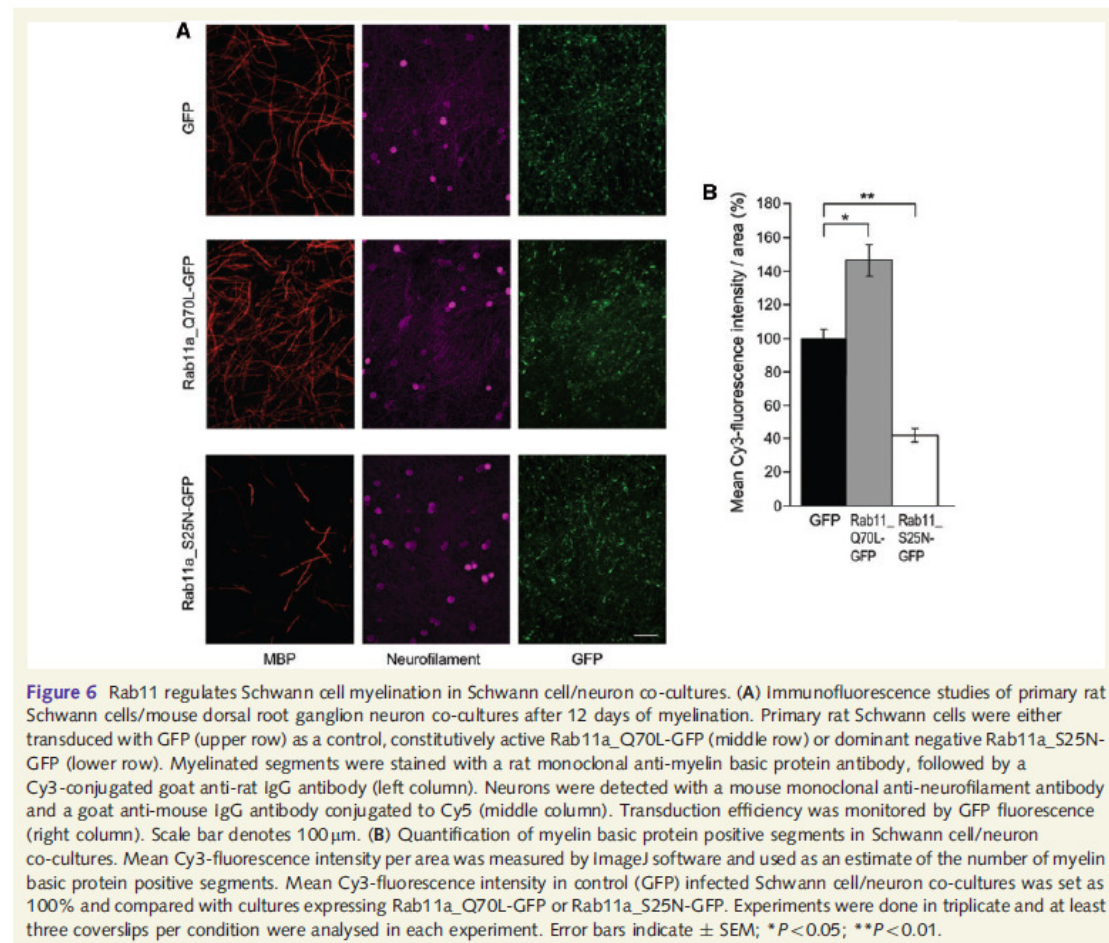
Our findings directly lead to the question of how endosomal recycling might be involved in myelin sheath formation. Myelination requires dramatic changes in the cellular architecture of differentiating glia and a high degree of cell polarization that partitions the plasma membrane into distinct domains (Pfeiffer *et al.*, 1993). Myelinating Schwann cells have at least five distinct membrane domains (Arroyo and Scherer, 2000; Simons and

Trotter, 2007) that differ in their membrane lipid and protein composition. The outer (abaxonal) Schwann cell plasma membrane is specialized for extracellular interactions, while the inner (adaxonal) Schwann cell plasma membrane contains cell adhesion molecules (Previtali *et al.*, 2001; Maurel *et al.*, 2007; Spiegel *et al.*, 2007). Compact myelin in the PNS is largely composed of lipids (mainly cholesterol and sphingolipids) and exhibits narrow lamellar spacings, mediated by homophilic adhesion molecules (Filbin *et al.*, 1990). Membranes of the paranodal loops are enriched for junctional proteins that permit intra-Schwann cell junctions and Schwann cell-axon junctions (Fannon *et al.*, 1995; Boyle *et al.*, 2001). Finally, the membranes of Schwann cell microvilli contain ligands for axonal cell adhesion molecules and contribute to sodium channel clustering at the nodes of Ranvier (Eshed *et al.*, 2005).

One crucial mechanism underlying establishment and maintenance of cellular polarity is differential sorting of proteins to distinct plasma membrane domains along the secretory and endosomal pathways (Keller *et al.*, 2001; Kreitzer *et al.*, 2003). Several lines of evidence indicate that protein transport and targeting play an important role in myelin membrane assembly. During myelination, Schwann cells establish specialized microtubule networks, suggesting increased rates of vesicle transport (Trapp *et al.*, 1995; Kidd *et al.*, 1996). Sorting in the trans-Golgi network partitions myelin proteins into separate transport vesicles (Trapp *et al.*, 1995) that are targeted to distinct Schwann cell compartments. Similarly, in polarized epithelial cells, transfected Schwann cell proteins are distinctly transported, potentially reflecting the segregation of compact and non-compact myelin components (Minuk and Braun, 1996; Kroepfl and Gardinier, 2001; Maier *et al.*, 2006). Finally, myelin proteins undergo endocytic recycling in oligodendrocytes (Winterstein *et al.*, 2008), which are the myelinating glia cells in the CNS. However, molecular pathways regulating vesicular transport during myelination have remained largely unknown.

Figure 5 Continued

controls. The cells were incubated for 30 min with fluorescently labelled transferrin and then chased with an excess of unlabelled transferrin for the indicated lengths of time. The y-axis represents the intensities of the fluorescent signals in a log scale. Graphs represent the mean of three experiments. Values of data points \pm SEM and significance levels are shown in Supplementary Table 1. (C) Effect of SH3TC2 on recycling endosome morphology. COS7 cells were transiently transfected with wild-type SH3TC2-FLAG, SH3TC2_N881S-FLAG or GFP. Endogenous Rab11a was labelled with a rabbit polyclonal anti-Rab11a antibody and a Cy3-conjugated goat anti-rabbit IgG antibody. Transfected cells were identified by GFP fluorescence or staining with a mouse monoclonal anti-FLAG and an Alexa Fluor 488-conjugated goat anti-mouse IgG antibody (not shown). One hundred cells were analysed per condition. Using stacks of confocal images (0.122 μ m intervals) the Rab11a-positive surface was calculated and corrected for cell size to estimate the surface of the recycling endosome. Immunofluorescence pictures and 3D reconstructions show representative examples of each category of surface area. (D) Rab11a distribution in Schwann cells of *Sh3tc2* wild-type and knockout littermates. Teased nerve fibres were prepared from sciatic nerves of adult mice (at post-natal day 56). Rab11a was detected with a rabbit polyclonal anti-Rab11a antibody followed by a goat anti-rabbit IgG antibody conjugated to Alexa Fluor 594. Nuclei were stained with DAPI. (E) *Rab11a* mRNA and Rab11a protein levels in sciatic nerves of *Sh3tc2* wild-type and knockout littermates. *Rab11a* mRNA levels were obtained from cRNA microarray data from post-natal day 5 sciatic nerves of *Sh3tc2* wild-type and knockout littermates (R. Chrast and E. Arnaud, unpublished data). The quantification graph shows *Rab11a* mRNA levels normalized against *Gapdh* expression. For western blot analysis of sciatic nerves of wild-type and *Sh3tc2* knockout mice at post-natal day 5, Rab11a was detected with a mouse monoclonal anti-Rab11a antibody followed by a goat anti-mouse IgG (Fc) antibody conjugated to horse radish peroxidase. To ensure similar loading, the membrane was probed with a mouse monoclonal anti-*Gapdh* antibody, followed by an alkaline phosphatase-conjugated goat anti-mouse IgG antibody. The blot shown is representative of three independent experiments. Quantification of these experiments is depicted in the graph showing Rab11a expression normalized against *Gapdh* levels. Error bars indicate \pm SEM. n.s. = not significant; ***P* < 0.01. CBB = Coomassie brilliant blue; MW = molecular weight; P = post-natal day; WB = western blot; WT = wild-type.



By demonstrating the SH3TC2/Rab11 interaction, we provide evidence for a distinct molecular mechanism, which probably involves the recycling of cargos that are critical for Schwann cell myelination. *Sh3tc2*-knockout mice may be instrumental for isolating such cargos by analysing the expression levels and transport routes of Schwann cell surface receptors that are known to undergo endocytic recycling and to be involved in the regulation of myelination.

While our immunoprecipitation, GST pull down and yeast-two-hybrid data clearly demonstrated the SH3TC2/Rab11 interaction, we were unable to define a shorter linear motif in the SH3TC2 protein which supports the interaction with Rab11 (Supplementary Fig. 2). Moreover, single amino acid substitutions disrupting the SH3TC2/Rab11 complex are spread throughout the protein. One potential explanation could be that mutations of certain residues result in misfolding of SH3TC2, ultimately leading to the loss of interacting or stabilizing regions. However, we did not observe degradation of SH3TC2 mutants when expressed in cells (data not shown). Therefore, a more likely explanation would be that

the mutated residues are all found on the surface of the protein, forming an extended Rab11-interacting domain. In line with this hypothesis, SH3TC2 does not contain a known Rab11-binding motif found in several other Rab11-interacting proteins (Prekeris *et al.*, 2001). Obviously, the presence of this motif is not a prerequisite to function as a Rab11 effector, as it does not occur in all Rab11-interactors (Wu *et al.*, 2005; Westlake *et al.*, 2007). An extended interaction domain consisting of several tetratricopeptide repeat repeats (which are contained in SH3TC2 as well) has been reported to enable p67phox to interact with Rac1, a small GTPase of the Rho family (Lapouge *et al.*, 2000).

In summary, the molecular dissection of the function of SH3TC2, a protein mutant in a comparatively rare genetic form of peripheral neuropathies, suggests a link between CNS demyelination and a key biological mechanism, endocytic recycling. The identification of Schwann cell and myelin proteins that undergo recycling endosome-dependent transport will extend and improve our understanding of the pathogenesis of peripheral neuropathies and will eventually provide us with a list of new candidate genes

and novel therapeutic targets. Assuming that endocytic recycling may assist morphogenesis of the myelin sheath by sorting and redirecting myelin components, it will be interesting to explore whether impaired endocytic recycling may be a common theme in demyelinating disorders of the PNS and maybe of the CNS as well.

During the preparation of our manuscript, another article reporting the SH3TC2/Rab11 interaction and a potential effect of SH3TC2 on recycling endosome function was published (Roberts *et al.*, 2010). While the data presented by Roberts *et al.* (2010) and by our group independently confirm that SH3TC2 is a new Rab11 effector molecule, we are going one step further and explore the role of Rab11 in Schwann cell myelination, demonstrating the relevance of the SH3TC2/Rab11 interaction for PNS pathology.

Acknowledgements

We thank Prof. M. McCaffrey (Department of Biochemistry, University College Cork, Ireland), Prof. L. A. Lapiere (Department of Surgery, Vanderbilt University Medical Center, Nashville, USA), Prof. B. Schlierf (Institut für Biochemie und Pathobiochemie, Friedrich-Alexander-Universität Erlangen-Nürnberg, Germany) and Prof. M. Zerial (Max Planck Institute for Molecular Cell Biology and Genetics, Dresden, Germany) for kindly providing us with Rab expression plasmids; and Prof. M. McCaffrey for her advice. J.S. is a Heisenberg fellow and C.S. a post-doctoral fellow of the Deutsche Forschungsgemeinschaft (DFG). A.R. received a PhD scholarship from RWTH Aachen University.

Funding

START program of RWTH Aachen University (to J.S.); the Interdisciplinary Centre for Clinical Research BIOMAT within the Faculty of Medicine; RWTH Aachen University (to J.S. and B.L.); the Swiss National Science Foundation (to R.C. and U.S.); the National Centre of Competence in Research; Neural Plasticity and Repair (to U.S.); Deutsche Forschungsgemeinschaft (to J.S. and B.L.).

Supplementary material

Supplementary material is available at *Brain* online.

References

- Arnaud E, Zenker J, de Preux Charles AS, Stendel C, Roos A, Médard JJ, et al. SH3TC2/KIAA1985 protein is required for proper myelination and the integrity of the node of Ranvier in the peripheral nervous system. *Proc Natl Acad Sci USA* 2009; 106: 17528–33.
- Arroyo EJ, Scherer SS. On the molecular architecture of myelinated fibers. *Histochem Cell Biol* 2000; 113: 1–18.
- Azzedine H, Ravisé N, Verry C, Gabreëls-Festen A, Lammens M, Grid D, et al. Spine deformities in Charcot-Marie-Tooth 4C caused by SH3TC2 gene mutations. *Neurology* 2006; 67: 602–6.
- Boyle ME, Berglund EO, Murai KK, Weber L, Peles E, Ranscht B. Contactin orchestrates assembly of the septate-like junctions at the paranode in myelinated peripheral nerve. *Neuron* 2001; 30: 385–97.
- Colomer J, Gooding R, Angelicheva D, King RH, Guillén-Navarro E, Parman Y, et al. Clinical spectrum of CMT4C disease in patients homozygous for the p.Arg1109X mutation in SH3TC2. *Neuromuscul Disord* 2006; 16: 449–53.
- Dyck PJ, Chance P, Lebo R, Carney JA. Hereditary motor and sensory neuropathies. In: Dyck PJ, Thomas PK, Griffin JW, Low PA, Poduslo JF, editors. *Peripheral Neuropathy*. 3rd edn., Philadelphia: W.B. Saunders; 1993. p. 1094–136.
- Eshed Y, Feinberg K, Poliak S, Sabanay H, Sarig-Nadir O, Spiegel I, et al. Gliomedin mediates Schwann cell-axon interaction and the molecular assembly of the nodes of Ranvier. *Neuron* 2005; 47: 215–29.
- Fannon AM, Sherman DL, Ilyina-Gragerova G, Brophy PJ, Friedrich VL Jr, Colman DR. Novel E-cadherin-mediated adhesion in peripheral nerve: Schwann cell architecture is stabilized by autotypic adherens junctions. *J Cell Biol* 1995; 129: 189–202.
- Filbin MT, Walsh FS, Trapp BD, Pizzey JA, Tennekoon GI. Role of myelin P0 protein as a homophilic adhesion molecule. *Nature* 1990; 344: 871–2.
- Gabreëls-Festen A, van Beersum S, Eshuis L, LeGuern E, Gabreëls F, van Engelen B, et al. Study on the gene and phenotypic characterisation of autosomal recessive demyelinating motor and sensory neuropathy (Charcot-Marie-Tooth disease) with a gene locus on chromosome 5q23–q33. *J Neurol Neurosurg Psychiatry* 1999; 66: 569–74.
- Ganley IG, Carroll K, Bittova L, Pfeffer S. Rab9 GTPase Regulates Late Endosome Size and Requires Effector Interaction for Its Stability. *Mol Biol Cell* 2004; 15: 5420–30.
- Gosselin I, Thiffault I, Tétreault M, Chau V, Dicaire MJ, Loiselle L, et al. Founder SH3TC2 mutations are responsible for a CMT4C French-Canadian cluster. *Neuromuscul Disord* 2008; 18: 483–92.
- Griffiths I, Klugmann M, Anderson T, Yool D, Thomson C, Schwab MH, et al. Axonal swellings and degeneration in mice lacking the major proteolipid of myelin. *Science* 1998; 280: 1610–3.
- Keller P, Toomre D, Díaz E, White J, Simons K. Multicolour imaging of post-Golgi sorting and trafficking in live cells. *Nat Cell Biol* 2001; 3: 140–9.
- Kessali M, Zemmouri R, Guilbot A, Maisonneuve T, Brice A, LeGuern E, et al. A clinical, electrophysiologic, neuropathologic, and genetic study of two large Algerian families with an autosomal recessive demyelinating form of Charcot-Marie-Tooth disease. *Neurology* 1997; 48: 867–73.
- Kidd G, Andrews SB, Trapp BD. Axons regulate the distribution of Schwann cell microtubules. *J Neurosci* 1996; 16: 946–54.
- Kleine H, Poreba E, Lesniewicz K, Hassa PO, Hottinger MO, Litchfield DW, et al. Substrate-assisted catalysis by PARP10 limits its activity to mono-ADP-ribosylation. *Mol Cell* 2008; 32: 57–69.
- Kretzer G, Schmoranz J, Low SH, Li X, Gan Y, Weimbs T, et al. Three-dimensional analysis of post-Golgi carrier exocytosis in epithelial cells. *Nat Cell Biol* 2003; 5: 126–36.
- Kroepfl JF, Gardinier MV. Mutually exclusive apicobasolateral sorting of two oligodendroglial membrane proteins, proteolipid protein and myelin/oligodendrocyte glycoprotein, in Madin-Darby canine kidney cells. *J Neurosci Res* 2001; 66: 1140–8.
- Lai F, Stubbs L, Artzt K. Molecular analysis of mouse Rab11b: a new type of mammalian YPT/Rab protein. *Genomics* 1994; 22: 610–6.
- Lapiere LA, Dorn MC, Zimmermann CF, Navarra J, Burnette JO, Goldenring JR. Rab11b resides in a vesicular compartment distinct from Rab11a in parietal cells and other epithelial cells. *Exp Cell Res* 2003; 290: 322–31.

- Lapouge K, Smith SJ, Walker PA, Gamblin SJ, Smerdon SJ, Rittinger K. Structure of the TPR domain of p67phox in complex with Rac-GTP. *Mol Cell* 2000; 6: 899–907.
- Lappe-Siefke C, Goebbels S, Gravel M, Nicksch E, Lee J, Braun PE, et al. Disruption of Cnp1 uncouples oligodendroglial functions in axonal support and myelination. *Nat Genet* 2003; 33: 366–74.
- LeGuern E, Guilbot A, Kessali M, Ravisé N, Tassin J, Maisonneuve T, et al. Homozygosity mapping of an autosomal recessive form of demyelinating Charcot-Marie-Tooth disease to chromosome 5q23-q33. *Hum Mol Genet* 1996; 5: 1685–8.
- Lindsay AJ, McCaffrey MW. Rab11-FIP2 functions in transferrin recycling and associates with endosomal membranes via its C-terminal region. *J Biol Chem* 2002; 277: 27193–9.
- Lupo V, Galindo MI, Martínez-Rubio D, Sevilla T, Vilchez JJ, Palau F, et al. Missense mutations in the SH3TC2 protein causing Charcot-Marie-Tooth disease type 4C affect its localization in the plasma membrane and endocytic pathway. *Hum Mol Genet* 2009; 18: 4603–14.
- Maier O, van der Heide T, Johnson R, de Vries H, Baron W, Hoekstra D. The function of neurofascin155 in oligodendrocytes is regulated by metalloprotease-mediated cleavage and ectodomain shedding. *Exp Cell Res* 2006; 312: 500–11.
- Maurel P, Einheber S, Galinska J, Thaker P, Lam I, Rubin MB, et al. Nectin-like proteins mediate axon Schwann cell interactions along the internode and are essential for myelination. *J Cell Biol* 2007; 178: 861–74.
- Maxfield FR, McGraw TE. Endocytic recycling. *Nat Rev Mol Cell Biol* 2004; 5: 121–32.
- Minuk J, Braun PE. Differential intracellular sorting of the myelin-associated glycoprotein isoforms. *J Neurosci Res* 1996; 44: 411–20.
- Nave KA, Trapp BD. Axon-glial signaling and the glial support of axon function. *Annu Rev Neurosci* 2008; 31: 535–61.
- Pfeiffer SE, Warrington AE, Bansal R. The oligodendrocyte and its many cellular processes. *Trends Cell Biol* 1993; 3: 191–7.
- Prekeris R, Davies JM, Scheller RH. Identification of a novel Rab11/25 binding domain present in Eferin and Rip proteins. *J Biol Chem* 2001; 276: 38966–70.
- Previtali SC, Feltri ML, Archelos JJ, Quattrini A, Wrabetz L, Hartung HP. Role of integrins in the peripheral nervous system. *Prog Neurobiol* 2001; 64: 35–49.
- Roberts RC, Peden AA, Buss F, Bright NA, Latouche M, Reilly MM, et al. Mistargeting of SH3TC2 away from the recycling endosome causes Charcot-Marie-Tooth disease type 4C. *Hum Mol Genet* 2010. Advance Access published on December 22, 2009, doi:10.1093/hmg/ddp565.
- Sager PR, Brown PA, Berlin RD. Analysis of transferrin recycling in mitotic and interphase HeLa cells by quantitative fluorescence microscopy. *Cell* 1984; 39: 275–82.
- Sakurada K, Uchida K, Yamaguchi K, Asaka K, Ito S, Ohmori T, et al. Molecular cloning and characterization of a ras p21-like GTP-binding protein (24KG) from rat liver. *Biochem Biophys Res Commun* 1991; 177: 1224–32.
- Senderek J, Bergmann C, Stendel C, Kirfel J, Verpoorten N, De Jonghe P, et al. Mutations in a gene encoding a novel SH3/TPR domain protein cause autosomal recessive Charcot-Marie-Tooth type 4C neuropathy. *Am J Hum Genet* 2003; 73: 1106–19.
- Simons M, Trotter J. Wrapping it up: the cell biology of myelination. *Curr Opin Neurobiol* 2007; 17: 533–40.
- Spiegel I, Adamsky K, Eshed Y, Milo R, Sabanay H, Sarig-Nadir O, et al. A central role for Ned4 (SynCAM4) in Schwann cell-axon interaction and myelination. *Nat Neurosci* 2007; 10: 861–9.
- Stein BS, Bensch KG, Sussman HH. Complete inhibition of transferring recycling by monensin in K562 cells. *J Biol Chem* 1984; 259: 14762–72.
- Stenmark H. Rab GTPases as coordinators of vesicle traffic. *Nat Rev Mol Cell Biol* 2009; 10: 513–25.
- Trapp BD, Kidd GJ, Hauer P, Mulrenin E, Haney CA, Andrews SB. Polarization of myelinating Schwann cell surface membranes: role of microtubules and the trans-Golgi network. *J Neurosci* 1995; 15: 1797–807.
- Trapp BD, Pfeiffer SE, Anitei M, Kidd GJ. Cell biology of myelin assembly. In: Lazzarini RA, editor. *Myelin biology and disorders*. London: Elsevier academic; 2004. p. 29–48.
- Ullrich O, Reinsch S, Urbé S, Zerial M, Parton RG. Rab11 regulates recycling through the pericentriolar recycling endosome. *J Cell Biol* 1996; 135: 913–24.
- Verheijen MH, Chrast R, Burrola P, Lemke G. Local regulation of fat metabolism in peripheral nerves. *Genes Dev* 2003; 17: 2450–64.
- Wallace DME, Lindsay AJ, Hendrick AG, McCaffrey MW. Rab11-FIP4 interacts with Rab11 in a GTP-dependent manner and its overexpression condenses the Rab11 positive compartment in HeLa cells. *Biochem Biophys Res Commun* 2002; 299: 770–9.
- Westlake CJ, Junutula JR, Simon GC, Pili M, Prekeris R, Scheller RH, et al. Identification of Rab11 as a small GTPase binding protein for the Evi5 oncogene. *Proc Natl Acad Sci USA* 2007; 104: 1236–41.
- Winterstein C, Trotter J, Krämer-Albers EM. Distinct endocytic recycling of myelin proteins promotes oligodendroglial membrane remodeling. *J Cell Sci* 2008; 121: 834–42.
- Wu S, Mehta SQ, Pichaud F, Bellen HJ, Quirocho FA. Sec15 interacts with Rab11 via a novel domain and affects Rab11 localization in vivo. *Nat Struct Mol Biol* 2005; 12: 879–85.

5.3 Characterization of a mouse model of Charcot-Marie-Tooth disease type 4A and 2K

(ongoing collaboration with Paula Juárez Gómez in the lab of Francesc Palau at the “Instituto de Biomedicina de Valencia” in Spain)

Mutations in genes encoding for mitochondrial proteins were previously linked to CMT disease (43). One of these genes is the ganglioside-induced-differentiation-associated protein 1 (GDAP1), which might be a member of the glutathione-S-transferase enzyme family (136, 137). GDAP1 is located at the outer membrane of the mitochondria and is most likely involved in the fission of these organelles. Previous studies demonstrated a strong expression of GDAP1 in both sensory and motor neurons of the PNS and in numerous neurons of the CNS (136, 138). While some studies report a glial expression of GDAP1 as well, others did not find any expression of GDAP1 in Schwann cells (138, 139).

More than 20 mutations in the GDAP1 gene are known to cause either a demyelinating (CMT4A) (140, 141), an axonal (CMT2K) (136, 142) or an intermediate (CMTRIA) (143, 144) form of CMT diseases. CMT4A shows autosomal recessive inheritance, whereas CMT2K can be both recessively and dominantly inherited. It has been difficult to demonstrate if GDAP1 mutations lead primarily to myelin or axonal defects in the PNS. Various missense constructs of GDAP1 tested *in vitro* led to contradictory results, mostly to mitochondrial fragmentation but also to mitochondrial aggregation (138). Therefore, different molecular mechanisms might cause the diverse phenotypes. In order to understand the role of GDAP1 in mitochondrial biology and in disease situation, the group of F. Palau in Valencia (Spain) has recently established a KO mouse model for GDAP1 (GDAP1^{-/-}). In GDAP1^{-/-} mice the first exon was conditionally deleted using the Cre/LoxP-system. I participated in the electrophysiological and morphological characterization of these mice as follows:

Rotarod experiments performed by Paula J. Gómez in Valencia (Spain) revealed a significantly reduced latency to fall for GDAP1^{-/-} mice as compared with GDAP1^{+/+} mice at 3 and 5 months of age. Furthermore, all GDAP1^{-/-} mice and even some GDAP1^{+/-} mice showed a typical hindlimb clasping phenotype, indicating a peripheral neuropathy. To further evaluate functional defects of GDAP1^{-/-} mice I received 2 and 5 months old male mice from P. Gomez. The mice were overall healthy although the GDAP1^{-/-} mice had significantly lower body weight at 5 months of age as compared with age-matched control mice (**Fig. 29A**). A slight increase in blood glucose levels was detectable for both genotypes at 2 months of age which was decreased at 5 months of age back to normal levels in both GDAP1^{-/-} and GDAP1^{+/+} mice (**Fig. 29B**). Interestingly, at both ages I obtained a slight reduction of the MNCV for GDAP1^{-/-} mice which became significant at 5 months of age probably due to a lower variability of the measurements (**Fig. 29C, Table 13**). Further analysis of the CMAP curve

revealed a significant reduction in CMAP latency, area and amplitude in GDAP1^{-/-} mice compared to GDAP1^{+/+} mice at 5 months of age but not at 2 months of age (**Table 13**).

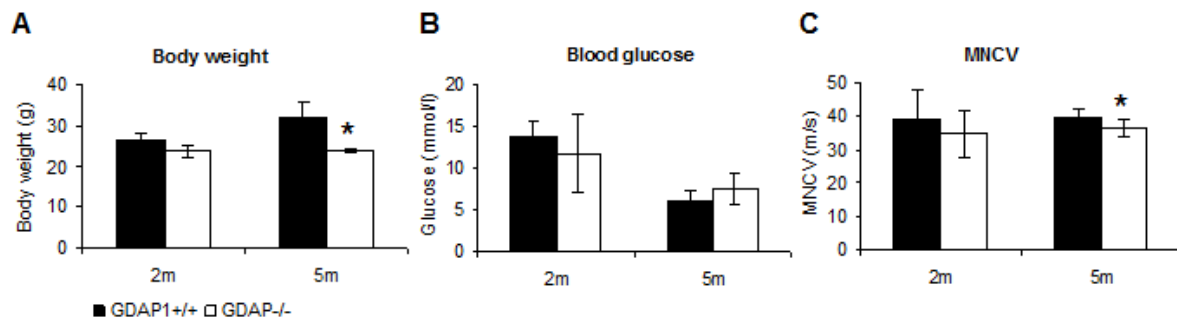


Figure 29 : Physiological properties of 2 and 5 months old GDAP1^{-/-} mice as compared to GDAP1^{+/+} mice.

(A) While the body weight was not different at 2 months of age, GDAP1^{-/-} mice had a significantly lower body weight at 5 months of age. (B) At 2 months of age both genotypes had slightly increased blood glucose levels, while it decreases to normal levels at 5 months of age for both GDAP1^{-/-} and GDAP1^{+/+} mice. (C) Interestingly, young as well as old GDAP1^{-/-} mice had a slight reduction in MNCV which became significant at 5 months as compared to GDAP1^{+/+} mice. n=4; * p-value < 0,05;

A	2m	MNCV (m/s)	Latency (ms)	Duration (ms)	Amplitude (mV)	Area (mV/ms)
	GDAP1 ^{+/+}	37,17 (+/- 7,97)	1,22 (+/- 0,02)	1,56 (+/- 0,18)	3,2 (+/- 0,99)	1,54 (+/- 0,4)
	GDAP1 ^{-/-}	34,87 (+/- 7,08)	1,2 (+/- 0,15)	1,38 (+/- 0,4)	2,42 (+/- 0,59)	1,22 (+/- 0,29)
	p-value	0,4645	0,951	0,3067	0,1413	0,184

B	5m	MNCV (m/s)	Latency (ms)	Duration (ms)	Amplitude (mV)	Area (mV/ms)
	GDAP1 ^{+/+}	39,69 (+/- 2,66)	1,36 (+/- 0,04)	0,85 (+/- 0,04)	3,6 (+/- 1,76)	1,48 (+/- 0,64)
	GDAP1 ^{-/-}	36,5 (+/- 2,47)	1,18 (+/- 0,05)	0,97 (+/- 0,05)	2,19 (+/- 0,98)	0,95 (+/- 0,38)
	p-value	0,0113	0,0024	0,1167	0,0264	0,0346

Table 13 : Shape of the CMAP curve of GDAP1^{-/-} and GDAP1^{+/+} mice at 2 and 5 months of age.

(A) At 2 months of age MNCV, CMAP latency, duration, amplitude and area were normal in GDAP1^{-/-} mice as compared to GDAP1^{+/+} mice. (B) At 5 months of age, MNCV and CMAP latency were significantly reduced. Furthermore, a significant reduction in CMAP amplitude and area suggested axonal loss in GDAP1^{-/-} mice. CMAP duration was not significantly altered in GDAP1^{-/-} versus GDAP1^{+/+} mice. n=4;

To corroborate our electrophysiological and behavioral observations, I performed semithin cross sections of the sciatic nerve of GDAP1^{-/-} and GDAP1^{+/+} mice at 2 and 5 months of age (**Fig. 30A, B**). Interestingly, I could not observe any gross alterations in both sciatic nerve myelination and axonal morphology. Furthermore, counting the number of myelinated fibers per sciatic nerve did not reveal any axonal loss in GDAP1^{-/-} as compared to GDAP1^{+/+} mice at both ages (**Fig. 30C**).

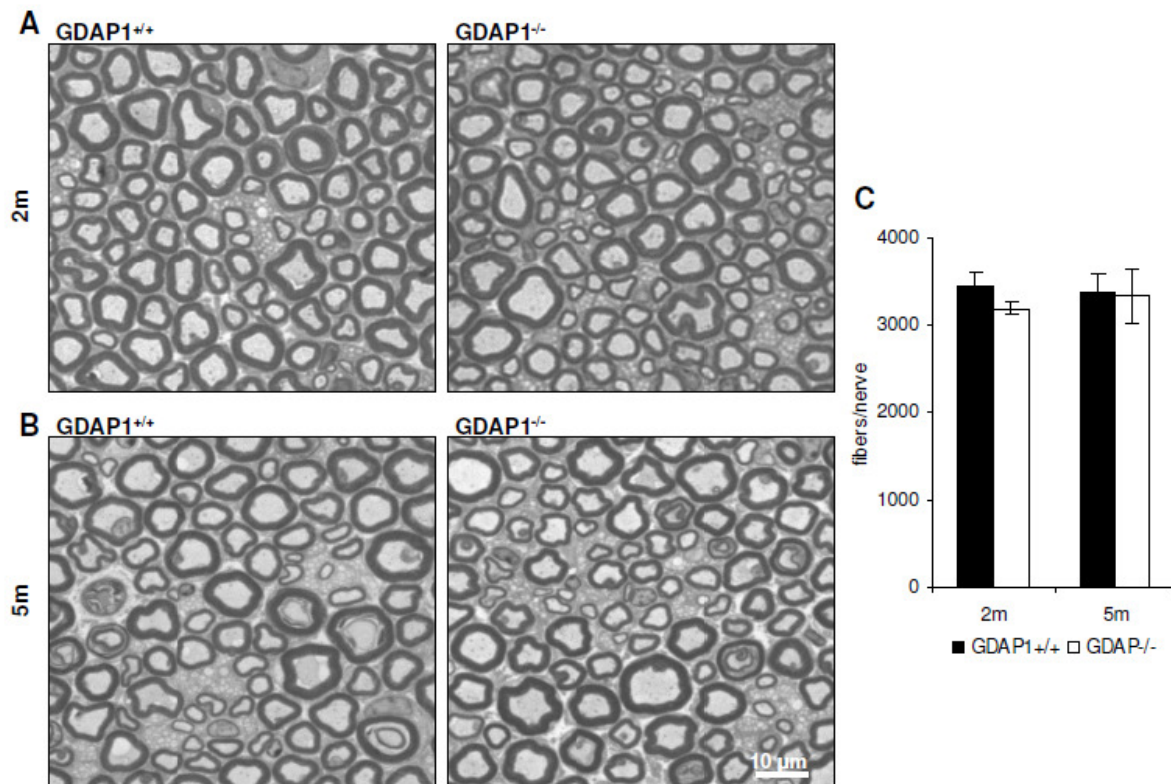


Figure 30 : Preserved sciatic nerve morphology of GDAP1^{-/-} mice at 2 and 5 months of age. (A) Semithin cross sections of GDAP1^{+/+} and GDAP1^{-/-} sciatic nerves at 2 months of age and (B) 5 months of age revealed no gross defects in the sciatic nerve myelination and axonal morphology. (C) Both GDAP1^{+/+} and GDAP1^{-/-} mice had equal numbers of axons per sciatic nerve at both ages. n=3;

The clinical characteristics of patients with GDAP1 mutations (CMT4A, CMT2K or CMT4RIA) are severe with an early-onset and progressive evolution of muscle weakness in feet and hands, atrophy, areflexia and motor-sensory neuropathy (142). However, the newly generated KO mouse model for GDAP1 developed normal. As the increased blood glucose levels were measured for both genotypes and only at 2 months of age, I conclude that this was unrelated to the GDAP1 mutation. Possibly, induced by the change of food or by the stress of the transport. Interestingly, GDAP1^{-/-} mice revealed a lower body weight at 5 months of age than GDAP1^{+/+} mice. In this regard, it would be of interest to measure specifically the weight of muscles in GDAP1^{-/-} mice as compared to GDAP1^{+/+} as it might reflect the severe muscle weakness and atrophy as reported for GDAP1 patients (142). At 2 months of age I could not observe any significant differences in sciatic nerve function and morphology of GDAP1^{-/-} versus GDAP1^{+/+} mice. Interestingly, at 5 months of age GDAP1^{-/-} mice had both a significant reduction in MNCV and CMAP latency indicative for a demyelinating phenotype and a significantly reduced CMAP amplitude and area indicative for axonal alterations. Such a mixed phenotype correlates with the clinical manifestations of GDAP1 patients as previously described (143). However, I could neither observe any signs of demyelination nor axonal loss on semithin cross sections of GDAP1^{-/-} as compared to GDAP1^{+/+} mice at 5 months of age. Potentially, structural alterations might be detectable in older animals (about 1 year of age) as previously described for a KO mouse model for

CMT2A (44). Furthermore it is possible that the electrophysiological alterations are due to changes in ion channels or defects at the neuromuscular junctions that were not evaluated. Even though I did not observe any demyelination, the electrophysiological deficits may be caused by more subtle myelin defects. If the resistance of myelin decreases it will lead to a partial loss of the electrical signal. Electron microscopic analysis and immunostainings on teased fibers for the various ion channels could clarify this hypothesis. Furthermore, since GDAP1 is a mitochondrial protein it might affect the functionality and/or morphology of neuronal mitochondria, a hypothesis which should be further explored as well.

5.4 Characterization of a knockout mouse model of PLEKHG5

Lower motor neuron diseases (LMND) are a group of heterogenous disorders defined by progressive paralysis due to motor neuron degeneration and consequent muscle denervation. In 2007, the pleckstrin homology domain-containing, family G member 5 (PLEKHG5) gene was identified to be one of the causative genes for LMND (145). This form of LMND is autosomal recessively inherited with an early onset leading to tetraplegia in adulthood (146). PLEKHG5 is known to be ubiquitously expressed with the highest expression in the PNS (145). Transfection of mutated PLEKHG5 protein *in vitro* demonstrated a reduced PLEKHG5 stability and reduced activity of the nuclear factor κ B (NF κ B) which is induced by PLEKHG5 as reported previously (145, 147). Interestingly, an accumulation of mutated PLEKHG5 protein was specifically observed in a neuronal cell line (145).

To investigate the role of PLEKHG5 in PNS and LMND pathology we received PLEKHG5 KO female mice (PLEKHG5^{-/-}) from Jay Baraban (John Hopkins Hospital in Baltimore (USA)). I performed physiological and electrophysiological measurements on these mice as compared to PLEKHG5^{+/+} mice at 6 months of age. PLEKHG5^{-/-} mice developed healthy like PLEKHG5^{+/+} mice without any obvious behavioral or walking deficits at 6 months of age. Body weight was normal while blood glucose levels were slightly increased in PLEKHG5^{-/-} mice (**Fig. 31A, B**). Interestingly, overall MNCV recordings on the sciatic nerve revealed a mild but significant reduction in PLEKHG5^{-/-} mice as compared to PLEKHG5^{+/+} mice (**Fig. 31C and table 14**). The resulting CMAP curves had a significant slower CMAP latency, duration and F-wave latency in mutant animals (**Table 14**).

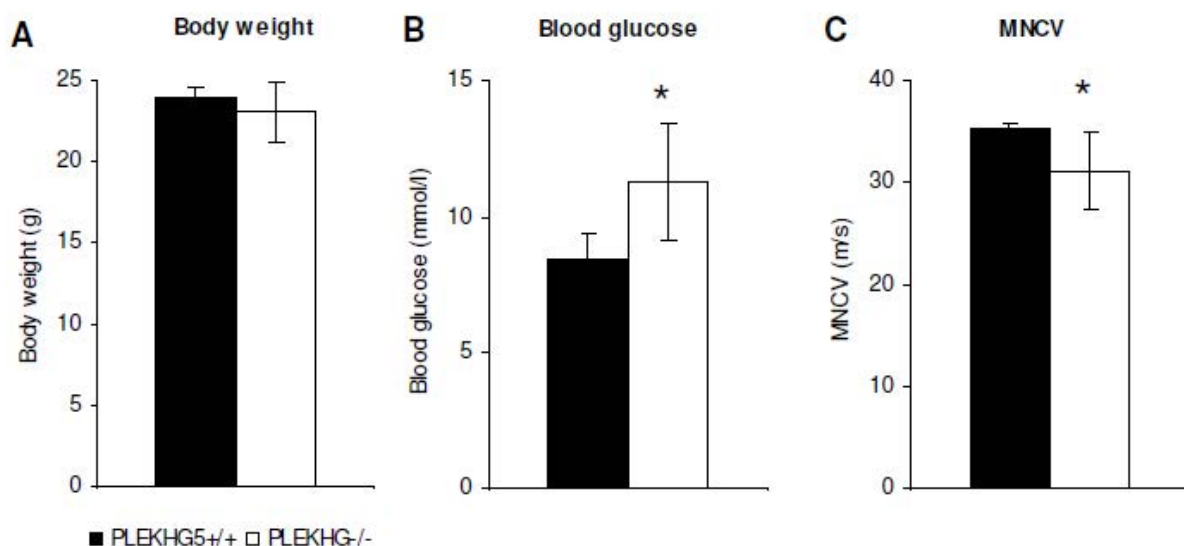


Figure 31 : Physiological characterization of PLEKHG5^{-/-} mice at 6 months of age. (A) PLEKHG5^{-/-} mice had same body weight as PLEKHG5^{+/+} mice at 6 months of age. (B) The blood glucose levels of PLEKHG5^{-/-} animals were slightly but significantly increased as compared to PLEKHG5^{+/+} mice. (C) Moreover, a slight but significant decrease in MNCV was observed in PLEKHG5^{-/-} mice. n of PLEKHG5^{+/+} = 3; n of PLEKHG5^{-/-} = 5; * p-value < 0,05.

	MNCV (m/s)	Latency (ms)	Duration (ms)	Amplitude (mV)	Area (mV/ms)	F-wave latency (ms)
PLEKHG5 ^{+/+}	35,4 (+/- 0,38)	1,34 (+/- 0,09)	0,94 (+/- 0,18)	2,96 (+/- 0,73)	1,45 (+/- 0,34)	6,45 (+/- 0,73)
PLEKHG5 ^{-/-}	31,2 (+/- 3,69)	1,58 (+/- 0,21)	1,22 (+/- 0,22)	2,05 (+/- 0,69)	1,22 (+/- 0,71)	7,22 (+/- 0,44)
p-value	0,0199	0,0376	0,0308	0,0502	0,4389	0,0165

Table 14 : Properties of the CMAP curve of 6 months old PLEKHG5^{-/-} and PLEKHG5^{+/+} mice.

In addition to the reduced MNCV, CMAP latency, duration and F-wave latency was significantly reduced in PLEKHG5^{-/-} mice. CMAP amplitude and area did not change significantly in PLEKHG5^{-/-} mice as compared to PLEKHG5^{+/+} mice. n of PLEKHG5^{+/+} = 3; n of PLEKHG5^{-/-} = 5;

Patients with mutated PLEKHG5 suffer of severe paralysis from childhood on accompanied with either a normal or reduced MNCV (145). While I could not observe any major phenotypical alterations of PLEKHG5^{-/-} mice compared to PLEKHG5^{+/+} mice at 6 months of age I observed a significant reduction in MNCV. However, only 3 PLEKHG5^{-/-} mice contributed to the overall reduction in MNCV whereas 2 other PLEKHG5^{-/-} mice had normal values as for PLEKHG5^{+/+} mice similar to the situation in patients. Together with the reduction of CMAP latency, duration and F-wave latency the reduced MNCV is suggestive for isolating defects of the myelin sheath around peripheral nerves. Moreover, motor neuron loss was observed in patients, most likely due to a downregulation of the anti-apoptotic factor NFkB (145). However, I could not observe any alterations in CMAP amplitude and area which are suggestive for motor axonal loss. Morphological analysis of the sciatic nerve, spinal cord and hind limb muscles will be carried out in our lab and should help to identify potential defects in peripheral nerve myelination, motor neuron survival and muscle innervation.

6. References

1. King, R.H.M. 2005. Nerve trunks and Spinal roots. In *Peripheral Neuropathy*. P.J. Dyck, and P.K. Thomas, editors. Philadelphia: Elsevier Saunders. 35-42.
2. Jessen, K.R., and Mirsky, R. 2005. The origin and development of glial cells in peripheral nerves. *Nat Rev Neurosci* 6:671-682.
3. Kandel, E.R., Schwartz, J.H., and Jessell, T.M. 2000. *Principles of neural science*. New York: McGraw-Hill, Health Professions Division. xli, 1414 p. pp.
4. Sherman, D.L., and Brophy, P.J. 2005. Mechanisms of axon ensheathment and myelin growth. *Nat Rev Neurosci* 6:683-690.
5. Hirokawa, N., and Takemura, R. 2005. Molecular motors and mechanisms of directional transport in neurons. *Nat Rev Neurosci* 6:201-214.
6. Hirokawa, N., Niwa, S., and Tanaka, Y. 2010. Molecular motors in neurons: transport mechanisms and roles in brain function, development, and disease. *Neuron* 68:610-638.
7. Newbern, J., and Birchmeier, C. 2010. Nrg1/ErbB signaling networks in Schwann cell development and myelination. *Semin Cell Dev Biol* 21:922-928.
8. Michailov, G.V., Sereda, M.W., Brinkmann, B.G., Fischer, T.M., Haug, B., Birchmeier, C., Role, L., Lai, C., Schwab, M.H., and Nave, K.A. 2004. Axonal neuregulin-1 regulates myelin sheath thickness. *Science* 304:700-703.
9. Svaren, J., and Meijer, D. 2008. The molecular machinery of myelin gene transcription in Schwann cells. *Glia* 56:1541-1551.
10. Masaki, T., Matsumura, K., Saito, F., Sunada, Y., Shimizu, T., Yorifuji, H., Motoyoshi, K., and Kamakura, K. 2000. Expression of dystroglycan and laminin-2 in peripheral nerve under axonal degeneration and regeneration. *Acta Neuropathol* 99:289-295.
11. Bunge, R.P., Bunge, M.B., and Bates, M. 1989. Movements of the Schwann cell nucleus implicate progression of the inner (axon-related) Schwann cell process during myelination. *J Cell Biol* 109:273-284.
12. Scherer, S.S., and Arroyo, E.J. 2002. Recent progress on the molecular organization of myelinated axons. *J Peripher Nerv Syst* 7:1-12.
13. Salzer, J.L. 2003. Polarized domains of myelinated axons. *Neuron* 40:297-318.
14. Devaux, J.J., Kleopa, K.A., Cooper, E.C., and Scherer, S.S. 2004. KCNQ2 is a nodal K⁺ channel. *J Neurosci* 24:1236-1244.
15. Dedek, K., Kunath, B., Kananura, C., Reuner, U., Jentsch, T.J., and Steinlein, O.K. 2001. Myokymia and neonatal epilepsy caused by a mutation in the voltage sensor of the KCNQ2 K⁺ channel. *Proc Natl Acad Sci U S A* 98:12272-12277.
16. Bhat, M.A., Rios, J.C., Lu, Y., Garcia-Fresco, G.P., Ching, W., St Martin, M., Li, J., Einheber, S., Chesler, M., Rosenbluth, J., et al. 2001. Axon-glia interactions and the

- domain organization of myelinated axons requires neurexin IV/Caspr/Paranodin. *Neuron* 30:369-383.
17. Boyle, M.E., Berglund, E.O., Murai, K.K., Weber, L., Peles, E., and Ranscht, B. 2001. Contactin orchestrates assembly of the septate-like junctions at the paranode in myelinated peripheral nerve. *Neuron* 30:385-397.
 18. Traka, M., Goutebroze, L., Denisenko, N., Bessa, M., Nifli, A., Havaki, S., Iwakura, Y., Fukamauchi, F., Watanabe, K., Soliven, B., et al. 2003. Association of TAG-1 with Caspr2 is essential for the molecular organization of juxtaparanodal regions of myelinated fibers. *J Cell Biol* 162:1161-1172.
 19. Poliak, S., Salomon, D., Elhanany, H., Sabanay, H., Kiernan, B., Pevny, L., Stewart, C.L., Xu, X., Chiu, S.Y., Shrager, P., et al. 2003. Juxtaparanodal clustering of Shaker-like K⁺ channels in myelinated axons depends on Caspr2 and TAG-1. *J Cell Biol* 162:1149-1160.
 20. Chrast, R., Saher, G., Nave, K.A., and Verheijen, M.H. 2011. Lipid metabolism in myelinating glial cells: lessons from human inherited disorders and mouse models. *J Lipid Res* 52:419-434.
 21. Garbay, B., Heape, A.M., Sargueil, F., and Cassagne, C. 2000. Myelin synthesis in the peripheral nervous system. *Prog Neurobiol* 61:267-304.
 22. Saher, G., and Simons, M. 2010. Cholesterol and myelin biogenesis. *Subcell Biochem* 51:489-508.
 23. Coetzee, T., Fujita, N., Dupree, J., Shi, R., Blight, A., Suzuki, K., and Popko, B. 1996. Myelination in the absence of galactocerebroside and sulfatide: normal structure with abnormal function and regional instability. *Cell* 86:209-219.
 24. Patzig, J., Jahn, O., Tenzer, S., Wichert, S.P., de Monasterio-Schrader, P., Rosfa, S., Kuharev, J., Yan, K., Bormuth, I., Bremer, J., et al. 2011. Quantitative and integrative proteome analysis of peripheral nerve myelin identifies novel myelin proteins and candidate neuropathy loci. *J Neurosci* 31:16369-16386.
 25. Jahn, O., Tenzer, S., and Werner, H.B. 2009. Myelin proteomics: molecular anatomy of an insulating sheath. *Mol Neurobiol* 40:55-72.
 26. Greenfield, S., Brostoff, S., Eylar, E.H., and Morell, P. 1973. Protein composition of myelin of the peripheral nervous system. *J Neurochem* 20:1207-1216.
 27. Vavlitou, N., Sargiannidou, I., Markoullis, K., Kyriacou, K., Scherer, S.S., and Kleopa, K.A. 2010. Axonal pathology precedes demyelination in a mouse model of X-linked demyelinating/type I Charcot-Marie Tooth neuropathy. *J Neuropathol Exp Neurol* 69:945-958.
 28. Yin, X., Crawford, T.O., Griffin, J.W., Tu, P., Lee, V.M., Li, C., Roder, J., and Trapp, B.D. 1998. Myelin-associated glycoprotein is a myelin signal that modulates the caliber of myelinated axons. *J Neurosci* 18:1953-1962.

29. Readhead, C., and Hood, L. 1990. The dysmyelinating mouse mutations shiverer (shi) and myelin deficient (shimld). *Behav Genet* 20:213-234.
30. Gould, R.M., Byrd, A.L., and Barbarese, E. 1995. The number of Schmidt-Lanterman incisures is more than doubled in shiverer PNS myelin sheaths. *J Neurocytol* 24:85-98.
31. Giese, K.P., Martini, R., Lemke, G., Soriano, P., and Schachner, M. 1992. Mouse P0 gene disruption leads to hypomyelination, abnormal expression of recognition molecules, and degeneration of myelin and axons. *Cell* 71:565-576.
32. Court, F.A., Brophy, P.J., and Ribchester, R.R. 2008. Remodeling of motor nerve terminals in demyelinating axons of periaxin-null mice. *Glia* 56:471-479.
33. Adlkofer, K., Martini, R., Aguzzi, A., Zielasek, J., Toyka, K.V., and Suter, U. 1995. Hypermyelination and demyelinating peripheral neuropathy in Pmp22-deficient mice. *Nat Genet* 11:274-280.
34. Mallik, A., and Weir, A.I. 2005. Nerve conduction studies: essentials and pitfalls in practice. *J Neurol Neurosurg Psychiatry* 76 Suppl 2:ii23-31.
35. Arimura, K., Sonoda, Y., Watanabe, O., Nagado, T., Kurono, A., Tomimitsu, H., Otsuka, R., Kameyama, M., and Osame, M. 2002. Isaacs' syndrome as a potassium channelopathy of the nerve. *Muscle Nerve Suppl* 11:S55-58.
36. Tomlinson, S.E., Tan, S.V., Kullmann, D.M., Griggs, R.C., Burke, D., Hanna, M.G., and Bostock, H. 2010. Nerve excitability studies characterize Kv1.1 fast potassium channel dysfunction in patients with episodic ataxia type 1. *Brain* 133:3530-3540.
37. Shibuya, K., Misawa, S., Arai, K., Nakata, M., Kanai, K., Yoshiyama, Y., Ito, K., Isole, S., Noto, Y., Nasu, S., et al. 2011. Markedly reduced axonal potassium channel expression in human sporadic amyotrophic lateral sclerosis: An immunohistochemical study. *Exp Neurol* 232:149-153.
38. Hart, I.K., Maddison, P., Newsom-Davis, J., Vincent, A., and Mills, K.R. 2002. Phenotypic variants of autoimmune peripheral nerve hyperexcitability. *Brain* 125:1887-1895.
39. Nagado, T., Arimura, K., Sonoda, Y., Kurono, A., Horikiri, Y., Kameyama, A., Kameyama, M., Pongs, O., and Osame, M. 1999. Potassium current suppression in patients with peripheral nerve hyperexcitability. *Brain* 122 (Pt 11):2057-2066.
40. Quasthoff, S. 1998. The role of axonal ion conductances in diabetic neuropathy: a review. *Muscle Nerve* 21:1246-1255.
41. Zhou, L., Messing, A., and Chiu, S.Y. 1999. Determinants of excitability at transition zones in Kv1.1-deficient myelinated nerves. *J Neurosci* 19:5768-5781.
42. Vabnick, I., Trimmer, J.S., Schwarz, T.L., Levinson, S.R., Risal, D., and Shrager, P. 1999. Dynamic potassium channel distributions during axonal development prevent aberrant firing patterns. *J Neurosci* 19:747-758.

43. Timmerman, V., Clowes, V.E., and Reid, E. 2012. Overlapping molecular pathological themes link Charcot-Marie-Tooth neuropathies and hereditary spastic paraplegias. *Exp Neurol*.
44. Cartoni, R., Arnaud, E., Medard, J.J., Poirot, O., Courvoisier, D.S., Chrast, R., and Martinou, J.C. 2010. Expression of mitofusin 2(R94Q) in a transgenic mouse leads to Charcot-Marie-Tooth neuropathy type 2A. *Brain* 133:1460-1469.
45. Arnaud, E., Zenker, J., de Preux Charles, A.S., Stendel, C., Roos, A., Medard, J.J., Tricaud, N., Kleine, H., Luscher, B., Weis, J., et al. 2009. SH3TC2/KIAA1985 protein is required for proper myelination and the integrity of the node of Ranvier in the peripheral nervous system. *Proc Natl Acad Sci U S A* 106:17528-17533.
46. Verheijen, M.H., Camargo, N., Verdier, V., Nadra, K., de Preux Charles, A.S., Medard, J.J., Luoma, A., Crowther, M., Inouye, H., Shimano, H., et al. 2009. SCAP is required for timely and proper myelin membrane synthesis. *Proc Natl Acad Sci U S A* 106:21383-21388.
47. Nadra, K., de Preux Charles, A.S., Medard, J.J., Hendriks, W.T., Han, G.S., Gres, S., Carman, G.M., Saulnier-Blache, J.S., Verheijen, M.H., and Chrast, R. 2008. Phosphatidic acid mediates demyelination in Lpin1 mutant mice. *Genes Dev* 22:1647-1661.
48. Inglis, H.R., Csurhes, P.A., and McCombe, P.A. 2007. Antibody responses to peptides of peripheral nerve myelin proteins P0 and P2 in patients with inflammatory demyelinating neuropathy. *J Neurol Neurosurg Psychiatry* 78:419-422.
49. Milner, P., Lovelidge, C.A., Taylor, W.A., and Hughes, R.A. 1987. P0 myelin protein produces experimental allergic neuritis in Lewis rats. *J Neurol Sci* 79:275-285.
50. Rostami, A., Brown, M.J., Lisak, R.P., Sumner, A.J., Zweiman, B., and Pleasure, D.E. 1984. The role of myelin P2 protein in the production of experimental allergic neuritis. *Ann Neurol* 16:680-685.
51. Gabriel, C.M., Hughes, R.A., Moore, S.E., Smith, K.J., and Walsh, F.S. 1998. Induction of experimental autoimmune neuritis with peripheral myelin protein-22. *Brain* 121 (Pt 10):1895-1902.
52. Tomlinson, D.R., and Gardiner, N.J. 2008. Glucose neurotoxicity. *Nat Rev Neurosci* 9:36-45.
53. Harvey, R.A., and Ferrier, D.R. 2011. *Lippincott's illustrated reviews: Biochemistry*. Philadelphia: Wolters Kluwer Health. 520 p. pp.
54. Nolan, C.J., Damm, P., and Prentki, M. 2011. Type 2 diabetes across generations: from pathophysiology to prevention and management. *Lancet* 378:169-181.
55. Robertson, D.M., and Sima, A.A. 1980. Diabetic neuropathy in the mutant mouse [C57BL/ks(db/db)]: a morphometric study. *Diabetes* 29:60-67.

56. Sima, A.A. 2003. New insights into the metabolic and molecular basis for diabetic neuropathy. *Cell Mol Life Sci* 60:2445-2464.
57. Zochodne, D.W. 2007. Diabetes mellitus and the peripheral nervous system: manifestations and mechanisms. *Muscle Nerve* 36:144-166.
58. Sima, A.A., Nathaniel, V., Bril, V., McEwen, T.A., and Greene, D.A. 1988. Histopathological heterogeneity of neuropathy in insulin-dependent and non-insulin-dependent diabetes, and demonstration of axo-glial dysjunction in human diabetic neuropathy. *J Clin Invest* 81:349-364.
59. Sugimoto, K., Murakawa, Y., and Sima, A.A. 2000. Diabetic neuropathy--a continuing enigma. *Diabetes Metab Res Rev* 16:408-433.
60. Malik, R.A., Tesfaye, S., Newrick, P.G., Walker, D., Rajbhandari, S.M., Siddique, I., Sharma, A.K., Boulton, A.J., King, R.H., Thomas, P.K., et al. 2005. Sural nerve pathology in diabetic patients with minimal but progressive neuropathy. *Diabetologia* 48:578-585.
61. Misawa, S., Kuwabara, S., Kanai, K., Tamura, N., Hiraga, A., Nakata, M., Ogawara, K., and Hattori, T. 2005. Axonal potassium conductance and glycemic control in human diabetic nerves. *Clin Neurophysiol* 116:1181-1187.
62. Misawa, S., Sakurai, K., Shibuya, K., Iose, S., Kanai, K., Ogino, J., Ishikawa, K., and Kuwabara, S. 2009. Neuropathic pain is associated with increased nodal persistent Na(+) currents in human diabetic neuropathy. *J Peripher Nerv Syst* 14:279-284.
63. Cao, X.H., Byun, H.S., Chen, S.R., Cai, Y.Q., and Pan, H.L. 2010. Reduction in voltage-gated K⁺ channel activity in primary sensory neurons in painful diabetic neuropathy: role of brain-derived neurotrophic factor. *J Neurochem* 114:1460-1475.
64. Craner, M.J., Klein, J.P., Renganathan, M., Black, J.A., and Waxman, S.G. 2002. Changes of sodium channel expression in experimental painful diabetic neuropathy. *Ann Neurol* 52:786-792.
65. Hummel, K.P., Dickie, M.M., and Coleman, D.L. 1966. Diabetes, a new mutation in the mouse. *Science* 153:1127-1128.
66. Herberg, L., and Coleman, D.L. 1977. Laboratory animals exhibiting obesity and diabetes syndromes. *Metabolism* 26:59-99.
67. Hirai, A., Yasuda, H., Joko, M., Maeda, T., and Kikkawa, R. 2000. Evaluation of diabetic neuropathy through the quantitation of cutaneous nerves. *J Neurol Sci* 172:55-62.
68. Shun, C.T., Chang, Y.C., Wu, H.P., Hsieh, S.C., Lin, W.M., Lin, Y.H., Tai, T.Y., and Hsieh, S.T. 2004. Skin denervation in type 2 diabetes: correlations with diabetic duration and functional impairments. *Brain* 127:1593-1605.
69. Sima, A.A., and Robertson, D.M. 1978. Peripheral neuropathy in mutant diabetic mouse [C57BL/Ks (db/db)]. *Acta Neuropathol* 41:85-89.

70. Sullivan, K.A., Hayes, J.M., Wiggin, T.D., Backus, C., Su Oh, S., Lentz, S.I., Brosius, F., 3rd, and Feldman, E.L. 2007. Mouse models of diabetic neuropathy. *Neurobiol Dis* 28:276-285.
71. Furuhashi, M., and Hotamisligil, G.S. 2008. Fatty acid-binding proteins: role in metabolic diseases and potential as drug targets. *Nat Rev Drug Discov* 7:489-503.
72. Liu, R.Z., Li, X., and Godbout, R. 2008. A novel fatty acid-binding protein (FABP) gene resulting from tandem gene duplication in mammals: transcription in rat retina and testis. *Genomics* 92:436-445.
73. Veerkamp, J.H., and Zimmerman, A.W. 2001. Fatty acid-binding proteins of nervous tissue. *J Mol Neurosci* 16:133-142; discussion 151-137.
74. Chmurzynska, A. 2006. The multigene family of fatty acid-binding proteins (FABPs): function, structure and polymorphism. *J Appl Genet* 47:39-48.
75. Narayanan, V., Kaestner, K.H., and Tennekoon, G.I. 1991. Structure of the mouse myelin P2 protein gene. *J Neurochem* 57:75-80.
76. Bharucha, V.A., Peden, K.W., Subach, B.R., Narayanan, V., and Tennekoon, G.I. 1993. Characterization of the cis-acting elements of the mouse myelin P2 promoter. *J Neurosci Res* 36:508-519.
77. Sedzik, J., and Jastrzebski, J.P. 2011. High-resolution structural model of porcine P2 myelin membrane protein with associated fatty acid ligand: fact or artifact? *J Neurosci Res* 89:909-920.
78. Kadlubowski, M., Hughes, R.A., and Gregson, N.A. 1984. Spontaneous and experimental neuritis and the distribution of the myelin protein P2 in the nervous system. *J Neurochem* 42:123-129.
79. Trapp, B.D., Dubois-Dalcq, M., and Quarles, R.H. 1984. Ultrastructural localization of P2 protein in actively myelinating rat Schwann cells. *J Neurochem* 43:944-948.
80. Trapp, B.D., McIntyre, L.J., Quarles, R.H., Sternberger, N.H., and Webster, H.D. 1979. Immunocytochemical localization of rat peripheral nervous system myelin proteins: P2 protein is not a component of all peripheral nervous system myelin sheaths. *Proc Natl Acad Sci U S A* 76:3552-3556.
81. Uyemura, K., Yoshimura, K., Suzuki, M., and Kitamura, K. 1984. Lipid binding activities of the P2 protein in peripheral nerve myelin. *Neurochem Res* 9:1509-1514.
82. Smyth, G.K. 2004. Linear models and empirical bayes methods for assessing differential expression in microarray experiments. *Stat Appl Genet Mol Biol* 3:Article3.
83. Benjamini, Y., and Hochberg, Y. 1995. Controlling the False Discovery Rate - a Practical and Powerful Approach to Multiple Testing. *Journal of the Royal Statistical Society Series B-Methodological* 57:289-300.
84. Verheijen, M.H., Chrast, R., Burrola, P., and Lemke, G. 2003. Local regulation of fat metabolism in peripheral nerves. *Genes Dev* 17:2450-2464.

85. Kodama, H., Fujita, M., and Yamaguchi, I. 1994. Development of hyperglycaemia and insulin resistance in conscious genetically diabetic (C57BL/KsJ-db/db) mice. *Diabetologia* 37:739-744.
86. Coleman, D.L. 1978. Obese and diabetes: two mutant genes causing diabetes-obesity syndromes in mice. *Diabetologia* 14:141-148.
87. Sun, X.Y., Takagishi, Y., Okabe, E., Chishima, Y., Kanou, Y., Murase, S., Mizumura, K., Inaba, M., Komatsu, Y., Hayashi, Y., et al. 2009. A novel Caspr mutation causes the shambling mouse phenotype by disrupting axoglial interactions of myelinated nerves. *J Neuropathol Exp Neurol* 68:1207-1218.
88. Stys, P.K., Ransom, B.R., and Waxman, S.G. 1991. Compound action potential of nerve recorded by suction electrode: a theoretical and experimental analysis. *Brain Res* 546:18-32.
89. Krishnan, A.V., and Kiernan, M.C. 2005. Altered nerve excitability properties in established diabetic neuropathy. *Brain* 128:1178-1187.
90. Bae, J.S., Kim, O.K., and Kim, J.M. 2011. Altered nerve excitability in subclinical/early diabetic neuropathy: evidence for early neurovascular process in diabetes mellitus? *Diabetes Res Clin Pract* 91:183-189.
91. Glazebrook, P.A., Ramirez, A.N., Schild, J.H., Shieh, C.C., Doan, T., Wible, B.A., and Kunze, D.L. 2002. Potassium channels Kv1.1, Kv1.2 and Kv1.6 influence excitability of rat visceral sensory neurons. *J Physiol* 541:467-482.
92. Eng, D.L., Gordon, T.R., Kocsis, J.D., and Waxman, S.G. 1988. Development of 4-AP and TEA sensitivities in mammalian myelinated nerve fibers. *J Neurophysiol* 60:2168-2179.
93. Honmou, O., Utzschneider, D.A., Rizzo, M.A., Bowe, C.M., Waxman, S.G., and Kocsis, J.D. 1994. Delayed depolarization and slow sodium currents in cutaneous afferents. *J Neurophysiol* 71:1627-1637.
94. Kocsis, J.D., Waxman, S.G., Hildebrand, C., and Ruiz, J.A. 1982. Regenerating mammalian nerve fibres: changes in action potential waveform and firing characteristics following blockage of potassium conductance. *Proc R Soc Lond B Biol Sci* 217:77-87.
95. Smart, S.L., Lopantsev, V., Zhang, C.L., Robbins, C.A., Wang, H., Chiu, S.Y., Schwartzkroin, P.A., Messing, A., and Tempel, B.L. 1998. Deletion of the K(V)1.1 potassium channel causes epilepsy in mice. *Neuron* 20:809-819.
96. Devaux, J., Gola, M., Jacquet, G., and Crest, M. 2002. Effects of K⁺ channel blockers on developing rat myelinated CNS axons: identification of four types of K⁺ channels. *J Neurophysiol* 87:1376-1385.

97. Schwarz, J.R., Glassmeier, G., Cooper, E.C., Kao, T.C., Nodera, H., Tabuena, D., Kaji, R., and Bostock, H. 2006. KCNQ channels mediate IKs, a slow K⁺ current regulating excitability in the rat node of Ranvier. *J Physiol* 573:17-34.
98. Sittl, R., Carr, R.W., Fleckenstein, J., and Grafe, P. 2010. Enhancement of axonal potassium conductance reduces nerve hyperexcitability in an in vitro model of oxaliplatin-induced acute neuropathy. *Neurotoxicology* 31:694-700.
99. Wang, H., Allen, M.L., Grigg, J.J., Noebels, J.L., and Tempel, B.L. 1995. Hypomyelination alters K⁺ channel expression in mouse mutants shiverer and Trembler. *Neuron* 15:1337-1347.
100. Devaux, J.J. 2010. The C-terminal domain of ssIV-spectrin is crucial for KCNQ2 aggregation and excitability at nodes of Ranvier. *J Physiol* 588:4719-4730.
101. Arroyo, E.J., Sirkowski, E.E., Chitale, R., and Scherer, S.S. 2004. Acute demyelination disrupts the molecular organization of peripheral nervous system nodes. *J Comp Neurol* 479:424-434.
102. Verdier, V., Csardi, G., de Preux-Charles, A.S., Medard, J.J., Smit, A.B., Verheijen, M.H., Bergmann, S., and Chrast, R. 2012. Aging of myelinating glial cells predominantly affects lipid metabolism and immune response pathways. *Glia*.
103. Zorick, T.S., Syroid, D.E., Arroyo, E., Scherer, S.S., and Lemke, G. 1996. The transcription factors SCIP and Krox-20 mark distinct stages and cell fates in Schwann cell differentiation. *Mol Cell Neurosci* 8:129-145.
104. Suresh, S., Wang, C., Nanekar, R., Kursula, P., and Edwardson, J.M. 2010. Myelin basic protein and myelin protein 2 act synergistically to cause stacking of lipid bilayers. *Biochemistry* 49:3456-3463.
105. Dupouey, P., Jacque, C., Bourre, J.M., Cesselin, F., Privat, A., and Baumann, N. 1979. Immunochemical studies of myelin basic protein in shiverer mouse devoid of major dense line of myelin. *Neurosci Lett* 12:113-118.
106. Mikoshiba, K., Kohsaka, S., Takamatsu, K., and Tsukada, Y. 1981. Neurochemical and morphological studies on the myelin of peripheral nervous system from Shiverer mutant mice: absence of basic proteins common to central nervous system. *Brain Res* 204:455-460.
107. Mikoshiba, K., Takamatsu, K., and Tsukada, Y. 1983. Peripheral nervous system of shiverer mutant mice: developmental change of myelin components and immunohistochemical demonstration of the absence of MBP and presence of P2 protein. *Brain Res* 283:71-79.
108. Winter, J. 1982. Shiverer peripheral myelin contains P2. *Nature* 298:471-472.
109. Krishnan, A.V., Lin, C.S., and Kiernan, M.C. 2008. Activity-dependent excitability changes suggest Na⁺/K⁺ pump dysfunction in diabetic neuropathy. *Brain* 131:1209-1216.

110. Bianchi, R., Marelli, C., Marini, P., Fabris, M., Triban, C., and Fiori, M.G. 1990. Diabetic neuropathy in db/db mice develops independently of changes in ATPase and aldose reductase. A biochemical and immunohistochemical study. *Diabetologia* 33:131-136.
111. Hanker, J.S., Ambrose, W.W., Yates, P.E., Koch, G.G., and Carson, K.A. 1980. Peripheral neuropathy in mouse hereditary diabetes mellitus. I. Comparison of neurologic, histologic, and morphometric parameters with dystonic mice. *Acta Neuropathol* 51:145-153.
112. Norido, F., Canella, R., Zanoni, R., and Gorio, A. 1984. Development of diabetic neuropathy in the C57BL/Ks (db/db) mouse and its treatment with gangliosides. *Exp Neurol* 83:221-232.
113. Wright, D.E., Johnson, M.S., Arnett, M.G., Smittkamp, S.E., and Ryals, J.M. 2007. Selective changes in nocifensive behavior despite normal cutaneous axon innervation in leptin receptor-null mutant (db/db) mice. *J Peripher Nerv Syst* 12:250-261.
114. Carson, K.A., Bossen, E.H., and Hanker, J.S. 1980. Peripheral neuropathy in mouse hereditary diabetes mellitus. II. Ultrastructural correlates of degenerative and regenerative changes. *Neuropathol Appl Neurobiol* 6:361-374.
115. Pickup, J.C., and Williams, G. 2003. *Textbook of diabetes*. Malden, Mass.: Blackwell Science.
116. Shirasaki, N., and Rosenbluth, J. 1991. Structural abnormalities in freeze-fractured sciatic nerve fibres of diabetic mice. *J Neurocytol* 20:573-584.
117. Cheng, H.T., Dauch, J.R., Hayes, J.M., Hong, Y., and Feldman, E.L. 2009. Nerve growth factor mediates mechanical allodynia in a mouse model of type 2 diabetes. *J Neuropathol Exp Neurol* 68:1229-1243.
118. Seneviratne, K.N., and Weerasuriya, A. 1974. Nodal gap substance in diabetic nerve. *J Neurol Neurosurg Psychiatry* 37:502-513.
119. Nagaya, N., and Papazian, D.M. 1997. Potassium channel alpha and beta subunits assemble in the endoplasmic reticulum. *J Biol Chem* 272:3022-3027.
120. Sobko, A., Peretz, A., Shirihi, O., Etkin, S., Cherepanova, V., Dagan, D., and Attali, B. 1998. Heteromultimeric delayed-rectifier K⁺ channels in schwann cells: developmental expression and role in cell proliferation. *J Neurosci* 18:10398-10408.
121. Gu, C., and Barry, J. 2011. Function and mechanism of axonal targeting of voltage-sensitive potassium channels. *Prog Neurobiol* 94:115-132.
122. Perdiz, D., Mackeh, R., Pous, C., and Baillet, A. 2011. The ins and outs of tubulin acetylation: more than just a post-translational modification? *Cell Signal* 23:763-771.
123. Gu, C., and Gu, Y. 2011. Clustering and activity tuning of Kv1 channels in myelinated hippocampal axons. *J Biol Chem* 286:25835-25847.

124. Sima, A.A., Zhang, W., Li, Z.G., Murakawa, Y., and Pierson, C.R. 2004. Molecular alterations underlie nodal and paranodal degeneration in type 1 diabetic neuropathy and are prevented by C-peptide. *Diabetes* 53:1556-1563.
125. Sima, A.A., and Kamiya, H. 2006. Diabetic neuropathy differs in type 1 and type 2 diabetes. *Ann N Y Acad Sci* 1084:235-249.
126. Brown, A.A., Xu, T., Arroyo, E.J., Levinson, S.R., Brophy, P.J., Peles, E., and Scherer, S.S. 2001. Molecular organization of the nodal region is not altered in spontaneously diabetic BB-Wistar rats. *J Neurosci Res* 65:139-149.
127. Elmas, I., Baslo, M.B., Ertas, M., and Kaya, M. 2002. Compound muscle action potential analysis in different death models: significance for the estimation of early postmortem interval. *Forensic Sci Int* 127:75-81.
128. Guttman, M., and Rinn, J.L. 2012. Modular regulatory principles of large non-coding RNAs. *Nature* 482:339-346.
129. Kowalczyk, M.S., Hughes, J.R., Garrick, D., Lynch, M.D., Sharpe, J.A., Sloane-Stanley, J.A., McGowan, S.J., De Gobbi, M., Hosseini, M., Vernimmen, D., et al. 2012. Intragenic Enhancers Act as Alternative Promoters. *Mol Cell*.
130. Shi, H., Kokoeva, M.V., Inouye, K., Tzameli, I., Yin, H., and Flier, J.S. 2006. TLR4 links innate immunity and fatty acid-induced insulin resistance. *J Clin Invest* 116:3015-3025.
131. Inoue, Y., Nakamura, R., Mikoshiba, K., and Tsukada, Y. 1981. Fine structure of the central myelin sheath in the myelin deficient mutant Shiverer mouse, with special reference to the pattern of myelin formation by oligodendroglia. *Brain Res* 219:85-94.
132. Hoshi, T., Suzuki, A., Hayashi, S., Tohyama, K., Hayashi, A., Yamaguchi, Y., Takeuchi, K., and Baba, H. 2007. Nodal protrusions, increased Schmidt-Lanterman incisures, and paranodal disorganization are characteristic features of sulfatide-deficient peripheral nerves. *Glia* 55:584-594.
133. Inouye, H., Ganser, A.L., and Kirschner, D.A. 1985. Shiverer and normal peripheral myelin compared: basic protein localization, membrane interactions, and lipid composition. *J Neurochem* 45:1911-1922.
134. Stoffel, W., Boison, D., and Bussow, H. 1997. Functional analysis in vivo of the double mutant mouse deficient in both proteolipid protein (PLP) and myelin basic protein (MBP) in the central nervous system. *Cell Tissue Res* 289:195-206.
135. Senderek, J., Bergmann, C., Stendel, C., Kirfel, J., Verpoorten, N., De Jonghe, P., Timmerman, V., Chrast, R., Verheijen, M.H., Lemke, G., et al. 2003. Mutations in a gene encoding a novel SH3/TPR domain protein cause autosomal recessive Charcot-Marie-Tooth type 4C neuropathy. *Am J Hum Genet* 73:1106-1119.
136. Cuesta, A., Pedrola, L., Sevilla, T., Garcia-Planells, J., Chumillas, M.J., Mayordomo, F., LeGuern, E., Marin, I., Vilchez, J.J., and Palau, F. 2002. The gene encoding

- ganglioside-induced differentiation-associated protein 1 is mutated in axonal Charcot-Marie-Tooth type 4A disease. *Nat Genet* 30:22-25.
137. Marco, A., Cuesta, A., Pedrola, L., Palau, F., and Marin, I. 2004. Evolutionary and structural analyses of GDAP1, involved in Charcot-Marie-Tooth disease, characterize a novel class of glutathione transferase-related genes. *Mol Biol Evol* 21:176-187.
 138. Pedrola, L., Espert, A., Valdes-Sanchez, T., Sanchez-Piris, M., Sirkowski, E.E., Scherer, S.S., Farinas, I., and Palau, F. 2008. Cell expression of GDAP1 in the nervous system and pathogenesis of Charcot-Marie-Tooth type 4A disease. *J Cell Mol Med* 12:679-689.
 139. Niemann, A., Ruegg, M., La Padula, V., Schenone, A., and Suter, U. 2005. Ganglioside-induced differentiation associated protein 1 is a regulator of the mitochondrial network: new implications for Charcot-Marie-Tooth disease. *Journal of Cell Biology* 170:1067-1078.
 140. Baxter, R.V., Ben Othmane, K., Rochelle, J.M., Stajich, J.E., Hulette, C., Dew-Knight, S., Hentati, F., Ben Hamida, M., Bel, S., Stenger, J.E., et al. 2002. Ganglioside-induced differentiation-associated protein-1 is mutant in Charcot-Marie-Tooth disease type 4A/8q21. *Nat Genet* 30:21-22.
 141. Fusco, C., Uchino, V., Barbon, G., Bonini, E., Mostacciuolo, M.L., Frattini, D., Pisani, F., and Giustina, E.D. 2011. The homozygous ganglioside-induced differentiation-associated protein 1 mutation c.373C > T causes a very early-onset neuropathy: case report and literature review. *J Child Neurol* 26:49-57.
 142. Sevilla, T., Cuesta, A., Chumillas, M.J., Mayordomo, F., Pedrola, L., Palau, F., and Vilchez, J.J. 2003. Clinical, electrophysiological and morphological findings of Charcot-Marie-Tooth neuropathy with vocal cord palsy and mutations in the GDAP1 gene. *Brain* 126:2023-2033.
 143. Senderek, J., Bergmann, C., Ramaekers, V.T., Nelis, E., Bernert, G., Makowski, A., Zuchner, S., De Jonghe, P., Rudnik-Schoneborn, S., Zerres, K., et al. 2003. Mutations in the ganglioside-induced differentiation-associated protein-1 (GDAP1) gene in intermediate type autosomal recessive Charcot-Marie-Tooth neuropathy. *Brain* 126:642-649.
 144. Kabzinska, D., Kochanski, A., Drac, H., Rowinska-Marcinska, K., Ryniewicz, B., Pedrola, L., Palau, F., and Hausmanowa-Petrusewicz, I. 2006. A novel Met116Thr mutation in the GDAP1 gene in a Polish family with the axonal recessive Charcot-Marie-Tooth type 4 disease. *J Neurol Sci* 241:7-11.
 145. Maystadt, I., Rezsohazy, R., Barkats, M., Duque, S., Vannuffel, P., Remacle, S., Lambert, B., Najimi, M., Sokal, E., Munnich, A., et al. 2007. The nuclear factor kappaB-activator gene PLEKHG5 is mutated in a form of autosomal recessive lower motor neuron disease with childhood onset. *Am J Hum Genet* 81:67-76.

146. Maystadt, I., Zarhrate, M., Leclair-Richard, D., Estournet, B., Barois, A., Renault, F., Roton, M.C., Durand, M.C., Lefebvre, S., Munnich, A., et al. 2006. A gene for an autosomal recessive lower motor neuron disease with childhood onset maps to 1p36. *Neurology* 67:120-124.
147. Matsuda, A., Suzuki, Y., Honda, G., Muramatsu, S., Matsuzaki, O., Nagano, Y., Doi, T., Shimotohno, K., Harada, T., Nishida, E., et al. 2003. Large-scale identification and characterization of human genes that activate NF-kappaB and MAPK signaling pathways. *Oncogene* 22:3307-3318.